

TWO PHOTON PHYSICS WITH THE ARGUS DETECTOR

KENNETH W. MCLEAN
Department of Physics
McGill University, Montreal, Quebec

M.Sc. Thesis

January 1985

copy 1

TWO PHOTON PHYSICS WITH THE ARGUS DETECTOR

KENNETH W. MCLEAN

Department of Physics

McGill University, Montreal, Québec

31/1/85

**A thesis submitted to the Faculty of Graduate Studies and
Research in partial fulfilment of the requirements for the
degree of Master of Science in Physics.**

c Kenneth McLean, 1985

ABSTRACT

The results of Monte Carlo simulations of measurements of $e^+e^- \rightarrow e^+e^- \gamma\gamma \rightarrow e^+e^- \text{hadrons}$ are presented. The opportunities for tagging the scattered e^+e^- using the unique beam optics of the DORIS II storage ring are described together with the design optimization of two high resolution arrays of Bismuth Germanium Oxide used to measure the energies of these leptons. These "taggers" will allow determination of the $\gamma\gamma$ invariant mass with small systematic error and relatively high acceptance. This will enable the ARGUS experiment, with the modifications suggested here, to perform the first measurement of the total hadronic cross-section in $\gamma\gamma$ collisions with reasonable systematic error at low invariant masses. These Monte Carlo studies involved development of a simple event generator for $e^+e^- \rightarrow e^+e^- \gamma^* \gamma^*$ and several final state generators for QED and Hadronic processes. Simulations of the ARGUS Detector, Trigger Software and DORIS Beam Optics were also developed for acceptance calculations in various tagging situations. The problems presented by spurious tagger signals caused by beam-beam bremsstrahlung events are described. Preliminary analysis of 2-photon events using the existing ARGUS detector is described and results on η' , $f(1270)$, 4π , $\mu^+\mu^-$, and e^+e^- exclusive final states are presented.

SOMMAIRE

Les résultats des simulations Monte Carlo de la mesure de $e^+e^- \rightarrow e^+e^- \gamma\gamma \rightarrow e^+e^- \text{hadrons}$ sont présentés. L'occasion de mesurer l'énergie des e^+e^- diffusés en utilisant deux matrices d'oxyde de Bismuth Germanium à haute résolution et les éléments d'optique magnétique de l'anneau de stockage DORIS II est décrite. Ces étiquetteurs à petits Q^2 permettront la détermination de la masse invariante $\gamma\gamma$ avec une petite erreur systématique et une acceptation relativement élevée. Ceci permettra à l'expérience ARGUS, grâce à la modification suggérée ici, d'exécuter la première mesure de la section efficace hadronique dans les collisions $\gamma\gamma$ avec une erreur systématique raisonnable à basses masses invariantes. Ces études Monte Carlo ont comporté le développement d'un générateur d'événements simple pour le processus $e^+e^- \rightarrow e^+e^- \gamma^* \gamma^*$ et plusieurs générateurs d'états finaux pour les canaux EDQ et hadroniques. Des simulations du détecteur ARGUS, du déclencheur et de l'optique magnétique de l'anneau DORIS ont été également développées pour les calculs d'acceptance dans diverses situations d'étiquetage (à petits Q^2). Les problèmes présentés par de faux signaux causés par les événements bremsstrahlung sont décrits. L'analyse préliminaire des événements $\gamma\gamma$ utilisant le détecteur ARGUS existant est décrite et des résultats portant sur les états finaux exclusifs η' , $f(1270)$, 4π , $\mu^+\mu^-$, et e^+e^- sont présentés.

ACKNOWLEDGEMENTS

~~I acknowledge the help and abundant patience of my thesis adviser P. Patel, McGill University.~~

W. Wagner, University of Aachen gave me his Two-Photon Monte Carlo which taught me a great deal though it had to be radically modified for application to 0° tagging and hadronic exclusive channels.

R. H. P. Kleiss, and P. H. Daverveldt of the Institute Lorentz, University of Leiden were very helpful and provided several advanced Monte Carlo programs for the QED final states. I would also like to thank the ARGUS collaboration - in particular L. Jönsson, Lund University and A. Philipp, DESY who with P. Patel and A. Nilsson compose the Two-Photon Group within ARGUS. L. Jönsson wrote the original version of the Doris Beam Optics simulation. I would like to thank my parents and friends for their encouragement which made my progress to this point possible.

TABLE OF CONTENTS

	Page
Abstract	2
Acknowledgements	3
Table of Contents	4
Preface	7
Introduction	9
1.1 General	9
1.2 General Properties of $\gamma\gamma$ Interactions at e^+e^- Storage Rings	12
1.3 Resonances in $\gamma\gamma$ Collisions	17
1.4 The Total Cross-Section for $\gamma\gamma \rightarrow$ Hadrons	24
1.5 Captions For Figures	29
The ARGUS Experiment	39
2.1 DESY	39
2.3 Principal Detector Components	40
2.3 The ARGUS Trigger	45
2.4 Monte Carlo Simulation of the ARGUS Detector	48
2.5 Captions For Figures	50
Separation of the $\gamma\gamma$ Signal	56
3.1 Beamgas and Cosmic Backgrounds	56
3.2 Observation of $\gamma\gamma \rightarrow \eta'$ at ARGUS	60

3.3.	Preliminary Observation of $\gamma\gamma \rightarrow 4\pi$ at ARGUS	64
3.4	Captions for Figures	65
	The ARGUS 0° Tagging Proposal	77
4.1	The DORIS Storage Ring	77
4.2	The ARGUS BGO Taggers	78
4.3	e^\pm Calorimetry and the Properties of BGO	82
4.4	Captions for Figures	85
	QED and Exclusive 3 Prong Channels in $\gamma\gamma$ Collisions	95
5.1	Introduction	95
5.2	Monte Carlo Studies of $\gamma\gamma \rightarrow e^+e^-, \mu^+\mu^-$ Acceptances	99
5.3	Preliminary Experimental Studies of $\gamma\gamma \rightarrow e^+e^-, \mu^+\mu^-$ and Observation of the $f(1270)$ Meson	102
5.4	Captions for Figures	108
	MC Studies of The Proposed Modifications to the ARGUS Detector and Prospects for the Measurement of the Total $\gamma\gamma$ Hadronic Cross Section	120
6.1	The ARGUS $\gamma\gamma$ Proposal	120
6.2	Hadronic Acceptance Calculations	124
6.3	MC Studies of Techniques for Small Angle Bremsstrahlen Background Rejection	132
6.4	Statistical Subtraction of SAB Background	140
6.5	Conclusion	144
6.6	Captions for Figures	146
	Conclusion	163

	Appendices	164
1	Expressions for $e^+e^- \rightarrow e^+e^-\gamma^*\gamma^*$ Kinematics	164
2	Monte Carlo Methods	168
3	The ARGUS Collaboration	173
	References	174

PREFACE

This thesis describes the results of work done at DESY concerning the feasibility of the proposed BGO Tagger extension to the ARGUS experiment currently taking data at DORIS II. The first chapter consists of a short review of $\gamma\gamma$ Physics. The general dynamical properties of $\gamma\gamma$ collisions at e^+e^- storage rings are described. The theoretical implications of the properties of s -channel $\gamma\gamma$ resonances are reviewed together with the theoretical expectations for the behaviour of $\gamma\gamma \rightarrow \text{hadrons}$ (as a prelude to their application in Chapter 6). The second chapter describes the ARGUS detector - its geometry, resolution, and particle identification capabilities. The ARGUS event trigger is also discussed. Chapter Three presents preliminary observations, with the ARGUS detector operating in the notag mode, of exclusive channels from two photon collisions. The problems of beamgas and cosmic backgrounds are reviewed together with preliminary results of studies of $\eta' \rightarrow \rho\gamma$ and the 4π final state. Chapter Four describes the proposed modifications to the ARGUS detector, i.e. the new vacuum chambers for DORIS and the BGO tagger. Some properties of BGO and electron calorimeters are also discussed. The fifth chapter describes preliminary studies of two prong final states and the problem of QED event subtraction. Preliminary observations of the $f(1270)$, $f'(1515)$ mesons are described. Chapter six describes the ideas behind the ARGUS $\gamma\gamma$ proposal and details Monte Carlo studies of the proposed total photon-photon hadronic cross-section measurement. Estimated acceptance and trigger rates for hadronic events are included together with calculation of the effect of various tagging conditions. The background from beam-beam small angle bremsstrahlung events (SAB) is studied in detail and techniques for statistical background subtraction and event filtering are described. The QED derivations of the $\gamma\gamma$ luminosity and kinematics are included in appendix 1 followed by a brief description of the DEPA (Double Equivalent Photon Approximation) while the second appendix reviews the basic techniques of Monte Carlo simulation.

This document is intended to fulfill the requirements for a Masters Thesis at McGill University. The work described here was carried out between May 1983 and August 1984 while the author resided in

Germany and took part in the day to day operation of the ARGUS experiment at DESY. Most of the work consisted of Monte Carlo studies and data analysis using IBM and VAX computers. At present, some experimental studies of BGO resolution are underway together with continuing Physics analysis of notag $\gamma\gamma$ events.

INTRODUCTION - A SHORT REVIEW OF TWO PHOTON PHYSICS

1.1 General : In recent years experiments with e^+e^- colliding beam machines have contributed a great deal to our understanding of the fundamental interactions. These studies have principally consisted of the analysis of "hard-scattering" event topologies, e.g. e^+e^- annihilation producing a highly virtual timelike photon which decays into a quark/antiquark pair (Figure 1.1). The high " q^2 " (invariant mass squared) of the virtual photon allows distances as small as 10^{-16} cm to be investigated. The simplicity of the initial state kinematics in e^+e^- collisions and the elementary nature of the incident particles allow a distinct improvement over fixed target or hadronic collider experiments for study of "low" energy "Standard Model" physics. Typical e^+e^- annihilation cross-sections are on the order of nanobarns while pp and $p\bar{p}$ cross-sections are ~ 40 millibarns at ISR energies¹⁰¹ due to the much stronger hadronic coupling. This difference in cross-sections is less of a drawback than it appears to be. The parton (quark/gluon) spectrum inside a hadron is soft. At high momentum transfer (small distances), where the application of QCD (Quantum Chromodynamics) is understood best, the hard parton "luminosities" inside hadrons decrease as more of the virtual parton cloud inside the proton is resolved. Consequently, the momentum distribution of the partons, the structure function, is shifted to lower momenta - the same energy is distributed amongst more "particles". It is apparent that most of the $p\bar{p}$ cross-section involves low momentum-transfer reactions while only a relatively small portion contributes to high q^2 collisions between the partons. A major limitation of experiments with colliding beams is the machine luminosity - an electron bunch is necessarily somewhat less dense than a liquid hydrogen target. For reference, some luminosities and energies reached by existing storage rings are listed in Table 1.

Phenomena analogous to soft hadronic reactions are accessible in e^+e^- collisions. These reactions arise from collisions between virtual particles in the leptons' structures. To lowest order in QED perturbation theory these can be interpreted as photon-photon collisions (Figure 1.2) since the dominant part of the electrons "soft" structure is the electromagnetic field. In hadronic collisions the QCD coupling constant, " α_s ", can become greater than one. In this case individual "particles" cannot be singled out in the hadron interaction or structure. In effect, each lepton beam in an e^+e^- storage ring emits a continuous spectrum of photons which may collide at the bunch crossing point producing a "fireball" of electromagnetic field. The investigation of this type of physics with the ARGUS detector concerns the rest of this thesis.

Facility	Start	Energy (GeV)	Luminosity $cm^{-2}sec^{-1}$	Interaction Regions
ADONE(Frascati) ¹⁰⁴	1963	2.4	$2 - 4 \cdot 10^{29}$	2
VEPP2(Novosibirsk) ¹⁰⁴	1970	~ 1.4	10^{28}	2
SPEAR(SLAC) ¹⁰⁴	1973	3-8	10^{31}	2
DORIS(DESY) ¹⁰⁴	1974	3-10.5	$3.5 \cdot 10^{29}$	2
PETRA(DESY) ¹⁰²	1978	10-45	$1.7 \cdot 10^{31}$	4
CESR(Cornell) ¹⁰⁴	1979	8-16	10^{31}	2
PEP(SLAC) ¹⁰⁴	1979	10-30	$7 \cdot 10^{30}$	6
ISR($pp, p\bar{p}$) ¹⁰¹	1972	6-60	$1.4 \cdot 10^{32}$	6
SPS($p\bar{p}$) ¹⁰⁸	1982	540	$1.6 \cdot 10^{30}$	2

Table 1.1 Colliding Beam Facilities

In classical electrodynamics the photon and electron are structureless particles. This assumption is directly responsible for the linearity of Maxwell's Equations. However, the Dirac Theory of Electromagnetism predicts¹⁰⁷ a small nonlinearity in Maxwell's Equations due to the presence of virtual particle/antiparticle pairs in the the-photon wavefunction. The cross-section for elastic $\gamma\gamma$ scattering (Figure 1.3a) can be estimated quite simply from elementary field theory and dimensional requirements. The effective Lagrangian is $L_{eff} \sim \alpha^2 F_{\mu\nu}^4/m^{-4}$ where m is the mass of the fermion appearing in the box diagram (Figure 1.3a) and $F_{\mu\nu}$ is the electromagnetic field tensor. The only other parameter in the problem is the CMS γ energy, ω , leading to the result: $\sigma(\gamma\gamma \rightarrow \gamma\gamma) = K \cdot \alpha^4 \omega^6 m^{-8}$. This calculation was first done in full about fifty years ago^{106...107} with the result:

$$\begin{aligned} \sigma_{1/2} &= (973/10125\pi)\alpha^4(\hbar/mc)^2(\omega/mc^2)^6 \\ \sigma_0 &= (119/10125\pi)\alpha^4(\hbar/mc)^2(\omega/mc^2)^6 \end{aligned} \quad (1-1)$$

Where the subscript of σ_S refers to the spin of the particle in the loop of the box diagram (Figure 1.3a). Well above the inelastic threshold $\gamma\gamma$ cross-sections are comparable to those of the annihilation channel. Due to the dominance of the virtual photon propagator ($\sim 1/4E^2$ where E is the e^\pm beam energy) the

e^+e^- annihilation channel cross-sections have the form¹⁰⁴:

$$\sigma(e^+e^- \rightarrow \mu^+\mu^-) = (2\pi\alpha^2/12E^2)\beta(3-\beta^2) \simeq 21.664nb/E^2$$

$$R_{e^+e^-} = \frac{\sigma(e^+e^- \rightarrow \text{hadrons})}{\sigma(e^+e^- \rightarrow \mu^+\mu^-)} = 3 \sum_{\text{flavours}} e_q^2 \quad (1-2)$$

Here, e_q refers to the quark charge. The sum over flavours runs over all quarks with (valence) masses less than the beam energy. This is only approximate and is altered by resonances at the flavour production thresholds and, at high energies, by QCD corrections. For $\gamma\gamma$ reactions at e^+e^- storage rings the total cross-section actually increases faster than the logarithm squared of the beam energy due to the bremsstrahlen-like incident photon beams. Approximate results for various channels using the Double Equivalent Photon Approximation (DEPA) are given below:

$$\begin{aligned} \text{Inclusive Hadrons}^{100} : \sigma &= \left(\frac{8\alpha^2}{\pi^2}\right) \ln^2\left(\frac{E}{m_e}\right) \ln^2\left(\frac{E}{W_{\text{minimum}}}\right) \sigma_0 \\ \text{Narrow Resonance}^{109} : \sigma &= \left(4\alpha \ln\left(\frac{E}{m_e}\right)\right)^2 4 \ln\left(\frac{2E}{M_R}\right) \frac{(2J+1)\Gamma_{\gamma\gamma}}{M_R^2} \\ \text{QED Fermions}^{108} : \sigma &= \frac{224\alpha^4}{27\pi m_f^2} \ln^2\left(\frac{2E}{m_e}\right) \ln\left(\frac{2E}{m_f}\right) \\ \text{QED Pions}^{110,118} : \sigma &= \frac{16\alpha^4}{9\pi m_\pi^2} \ln^2\left(\frac{E}{m_e}\right) \ln\left(\frac{E}{m_\pi}\right) \end{aligned} \quad (1-3)$$

These DEPA results are usually reliable within a factor of two. Most of the growth in the $\gamma\gamma$ total cross-section is concentrated either in the prodigious production of low invariant mass final states or states with a high Lorentz boost (e.g. the mass spectrum for the channel $\gamma\gamma \rightarrow e^+e^-, \mu^+\mu^-$ peaks at $s = 8m_f^2$).

Why study $\gamma\gamma$ Physics? Perhaps the least convincing response to this question possible is "because it's there" - one should not ignore a process merely because it is not expected to present any startlingly new results - especially if it does not require a major research effort. $\gamma\gamma$ collisions are an unavoidable part of the data taken at e^+e^- storage rings. Some of the achievements and opportunities of $\gamma\gamma$ physics will be discussed in the next few sections.

1.2 General Properties of $\gamma\gamma$ Interactions at e^+e^- Storage Rings : Most properties of $\gamma\gamma$ interactions with both virtual photons nearly real (i.e. the photon mass $q_i^2 \sim 0$) may be understood in terms of the bremsstrahlen processes in the initial state. The interaction can always be split up into the production of the $\gamma\gamma$ CMS - a pure QED process ($e^+e^- \rightarrow e^+e^-\gamma^*\gamma^*$) and the decay of the CMS - the process which is to be measured.¹ The characteristics of the $\gamma\gamma$ CMS are illustrated in Figures 1.4...1.8. Each figure shows the shapes of the differential "luminosity" distributions for transverse photon collisions as a function of one variable with all others integrated over.² These "luminosity" distributions are actually $e^+e^- \rightarrow e^+e^-\gamma\gamma \rightarrow e^+e^-X$ cross-sections with $\sigma(\gamma\gamma \rightarrow X)$ constant - they reflect the dynamics of the $\gamma\gamma$ CMS independent of specific final state. The most notable aspects of these curves are the steep decreases of luminosity as the colliding photons become more virtual and as the mass of the $\gamma\gamma$ system increases. The former is a consequence of the photon propagator and the decrease in invariant mass can be partially understood as the product of the two bremsstrahlen spectra, $1/E_{\gamma_i}$, with $W_{\gamma\gamma}^2 \simeq 4E_{\gamma_1}E_{\gamma_2}$. It is also important to note the wide rapidity distribution (Figure 1.8). This variable is related to the Lorentz boost of the $\gamma\gamma$ CMS along the beam axis:

$$\begin{aligned} \gamma_{\text{Lorentz}} &= \cosh \eta = \frac{E_{\gamma\gamma}}{W_{\parallel}} & W_{\parallel}^2 &= E_{\gamma\gamma}^2 - P_{\parallel}^2 \\ \eta &= \frac{1}{2} \ln \frac{(E + P_{\parallel})}{(E - P_{\parallel})} = \frac{1}{2} \ln \frac{E_{\gamma_1}}{E_{\gamma_2}} \end{aligned} \quad (1-4)$$

This Lorentz boost can severely limit the acceptance by focusing particles towards the detector gaps that allow the passage of the e^{\pm} beams. The laboratory (e^+e^- CMS) P_{\perp} of the $\gamma\gamma$ CMS is quite small as both photons are emitted nearly collinear to the beams. This characteristic can be used to separate $\gamma\gamma$ events from background or as a weak requirement in a kinematic fit (Chapter 3.2 discusses these applications to the separation of the $\gamma\gamma \rightarrow \eta'$ signal). The angular distribution of the scattered e^+/e^- (Figure 1.6) decreases rapidly for nonzero θ , due to this the scattered beam leptons from $\gamma\gamma$ reactions are rarely observed - most investigations must be done in what is known as the "notag mode". The terms single and double tag refer to the experimental situation where the momenta of one or both of the beam leptons are measured, respectively.

One expects the matrix element squared for the process $\gamma\gamma \rightarrow X$ to have $3^4 = 81$ independent components (the cross-section is related to the imaginary part of the elastic scattering amplitude via

¹The derivations of the expressions presented here are given in Appendices I together with a description of the notation used.

²These figures were generated with the Monte Carlo discussed in Chapter 6 with $W_{\gamma\gamma} \geq 1$ GeV and $E_{\text{Beam}} = 6$ GeV.

the optical theorem and each virtual photon has three independent helicity states) but this number is reduced to 8 by considerations of symmetry under time-reversal, parity, and rotation. The cross-section for any process $e^+e^- \rightarrow e^+e^-X$ can be expressed as:

$$d\sigma = \frac{\alpha^2}{16\pi^4 q_1^2 q_2^2} \sqrt{\frac{(q_1 \cdot q_2)^2 - q_1^2 q_2^2}{(p_1 \cdot p_2)^2 - m_e^4}} [4\rho_1^{++}\rho_2^{++}\sigma_{TT} + 2|\rho_1^{+-}\rho_2^{+-}|r_{TT} \cos 2\phi + 2\rho_1^{++}\rho_2^{00}\sigma_{TS} + 2\rho_1^{00}\rho_2^{++}\sigma_{ST} + 2\rho_1^{00}\rho_2^{00}\sigma_{SS} - 8|\rho_1^{+0}\rho_2^{+0}|r_{TS} \cos \phi] \frac{d^3 p'_1 d^3 p'_2}{E'_1 E'_2} \quad (1-5)$$

Where:

$$q_i^2 = -4E_i E'_i \sin^2(\theta_i/2) - q_{min}^2 < 0, \quad q_{min}^2 = m_e^2 \omega_i^2 / (E \cdot E'_i)$$

$$X = (q_1 q_2)^2 - q_1^2 q_2^2$$

$$2\rho_1^{++} = \rho_1^{\mu\nu} R^{\mu\nu} = X^{-1} (4E\omega_2 - q_2^2 - q_1 q_2)^2 + 1 + 4m_e^2/q_1^2 \quad (1-6)$$

$$\rho_1^{00} = \rho_1^{\mu\nu} Q_1^\mu Q_1^\nu = X^{-1} (4E\omega_2 - q_2^2 - q_1 q_2)^2 - 1$$

$$|\rho_1^{+0}| = \sqrt{(\rho_1^{00} + 1)} |\rho_1^{+-}|$$

$$|\rho_1^{+-}| = \rho_1^{++} - 1$$

The ρ 's can be treated as photon luminosity spectra. Two of the eight amplitudes mentioned above are not shown in equation 1 - 5 because they only contribute to processes with polarized e^+e^- beams. The "r" amplitudes can only be measured if both the scattered beam particles are measured or "tagged". As most experiments cannot measure particles scattered at small angles the tagging requirement restricts the q^2 of the virtual photons to be quite large. The $\gamma\gamma$ luminosity for these double tag processes is accordingly suppressed, making accurate measurements in these kinematic regions difficult. The amplitudes involving collisions of scalar photons are also suppressed by factors proportional to the photon mass (e.g. $\sigma_{SS} \sim q_1^2 q_2^2$) as they must vanish for real photons. This leaves only one amplitude, σ_{TT} , measurable in the easily accessible "notag" mode where neither scattered beam particle is detected (i.e. q^2 for both photons are limited to be less than a maximum determined by the minimum scattering angle measurable by the detector).

Historically, the production of hadrons in $\gamma\gamma$ collisions was first suggested in 1960 when F.E.Low¹¹¹ discussed the measurement of the π_0 lifetime via the production cross-section for π_0 's in "inelastic Bhabha scattering". Independently that year, Calogero and Zemach¹¹² suggested the measurement of pion pair production in $\gamma\gamma$ scattering at e^+e^- storage rings. Indeed, it is this paper which first suggested the possibility of using the storage ring optics to "tag" the scattered e^+e^- at small angles - the slight difference

between their trajectories and that of the beam allowing their magnetic separation and measurement. This idea is only now within reach of being achieved experimentally and is the core of the proposed $\gamma\gamma$ modification of the ARGUS experiment. In the early seventies a plethora of theoretical papers discussing the rates, cross-sections and angular distributions of simple final states were published ^{110,118...119}. These efforts used all the technology of Particle Physics available at that time: PCAC, soft-pion theorems, current algebra, Finite Energy Sum Rules etc. Few of these predictions appear likely to be confronted with experimental results at present. Since then the picture has been changed radically by the acceptance of QCD as a theory of the strong interactions. Results of this period of theoretical research are reviewed by Brodsky et al.¹¹⁰, Terazawa¹¹⁸, and Budnev et al.¹¹⁹.

The rise of the standard model and the appearance of the new "charm" and "beauty" physics in the second half of the 1970's led to diminished theoretical interest in $\gamma\gamma$ processes. The first observation of $\gamma\gamma \rightarrow e^+e^-$ was made in 1970 at the VEPP-2 storage ring in Novosibirsk but clear evidence for hadronic processes was not found until 1979 when the MARKII collaboration⁸¹¹ discovered the process $e^+e^- \rightarrow e^+e^- \gamma\gamma \rightarrow e^+e^- \eta'$ at the SPEAR storage ring at SLAC in the U.S.A.

Interest in $\gamma\gamma$ physics was revived in 1977 when Witten¹²⁰ suggested that since the photon was an elementary particle the photon structure function could be calculated in QCD - quantitatively. This was the only situation where this seemed to be possible. The measurement would involve the finite angle tagging of one scattered beam lepton to insure that one photon had high q_2^2 and the antitagging of the second lepton (requiring it to have $\theta \leq \theta_0$ with θ_0 sufficiently small so that $q_1^2 \sim 0$). This process is referred to as deep inelastic photon electron scattering⁵⁰⁴ - the highly virtual photon acts as a short distance probe of the electron's structure:

$$\frac{d\sigma}{dx dy d\phi} = \frac{8\alpha^2 EE_{\gamma^2}}{Q^4} \left[(1-y)F_2(x, Q^2) + xy^2 F_1(x, Q^2) \right]$$

$$F_1^{\gamma} = \sigma_{TT} \cdot Q^2 / (8\pi^2 \alpha x)$$

$$F_2^{\gamma} = 2xF_1^{\gamma} + \sigma_{ST} / 4\pi^2 \alpha$$

$$Q^2 = -q_2^2 \quad P^2 = -q_1^2 \sim 0 \quad (1-7)$$

$$X = Q^2 / (2q_1 q_2) \simeq Q^2 / (Q^2 + W_{\gamma\gamma}^2)$$

$$y = (q_1 q_2) / (p_2 q_1) \simeq 1 - (E_2'/E) \cos^2 \theta_2 / 2$$

$$z = (q_1 q_2) / (p_1 q_2) \simeq \omega_1 / E$$

The F_i are known as photon structure functions and represent the momentum distribution of the partons inside a photon. A third structure function appears if the scattering planes of the e^+e^- are measured. Normally only F_2^γ is measurable as xy^2 is usually small compared to $(1-y)$.

The measurement of the photon structure function was eagerly anticipated in the hope that it would determine the QCD scale parameter, Λ_s , from the absolute value of the structure function at finite Q^2 . Previous measurements of Λ_s were made from the Q^2 evolution of nucleon structure functions. Since this evolution is logarithmic on top of a large background, this is a difficult task. The nucleon structure functions also decrease with increasing x (which is proportional to the momentum of a parton inside the nucleus). In contrast the γ structure function increases with x and is directly proportional to $\ln Q^2$. The first order QCD (corresponding to the ungauged Quark model without gluons) result is ¹⁰⁰:

$$F_2^\gamma = 3 \sum_{\text{flavours}} e_f^4 \frac{\alpha}{\pi} x(x^2 + (1-x)^2) \ln \frac{Q^2}{Q_0^2} \quad (1-8)$$

For the Quark Parton Model $Q_0^2 = m_q^2 x^2 / (1-x)$ where m_q is a quark mass. The logarithmic term arises from the integration over the target photon Q^2 . In QCD it is not realistic to integrate over the whole phase space - the parameter Λ_s sets a scale below which the perturbative diagram (Figure 1.3b) becomes meaningless, this implies $Q_0^2 \approx \Lambda_s^2$. When higher order corrections are calculated, infrared singularities appear in F_2^γ . For a while it looked like these would completely destroy the calculability of the photon structure functions. It was soon realized that these infrared gluon bremsstrahlung corrections had to be cancelled by non-perturbative "vertex correction" contributions (Figure 1.9). This reduced γ structure functions to the status of Nucleon structure functions - only the q^2 evolution could be predicted. This fact was confirmed¹²⁶ when next to leading logarithm calculations were made using renormalization group techniques. It is still hoped that some progress may be made in extracting Λ_s from photon structure function data. The photon structure function can be calculated reliably in the case where the target photon is also highly virtual (i.e. $Q^2 \gg P^2 \gg \Lambda_s^2$) but in this case the scale breaking is proportional to $\ln Q^2/P^2$ and ~~most of the information on Λ_s is lost together with most of the experimental luminosity.~~ Current experimental results using lower order QCD analyses give reasonable estimates for Λ_s but with large systematic error.

At this point the most recent generation of e^+e^- storage rings (PETRA(DESY), PEP(SLAC)) started to operate - the first machines where $\gamma\gamma$ collisions constituted a significant part of the available reactions.

This led to measurement of the $\gamma\gamma$ widths of the pseudoscalar and tensor mesons together with some controversial determinations of the $\gamma\gamma$ total hadronic cross-section and structure functions. At present, experiment has nearly saturated the capabilities of existing machines and, aside from the accumulation of statistics (most of the experiments have 2-4 years running behind them), no drastic progress is expected. In the future, experiments at LEP and TRISTAN may be able to improve measurements of the photon structure functions in asymptotic kinematic regions where QCD can be unambiguously applied. Additionally, high luminosity "low energy" experiments will allow the study of exclusive channels in $\gamma\gamma$ collisions in much greater detail.

1.3 Resonances in $\gamma\gamma$ Collisions : The first suggestion of the possibility of observing resonances in $\gamma\gamma$ collisions was made by F.E.Low¹¹¹ in 1960. Little more was heard of the subject until the early 1970's when the production of $\gamma\gamma$ resonances was discussed in detail theoretically and derivations of cross-sections were first presented for η , and σ production^{110,112}. At that time it was hoped that data from $\gamma\gamma$ collisions could be used to study $\pi\pi$ phase shifts and determine whether the controversial σ meson actually existed. Some progress in this direction has been made and data now seem to indicate¹²² a σ meson of 600 MeV mass with a 600 MeV width.

The study of resonances in $\gamma\gamma$ collisions is interesting due to the low background and varied quantum numbers available in the final state. While s -channel resonances in e^+e^- annihilation must have the quantum numbers of the photon, i.e. $J^{CP} = 1^{--}$ the $\gamma\gamma$ s -channel is much less restrictive, the main requirement being positive C-parity. Though these types of resonance can often be observed inclusively in other processes, $\gamma\gamma$ collisions present the sole opportunity for their observation in a background free channel. C. N. Yang showed in 1950¹²⁹ that mesons decaying into two real photons cannot have $J=1$ because of helicity and parity conservation. In $e^+e^- \rightarrow e^+e^-\gamma^*\gamma^*$ the photons can become sufficiently virtual ($q^2 \sim m_V^2$), so that production of $J^{CP} = 1^{\pm+}$ resonances is allowed¹³⁰. The possibility of observing particles with the exotic quantum numbers 1^{-+} (e.g. $q\bar{q}\bar{q}$) is of particular interest. In this case at least one of the scattered e^+e^- must be tagged to insure that the corresponding photon is sufficiently offshell and to allow determination of the resonance cross-section q^2 dependence. No experimental evidence for $J = 1$ meson production in virtual $\gamma\gamma$ collisions has, as yet, been published.

For a new resonance with undefined $I_G^{J^{CP}}$ evidence from production in $\gamma\gamma$ collisions could be quite useful. This opportunity has not presented itself as only upper limits on the production of exotics are available. The principal item of information that one can extract from $\gamma\gamma$ production of a known resonance is the production width, $\Gamma_{\gamma\gamma}^R$, which yields information on the meson wavefunction. The resonance production cross-section is given, approximately, by a relativistic Breit-Wigner function:

$$\sigma(\gamma\gamma \rightarrow R) = 8\pi(2J+1) \frac{\Gamma_{Total} \cdot \Gamma_{\gamma\gamma}}{(W_{\gamma\gamma}^2 - M_R^2)^2 + \Gamma^2 M_R^2} \quad (1-9)$$

Where $W_{\gamma\gamma}$ is the mass of the $\gamma\gamma$ final state, J is the spin of the resonance, and M_R is its mass. This formula is actually an oversimplification as modifications occur when field theoretically correct matrix elements are used^{126,213}. For nonzero q^2 a form factor to parametrize the q^2 dependence of $\Gamma_{\gamma\gamma}$ must

be used (if the notag restriction is poor this correction may be necessary even if the scattered e^+e^- are left untagged), and for tensor mesons one must consider centrifugal barrier effects¹⁸¹. Additionally, the $\gamma\gamma$ couplings of resonances with $J^P \geq 2^+$ are described by two independent parameters corresponding to spin-flip and non spin-flip amplitudes (σ_{TT} and τ_{TT} in Appendix 1). The measurement of both of these requires double tagging of the event. In the narrow resonance approximation formula 1 - 4 becomes:

$$\sigma(\gamma\gamma \rightarrow R) = 8 \cdot \pi^2 \cdot (2J + 1) \frac{\Gamma \cdot \Gamma_{\gamma\gamma}}{M_R} \delta(W_{\gamma\gamma} - M_R) \quad (1-10)$$

This can be used as input in a DEPA calculation of the total cross-section with the result^{504,111}:

$$\sigma(e^+e^- \rightarrow e^+e^-R) = 16\alpha^2 \left(\ln \frac{E}{m_e}\right)^2 f(M_R/2E) \frac{(2J + 1)\Gamma_{\gamma\gamma}}{M_R^8} \quad (1-11)$$

$$f(x) = (2 + x^2)^2 \ln(1/x) - (1 - x^2)(3 + x^2)$$

The two main characteristics of this equation are the M^{-8} dependence of the cross-section on the resonance mass and the logarithm squared energy dependence of the cross-section. Experimental cross-sections increase slower than the total cross-section with beam energy as a great deal of the extra luminosity is concentrated in regions of high rapidity and low acceptance. If one or both of the scattered e^+e^- are tagged, one or both of the logarithmic factors in equation 1 - 11 is replaced (in a first approximation) by a $1/q^2$ factor. Due to this only two measurements^{304,518} of resonance "form factors" (the q^2 dependence of $\Gamma_{\gamma\gamma}$) have been made. Experimental values and upper limits on $\Gamma_{\gamma\gamma}^R$ are given in tables 1.2, 1.3 respectively. The world average values have been calculated, with only the newest result of each experiment, and are error weighted.

The two gamma width of a meson can be used to determine mixing between states of the same quantum numbers with different parton content, as predicted by models of hadron structure. This mixing can be of two types: the $SU(3)$ flavour symmetries of the old Quark Parton Model or "accidental" degeneracies (from an $SU(3)$ standpoint) between "normal" mesons, glueballs (mesons with valence gluons only), meiktons (mesons with valence quarks and gluons), and multiquark states (i.e. $qq\bar{q}\bar{q}$ states). The current theoretical status of these particles is reviewed by Renard¹⁸² together with expectations for the $\gamma\gamma$ widths of these exotic states. Quark content of a glueball can show up as an unexpectedly strong $\gamma\gamma$ coupling (this is expected to be suppressed for glueballs as they contain no charged valence particles and they can only couple to $\gamma\gamma$ through an intermediate quark loop). Mixing can produce destructive interference leading to the suppression of certain decays. The $\Theta(1690)$ is commonly suspected to contain some glueball in its wavefunction because of its production in radiative $J\psi$ decays (i.e. $J/\psi \rightarrow \gamma\theta\theta \rightarrow \gamma\Theta$).

Resonance	Group	Reference	Channel	$\Gamma_{\gamma\gamma}$ [keV]
π^0	average			$(7.59 \pm 0.09) \cdot 10^{-3}$
	NA20	156	$\pi^0 \rightarrow \gamma\gamma$	$(7.59 \pm 0.09) \cdot 10^{-3}$
	PDG	303	Primakof	$(7.65 \pm 0.54) \cdot 10^{-3}$
	C.Ball	506	$\pi^0 \rightarrow \gamma\gamma$	$(7.9 \pm 1.4 \pm 1.6) \cdot 10^{-3}$
η	average			0.37 ± 0.04
	PDG	303	Primakof	0.324 ± 0.046
	C.Ball	505	$\eta \rightarrow \gamma\gamma$	$0.56 \pm 0.12 \pm 0.10$
	JADE	506	$\eta \rightarrow \gamma\gamma$	$0.56 \pm 0.05 \pm 0.08$
η'	average			$4.67 \pm .35$
	MARKII	311	$\eta' \rightarrow \rho\gamma$	$5.8 \pm 1.1 \pm 1.2$
	CELLO	302	$\eta' \rightarrow \rho\gamma$	$6.2 \pm 1.1 \pm 0.8$
	JADE	301	$\eta' \rightarrow \rho\gamma$	$5.0 \pm 0.5 \pm 0.9$
	TASSO	521	$\eta' \rightarrow \rho\gamma$	$4.1 \pm 0.4 \pm 1.5$
	MARKII	506	$\eta' \rightarrow \eta\pi^+\pi^-$	3.8 ± 1.0
	PLUTO	304	$\eta' \rightarrow \rho\gamma$	$3.8 \pm .26 \pm .43$
	TASSO	312	$\eta' \rightarrow \rho\gamma$	$5.1 \pm .4 \pm .7$
$f(1270)$	average			2.5 ± 0.2
	PLUTO	517	$f \rightarrow \pi^+\pi^-$	$2.3 \pm 0.5 \pm 0.3$
	TASSO	518	$f \rightarrow \pi^+\pi^-$	$3.2 \pm 0.2 \pm 0.6$
	MARKII	519	$f \rightarrow \pi^+\pi^-$	$3.6 \pm 0.3 \pm 0.5$
	C.Ball	524	$f \rightarrow \pi^0\pi^0$	$2.7 \pm 0.2 \pm 0.6$
	CELLO	121	$f \rightarrow \pi^+\pi^-$	$2.5 \pm 0.1 \pm 0.5$
	JADE	521	$f \rightarrow \pi^+\pi^-$	$2.3 \pm 0.2 \pm 0.5$
	MARKII	121	$f \rightarrow \pi^+\pi^-$	$2.5 \pm 0.1 \pm 0.4$
	PEP 4/9	157	$f \rightarrow \pi^+\pi^-$	$2.39 \pm .06 \pm .30$
$A_2(1318)$	average			0.85 ± 0.11
	C.Ball	524	$A_2 \rightarrow \eta\pi$	$0.77 \pm 0.18 \pm 0.27$
	CELLO	302	$A_2 \rightarrow \rho^\pm\pi^\mp \rightarrow \pi^+\pi^-\gamma(\gamma)$	$0.81 \pm 0.19 \pm 0.27$
	JADE	521	$A_2 \rightarrow \rho^\pm\pi^\mp \rightarrow \pi^+\pi^-\pi^0$	$0.84 \pm 0.07 \pm 0.16$
	TASSO	158	$A_2 \rightarrow \rho^\pm\pi^\mp \rightarrow \pi^+\pi^-\pi^0$	$1.06 \pm 0.18 \pm 0.19$
$f'(1518)$	TASSO	310	$f' \rightarrow K^+K^-, f' \rightarrow K_s^0K_s^0$	$0.11 \pm 0.02 \pm 0.04$
$\chi_2(3556)$	C.Ball	126	$\psi' \rightarrow \gamma\chi \rightarrow 3\gamma$	1.8 ± 1.3
$?(2100)$	TASSO	127	$? \rightarrow 2\pi^+2\pi^-$	$1.25 \pm 0.5 \pm 0.5$

Table 1.2 $\gamma\gamma$ Widths of Resonances

Resonance	Group	Reference	Final State	$\Gamma(R \rightarrow \gamma\gamma) \cdot Br(R \rightarrow X)$ [keV]	Confidence Limit
$S^*(976)$	C.Ball	524	$\pi\pi$	< 0.8	95%
	JADE	521	all	< 0.8	95%
$\epsilon(1300)$	TASSO	518	$\pi^+\pi^-$	< 1.5	95%
$\omega(1440)$	TASSO	305	$\rho^0\rho^0$	< 1.0	95%
	MARKII	123	$KK\pi$	< 8.0	95%
	TASSO	521	$KK\pi$	< 7.0	95%
$\Theta(1690)$	TASSO	305	$\rho^0\rho^0$	< 1.2	95%
	TASSO	310	KK	< 0.3	95%
	MARKII	124	KK	< 0.4	95%
	C.Ball	125	$\eta\eta$	< 0.3	95%
$\eta_c(2980)$	C.Ball	128	all	< 20.	90%
	TASSO	521	$p\bar{p}$	< 0.4	95%
	TASSO	521	$KK\pi$	< 27.	95%
	TASSO	521	$2\pi^+2\pi^-$	< 0.7	95%
	JADE	521	$\pi^+\pi^-2\pi^0$	< 4.2	95%
	JADE	521	$\eta\pi^+\pi^-$	< 2.3	95%
$\chi_0(3415)$	C.Ball	126	all	< 10.	90%

Table 1.3 Upper Limits on $\gamma\gamma$ Widths of Resonances

Unfortunately, a pure glue interpretation conflicts with the suppression of the $\Theta \rightarrow \pi\pi$ decay - the major decay mode is $\Theta \rightarrow KK$ but glue should couple to hadrons flavour independently. One model for mixing¹³² of $\Theta, f(1270), f'(1515)$ arranged the suppression of the $\Theta \rightarrow \pi\pi$ decay but also required a vanishing $\Gamma_{\gamma\gamma}(f'(1515))$ and was therefore incorrect.

The $SU(3)_{flavour}$ mixing of the 0^{-+} and 2^{++} meson nonets can be determined from the $\gamma\gamma$ widths

of their members. The $SU(3)$ wave functions for the qq octet and singlet are:

$$\begin{aligned}
 \pi_0 (A_2) &= \frac{1}{\sqrt{2}}(dd - uu)F_8 && \text{isovector} \\
 \eta_8 (f_8) &= \frac{1}{\sqrt{6}}(uu + dd - 2ss)F_8 && \text{isoscalar} \\
 \eta_1 (f_1) &= \frac{1}{\sqrt{3}}(uu + dd + ss)F_1 && \text{isoscalar} \\
 \eta &= \eta_8 \cos \theta - \eta_1 \sin \theta \\
 \eta' &= \eta_1 \cos \theta + \eta_8 \sin \theta \\
 f' &= f_8 \cos \theta - f_1 \sin \theta \\
 f &= f_1 \cos \theta + f_8 \sin \theta
 \end{aligned} \tag{1-12}$$

The F_i represent the spatial wavefunctions - for nonet symmetry $r = F_1/F_8 = 1$. The two gamma widths of the mesons can be related to the quark content by the approximate expression¹²⁷:

$$\begin{aligned}
 \Gamma_{\gamma\gamma}(R) &= m_q^3 \cdot K \left[\sum_q e_q^2 \cdot F_q(r=0) \right]^2 \\
 \frac{3\Gamma_{\gamma\gamma}(\eta)}{m_\eta^3} &= \frac{\Gamma_{\gamma\gamma}(\pi_0)}{m_{\pi_0}^3} [\sqrt{8}r \sin \theta - \cos \theta]^2 \\
 \frac{3\Gamma_{\gamma\gamma}(\eta')}{m_{\eta'}^3} &= \frac{\Gamma_{\gamma\gamma}(\pi_0)}{m_{\pi_0}^3} [\sqrt{8}r \cos \theta + \sin \theta]^2
 \end{aligned} \tag{1-13}$$

Where e_q is the charge of the quark q ($q = u, d, s$). These can be used to calculate r and θ , the former is consistent with nonet symmetry at a 2σ level, i.e. $r(0^{-+}) = .92 \pm .05$, $r(2^{++}) = 1.09 \pm .11$. θ is consistent with perfect mixing ($\theta = 35.3^\circ$) for the 2^{++} nonet, $25^\circ < \theta(2^{++}) < 35^\circ$, this limits the u and d quark content of the $f'(1515)$ to be less than 2%⁵⁰⁶. The pseudoscalar nonet has $-5^\circ \geq \theta \geq -43^\circ$ the large error bars being due to inconsistencies between old analysis and the new PLUTO study⁵⁰⁴ which derives a lower value of $\Gamma_{\gamma\gamma}(\eta')$. A large departure from perfect mixing is expected in the 0^{-+} nonet due to the large mass differences⁵⁰⁴.

The π_0 two gamma width can be determined independently from all of this by using PCAC¹⁸⁸ and the triangle anomaly¹⁸⁹ (Figure 1.10) with the result:

$$\begin{aligned}
 \Gamma_{\gamma\gamma}(\pi_0) &= \frac{m_{\pi_0}^3}{64\pi} g_{\pi_0\gamma\gamma}^2 \\
 g_{\pi_0\gamma\gamma} &= \frac{\sqrt{2}\alpha}{\pi f_\pi} N_c \langle e_q^2 \rangle_{\pi_0}
 \end{aligned} \tag{1-14}$$

The experimental value for $\Gamma_{\gamma\gamma}(\pi_0)$ is $7.59 \pm .09 eV$ to be compared with the result of equation⁵⁰⁴ 1 - 14, $7.63 eV$. This agreement is one of the earliest and most important pieces of evidence for the extra colour degree of freedom for quarks.

The $\gamma\gamma$ widths of mesons can be used to differentiate between models with different charge assignments for the quarks. In the Han-Nambu¹⁸⁴ Integer Charge Quark(ICQ) Model $SU(3)$ flavour and $SU(3)$ colour are not independent - the charge of a quark depends on both colour and flavour though the colour-averaged quark charges in the ICQ are identical to those in the Gell-Mann/Zweig¹⁸⁴ Fractionally Charged Quark Model(FCQ) (Table 1.4). The current data on $R_{e^+e^-}$ and $\Gamma_{\gamma\gamma}(\pi_0)$ do not rule out the ICQ. These results can only measure the colour singlet part of the photon wavefunction below the threshold for open colour (which, given current theories of quark confinement, could be infinitely far away from current energies). In $SU(3)_{flavour} \times SU(3)_{colour}$ $8 \times 8 = 1 + 8 + \dots$ so in $\gamma\gamma$ collisions there is some contribution from the colour octet part of the photon, if it exists. If one evaluates equation 1 - 13 with the wavefunctions given in 1 - 12 for the ICQ and FCQ models using Table 1.4:

$$\begin{aligned} \Gamma_{\gamma\gamma} &\sim \langle \gamma\gamma | R | \gamma \rangle^2 \\ \langle \gamma\gamma | \pi^0 \rangle &\simeq 3F_8 (\langle Q_d^2 \rangle_c - \langle Q_u^2 \rangle_c) \\ \langle \gamma\gamma | \eta^1 \rangle &\simeq 3F_1 (\langle Q_s^2 \rangle_c + \langle Q_d^2 \rangle_c + \langle Q_u^2 \rangle_c) / 3 \\ \langle \gamma\gamma | \eta^8 \rangle &\simeq 3F_8 (\langle Q_d^2 \rangle_c + \langle Q_u^2 \rangle_c - 2 \langle Q_s^2 \rangle_c) / 6 \\ \langle Q_u^2 \rangle_{ICQ} &= 2/3 \quad \langle Q_d^2 \rangle_{ICQ} = 1/3 \\ \langle Q_u^2 \rangle_{FCQ} &= 4/9 \quad \langle Q_d^2 \rangle_{FCQ} = 1/9 \end{aligned} \tag{1-15}$$

$\langle e_q \rangle_c$ refers to the quark charge averaged over colour. It is apparent that $\Gamma_{\gamma\gamma}(\eta_1)$ in the ICQ is 4 times that in the FCQ model while the other $\gamma\gamma$ widths remain the same. For the FCQ, assuming the η' is pure singlet, $\Gamma_{\gamma\gamma}(\eta') \simeq 6$ keV which, when compared to the experimental value of $4.57 \pm .35$, heavily favours fractionally charged quarks.

Additional data on the question of quark charges may come from analysis of $\gamma\gamma \rightarrow qq$, where the quarks form hadronic jets¹⁴⁰. One can calculate the ratio between the hadronic jet cross-section and the cross-section for $\gamma\gamma \rightarrow \mu^+\mu^-$, - $R_{\gamma\gamma}$. This quantity is analogous to that calculated in annihilation phenomena (equation 1 - 2):

$$R_{\gamma\gamma} = \frac{d\sigma/dt(\gamma\gamma \rightarrow qq)}{d\sigma/dt(\gamma\gamma \rightarrow \mu^+\mu^-)} = \left(\frac{3 \cdot \sum_{flavours} Q_f^4}{1/3 \cdot \sum_{flavours} (\sum_{colours} Q_{f,c}^2)^2} \right) = \left(\frac{34/27}{10/3} \right) \quad \left(\begin{array}{l} \text{for FCQ} \\ \text{for ICQ} \end{array} \right) \tag{1-16}$$

In this equation the flavours u, d, s, c are summed over. $R_{\gamma\gamma}$ only becomes constant for high particle P_{\perp} due to the influence of QCD. At present, data from $\gamma\gamma \rightarrow jets$ at high q^2 (Figure 1.11) seem to rule out the ICQ model⁵⁰⁴. It is suggested¹⁴⁰ that this may be misleading, in gauged ICQ models a direct photon coupling to the gluon occurs, and the proposed colour octet coupling of the photon is suppressed at high q^2 by a gluon propagator effect.

Resonance	Group		Reference		Channel	$\Gamma_{\gamma\gamma}$ [keV]
	Red	White	Blue	FCQ Model		
u	1	1	0	2/3		
d	0	0	-1	-1/3		
c	1	1	0	2/3		
s	0	0	-1	-1/3		
b	0	0	-1	-1/3		

Table 1.4 Quark Charges in the Han-Nambu(ICQ) and Gellmann-Zweig(FCQ) Models

Searches have been made for most exotic resonances in the various channels available in $\gamma\gamma$ collisions. The only channel to produce any serious theoretical confusion is the $\gamma\gamma \rightarrow \rho\rho$ channel. Several collaborations have observed this⁸⁰⁶⁻⁸⁰⁹ and TASSO have performed the most complete analysis to date⁸⁰⁶. They find a large enhancement in $\gamma\gamma \rightarrow 2\pi^+2\pi^-$ near the $\rho^0\rho^0$ threshold. The angular correlation analysis suggests that the data is best fitted by $C=+$ states with the dominant contributions being 0^{++} below 1.7 GeV and 2^{++} above. The data is such that TASSO can't rule out an isotropic phase space contribution... Theoretical expectations for $\gamma\gamma \rightarrow \rho\rho$ from the Vector Dominance Model (discussed in the next section) suggest:

$$\frac{d\sigma(\gamma\gamma \rightarrow \rho\rho)}{dt} = (p^*/k^*)^2 \frac{\alpha\pi^2}{\gamma_\rho} \frac{d\sigma(\rho\rho \rightarrow \rho\rho)}{dt} \quad (1-17)$$

Where k^* , p^* are the γ and ρ momenta in the $\gamma\gamma$ CMS. The measured value (Figure 1.12) is on the order of a 100 nb near threshold - clearly inconsistent with the above result and with most attempted explanations of the effect. In addition, the JADE Collaboration⁶⁰⁴ has observed $\gamma\gamma \rightarrow \rho^+\rho^-$ and see no analogous threshold enhancement. If the $\rho\rho$ signal had resulted from a single resonance isospin conservation would require: $Br(X \rightarrow \rho^+\rho^-)/Br(X \rightarrow \rho^0\rho^0) = 2, 1/2$ for $I_X = 0, 2$, respectively. There is no clear explanation of this signal - one popular model format suggests a pair of four quark resonances interferes to produce a suppressed $\rho^+\rho^-$ mode. More data on this final state and related final states ($\rho\omega$, $\omega\omega$ etc.) are needed to distinguish between the theoretical possibilities.

1.4 The Total Cross-Section for $\gamma\gamma \rightarrow \text{Hadrons}$: The photon has a dual nature in hadronic interactions - it can couple to hadrons either through their charges (or, at high photon q^2 , through the charges of the constituent quarks) in an electromagnetic interaction, or it may oscillate into a vector meson (ρ , ω , $\phi \dots$) and interact via the strong force. This latter view is known as the Vector Dominance Model or VDM, expressing the fact that, in soft hadronic interactions, the photon behaves rather like a hadron. The VDM contribution to hadronic processes in $\gamma\gamma$ collisions is:

$$\sigma(\gamma\gamma \rightarrow \text{hadrons}) = \sum_{V, V'} (\alpha\pi/\gamma_V^2)(\alpha\pi/\gamma_{V'}^2)\sigma(VV' \rightarrow \text{hadrons}) \quad V, V' = \rho, \omega, \phi \quad (1-18)$$

Where the γ_V can be calculated from the vector meson decay constants¹⁴² and flavour $SU(3)$ implies:

$$\sigma(\gamma\rho \rightarrow \rho\rho) : \sigma(\gamma\rho \rightarrow \omega\rho) : \sigma(\gamma\rho \rightarrow \phi\rho) = 9 : 1 : 2 = \gamma_\rho^2 : \gamma_\omega^2 : \gamma_\phi^2 \quad (1-19)$$

This concept implies that hadrons in $\gamma\gamma$ collisions should be produced with a limited P_\perp phase space distribution - similar to that found in low momentum-transfer hadronic reactions. Additionally, Regge Model results can be used to relate $\gamma\gamma$ cross-sections^{110,109,504} to Nucleon cross-sections. At high energies only the $\alpha = 1$ Regge trajectory contributes, as Regge Models have $\sigma \sim W_{\gamma\gamma}^{2\alpha-2}$. Assuming factorization (i.e. that each process can be described by two independent vertex coupling constants, Figure 1.13) the asymptotic $\gamma\gamma$ total hadronic cross-section can be derived from the total cross-sections for γp and pp scattering¹⁴³:

$$\sigma(\gamma\gamma) = \sigma(\gamma p)^2 / \sigma(pp) = 250 \pm 50nb \quad (1-20)$$

Exchange of the $\alpha = 1/2, 0$ trajectories (Figure 1.14) produces elements in the cross-section proportional to $1/W_{\gamma\gamma}, 1/W_{\gamma\gamma}^2$ respectively. The latter is expected to contribute little but the $\alpha = 1/2$ trajectory (corresponding to f and A_2 exchange) is calculated by W.Wagner¹⁰⁰ to be $270nb \cdot GeV/W_{\gamma\gamma}$. Ginzburg and Serbo¹⁴⁸ estimate this contribution to be $315 \pm 55nb \cdot GeV/W_{\gamma\gamma}$. The $1/W$ term is expected to be only an average estimate of resonant contributions at low masses.

As discussed in the section 1.2, much work has been done on photon structure functions and these are directly related to cross-sections. However, for both photons nearly real the QCD treatments are not expected to apply. The Quark Parton Model does predict that the photon will have a pointlike coupling to quarks:

$$\sigma(\gamma\gamma \rightarrow qq) = 2\pi\alpha^2 \sum_{q_i} \frac{e_i^4}{W_{\gamma\gamma}^2} [2\beta^3 - 4\beta + (3 - \beta^4) \cdot \ln\left(\frac{1+\beta}{1-\beta}\right)] \quad (1-21)$$

Where $\beta = P/E$ (P and E are, respectively, the momentum and energy of the $\gamma\gamma$ CMS). This may produce a $1/W^2$ term in the $\gamma\gamma$ total hadronic cross-section if its behaviour is not drastically altered by QCD. As mentioned in the previous section, the observation of two jet events in $\gamma\gamma$ collisions is fundamental evidence for a pointlike contribution. In addition, the pointlike coupling shows up at large hadron P_{\perp} as a slower decrease ($\sim 1/P_{\perp}^4$) in $d\sigma/dP_{\perp}^2$ (Figure 1.15) than one would expect from the limited P_{\perp} phase space of soft hadronic interactions ($d\sigma/P_{\perp}^2 \sim \exp(-6P_{\perp}^2)$).

The VDM can be used to estimate the Q^2 dependence of $\gamma\gamma$ cross-sections. The vector meson appears as an internal line in the Feynmann diagram (Figure 1.16) and modifies the $1/q^2$ photon propagator to be $1/q^2(1 - q^2/m_{\rho}^2)$, $q^2 < 0$. This suggests:

$$\sigma_{\gamma\gamma}(W^2, q_1^2, q_2^2) = \sigma_{\gamma\gamma}(W^2, 0, 0) \left(\frac{1}{1 - q_1^2/m_{\rho}^2} \right)^2 \left(\frac{1}{1 - q_2^2/m_{\rho}^2} \right)^2 \quad (1-22)$$

The rho propagator hypothesis agrees well with data at small q^2 (Figure 1 - 17a, b) but for q^2 on the order of 1 GeV^2 it estimates too steep a decrease in the cross-section (Figure 1 - 17c). Ginzburg and Serbo¹⁴⁸ have suggested that at moderately high q^2 the contribution of the other vector mesons must be taken into account and suggest the formula:

$$\sigma(W^2, q^2, 0) = \sigma(W^2, 0, 0) F_{GVDM}^2(q^2) \quad (1-23)$$

$$F_{GVDM} = \sum_{V=\rho, \omega, \phi} r_V \frac{1 + q^2/4m_V^2}{1 + q^2/m_V^2} + \frac{0.22}{1 + Q^2/1.4^2}$$

with $r_{\rho} = .65$, $r_{\omega} = .08$, and $r_{\phi} = .05$. This expression is also meant to include the contribution of σ_{ST} for nonzero q^2 (i.e. the terms in equation 1 - 23 proportional to q^2). The GVDM propagator seems to agree with the data at moderate q^2 (Figure 1 - 17c). Expression 1 - 23 also describes similar propagator effects in eN and μN scattering¹⁴⁸ where it was originally applied. Some question has arisen¹⁵⁰ about whether the propagators factor as implied in equation 1 - 22 for both photon $q_0^2 \sim O(m_V^2)$.

The first measurements of $\sigma(\gamma\gamma \rightarrow \text{Hadrons})$ were made by TASSO^{146,147}, PLUTO^{144,145}, and SPEAR¹⁴⁸. The first two of these are single-tag measurements while the SPEAR experiment operated in double-tag mode. The SPEAR experiment had very low statistics and expressed its results in terms of $R_{\gamma\gamma}$ (Equation 1 - 16):

$$R_{\gamma\gamma} = 1.1 \pm 0.3 \pm 0.3 \quad (1-24)$$

The analyses of PLUTO and TASSO had much more statistics but had the distinct disadvantage that the true $W_{\gamma\gamma}$ was unknown due to detector acceptance and resolution. This quantity had to be estimated

using an unfolding algorithm based on a Monte Carlo for the fragmentation of the final state. As the Monte Carlo had to be adjusted to the experimental data there is an element of circular logic involved in this type of analysis. This systematic uncertainty led to the two different "unfolded" $\gamma\gamma$ cross-sections shown in Figure 1 - 18. The 1σ error contours in Figure 1 - 18 are only statistical errors - the difference between the two results can be attributed entirely to systematic effects in the unfolding procedure. The results of the two experiments are:

$$\sigma(\gamma\gamma \rightarrow \text{hadrons}) = (A(240\text{nb} + 270\text{nb} \cdot \text{GeV}/W) + B \text{nb} \cdot \text{GeV}^2/W^2)F_\rho^2 \quad \text{PLUTO}$$

$$A = .97 \pm .16 \quad B = 2250 \pm 500$$

1 - -25

$$\sigma(\gamma\gamma \rightarrow \text{hadrons}) = (C + D \text{nb} \cdot \text{GeV}/W)F_\rho^2 \quad \text{TASSO}$$

$$C = 370 \pm 35 \quad D = 570 \pm 100$$

Where F_ρ refers to the ρ propagator hypothesis for the cross-section q^2 dependence as described above. Kolanoski⁵⁰⁴ discusses the different points of the two analyses in detail. The PLUTO experiment used a limited P_\perp phase space algorithm:

$$\begin{aligned} \frac{dN}{dP_\perp^2} &\sim \exp(-5p_\perp^2) & 75\% \\ \frac{dN}{dP_\perp^2} &\sim \exp(-p_\perp^2) & 25\% \\ \langle n_\pm \rangle &= 2.0 + 1.4 \ln(W_{\gamma\gamma}/\text{GeV}) & \text{Poisson} \end{aligned} \quad (1-26)$$

$$\langle n_{\pm} \rangle / \langle n_{\pi^0} \rangle = 2$$

Though these parameters appeared to describe the data, they were not allowed to vary simultaneously with the cross-section parameters in a fit. TASSO had a larger $W_{\pi^0} \rightarrow W_{\gamma\gamma}$ correction because it only used charged particles in its analysis but it simultaneously fitted C,D and the multiplicity distribution to the data. The P_\perp distribution was fitted separately. In a later analysis with 9 pb^{-1} luminosity (the original analysis used 2.3 pb^{-1}), TASSO^{149,604} found that if the parameters for the P_\perp distribution were included in the fit the correlation was sufficient to destroy the ability of the experiment to determine any cross-section $W_{\gamma\gamma}$ dependence. For visible invariant masses greater than 3 GeV it was assumed that the cross-section was flat. This ansatz produced the result $\sigma_0 = 285 \pm 55 \text{ nb}$. It was impossible to determine the fragmentation parameters independently of the cross-section and, if all parameters were fit simultaneously, the range of cross-sections allowed within the 95% confidence limit was $150 \text{ nb} < \sigma_0 < 1300 \text{ nb}$.

More recently PLUTO⁶⁰² has published an improved analysis with higher luminosity (19 pb^{-1} as opposed to 2.7 pb^{-1} in the original analysis) and an improved detector. The PLUTO result is shown in

Figure 1-19. The PEP 4/9 collaboration have recently started analysis of $\gamma\gamma \rightarrow \text{hadrons}$ with 50 pb^{-1} luminosity and have^{150,159} announced a preliminary result from a double tag measurement:

$$\sigma(\gamma\gamma \rightarrow X) = (360 \pm 60) \text{ nb} + (10 \pm 290) \text{ nb} \cdot \text{GeV}/W$$

$$\frac{r_{TT}}{\sigma_{eff}} = -.49 \pm .24, \quad \sigma_{eff} = \sigma(e^+e^- \rightarrow e^+e^- \text{ hadrons})/L_{TT} \quad (1-27)$$

$$\frac{r_{TS}}{\sigma_{eff}} = -.02 \pm .04$$

PLUTO¹⁶¹ has measured $\frac{r_{TT}}{\sigma_{eff}} = -.31 \pm .12$. A double tag measurement has a much better control of systematic uncertainties since the $W_{\gamma\gamma}$ can be determined from the energies of the tagged beam particles and no $W_{variable} \rightarrow W_{\gamma\gamma}$ unfolding is needed. However, the statistics are very limited (PEP 4/9 has ~ 800 events while the PLUTO analysis has ~ 3000 with less than half the luminosity). There is still systematic uncertainty from trigger efficiency, event selection, and various background contributions. It is also difficult to get a good mass resolution in double tag measurements as $W_{\gamma\gamma}^2 \simeq 4(E_{Beam} - E_{Tag1}) \cdot (E_{Beam} - E_{Tag2})$ and $E_{Tag} \gg E_{Beam} - E_{Tag}$. For either (ST or DT) finite angle tag measurements it is necessary to estimate the cross-section for real photon collisions from measurements at finite Q^2 .

In summary, $\gamma\gamma$ physics is an alternative to e^-e^+ annihilation with many unique opportunities. The complexity of hadronic interactions and the simplicity of QED both manifest themselves providing a middle ground where some aspects of hadronic interactions are more susceptible to theoretical attack. The measurement of the photon structure function has attracted a large amount of theoretical and experimental effort which shows no sign of lessening. Investigations of resonance production have nearly saturated the capabilities of present facilities but many allowed channels have not yet been seen. The observation of the weaker processes would assist in the analysis of meson wavefunctions, the quark content of exotic mesons being particularly interesting. Low intensity channels, like vector meson pair production, may reveal the existence of four quark states. It is also expected that high P_{\perp} hadron production may be partially calculable in QCD¹⁶²⁻¹⁶⁴. The $\gamma\gamma$ cross-section has not created any theoretical controversies - the Regge theory estimates have not changed significantly since the early seventies and sound evidence for the presence of a $1/W_{\gamma\gamma}^2$ term, evidence of QCD effects, does not yet exist (other evidence for pointlike coupling in $\gamma\gamma$ processes does exist in the form of jet production and high P_{\perp} processes). The difficult experimental situation has prevented the measurement of $\gamma\gamma$ cross-sections to an accuracy that can challenge the theoretical estimates. The $\gamma\gamma$ cross-sections are fundamental quantities and it is clear that their accurate measurement and eventual calculation in QCD, clearly a much easier task than calculation

of other channels involving soft hadronic processes, would be a triumph of experimental and theoretical technique.

1.5 CAPTIONS FOR FIGURES

- 1.1 Feynmann Diagram for $e^+e^- \rightarrow qq$.
- 1.2 Feynmann Diagram for $e^+e^- \rightarrow e^+e^-\gamma^*\gamma^* \rightarrow e^+e^-X$.
- 1.3 (a) Feynmann Diagram for $\gamma\gamma \rightarrow \gamma\gamma$ ("Box Diagram"), (b) Feynmann diagram for Fermion pair production.
- 1.4 $\frac{1}{N} \frac{dN}{dQ^2}$ vs. Q^2 . In Diagrams 1.4-1.8 N is proportional to the cross-section for $e^+e^- \rightarrow e^+e^-\gamma\gamma \rightarrow e^+e^-X$ with $\sigma_{\gamma\gamma \rightarrow X}$ a constant. Q^2 is the invariant mass squared of one of the virtual photons in the interior of the Feynmann diagram in Figure 1.2.
- 1.5 $\frac{1}{N} \frac{dN}{dE_\gamma}$ vs. E_γ - the photon energy spectrum.
- 1.6 $\frac{1}{N} \frac{dN}{d\cos\theta}$ vs. $\cos\theta$. θ is the scattering angle of a beam particle in Figure 1.2.
- 1.7 $\frac{1}{N} \frac{dN}{dW_{\gamma\gamma}^2}$ vs. $W_{\gamma\gamma}^2$. $W_{\gamma\gamma}$ is the invariant mass of the $\gamma\gamma$ CMS.
- 1.8 $\frac{1}{N} \frac{dN}{d\eta}$ vs. η (the rapidity of the $\gamma\gamma$ CMS).
- 1.9 Feynmann Diagrams for gluon bremsstrahlung correction to the 0th order QCD derivation of the photon structure function. Graph (b) would, in QED, cancel the infrared divergence of graph (a), however, in QCD the Q^2 of the gluon can easily be small enough so that the running coupling constant $\alpha(Q^2)$ becomes greater than 1 and the correction can no longer be calculated perturbatively.
- 1.10 Feynmann Diagrams for decay $\pi^0 \rightarrow \gamma\gamma$.
- 1.11 $R_{\gamma\gamma}$ from PLUTO¹⁴¹ single tag events showing approach to value predicted by the fractionally charged quark model at high q^2 .
- 1.12 The TASSO result²⁰⁶ for $\sigma(\gamma\gamma \rightarrow \rho\rho)$.
- 1.13 These diagrams¹⁰⁹ illustrate the assumptions underlying the factorization of Regge exchange terms.
- 1.14 The $\alpha = 0, \frac{1}{2}, 1$ Regge Trajectories¹⁰⁹.
- 1.15 Experimental $d\sigma/dP_\perp^2$ distribution from TASSO (this is the P_\perp of individual particles in each event). At low P_\perp an exponential decrease is evident as expected from VDM considerations. At high P_\perp evidence for pointlike structure is observed in the form of a slower decrease in $d\sigma/dP_\perp^2 \sim 1/P_\perp^4$.
- 1.16 Feynmann diagram showing origin of ρ propagator contribution to $\sigma_{VDM}(\gamma\gamma \rightarrow X)$.
- 1.17 Data from PLUTO^{109,161} showing $\sigma_{\gamma\gamma}(s, q_1^2, q_2^2 \sim 0)$. The rho propagator reproduces the distribution at low q^2 as can be seen in Figure 1.17a,b. However, the ρ propagator assumption underestimates the cross-section at moderately high q^2 (Figure 1.17c) where the GVDM propagator seems to fit the data better.

1.18 Results from PLUTO^{144,145} and TASSO^{146,147} on the $\gamma\gamma$ hadronic cross-section. The 1σ contours shown are for statistical errors only.

1.19 (a) Results from PLUTO⁶⁰² on the $\gamma\gamma$ hadronic cross-section. The dashed line represents the VDM prediction, $\sigma = 240 + 270/W_{\gamma\gamma}$ while the shaded area represents an extended VDM result of G. Alexander et al.¹⁵⁵. **(b)** Results¹⁵⁰ from PEP 4/9 on the $\gamma\gamma$ hadronic cross-section. The prediction of Alexander et al.¹⁵⁵ is also shown.

Figure 1.1

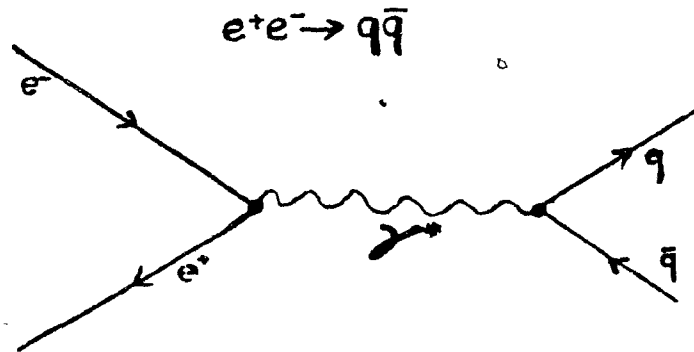


Figure 1.2

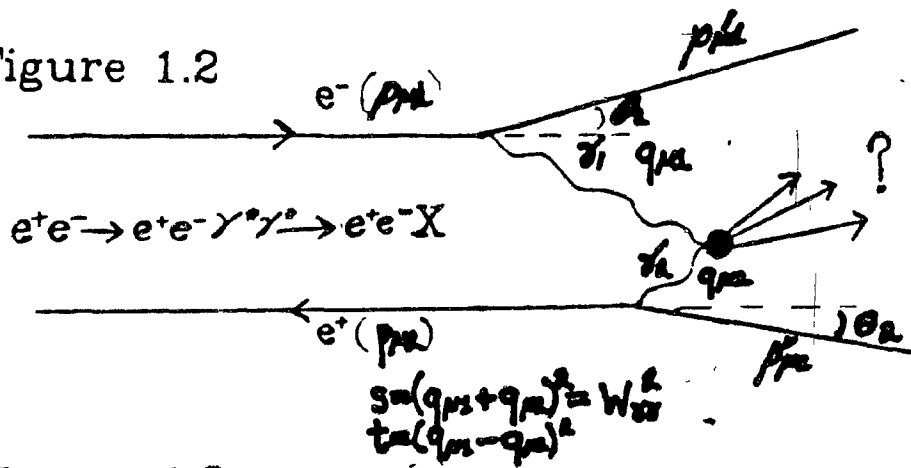


Figure 1.3a

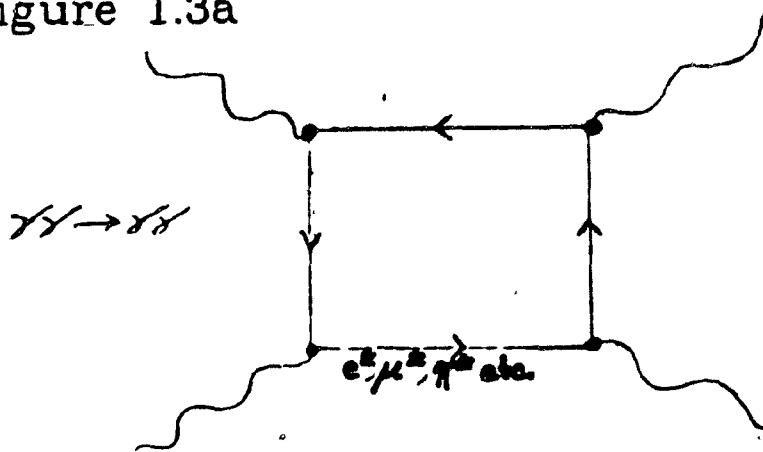
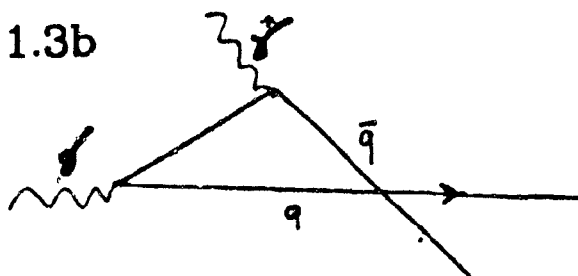
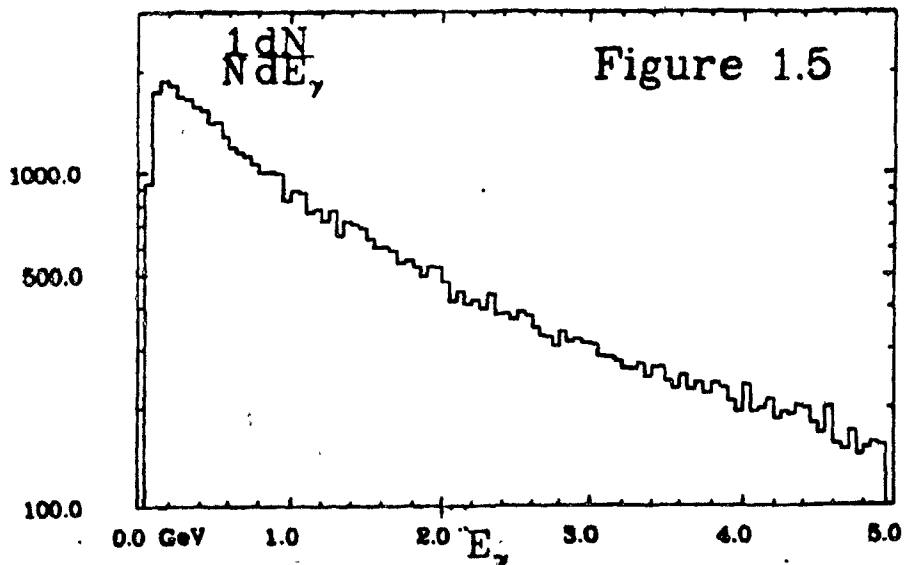
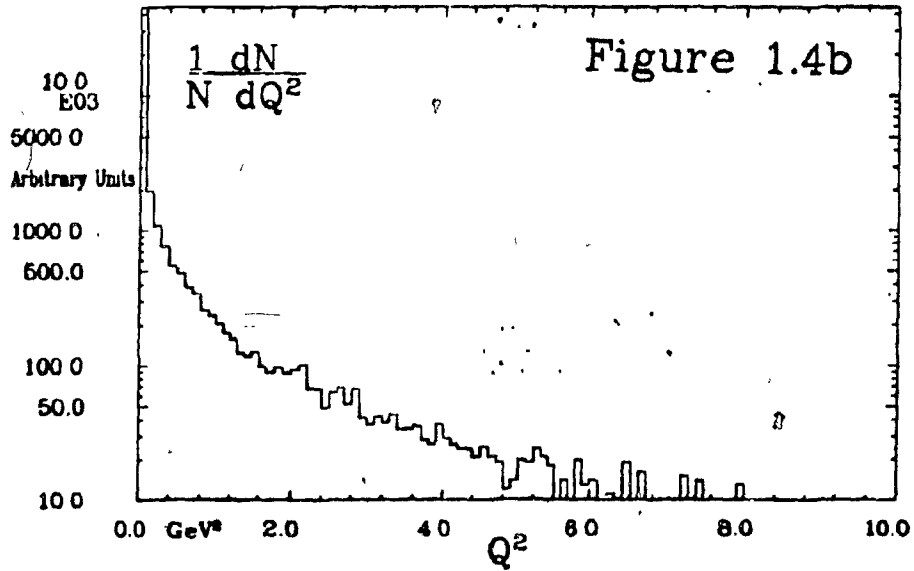
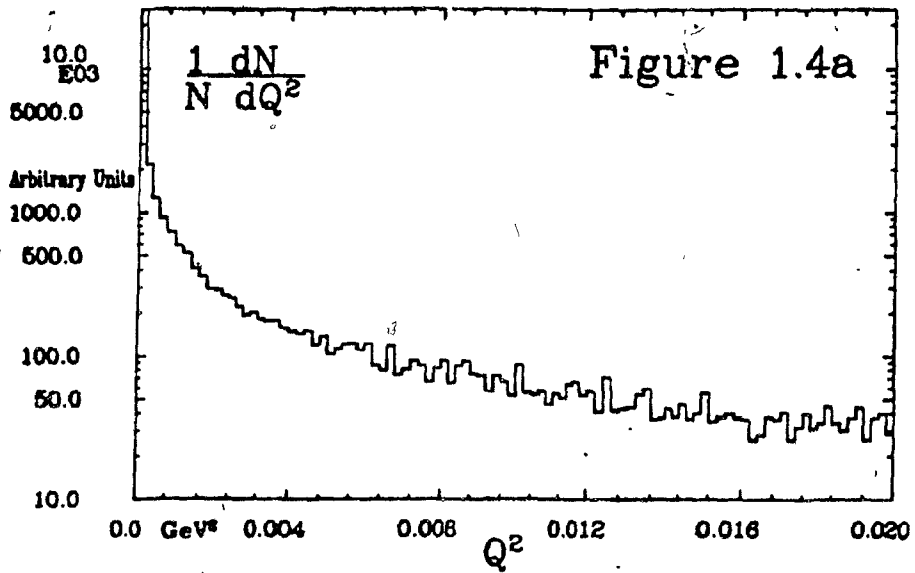


Figure 1.3b





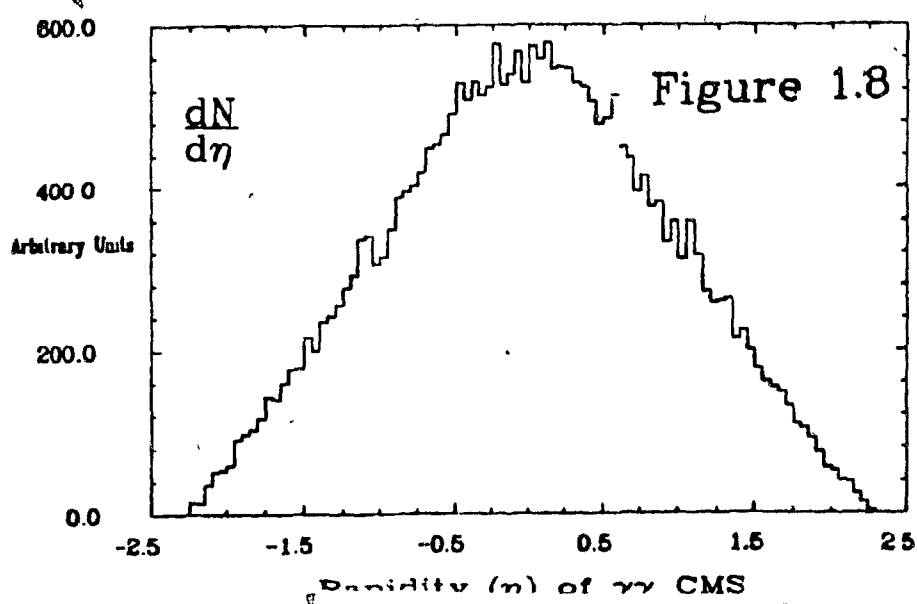
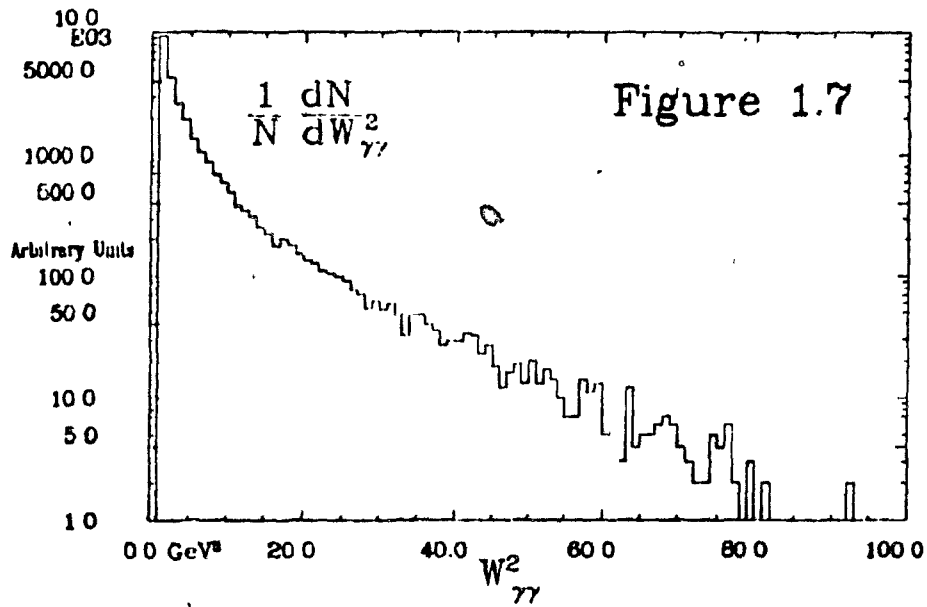
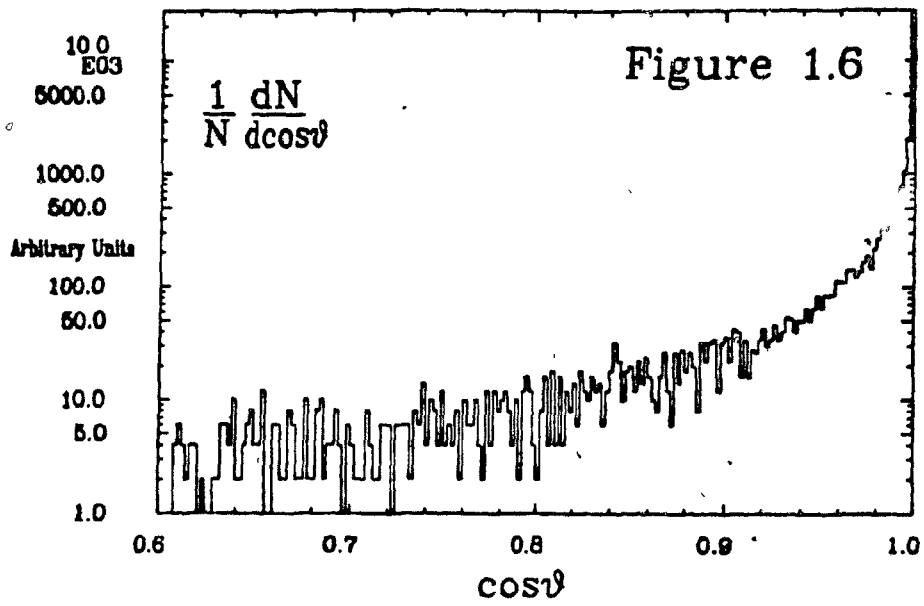


Figure 1.9

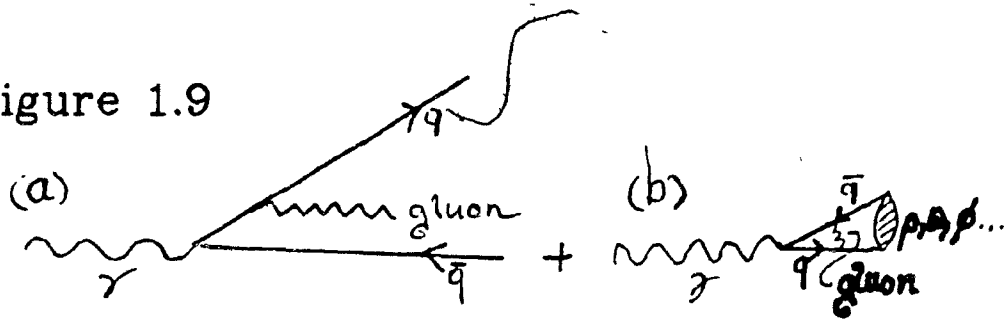


Figure 1.10

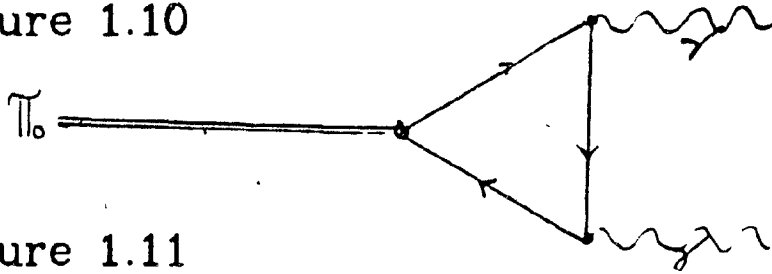


Figure 1.11

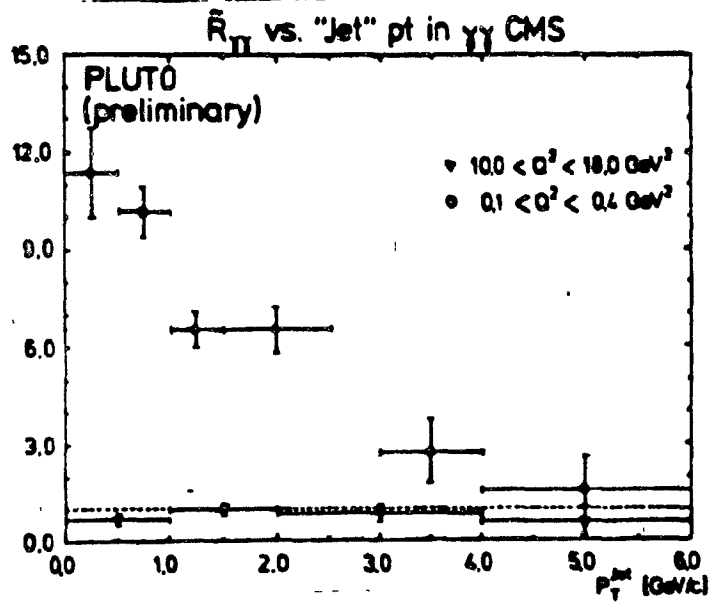
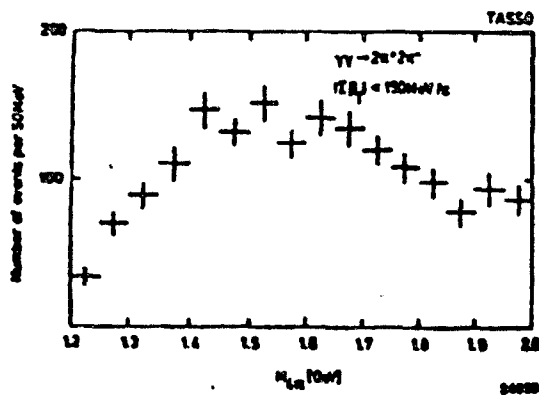


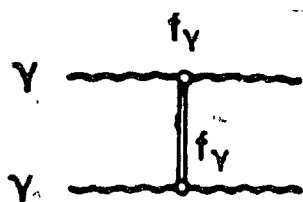
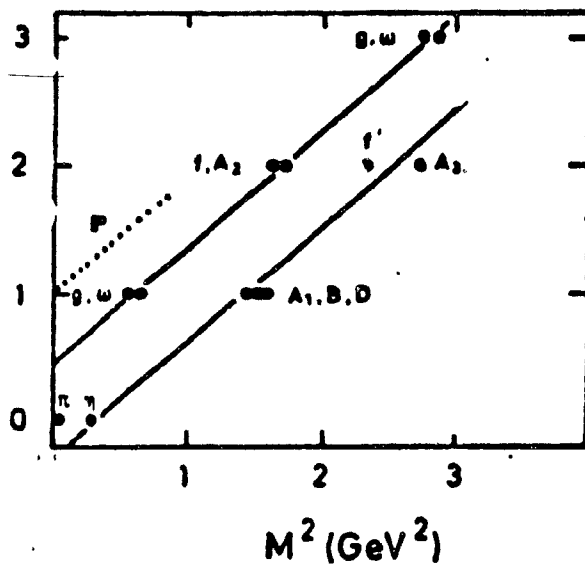
Figure 1.12



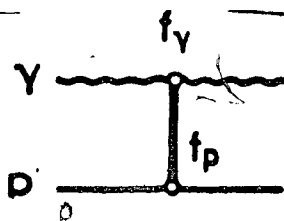
$\pi^+\pi^-\pi^+\pi^-$ mass distribution (Tasso)

Figure 1.14

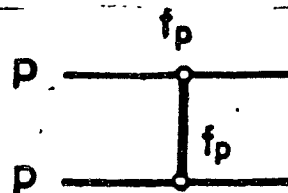
$$J = \text{Re}(\alpha)$$



$$\sigma_{YY} = c f_Y^2$$



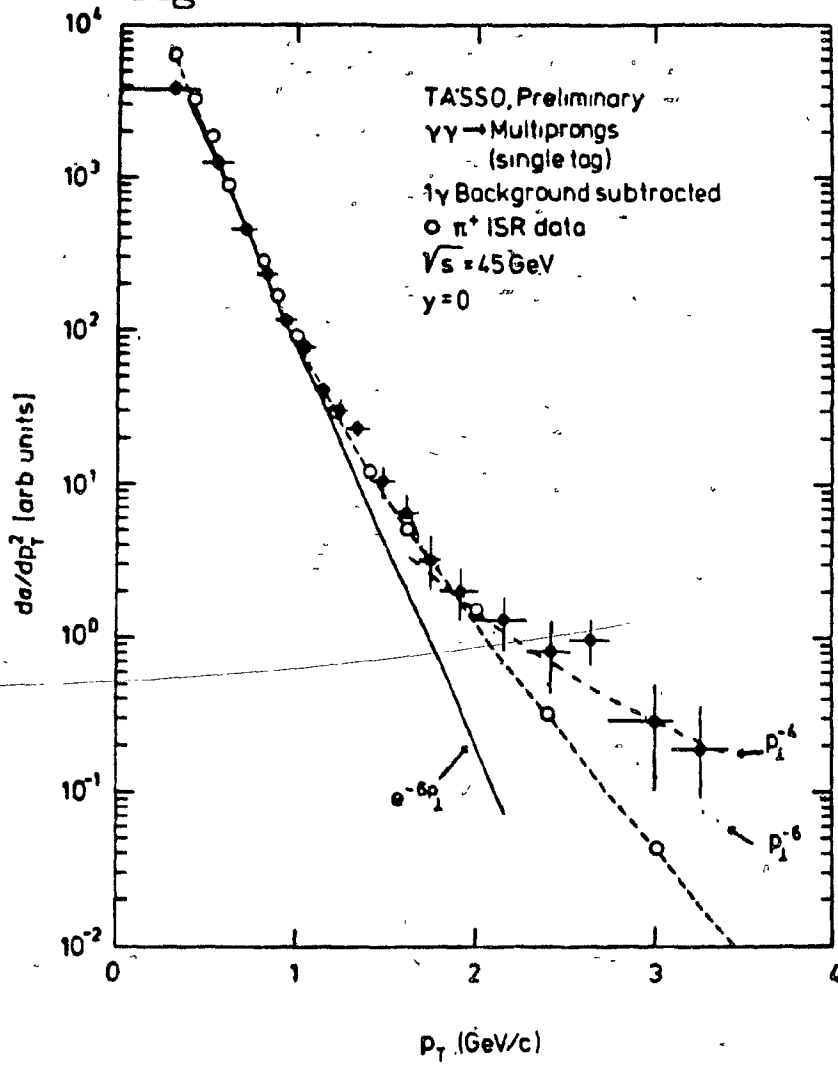
$$\sigma_{Yp} = c f_Y f_p$$



$$\sigma_{pp} = c f_p^2$$

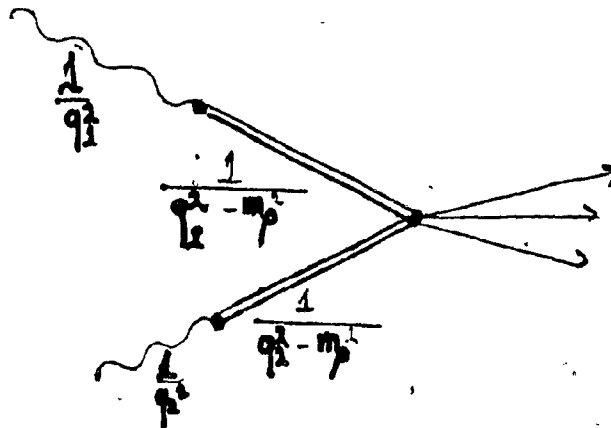
Figure 1.13 Factorization

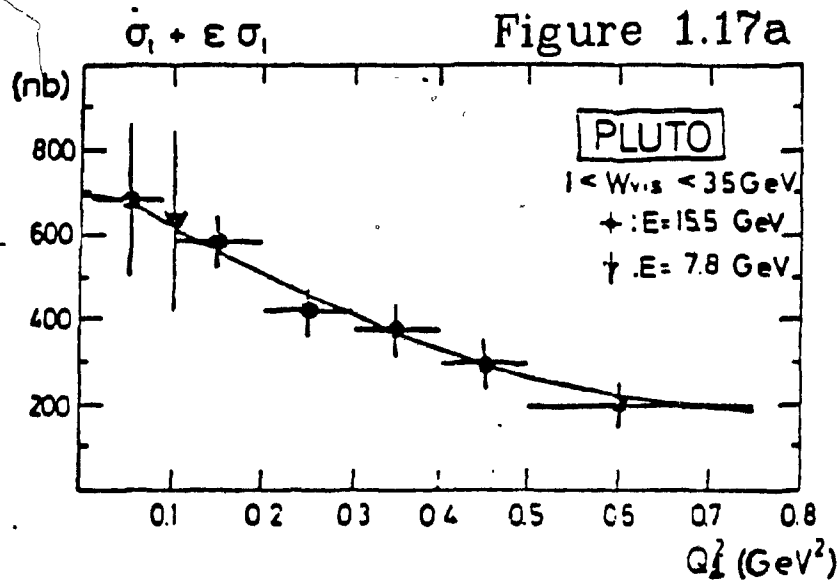
Figure 1.15



$d\sigma/dp_T^2$ for $\gamma\gamma$ -multihadron events (single tag) in comparison with ISR data (open circles)

Figure 1.16





Data Also Compatible With GVDM

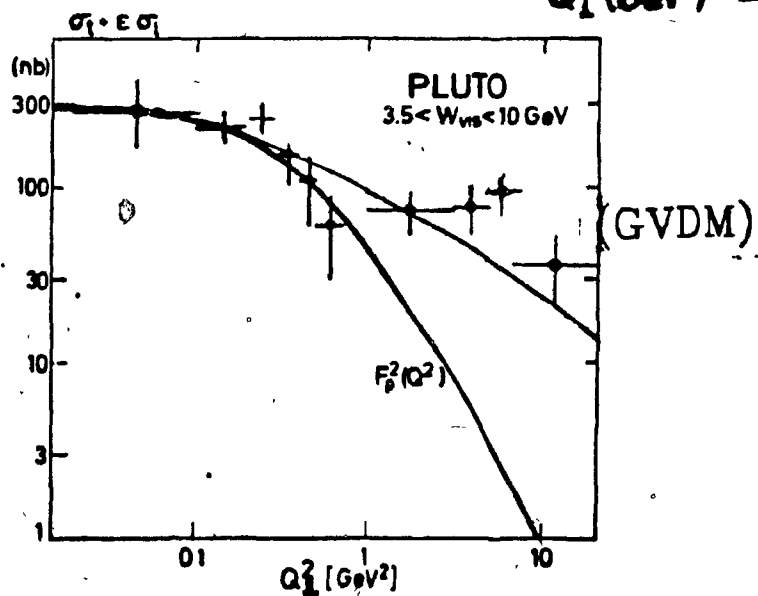
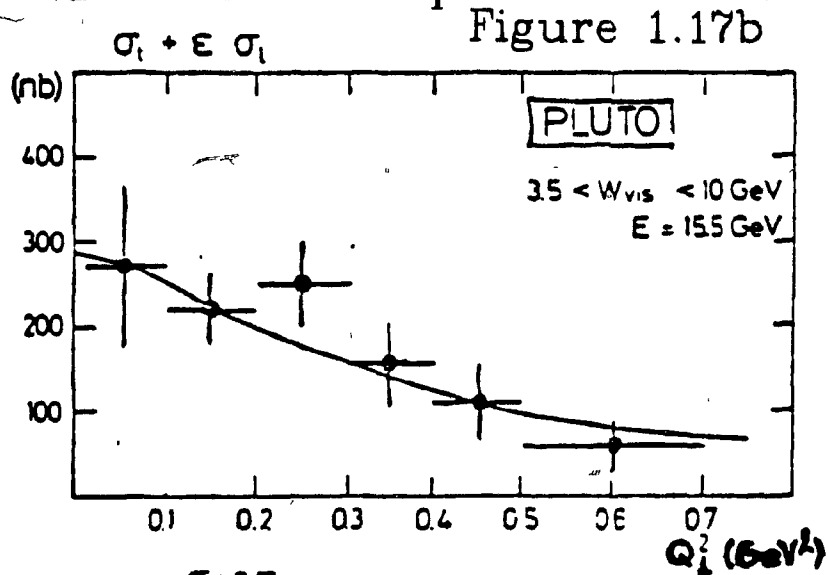


Figure 1.17c

Figure 1.18

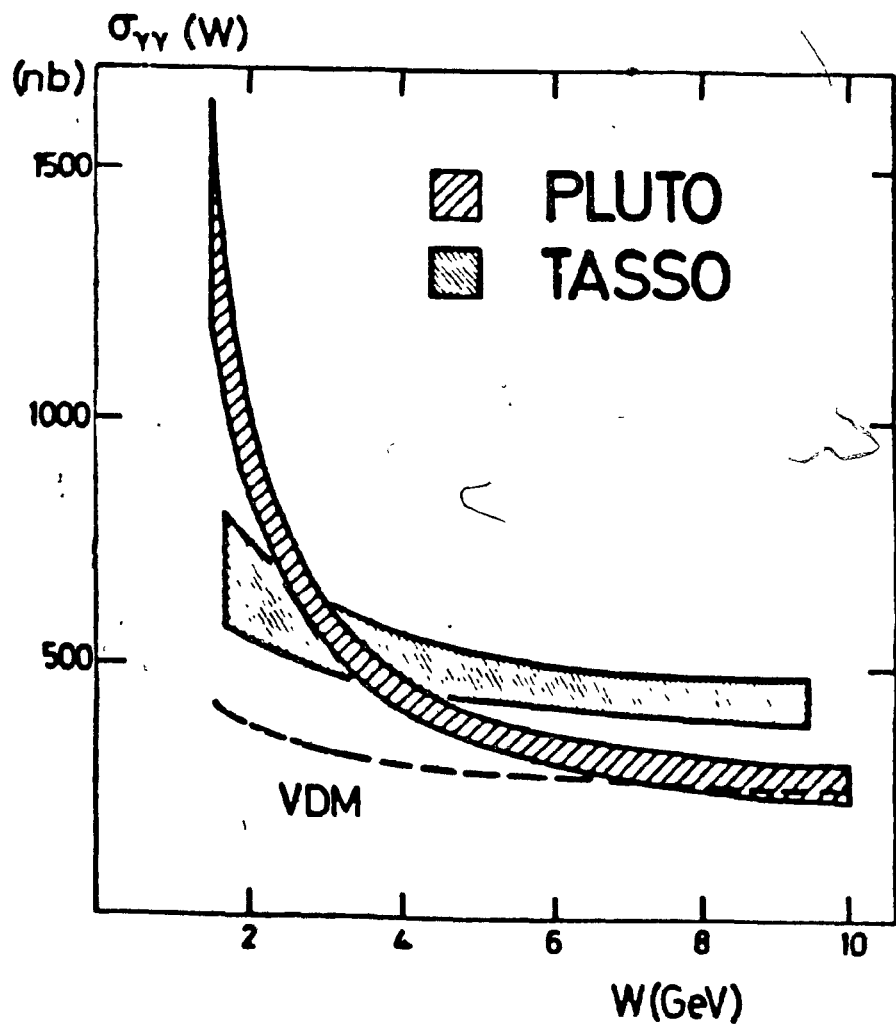


Figure 1.19a

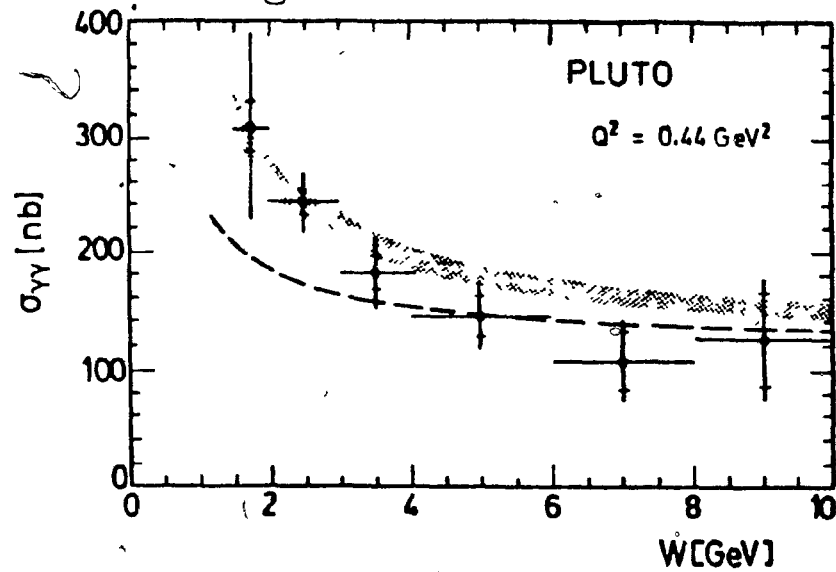
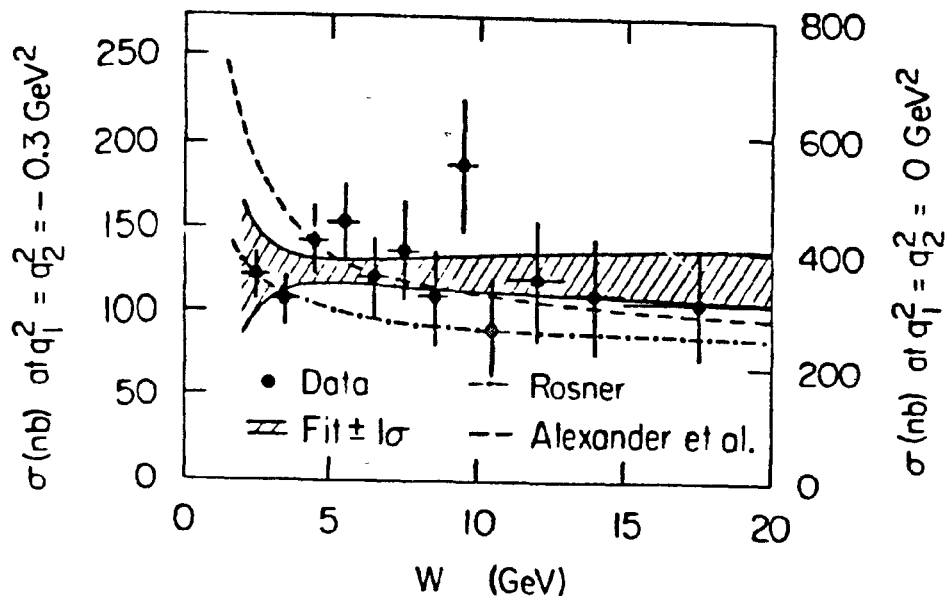


Figure 1.19b



CHAPTER 2: THE ARGUS EXPERIMENT

2.1 DESY : The ARGUS experiment was designed to operate in one of the two interaction regions of the DORIS (Double Ring Storage) e^+e^- collider. This machine is part of a larger accelerator facility known as DESY (Deutsches Elektronen-Synchrotron), and is operated as a joint project of the City of Hamburg and the Federal Republic of Germany. The central component of the facility is a 6 GeV synchrotron, which acts as a source of high energy electrons for both the PETRA and DORIS rings. The arrangement of the accelerator network is shown in Figure 2.1. The DORIS ring was operational in 1974 but was extensively altered between 1980-82. These modifications were designed to improve machine operation at the energies required for Υ meson physics. The other experimental site at DORIS is currently occupied by the Crystal Ball Detector. In addition to several high energy physics experiments, DESY supports research with synchrotron radiation at HASYLAB. This year construction was begun on a 30 GeV electron / 820 GeV proton collider known as HERA, which will start operating in 1990.

2.2 Principal Detector Components : The original proposal for the ARGUS detector was submitted in October 1978²⁰² (the acronym stands for "A Russian German United States Swedish Collaboration" - subsequently groups from IPP Canada(1982) and Yugoslavia(1984) joined the collaboration). ARGUS was designed as an advanced "second generation" detector (taking DASP's place at the DORIS storage ring) to study the new physics of the CMS energy region around 10 GeV. This included the spectroscopy of the recently discovered Υ states, first seen^{203,209} in fixed target experiments. These are "flavourless" meson states composed of b (or beauty) quarks. Additionally, the $\Upsilon(4S)$ (10.576 GeV) resonance is known to fragment into B, \bar{B} mesons (open beauty states). These investigations are significant for much of particle physics, as they provide information on heavy quark potentials, weak interaction universality for the third quark/lepton generation, and the Kobayashi-Maskawa parametrization of the weak interactions of quarks (including CP violation). In a similar vein, the study of charm quark production in the continuum was considered. This study has proved fruitful, and results on the production of F, F^* mesons have been published^{201,208}. The study of the new heavy lepton τ (1.74 GeV) was also considered in the detector design - the ability of the detector to study τ -physics being significantly enhanced by the recent addition of a vertex chamber²⁰⁴ to the experiment. Although the detector was not explicitly designed for $\gamma\gamma$ physics it is, nevertheless, quite well suited for this study as will be demonstrated in the next chapter. This capability is the result of the detector's ability to reconstruct high multiplicity events from Υ meson decays which often produce several tracks of momentum less than 1 GeV/c. The fourth chapter will describe some proposed modifications to ARGUS designed to enhance its aptitude for $\gamma\gamma$ physics - the installation of the BGO small angle taggers. The experiment started running in October 1982, and has since collected approximately 84 pb^{-1} luminosity divided between the $\Upsilon(1S)$, $\Upsilon(2S)$, and $\Upsilon(4S)$ vector meson resonances.

The central component of the ARGUS detector is the drift chamber²⁰⁵, a hollow gas filled cylinder two meters long with inner and outer diameters of 15cm and 86cm respectively. The drift chamber has 5940 sense wires and 24588 field wires arranged in 36 layers. The sense wires record pulses produced when they are hit by ions created by the passage of a high energy charged particle. The field wires shape the electric field around each sense wire, so that the timing of the pulses may be used to determine the distance of closest approach of the charged particle to the wire - information used offline by a pattern recognition program that searches for tracks of definite 3-momenta (Figure 2.2). Eighteen of the layers provide "stereo" views i.e. while half the sense wires make a right angle with the endcaps - each of these layers

forming a cylinder – the other layers are “twisted” about the symmetry axis of the detector, alternately right and left. These “stereo layers” lie in hyperboloidal surfaces which intersect the cylindrical surfaces. This geometry allows the reconstruction of the path of a charged particle in three dimensions and yields five times better spatial resolution than charge division read out, while requiring less electronics. The momentum resolution achieved is $\frac{\Delta p}{p} = .012\sqrt{1.0 + \frac{p^2 c^2}{2E^2}}$ and is limited below 1 GeV by scattering in the inner wall of the chamber (which is composed of carbon fiber and epoxy to minimize this effect) and beampipe. The chamber gas is almost completely propane – chosen because of its narrow Landau distribution i.e. the energy loss along the length of a particle track fluctuates less with propane than with other gases typically used in this application. This is important because the energy loss (referred to as dE/dX) is determined by a particle’s mass and charge. Therefore, an accurate dE/dX measurement can be used to identify the particle. Since this is a statistical process, only the most probable energy loss is known and the width of the distribution limits the particle separation. The capabilities of this particle ID method will be discussed in chapter three, where its use in rejecting background events from beam-gas collisions is described. The dE/dX resolution achieved is 5% for cosmic events and 5.6% for pions in e^+e^- annihilation events. The chamber runs in a magnetic field of .8 Tesla and has achieved a track reconstruction efficiency of 95% over 93% of 4π . A spatial resolution of $200\mu m$ in half the drift cell was achieved for high momentum (≥ 2.5 GeV/c) tracks. It is expected that, with certain improvements, a resolution of $150\mu m$ may be achieved.

The Vertex Detection Chamber or VDC was installed in the spring of 1984 and is the newest detector component. When fully operational, it will allow improved track recognition and momentum resolution for tracks that have low P_{\perp} , or originate from secondary vertices. It will also, of course, aid greatly in determining the main vertex location – allowing tighter cuts against the beamgas background (discussed in the next chapter) to be made. Secondary vertex analysis can be used in studies of channels involving τ particles, K_S^0 ... and even gluinos! The VDC reduces the minimum distance a track must be extrapolated to reach the interaction point from 17cm to 9cm. This chamber is one meter long with inner and outer radii of 5cm and 14cm respectively leading to an acceptance of 95% of 4π . It uses approximately the same technique as the surrounding drift chamber except it attempts no analysis of the Z displacement of tracks – all wires being parallel to the beams. The chamber has 594 sense wires arranged in hexagonal cells with 1412 field wires. The chamber walls are made of carbon fiber and epoxy to minimize scattering. The spatial resolution achieved by the VDC in a test beam is $90\mu m$.

The "Time of Flight" or ToF²⁰⁶ system of the ARGUS detector serves two main purposes. First, it is a fundamental component of the trigger, as discussed below, and second, it serves as one of the main sources, together with dE/dX analysis, of information regarding particle identity. Very simply, the information on charged particle path length and momentum from the Drift Chamber (and eventually VDC) analysis is used with the Time of Flight information to provide an estimate of the particle's mass. The particle identification ability is limited by the Lorentz boost and mass differences of the particles in question i.e. K,p are separated to quite high momenta (~ 1.2 GeV/c) while e/ π separation is only good below 200 MeV/c and π /K separation below 700 MeV/c (the masses of muons and pions are too close to allow any decision on this type of evidence). Since the time resolution - 220 picoseconds - is comparable to the differences in flight time induced by different masses the ToF particle ID information can only be expressed statistically. Generally, one defines a χ^2 to measure the probability of a particular identity hypothesis:

$$\chi^2 = \left\{ \frac{1}{\beta_{ToF}} - \frac{1}{\beta_{expected}} \right\}^2 / [\sigma_1^2 + \sigma_2^2] \quad (2-1)$$

where $\beta_{expected}$ is the velocity calculated for a given mass hypothesis from the path length and momentum information, and σ_1 , and σ_2 are the expected errors for $1/\beta_{ToF}$, and $1/\beta_{expected}$ determined by the ToF and Drift Chamber resolution. If all the statistical distributions involved are gaussian one can determine the probability of a particle to be of identity "X" from:

$$P(X) = \frac{f_X \exp(-\chi_X^2/2)}{\sum_{i=e,\mu,K,X,P,\pi} f_i \exp(-\chi_i^2/2)} \quad (2-2)$$

Where the f_i are the relative abundances of the different particle types. As this is an absolute probability, this form of expressing the particle ID information can be unambiguously combined with similarly formatted information from entirely different sources, e.g. drift chamber dE/dX measurements.

The ToF system is divided into three segments, the barrel section, covering 75% of 4π , (64 counters viewed by two phototubes, one at each end, arranged axially on a 95cm radius cylinder), and two 48 counter endcap segments, each one viewed by one phototube. The endcaps cover 17% of 4π . The counters are composed of NE110 scintillating material. The ToF counters are located (Figure 2.3) in the space between the drift chamber and the shower counters and are connected to the phototubes by lightguides which pass through holes in the ARGUS magnet yoke. The phototubes are located outside the magnet because they must operate in regions relatively free from magnetic fields. They are shielded from any remaining field by soft iron and μ metal cylinders. The counters operate in common start mode, i.e. the

beam crossing signal starts the TDCs (Time/Digital Converters) which are stopped by the output of a discriminator (with 80% of the corresponding ADC (Analog/Digital Converter) signal as input) after a fixed time delay of 200 ns. The discriminator also sends signals to the CPPT (Charge Particle Pretrigger) logic and LTF (Little Track Finder). 20% of the ADC signal is used for offline correction of the ToF time. The intrinsic time resolution of the ToF counters, determined from Monte Carlo analyses, is 170 picoseconds. The effective resolution is 220 picoseconds due to phototube gain variability and timing uncertainty in the bunch crossing signal.

The ARGUS Electron/Photon Calorimeters²⁰⁷ (otherwise known as shower counters) were designed to measure the energies of electromagnetically showering particles and provide limited particle identification capability. Electrons and photons deposit nearly all of their energy in the shower counters while minimum ionizing particles, muons, and hadrons (those which don't start a shower hadronically) deposit on the order of 200-300 MeV in a wide Landau distribution. As the extent of light losses have been extensively studied in a test beam and via the EGS (Electron-Gamma Shower) Monte Carlo, the total energy for electromagnetic showers can be determined accurately. This leads to an energy resolution of:

$$\frac{\sigma}{E} = (.068^2 + \frac{.08^2}{E})^{\frac{1}{2}} \quad (2-3)$$

If one plots the measured drift chamber momentum vs. $\delta = \frac{1}{p} - \frac{1}{E}$ (Figure 2.4), it is apparent that the electrons, which appear as a horizontal band near $\delta = 0$, are well separated down to momenta of 600 MeV/c. Hadronic showers can be characterized by their shape which is much wider than that of an electromagnetic or minimum ionizing shower.

There are a total of 1888 shower counters, 1536 barrel and 352 endcaps. These are located within the ARGUS magnet yoke and are read out by wavelength shifter bars which extend through slits in the yoke. The photomultipliers are located outside the magnet to avoid its field. The design resolution of the counters, $7.5\%/\sqrt{E}$, was achieved in test beam experiments. However, during installation, distortion of the light guides and fibre optics (which are used for laser calibration of the shower counters) introduced additional uncertainties, producing the constant error term in equation 2-3. The counters are composed of alternating lead plates and scintillator (1 & 5mm thick respectively), 39cm long, providing 12.5 radiation lengths of electromagnetic shower absorber. The light from the scintillators is absorbed by a wavelength shifter bar that runs along the side of the shower counter (each sheet of scintillator is perpendicular to

the wavelength shifter bar). The wave length shifter then emits light isotropically, allowing some of light to make its way to the photomultiplier outside the magnet coil.

The ARGUS magnet produces a field of .8 Tesla and is composed of 13 coils, slits between which allow the Shower Counter and ToF light guides to pass outside. The total mass of the magnet and yoke is 365 metric tons. The effect of the magnetic field on the DORIS beams is compensated by two sets of four electromagnets at each end of the detector. These coils are close to the beam and collisions between the beam halo and the compensation coils can produce many "noise" events depending on the machine conditions.

The muon chambers (Figure 2.5) operate over 85% of 4π and consist of 1744 proportional tubes of 6cm x 6cm cross-section. There are two layers of chambers. The inner layer uses the copper coil and iron shielding as a hadron filter of 3.3 absorption lengths. The second set of chambers is located outside the flux return yoke (which provides an extra 1.8 absorption lengths of hadron filter). The inner layer covers 50% of 4π and a muon must have at least 720 MeV/c momentum to penetrate this far. The outer layer covers 85% of 4π with a cutoff momentum of 1110 MeV/c. The "punch-through" probabilities of hadronic showers and the contribution of μ s from K or π leptonic decays are on the order of 1-2%.

2.3 The ARGUS Trigger : The ARGUS detector trigger is divided into two main stages: the pre-triggers, derived from discriminators operating on ToF counter outputs or the analog sums of groups of shower counters; and the LTF or Little Track Finder which does an efficient two dimensional track search using the drift chamber ADC information. The LTF is a programmed hardware unit - it matches a number of geometric masks starting from a ToF hit to the drift chamber information and counts the number of drift chamber ADC hits within this area (each drift chamber ADC sends one "bit" to the LTF). If enough hits intersect an LTF mask, the LTF counts one track. Each mask represents the area of the drift chamber XY projection intersected by tracks of a small P_{\perp} interval - the range of ϕ being determined by the ToF counter size. Only the barrel ToF are used by the LTF as starting points for track searches at present. It is possible to include the endcap ToF counters and a set of masks has been produced for this type of track. With the presence of the vertex chamber, the LTF will be able to have a good efficiency for low momenta tracks - possibly as low as 65 MeV/c.

The total energy trigger (ETOT) requires at least a ~ 350 MeV from the shower counters in each of the $\pm Z$ halves of the detector (the Z axis of the detector is tangent to the beam orbit). This is only visible energy in the form of an analog sum of the shower counter pulse heights for each half of the detector - no calibration, or compensation for energy loss or absorption, can be carried out online. Therefore, one cannot really say that the threshold is 350 MeV for each event, this depends on the actual discriminator thresholds and the effects of calibration. Additionally, Bhabha events ($e^+e^- \rightarrow e^+e^-$) always set the ETOT triggers, while mu-pairs ($e^+e^- \rightarrow \mu^+\mu^-$) seldom deposit enough energy in the shower counters as the muons are minimum ionizing particles. ETOT triggers do not require any LTF tracks - the trigger logic sends a signal to the LTF disabling its event veto for the duration of the detector readout period.

The triggers with the highest acceptance for $\gamma\gamma$ events are the CPPT (charge particle pretrigger) and CMATRIX (coincidence matrix). These are built out of CPPT elements. Two CPPT elements are formed by coincidences between one of 32 groups of 4 ToF Counters which run the length of the detector and a pair of shower counter groups directly behind the ToF group dividing it into $\pm Z$ regions. At present, only the barrel ToF and shower counters contribute to the CPPT elements. This geometric restriction limits the P_{\perp} to be at least 125 MeV/c and θ (the angle between a particle track and the Z axis) to be at least 45 degrees - for a particle to graze the barrel shower counters. If the CPPT elements are extended to include the endcap the trigger acceptance increases to include P_{\perp} as low as 65 MeV/c with

an acceptance of 90% of 4π . The CPPT trigger requires one LTF track and one CPPT element set in each Z-hemisphere. This trigger is important for μ pairs and is present in about 60% of the observed $\gamma\gamma$ events. However, as the CPPT trigger requires one charged track in each hemisphere of the detector it misses two photon events with a large Lorentz boost along the Z axis - a common occurrence. The CMATRIX (Figure 2.8) trigger partially compensates for this - it requires two LTF tracks and two CPPT hits separated by at least 90 degrees in ϕ (the azimuthal angle) with no requirement on the hemisphere of the CPPT groups. The CMATRIX was designed to catch events with some hope of total P_{\perp} balance. However, as tracks with low P_{\perp} are strongly curved, charge balance events with two coplanar 125 MeV/c tracks will set only one CPPT element. The requirement of a 90 degree separation between the CPPT elements hit raises the threshold P_{\perp} for CMATRIX triggers to 250 MeV/c if the event is coplanar (this property implies total P_{\perp} balance in two body events) with $\sum Q = 0$.

The last trigger added to the experiment was the HESH or High Energy Shower trigger. This consists of eight groups of 110 barrel shower counters in each half of the detector. Each group spans 75 degrees in ϕ and shares 22 counters with the group on either side. The HESH requires at least 1 track from the LTF and ~ 600 MeV/c visible shower counter energy in any HESH shower counter group.

If the synchrotron running conditions are bad and a high level of noise events from beamgas or beam halo/detector collisions occur, deadtime induced by the finite readout time of events (~ 50 msec) will become large enough to necessitate an artificial decrease in trigger acceptance. A coincidence can be required between the CPPT and CMATRIX triggers and/or the LTF track threshold can be increased. The latter panacea is usually chosen. Both of these changes reduce the visible $\gamma\gamma$ event rates, but the latter is the more serious (on the order of 10% of the full barrel trigger $\gamma\gamma$ cross-section survives) as even a $\gamma\gamma$ multiprong event may not contain enough high P_{\perp} particles. Clearly, as the Lorentz boost of $\gamma\gamma$ events along the Z axis decreases acceptance, it is desirable to have a full detector trigger - ideally two tracks anywhere in the drift chamber should be the only requirement. Including the endcaps in the trigger would lead to an increase in the $\gamma\gamma$ rate on the order of 100% for QED events and as much as a 70% increase for hadronic channels. Table 2.1 gives the experimentally determined trigger rates for 4 classes of events. The charge balance two prong and multiprong categories are considered to be clean $\gamma\gamma$ event samples. The description of the Cosmic and beamgas event selection is given in the next chapter.

Trigger Type	2 Prongs $Q = 0$	Multiprongs $Q = 0$	Cosmics	Beam/Gas Collisions
%Abundance	62	5.7	5.6	18.3
%ETOT	2.3	5.7	3.0	.4
%CPPT	56.0	64.6	76.8	47.3
%CMATRIX	78.2	81.7	86.4	85.2
%HESH	1.3	1.6	2.5	.3
%ETOT only	1.4	1.4	2.0	.1
%CPPT only	18.2	14.2	8.3	13.1
%CMATRIX only	40.3	31.3	17.7	51.0
%HESH only	.5	.6	1.4	.2
%CPPT&CMATRIX only	37.6	49.7	68.4	34.1

Table 2.3 Trigger Analysis For Various Event Classes

There is some hope for a better trigger in the near future. The most optimistic point is the use of a CAB (CAMAC Booster) to organize all the detector/computer interaction into one burst for each event. At present, each group of components is read into a PDP-11 separately producing a delay as the computer prepares each data transfer. The PDP then transfers the data to a VAX 11/780 which temporarily stores the data and eventually transfers it to an IBM which writes it to tape. The limiting time per event due to the CAB is 5ms but the PDP response limits this to 10-15ms - still a great improvement over the 50msec readout time limiting the present arrangement. The situation may be improved further with the implementation of the VDC in the LTF. This will provide a strong Z restraint on the interaction vertex allowing most of the beam halo/compensation coil and beam-gas events to be eliminated at a much earlier stage in the experiment. If both these improvements are made, it will be possible to include the endcaps in the trigger.

3.4 Monte Carlo Simulation of the ARGUS Detector : Detector Monte Carlo programs can be separated into two main types: a simplistic one generally called a "MiniMC" and a "full detector simulator". The latter provides an output that is similar to the data record produced by the experiment. The "full detector" Monte Carlo for ARGUS is called SIMARG and is based on the CERNLIB drift chamber simulation program GEANT. SIMARG attempts to simulate every physical process involved in the operation of the detector except the actual e^+e^- or $\gamma\gamma$ collision - the description of the collision is supplied by a separate program called an event generator. Each track provided by the event generator is traced by SIMARG through the material of the detector, with scattering probabilities, energy loss, and decay probabilities being taken into account. The energy loss in the drift chamber is calculated together with the ADC and TDC signals. The shower counter pulse heights are calculated from a detailed Monte Carlo (derived from EGS, the Electron-Gamma Shower simulator program developed at SLAC). The whole process is CPU (computer time) intensive - most of the computer time consumption being concentrated in the shower Monte Carlo. This only simulates minimum ionizing and electromagnetic shower types. It is expected that hadronic shower simulation will be available in the near future.

Due to the SIMARG program's enthusiastic CPU consumption the statistics available with this type of acceptance simulation are limited. It is possible to understand the acceptance for a reaction to a high degree if only geometric effects and resolution are considered. This can usually be accomplished in a program on the order of a thousand times faster (in computer time consumption) than SIMARG. This type of program is known as a MiniMC and cannot include efficiencies or the resolution of detector components, unless they have been parametrized from experimental widths or SIMARG-generated data. However, the major factors in detector acceptance - geometric cuts - can be included easily. In performing the analysis described in chapters five and six, the MiniMC used evolved constantly. The original version used simple geometric cuts to determine acceptance:

$$|\cos(\theta)| \leq .9 \quad ; \quad P_{\perp} \geq 40 \text{ MeV}/c \quad (2-4)$$

If two tracks passed these cuts the event was considered to have been triggered. For photons the following cuts were used:

$$|\cos(\theta)| \leq .94 \quad ; \quad E_{\gamma} \geq 50 \text{ MeV} \quad (2-5)$$

The acceptance results for the total $\gamma\gamma$ hadronic cross-section measurement presented to the DESY Program Committee in October 1983 were derived using this simulation. It was assumed that the barrel

trigger would be extended to the full trigger described in section 2.3 by the time the $\gamma\gamma$ total cross-section measurement with ARGUS became feasible. When the investigation of exclusive channels in $\gamma\gamma$ was considered in early 1984 it was realized that the current restrictive trigger conditions must be considered. This led to a program that included the CPPT and CMATRIX in the trigger simulation. ETOT trigger simulation was considered but it became apparent that this contributed little to the $\gamma\gamma$ data so this extension was not completed. In addition, the energy resolution of the shower counters and the P_{\perp} and $\cot\theta$ resolution were included in the new version of the MiniMC. Some main effects neglected by the MiniMC at present are:

- (1) Drift chamber efficiencies for tracks in extreme regions of P_{\perp} and $\cot\theta$.
- (2) Shower counter efficiency for low energy γ s.
- (3) Threshold efficiencies for CPPT elements.
- (4) Minimum ionizing particle shower energy deposition.
- (5) Particle ID with ToF counters.
- (6) Hadronic Shower Energy Deposition.
- (7) Particle ID with dE/dX .

These are arranged in order of their probability of ever being included in a MiniMC. The first three categories would be quite easy to parametrize, given sufficient statistics from SIMARG. The fourth category could be parametrized using information from μ -pair events at high momenta and the second half of cosmic ray tracks (i.e. the half incident on the shower counters from the inside of the detector) at low momenta. The last three categories will probably never be included, and are the main reasons that a full detector Monte Carlo is necessary for some analyses. This is mainly due to the importance of shower fluctuations and the influence of software shower separation algorithms. In a similar manner the implementation of the efficiency of dE/dX or ToF particle separation is quite difficult due to the statistical nature of these measurements.

2.5 CAPTIONS FOR FIGURES

2.1 The DESY e^+e^- Accelerator Facility.

2.2 Reconstruction of A High Multiplicity Event in The ARGUS Drift Chamber.

2.3 The ARGUS Detector: 1) Muon Chambers, 2) Shower Counters, 3) Drift Chamber, 4) Time-of-Flight Counters, 5) Mini Beta Quadrupoles, 6) Iron Yoke, 7) Solenoid Coils, 8) Compensation Coils.

2.4 $\delta = \frac{1}{p} - \frac{1}{E_{\text{tot}}}$ vs. Momentum. Figure 2.4a shows data from two prong events with cosmics and beamgas removed while Figure 2.4b shows data for minimum ionizing particles (muons) simulated by the SIMARG program. Evidence for the presence of electrons is seen in Figure 2.4a as a horizontal band at $\delta = 0$.

2.5 This event appears to be a radiative μ pair ($e^+e^- \rightarrow \mu^+\mu^-\gamma$) with the photon converting to an e^+e^- pair in the beam tube. The tracks reconstructed in the drift chamber are shown in Figure 2.5a while one view of the muon chambers is shown in Figure 2.5b with the extrapolation of the drift chamber tracks to the muon chambers overlaid. The muon chamber hits appear as lines of squares. Track 3 hits the forward muon chambers which are not visible in the drawing.

2.6 This diagram shows the geometric requirement imposed by the CMATRIX trigger. For this trigger to be set there must be at least one track hitting each of the shaded areas.

Figure 2.1

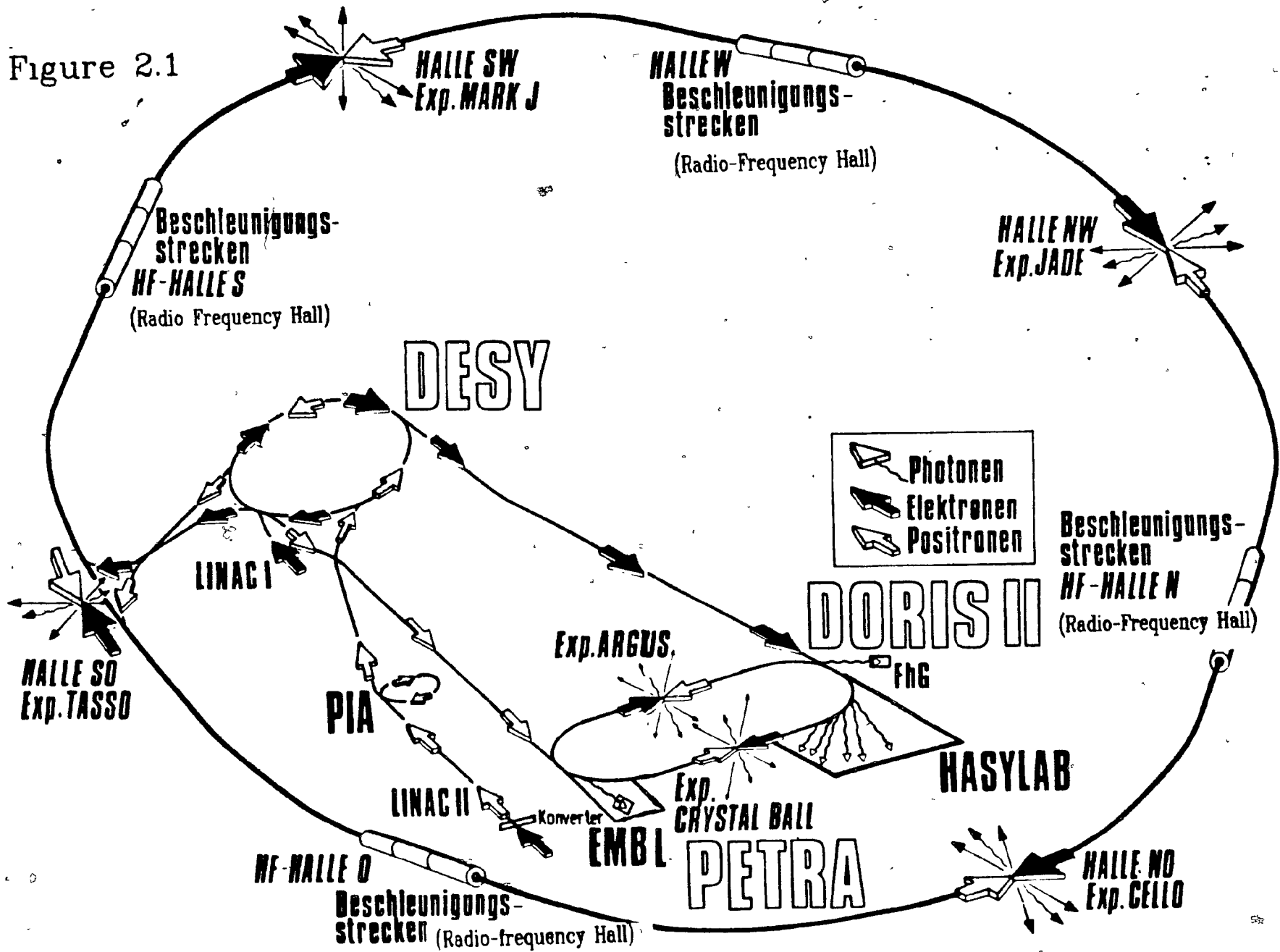


Figure 2.2

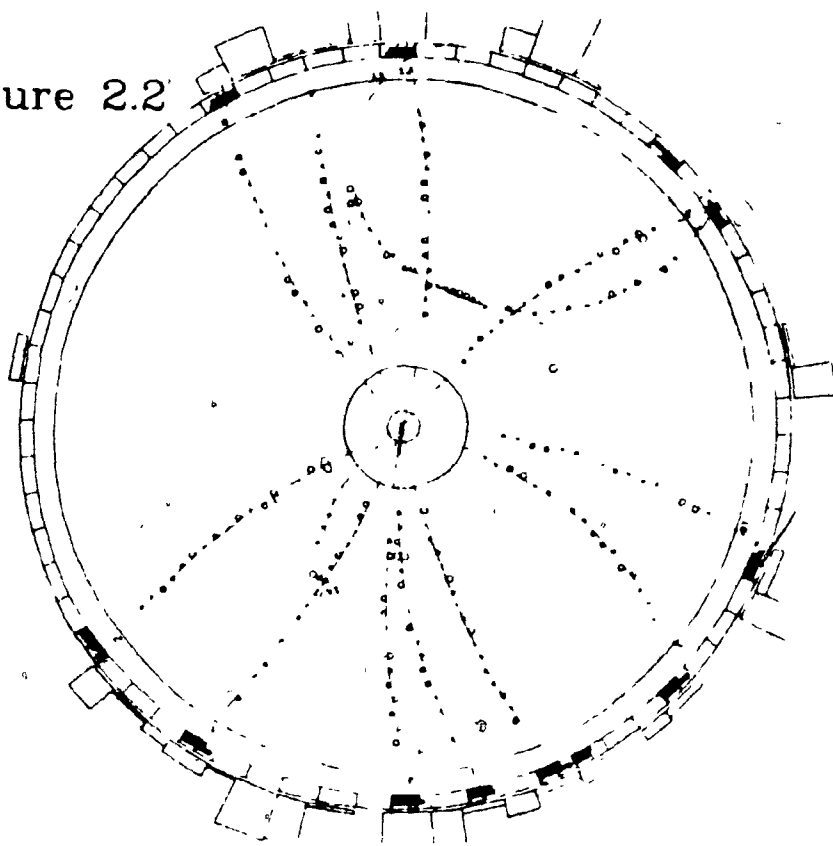
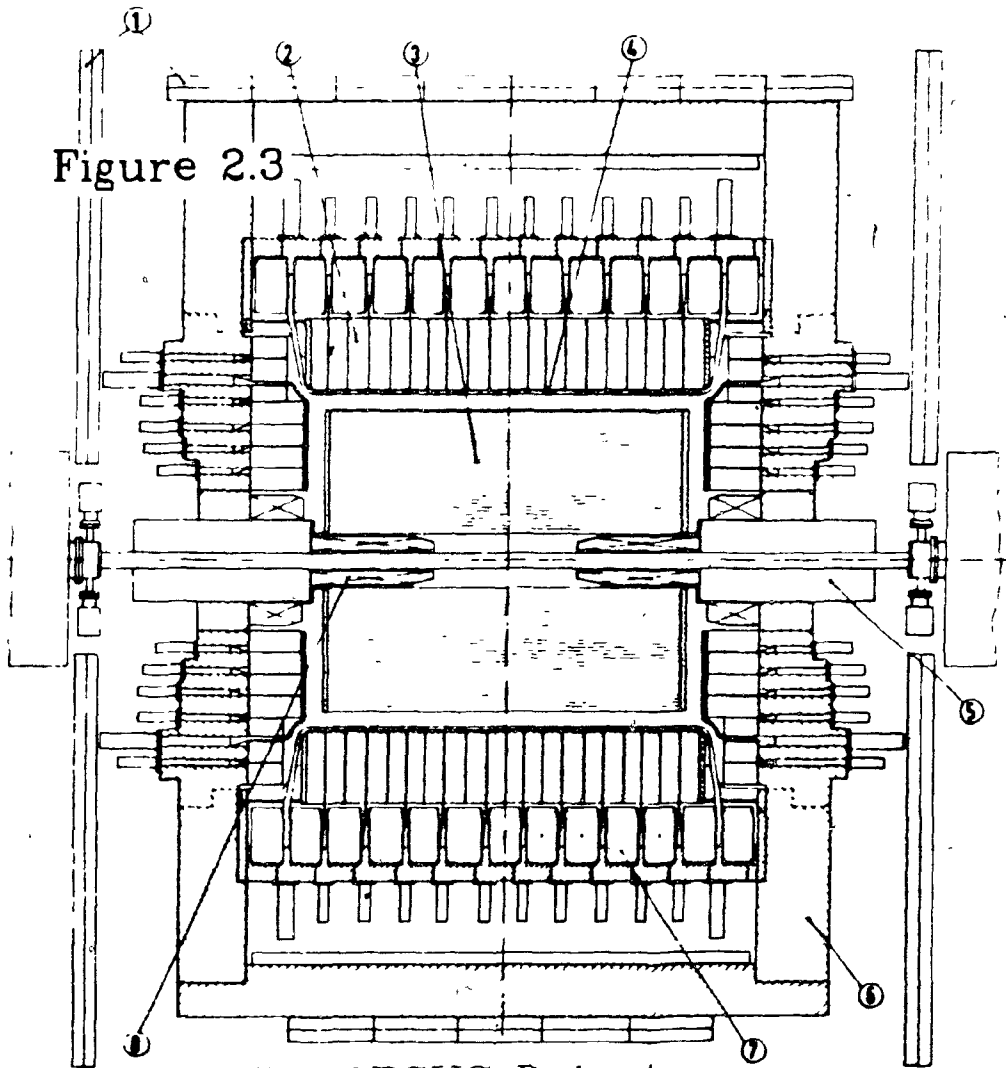
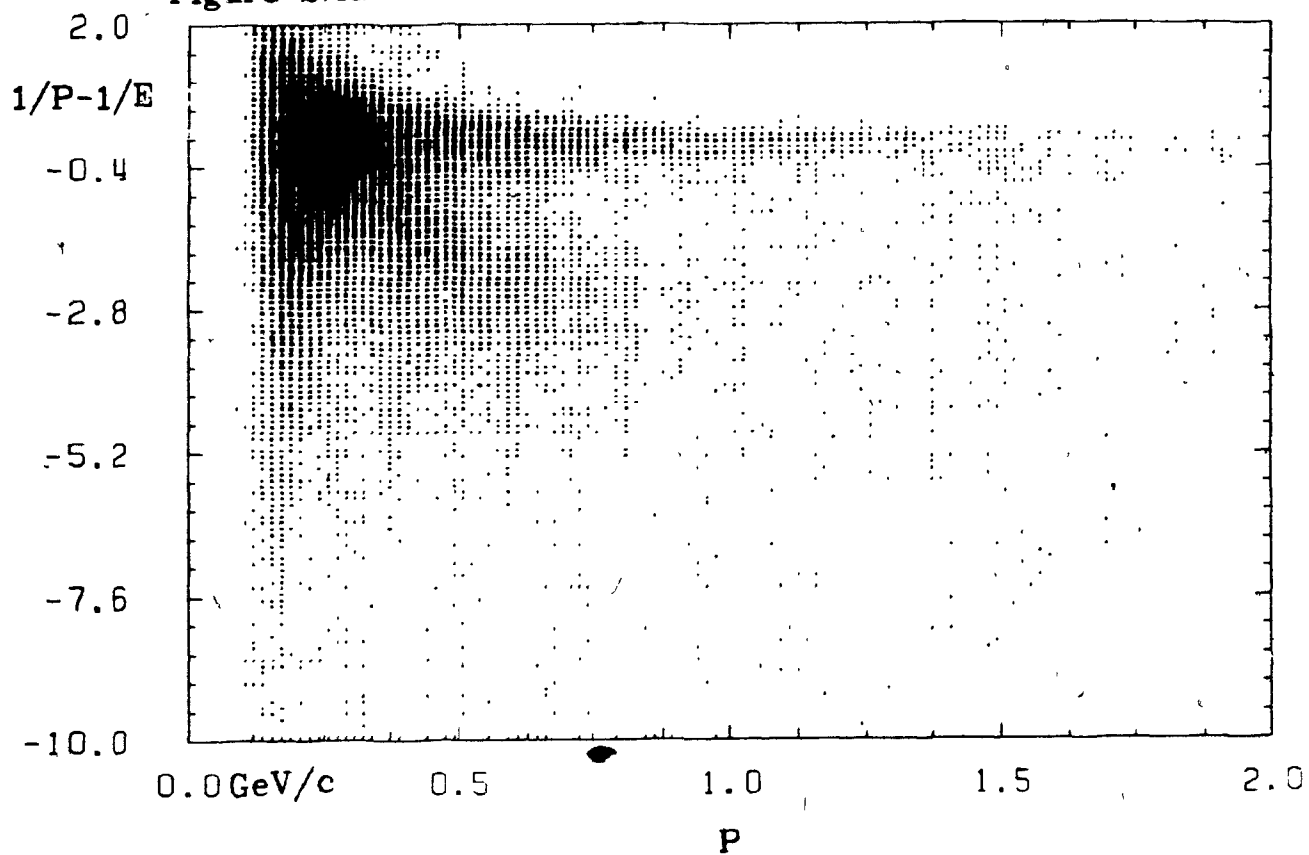


Figure 2.3



THE ADCIS DETECTOR

Figure 2.4a



E = Energy Deposited in Shower Counters

P = Momentum from Drift Chamber Information

Figure 2.4b

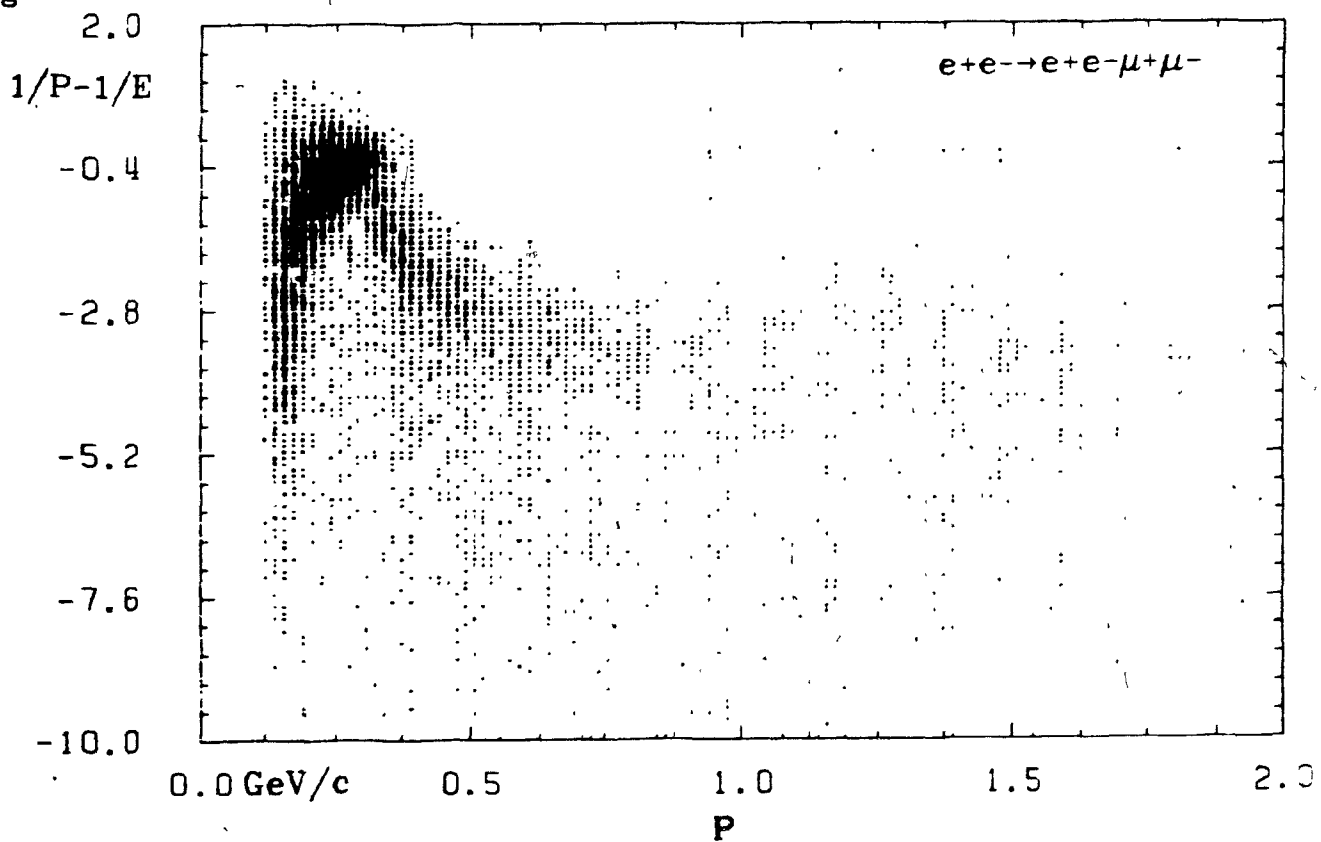


Figure 2.5b

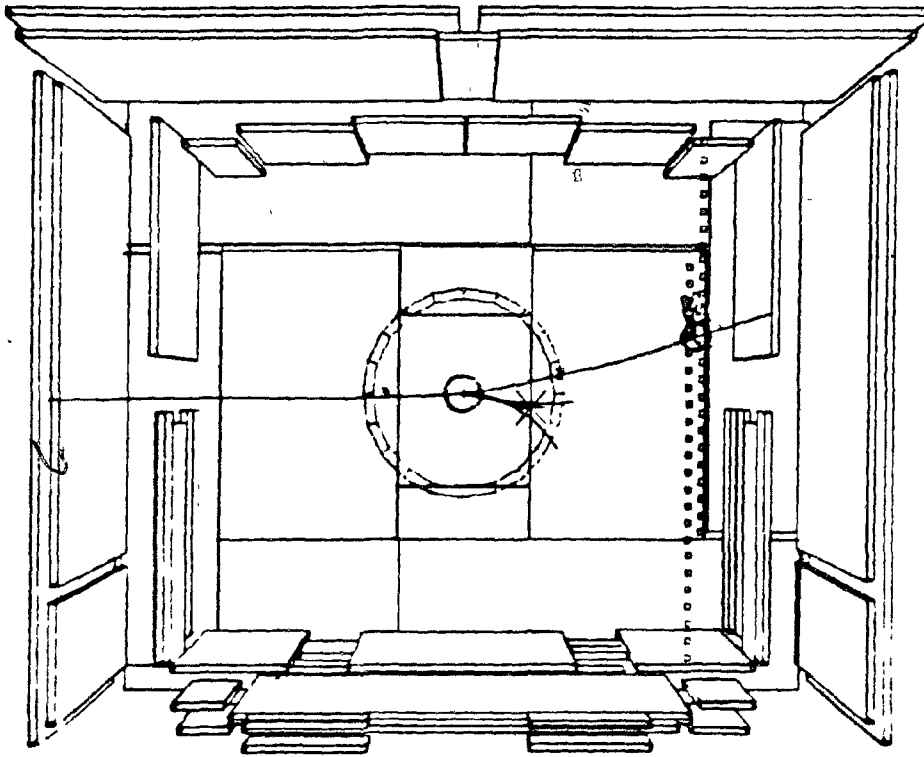
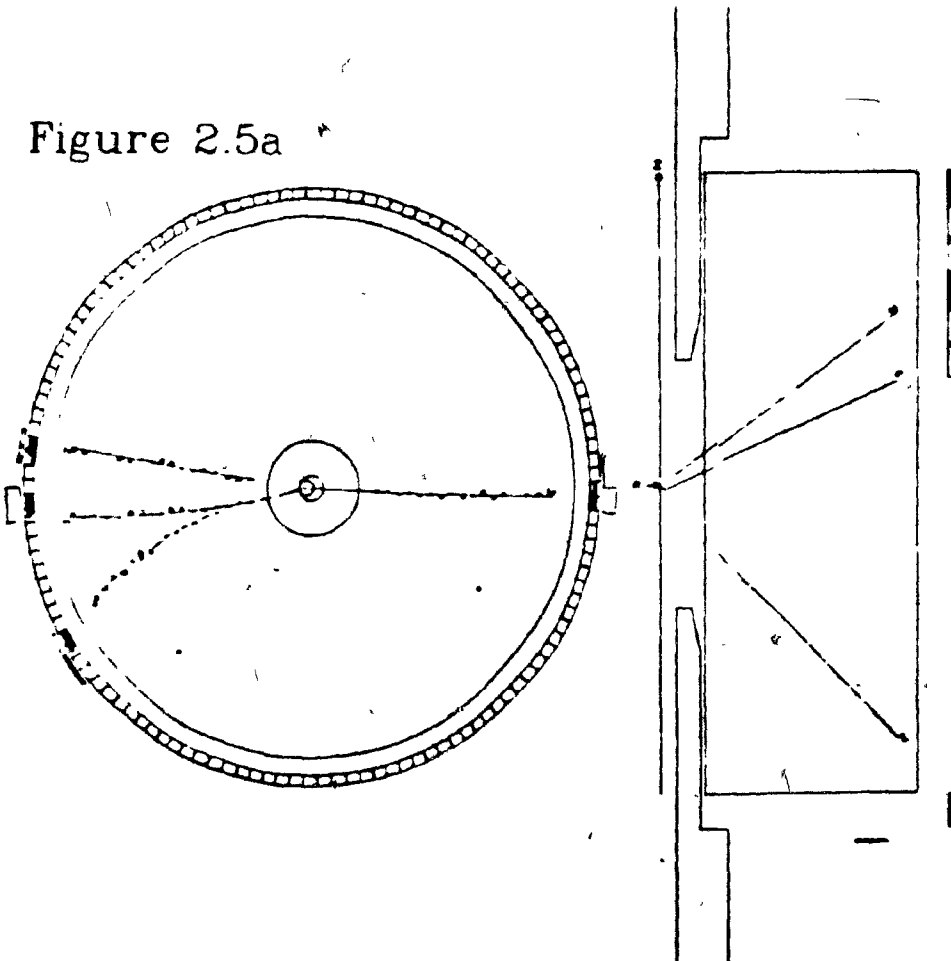


Figure 2.5a



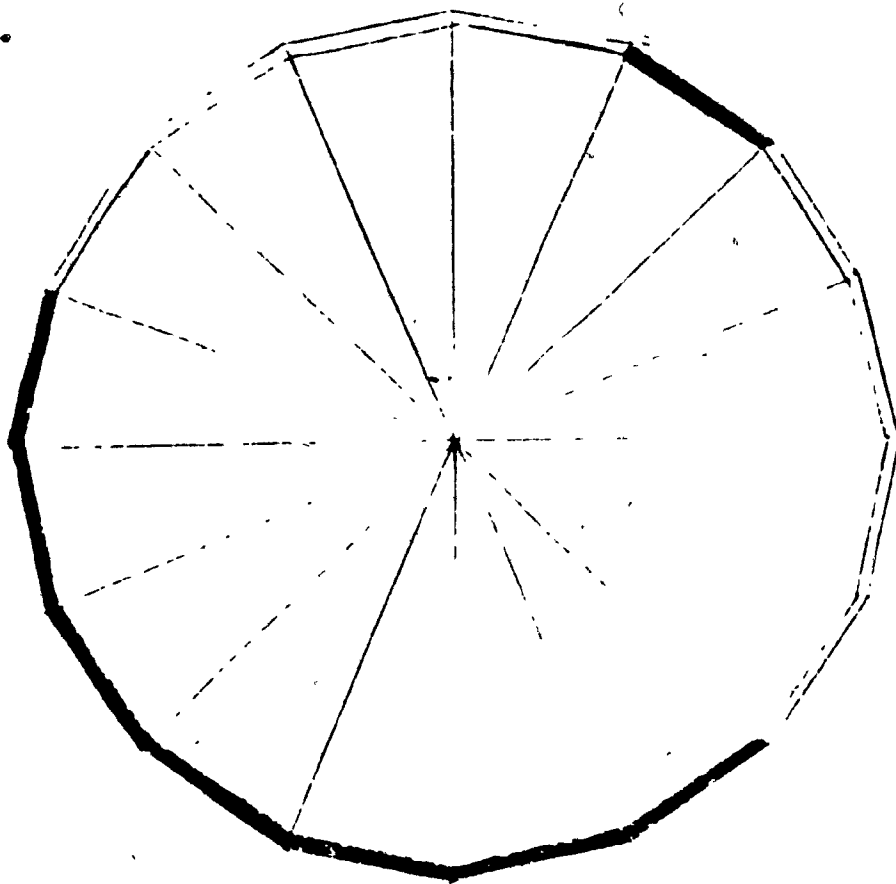


Figure 2.6

3.1 Cosmic and Beamgas Backgrounds : In the summer of 1983 the first search for two gamma events in the ARGUS data was completed. This preliminary investigation used only the data from ARGUS Experiment 1 (Fall 1982) and produced negative results. As the triggers used during 1982 did not include the CMATRIX (this is the most critical trigger component for two gamma acceptance) this result was not entirely unexpected. Additionally, the CPPT and ETOT triggers were still under development. Nevertheless, this experience was useful in developing techniques for separating $\gamma\gamma$ events from the experimental data.

Originally, only exclusive two prong events were studied as the simple QED channels were known to be the dominant final state in $\gamma\gamma$ collisions ($e^+e^- \rightarrow e^+e^-\mu^+\mu^-$, $e^+e^-e^+e^-$ events with the "beam" leptons lost down the beampipe). Energy and total P_\perp cuts were used to separate the annihilation channel events. The second cut was used because exclusive two photon events have small $|\sum \vec{P}_\perp|$ (the colliding photons are emitted almost collinearly with the beams). Fortunately, annihilation channel events with visible energies low enough to be confused with two photon events usually have lost one or several particles due to detector acceptance, or, as in $e^+e^- \rightarrow \tau^+\tau^-$, have lost visible energy by neutrino emission. It is rare that there is good P_\perp balance for these event classes. The missing energy and the total visible momentum tend to be correlated for degraded annihilation events - the correlation is complete when there is only one missing particle (e.g. radiative bhabha scattering with a photon lost) and decreases when the number and momenta of the missing particles increase. Notag two gamma events always have the greater part of their energy lost through the e^+e^- pair scattered at very small angles, hence these events show little (missing energy)/momentum correlation. The total energy spectrum of two gamma events can be understood qualitatively as the product of two bremsstrahlung spectra ($1/E_\gamma$) producing a dependence proportional to $\sim 1/s$ ("s" is the mass squared of the two gamma system, $s \cong 4E_{\gamma_1}E_{\gamma_2}$). A maximum energy cut is usually placed around 30% to 40% of the CMS energy to reject annihilation events.

Unfortunately, in the first analysis those events left after the annihilation events were removed were almost all background events caused by cosmic rays. When new data from Experiment 2 (1983) was searched for two-photon events in the spring of 1984 a definite signal was found (Figure 3.1). Here

evidence for two gamma events appears as an enhancement of the visible energy spectrum at low visible energies (note the similar low energy behaviour of all the distributions shown in Figure 3.1 - including those of Cosmic and Beamgas events). The annihilation channel produces a wide peak below the actual CMS energy due to detector inefficiencies and the pion mass hypothesis used for all charged tracks in the events. All of this data was taken on the $T(2S)$ or $T(1S)$ resonances (this terminology refers to the resonant production of this meson in the e^+e^- annihilation channel at the machine energy used) when the full barrel trigger was implemented: ETOT(LTF threshold 0), HESH(LTF threshold 1), CMATRIX(LTF threshold 2), and CPPT(LTF threshold 2). Unfortunately, other data taken early in 1983 (mostly on the $T(1S)$) had only CPPT and ETOT triggers operating leading to a 50% reduction in the $\gamma\gamma$ rate. During the $T(4S)$ running the trigger was nominally complete, but the LTF threshold was raised to three tracks for events with only CPPT or CMATRIX triggers. At this energy the synchrotron beams produced noise (beam scatter off compensation coils etc.) that increased the raw trigger rate to the point where the deadtime became prohibitive when the low LTF threshold was used. The reduction in trigger acceptance effectively decimated the visible $\gamma\gamma$ rates in the $T(4S)$ data - the effect being serious even for multiprong events as several of the extra tracks usually have low P_{\perp} and do not reach the barrel ToF counters to contribute to a trigger. Further analysis was only carried out over the data taken with the complete trigger.

The Experiment 2 data was not without contamination. Cosmics were easily separated. These events consisted of cosmic ray muons that passed close enough to the interaction vertex for the analysis program to confuse them with true two track events. Cosmics can be identified by several clear event signatures. The two halves of the track are nearly always highly collinear compared to normal $\gamma\gamma$ two prong events (Figure 3.3), providing the muon momentum is high enough so that it doesn't scatter significantly in the inner wall of the drift chamber. One can also separate cosmic events using ToF (Time of Flight) information - the difference between the ToF times for the counters at each end of the drift chamber track should be greater than six nanoseconds as the straight line distance between two diametrically opposite ToF counters is 1.902 meters and the path length (transit time) increases with curvature in the magnetic field. Normal two prong events rarely have a time difference greater than two nanoseconds even if the event is very asymmetric. Since the ToF resolution is approximately 220 picoseconds there is an unambiguous separation between normal events and cosmics (Figure 3.2). Finally, cosmic events often hit the Muon chambers and reach the experiment (after losing energy in the magnet coils and hadron

filters) with an energy that is obviously too low to allow the particle to penetrate the hadron filters and reach the Muon chambers if it had really originated at the interaction point.

A much more difficult problem is the separation of beamgas and beamwall events from the $\gamma\gamma$ data, i.e. identifying the results of collisions between beam particles and residual gas in the beampipe or some of the material surrounding the beam. With accurate vertex analysis - only available in the more recent versions of the ARGUS analysis program - a great deal of the beamgas and almost all of the beamwall events can be rejected. Unfortunately, there still exists a significant number of beamgas events with vertices in the fiducial region (usually defined as $r < 1$ cm and $|z| < 5$ cm). These tend to have high total P_{\perp} and could be limited (along with feed-down from incompletely reconstructed annihilation channel events) to some extent by appropriate cuts in this variable (Figure 3.5). However, a much more effective technique involves using the particle identification abilities of the detector to separate events with protons in them. These events are highly suspicious as it is rare for $\gamma\gamma$ collisions to produce baryons. In addition there is an unexpected abundance of these events with total charge positive - resulting, perhaps, from e^+p collisions or low energy protons from breakup of nuclei in beamgas collisions. Unfortunately, ToF mass information isn't calibrated on the datasets which contain most of the two gamma events¹. The only baryon-sensitive identification technique left then is dE/dX identification (Fig. 3.4b) (antibaryons may be detected by their anomalous shower counter energies). This analysis produces a " χ^2 " for five possible particle hypotheses: e, μ, π, K, p . (this " χ " can be understood as the difference between the most likely dE/dX for a particle hypothesis and the actual measurement in units of its estimated error). After studying various possibilities, an optimized algorithm was developed for beamgas event separation. An event is considered to be a beamgas collision if any of the following criteria are satisfied: 1) any track in the event has a minimum χ^2 for the proton hypothesis and the track's momentum is in a region where there is at least a 3σ ($1\sigma = 1$ standard deviation) separation between the theoretical proton dE/dX and any of the e, μ, π, K theoretical dE/dX's (Figure 3.4a), 2) any track in the event has a χ^2 for the proton hypothesis less than 3 (with the same qualifications), 3) any track in the event has a momentum and dE/dX value in a region of the (p,dE/dX) plane where there is no significant chance of the track being any

¹The offline data processing is restrained by available computer time. In an attempt to limit the amount of data that has to be reprocessed every time improvements are made to the calibration or analysis software three levels of data exist. The raw experimental data ("EXDATA" tapes) are processed into a second set of datasets ("EXPDST" tapes) which are in turn compressed into Multihadron/dimuon datasets ("EXMUHA" tapes). The analysis level of these last datasets is always kept "state of the art" but unfortunately most of the two gamma events are left behind in the data compression. Very recently datasets ("EXTWOP") consisting of low multiplicity events (with Bhabha scattering ($e^+e^- \rightarrow e^+e^-$) events removed) have been introduced into this last category.

of e , μ , π , or K . This algorithm assumes there is no significant baryon production in any "clean" channel so it has to be used in conjunction with a maximum energy cut to prevent it confusing annihilation channel events with beamgas. This is apparent in Figure 3.1 which shows a false enhancement of the beamgas contribution above 5 GeV. This is, of course, impossible and really represents the false labeling of annihilation events containing baryons as beamgas. In practice, no events with more than 3.5 GeV total energy are used in the $\gamma\gamma$ analysis, so this is not really a problem.

Studies of the effect of this algorithm on events with vertices outside the normal interaction region (i.e. events that are likely to be beamgas or beamwall) suggest that it eliminates more than 90% of the beamgas contamination. On application of the algorithm to Monte Carlo events, simulating $\gamma\gamma \rightarrow \mu\mu$, a negligible portion were falsely rejected as beamgas. The lower limit is derived by assuming that there are no good events outside the normal fiducial region i.e. after application of the beamgas rejection to these "exterior" events 10% are not flagged as beam gas - if any of these unidentified events aren't beamgas the actual efficiency of the algorithm will be higher. The vertex distribution for the events rejected by the beamgas filter is flat (Figures 3.6) suggesting that there is little accidental flagging of good events as beamgas - with a 3.5 GeV maximum energy cut. There are many interesting low intensity channels accidentally included in this "beamgas" sample (e.g. $\gamma\gamma \rightarrow p\bar{p}$) but these require special analysis - it was decided to look at more easily separable channels first.

In summary, early in 1984, a definite $\gamma\gamma$ signal was seen and was attributed mostly to QED two prong events. The progress in understanding these channels will be described in chapter five where they will be discussed in the context of the $f(1270)$ meson signal, their importance in understanding ARGUS' behaviour, and their importance as a background in the $\gamma\gamma$ total cross-section measurement. The next section illustrates what can be achieved with ARGUS in the field of $\gamma\gamma$ resonance physics even without the benefit of taggers.

3.2 Observation of $\gamma\gamma \rightarrow \eta'$ at ARGUS: The first resonance^{801,802,811} to be observed in $\gamma\gamma$ collisions was the η' (958) ($I^G(J^P)C = 0^+(0^-)+$) in the decay mode $\eta' \rightarrow \rho^0\gamma \rightarrow \pi^+\pi^-\gamma$ (branching ratio 30%). The only other decay chain for this resonance with a comparable branching ratio (17%) is $\eta' \rightarrow \eta\pi^+\pi^- \rightarrow \gamma\gamma\pi^+\pi^-$ but since the major factor limiting analysis is the detector's trigger acceptance, no results in this channel have been published to date as the pions are of significantly lower kinetic energy - near the acceptance threshold for most experiments. The second channel does have the advantage that the photons are marginally more energetic. It is quite common to require that a photon deposit energy in two contiguous shower counters to be used in analysis - this prevents the accidental use of spurious signals due to noise and pedestal fluctuations in photomultipliers - it also reduces the efficiency for low energy photons. Additionally, as the η is a narrow resonance ($\Gamma_{total} \simeq .83\text{keV}$) most of the effects of detector photon resolution can be compensated for by a kinematic fit of the two decay γ s.

It was decided to search for the η' in the $\rho^0\gamma$ channel. $X^+X^-\gamma$ events were separated and analysed using a pion mass hypothesis for the charged tracks. No particle ID was used as most of the backgrounds could be removed by much simpler cuts. Previous experiments^{802,811} had used a property of $\gamma\gamma$ kinematics to compensate for poor γ energy resolution - since total P_{\perp} had to balance fairly well for a two-photon event the momentum of the observed photon was scaled to make the absolute P_{\perp} of the photon match that of the $\pi^+\pi^-$ pair:

$$p'_{\mu}(\gamma) = \frac{|P_{\perp}(\pi\pi)|}{|P_{\perp}(\gamma)|} p_{\mu}(\gamma) \quad \chi^2 = \frac{(1 - E'_{\gamma}/E_{\gamma})^2}{((.068)^2 + \frac{(.08)^2}{E})}$$

Since all cuts used in the analysis were based on purely geometric information except a total P_{\perp} cut (< 25 MeV/c) calculated after the γ momentum was scaled, the effect of this energy "tuning" technique can easily be checked. The mass spectra for events with multicounter photons are shown in Figures 3.8a and 3.8b which contain the same events before and after the γ "tuning" - it is clear that the peak is narrowed by the adjustment and there is no apparent migration of the background into the peak. In addition the χ^2 distribution (Figure 3.10) suggests that the technique is reasonable, as the changes introduced are for the most part within 1σ of the measured values. For reference, the photon spectra before and after the P_{\perp} scaling for events with the $\pi^+\pi^-\gamma$ mass in the η' region (930 MeV - 980 MeV) are given in Figures 3.11 a,b respectively.

To supplement the P_{\perp} cut it was required that the $\pi^+\pi^-$ momentum vector be $\geq \pm 143$ degrees in ϕ from the photon momentum vector. This coplanarity cut and the P_{\perp} scaling are enough to produce

a clear η' signal (the top curves in Figures 3.9 a,b,c). To reject the rest of the background (the shaded areas in Figures 3.9 a,b,c) several other cuts were introduced. The $\pi^+\pi^-$ vector was required to have a 50 MeV/c minimum P_{\perp} (Figure 3.12) to prevent scaling of the γ energy into regions where there is poor photon efficiency and resolution (i.e. no γ was considered unless it had at least 50 MeV attributed to it, before and after scaling). Upon examining the distribution of $\cos(\theta_{\pi\gamma})$ it became apparent that there was a strong contribution from events with final state bremsstrahlen (Figure 3.13a, most probably $e^+e^- \rightarrow e^+e^-e^+e^-\gamma$). Bremsstrahlen from the beam electrons (Figure 3.13b) are more abundant due to the higher "gamma", but this contribution is focused along the beampipe (this is the Lorentz boost $\gamma = E/m$, the probability of bremsstrahlung emission is generally proportional to $\log(\gamma)$). Figures 3.14, 3.15 clearly demonstrate the nature of these $X^+X^-\gamma$ events - the character of the $\cos(\theta_{\pi\gamma})$ distribution changes drastically around $\cos(\theta_{\pi\gamma}) \sim .9$ - suggesting bremsstrahlen emitted from the outgoing particles, perhaps in traversing the detector material. For this reason .8 was set as an upper acceptable limit for $\cos(\theta_{\pi\gamma})$.

There was some question as to what cuts should be made on the photon so three samples of events were made: 1) single counter photons, 2) multiple counter photons, 3) multiple counter photons with at least 100 MeV and at least one additional single counter photon (≤ 100 MeV) in the event - the second photon being considered noise and ignored in the analysis. It turned out that there was a significant signal even in the first sample of events (Figure 3.9a), and a much reduced signal in the third class suggesting that most of the low energy class 1 photons cannot be considered noise, as was initially suspected. Indeed, there seems to be some evidence in the third sample for A_2 production via $A_2 \rightarrow \rho^{\pm}\pi^{\mp} \rightarrow \pi^+\pi^-\gamma\gamma$ (Figure 3.9b), even with one γ missing (the A_2 was first observed in $\gamma\gamma$ collisions through this same partially reconstructed channel³⁰²). Evidence for A_2 production at ARGUS via the fully reconstructed $\rho^{\pm}\pi^{\mp}$ channel has been seen and will be studied in detail in the near future.

Unfortunately, a value of $\Gamma_{\gamma\gamma}(\eta')$ is not yet available from ARGUS. An event generator for the process, which will allow detailed acceptance calculations in conjunction with the SIMARG program, is nearing completion. However, it is expected that the final result will be limited by uncertainties in the trigger efficiency. At present, the trigger efficiency is poorly understood for events with invariant masses below 1 GeV. The results are rather more dependent on resolving this problem (discussed further in Chapter 5) than on acceptance calculations, which should be completed fairly quickly once the event

generator is ready. The preliminary analysis of the η' signal produces a mass of 958.2 ± 1.5 MeV compared to the Particle Data Book³⁰³ value of 957.57 MeV. Using a gaussian peak on a polynomial background the signal (Figure 3.16) was fitted and found to have 295 ± 20 events - the largest sample yet reported. The experimental luminosity analysed was 40.8 pb^{-1} - less than half the available data (though a significant portion of that remaining was taken with triggers having reduced $\gamma\gamma$ acceptance). Figure 3.17 is the most recent result of the PLUTO detector^{304,313} which has a sample of 243 ± 17 events. PLUTO's result also shows evidence for A_2 production via the partially reconstructed $\rho^\pm \pi^\mp$ channel. This background is not present in the ARGUS analysis due to ARGUS' higher efficiency for detecting low energy photons - PLUTO's minimum γ energy is 100 MeV while the ARGUS analysis accepts photons with 50 MeV energy. This leads to a higher efficiency for fully reconstructed A_2 mesons and less A_2 contamination in the η' channel. PLUTO's measurement and another recent measurement by the TASSO collaboration³¹² are compared with the ARGUS analysis in Table 3.1 - it is apparent that ARGUS is competitive in this field of physics!¹ The experimental width measured by ARGUS is completely dominated by detector resolution and was measured to be 21 MeV - after the P_\perp scaling and about three times this value before this technique was applied.

In addition to the rather clear peak centered on the accepted η' mass there exists other evidence of the interpretation of this signal as $\eta' \rightarrow \rho^0 \gamma$. The $\pi^+ \pi^-$ mass is plotted versus the $\pi^+ \pi^- \gamma$ mass in Figure 3.18 showing clear evidence for $\eta' \rightarrow \rho \gamma$. As real photons can only exist in helicity states ± 1 and the η' is a pseudoscalar the ρ in these events must be polarized. This effect shows up in the $\pi\gamma$ angle in the $\pi^+ \pi^-$ CMS - a quantity which is not affected by any of the experimental cuts. The data (Figure 3.19) is consistent with 90% Y_{11} again providing evidence for the interpretation of this signal as $\eta' \rightarrow \rho \gamma$. The mass distribution of the ρ (Figure 3.20) is as expected except for a strong kinematic suppression on the high side of the peak due to the lower photon phase space for high ρ masses.

¹The TASSO γ Detectors are of two types: LABC(Liquid Argon Lead Counters) and HASH(Hadron Arm Shower Counters) because of this several of the TASSO parameters in Table 3.1 have two entries for events where the photon hits the LABC or HASH respectively.

EXPERIMENTS			
CUTS	ARGUS	PLUTO	TASSO
Luminosity	$\sim 40.8 pb^{-1}$	$46 pb^{-1}$	$66-76 pb^{-1}$
#Events in Peak	295 ± 20	243 ± 17	~ 240
E_γ minimum	50 MeV	100 MeV, ≤ 600 MeV	100, 160 MeV
Minimum $P_\perp (\pi^+ \pi^-)$	50 MeV/c	100 MeV/c	-
$\cos(\phi_{\pi^+ \pi^-} - \phi_\gamma)$	$\leq -.8$	$\leq -.88$	-
Maximum $\parallel \sum \vec{P}_\perp \parallel$	25 MeV/c	100 MeV/c	70 MeV/c
Momentum Resolution $\frac{\sigma}{p}$	1.2%p	3%p	1.7%p
γ energy resolution $\frac{\sigma}{E}$	$((.068)^2 + \frac{(.08)^2}{E})^\dagger$	$35\%/\sqrt{E}$	$\{.11 + \frac{.02}{E-.8}\}/\sqrt{E}$
γ Acceptance	94%	96%	40%, 18%
DC Coverage (Trigger)	71%	71%	82%
Maximum $\cos(\theta_{\gamma\pi})$.8	.95	.98, .96
Minimum $\cos(\theta_{\pi^+ \pi^-})$	-	$-.97, \leq .95$	-.98
Maximum Δ ToF	5.5 nsec	-	-
σ ToF	220 psec	-	380 psec
P_\perp Threshold	125-250 MeV/c	150 MeV/c	170-290 MeV/c
E_{Beam}	~ 5 GeV	17.34 GeV	7-18 GeV
$\Gamma(\eta' \rightarrow \gamma\gamma)$	-	$3.8 \pm .26 \pm .43$ keV	$5.1 \pm .4 \pm .7$ keV
$\parallel \cos \theta_{\pi\gamma CM} \parallel$	-	-	$\leq .7$
$\parallel 180 - \phi_{\pi^+} + \phi_{\pi^-} \parallel$	-	≥ 5.7	≥ 5.7
γ Energy Tuning	Yes	Yes/	No

Table 3.1 Comparison of η' Analyses

3.3 Preliminary Observation of $\gamma\gamma \rightarrow 4\pi$ at ARGUS : Some initial studies of multiprong final states have been made. The limited efforts in this direction have been focused on the final state $\pi^+\pi^-\pi^+\pi^-$. Some studies have been done on inclusive neutral production (π^0, η) and though these appear to exist in the data no significant result is available as yet. Previous results in the 4π channel resulted in observation of $\gamma\gamma \rightarrow f' \rightarrow K_S^0 K_S^0$ ³¹⁰ and $\gamma\gamma \rightarrow \rho^0 \rho^0$ ³⁰⁵⁻³⁰⁹. So far, only K_S^0 and ρ^0 inclusive production has been observed. Figure 3.21 shows the mass spectrum of opposite sign pion pairs (four combinations per event) with the combinatoric background removed by subtracting out twice the mass spectrum of like signed pairs, i.e. it is assumed that the two particles initially produced are not correlated kinematically - a dubious assumption at best and obviously wrong in this case as the subtracted distribution becomes negative at low invariant mass. Still, evidence for inclusive K_S^0 and ρ production is clear.

Figure 3.21 was obtained without using a sophisticated vertex program - the analysis assumed all tracks were emitted from the origin of the event. After this analysis was completed a vertex finding program was implemented in the ARGUS analysis program. If the decay vertex is calculated and this information employed in the momentum calculation, the K_S^0 mass distribution in multihadron events becomes much narrower (13 MeV FWHM). Of course, having even two tracks identified as a K_S^0 completely removes the combinatorial background from a 4π event. More attention will be paid to the possibilities of this analysis in the near future.

3.4 CAPTIONS FOR FIGURES

- 3.1** Total Energy spectra for "clean" events and various background phenomena - limited data samples. This illustrates the separability of $\gamma\gamma$ channels, via energy cuts. The events from "EXPDST" tapes (Figure 3.1c) include all two prongs and Bhabhas while only μ pairs and multihadrons (\geq three prongs) are included in the "EXMUHA" events.
- 3.2** ToF Difference for two prong events with beamgas removed - this demonstrates the separability of two prong $\gamma\gamma$ events from cosmics via a ToF time difference cut.
- 3.3** Acollinearity Distributions for Cosmics and "clean" charge balance two prongs.
- 3.4a** dE/dX Separation for various particle combinations. The y-variable of each figure is the mean separation between the energy losses of the two particle types in units of the expected error.
- 3.4b** $(p, dE/dX)$ Distribution for charged tracks from Beamgas Events
- 3.5** P_{\perp} distribution for two prong charge balance beamgas events and charge balance two prong events with the cosmics and beamgas events removed.
- 3.6** Z Projection of Vertex Distribution for "clean" charge balance two prong events. Since the beam gas distribution is flat (Figure 3.7) it is assumed that very few events from $\gamma\gamma$ collisions are rejected by the beamgas algorithm. The rather curious delta function peak in the center of these vertex distributions arises from an attempt at streamlining the vertex finding algorithm (this peak is just offscale in the vertex distribution for beamgas events, Figure 3.7). If the first vertex hypothesis i.e. (0,0,0) has a sufficiently small χ^2 value no further iterations are attempted. Due to this, events close to the origin are forced to (0,0,0) to varying degrees depending on the exact event geometry (e.g. degree of collinearity for two prong events).
- 3.7** Vertex distribution for events identified with beamgas algorithm.
- 3.8** Mass Distributions of $\pi^+\pi^-\gamma$ events, with all η' selection cuts, before and after P_{\perp} scaling of the γ energy. The photon shower must set at least two shower counters.
- 3.9** Mass Distributions of $\pi^+\pi^-\gamma$ events (with only the $\pi\pi/\gamma$ coplanarity cut) for three γ analysis classes similar to those discussed in the text. The shaded areas are the events rejected when all of the η' selection cuts are applied. Distribution (a) is the $\pi\pi\gamma$ mass spectrum for photons with less than 100 MeV energy or with only one shower counter associated with the photon. Distribution (b) is the $\pi\pi\gamma$ mass spectrum when two photons are observed (one of type (a) and one of type (c)), - the type (a) photons are ignored in the analysis. Some evidence for η' productions is seen suggesting only a few photons of type (a) are

false signals from background noise. Distribution (c) shows the $\pi\pi\gamma$ mass spectrum for photons of at least 100 MeV energy with ≥ 2 shower counters hit.

3.10 χ^2 distribution for the P_{\perp} rescaling of the γ energy for events passing all η' selection criteria including an η' mass cut: $930 \leq m_{\pi\pi\gamma} \leq 980$ MeV. Most of the events have had the γ energy changed by less than one standard deviation demonstrating the technique's consistency.

3.11 Energy spectra for γ s coming from η' s, before and after the rescaling of the γ energy.

3.12 P_{\perp} distribution for the $\rho^0 \rightarrow \pi^+\pi^-$ coming from the η' .

3.13 Feynmann Diagrams for the bremsstrahlung corrections to $\gamma\gamma$ events.

3.14 Minimum $\cos(\theta_{\pi\gamma})$ distribution for all events with the coplanarity cut.

($\cos\theta_{\pi\pi/\gamma} \leq -.8$). Note the drastic change in the character of this distribution for small angles caused by the bremsstrahlen background.

3.15 Minimum $\cos(\theta_{\pi\gamma})$ distribution for all events with the coplanarity cut

($\cos\theta_{\pi\pi/\gamma} \leq -.8$) plotted against the mass of the $\pi\pi\gamma$ system. Clear evidence for η' production exists outside the region contaminated by QED bremsstrahlen.

3.16 η' signal, all cuts.

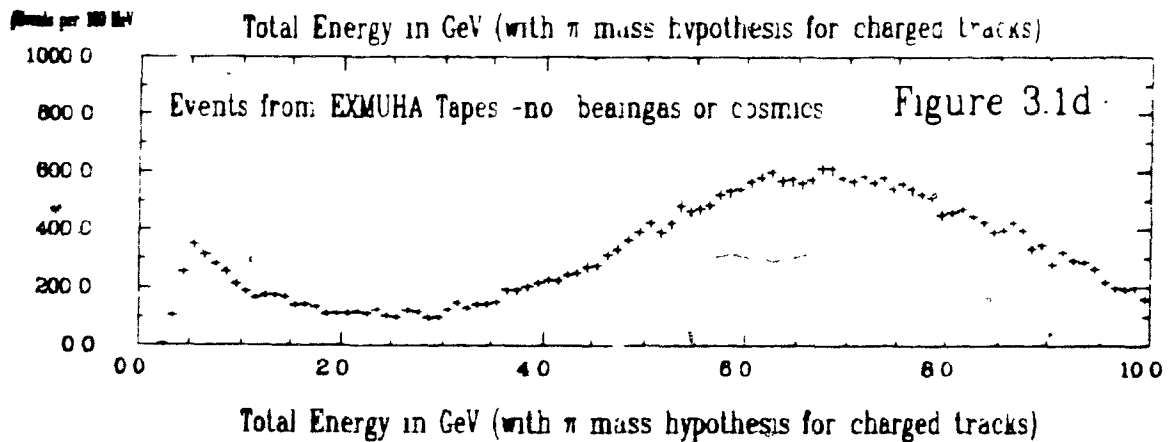
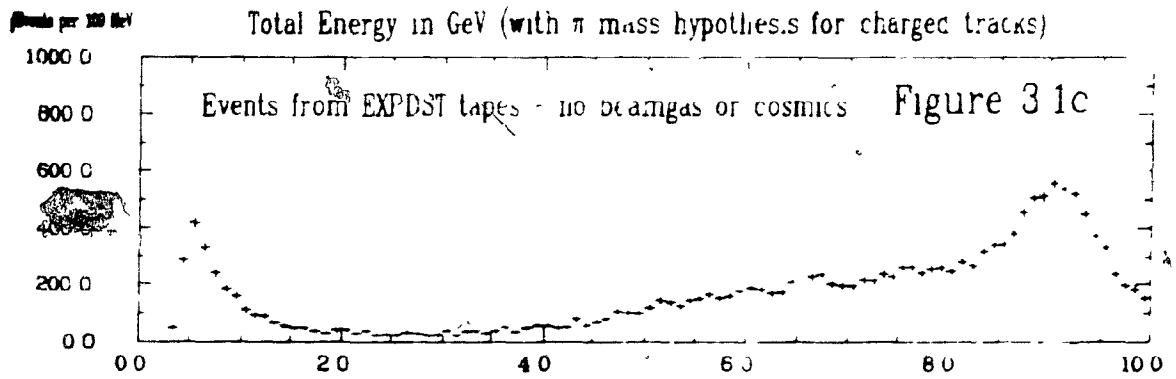
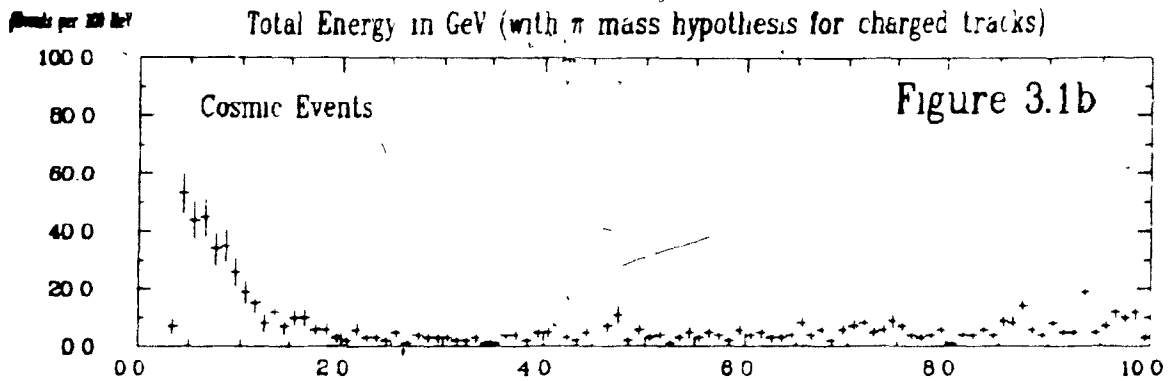
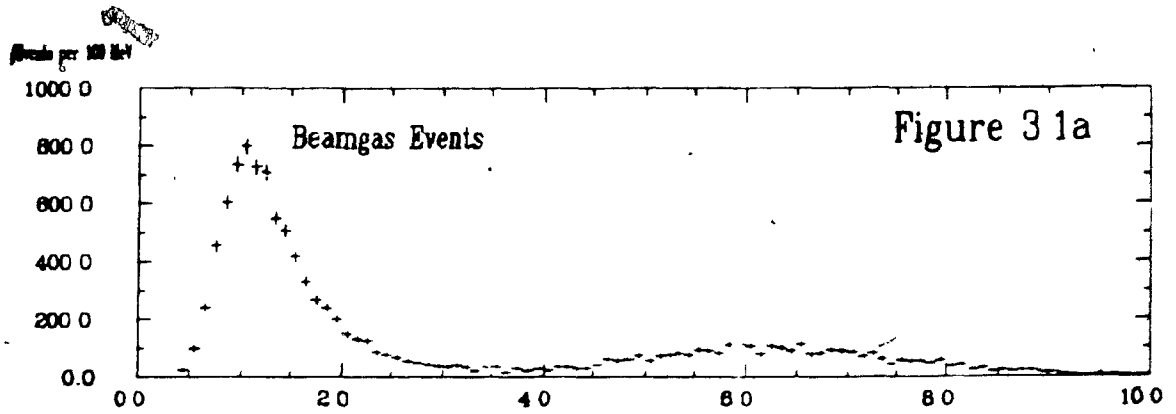
3.17 η' signal - PLUTO detector 1984 Analysis²⁰⁴.

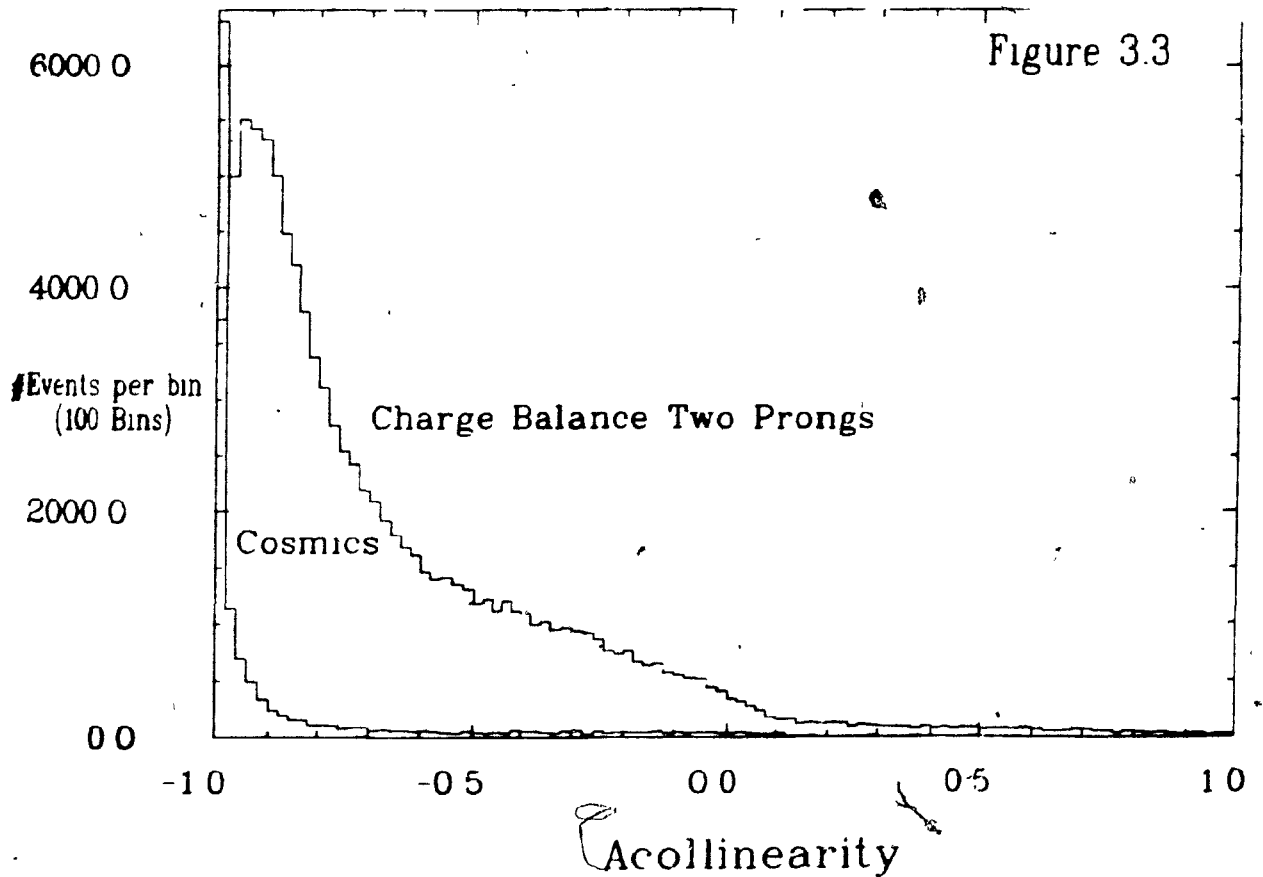
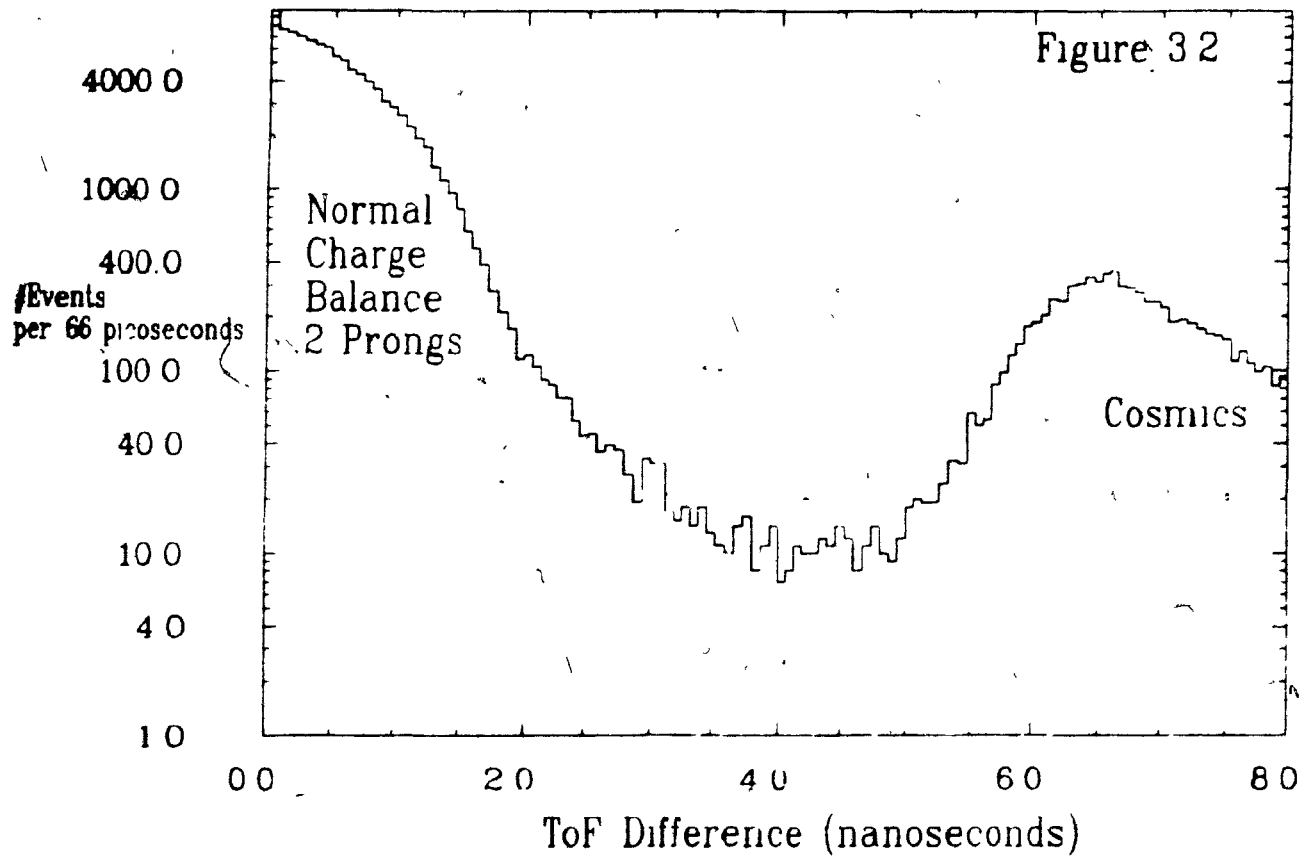
3.18 $m_{\pi\pi\gamma}$ vs. $m_{\pi\pi}$, all cuts.

3.19 $\cos(\theta_{\pi\gamma})$ in the $\pi\pi$ CMS for η' s. This distribution shows Y_{11} polarization supporting the interpretation of the decay as $\eta' \rightarrow \rho\gamma$.

3.20 $m_{\pi\pi}$ distribution for η' s. Note that high ρ masses are suppressed by the γ phase space and M1-dipole matrix element²¹³.

3.21 $m_{\pi^+\pi^-}$ distribution for 4π events (four entries per event) with the combinatoric background removed by subtracting twice the distribution for like sign combinations.





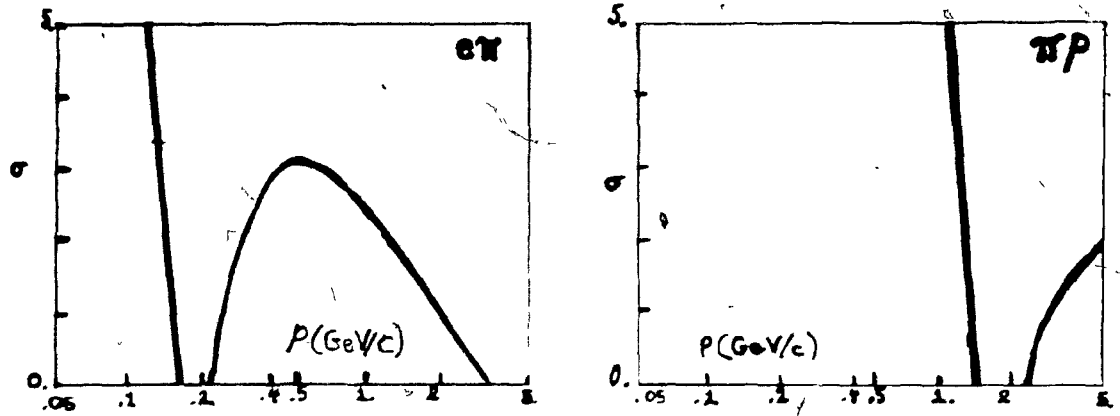


Figure 3.4a

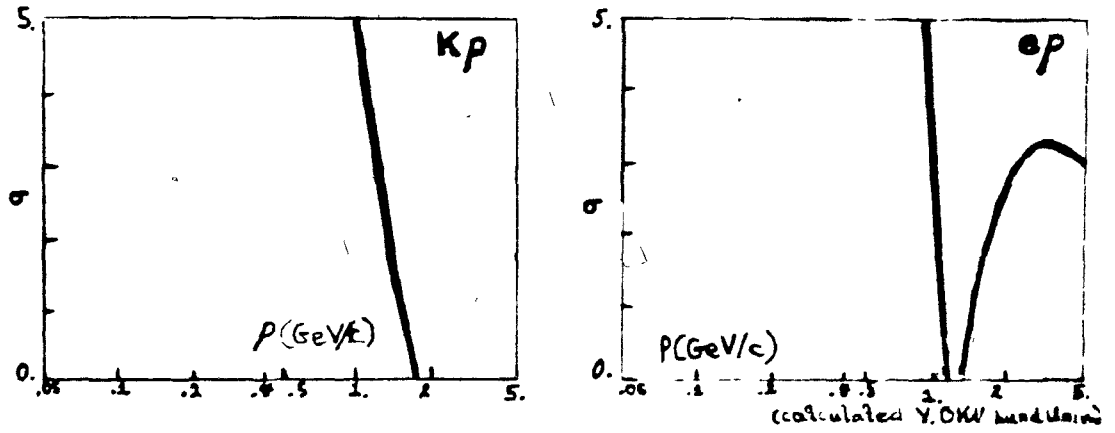
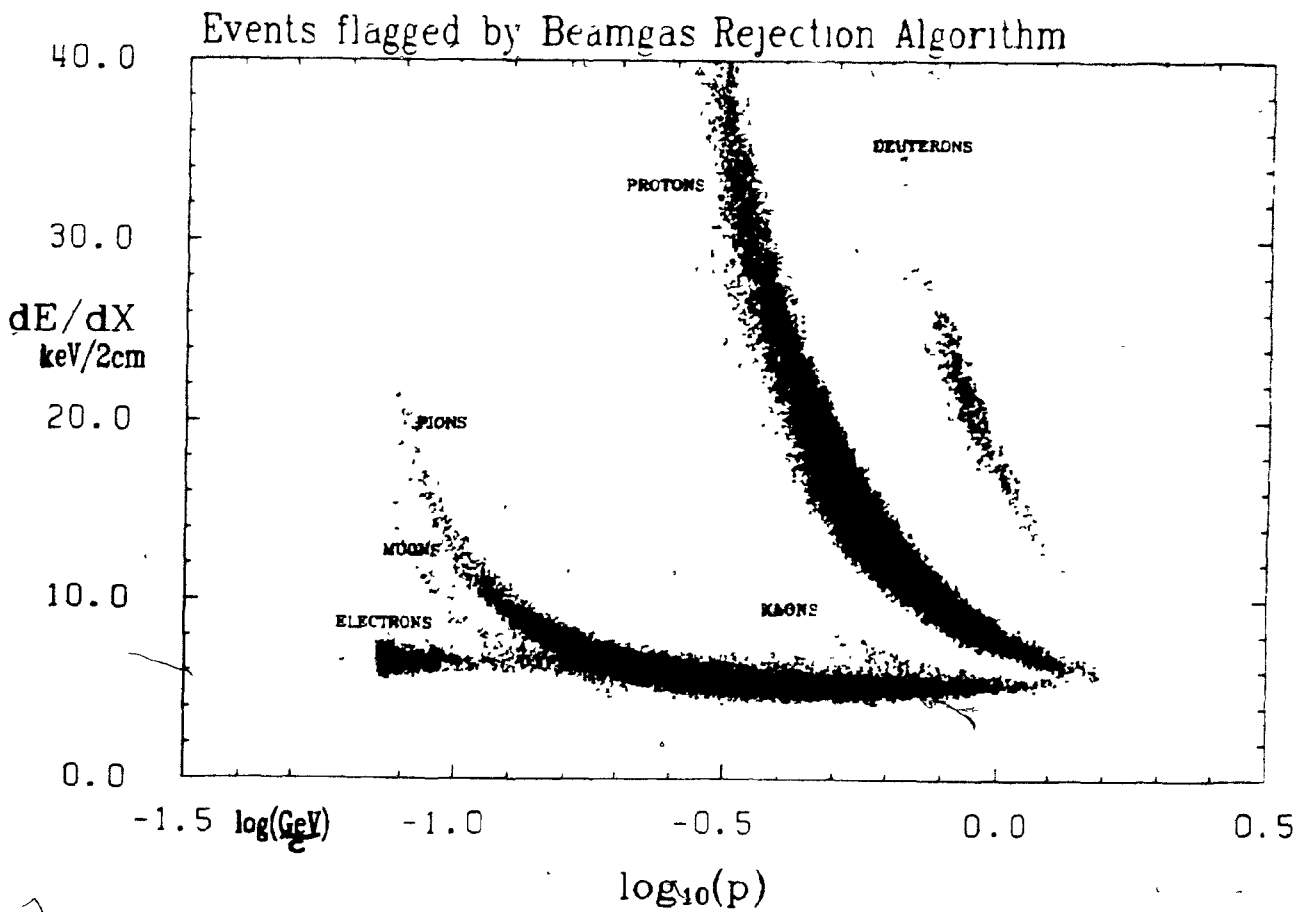


Figure 3.4b



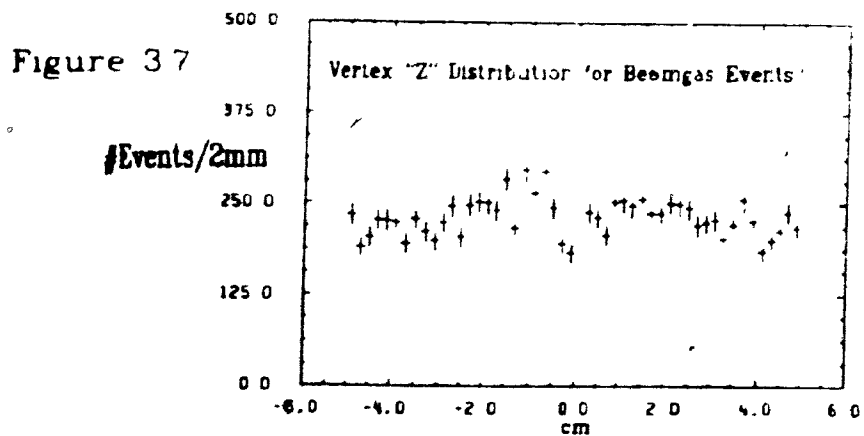
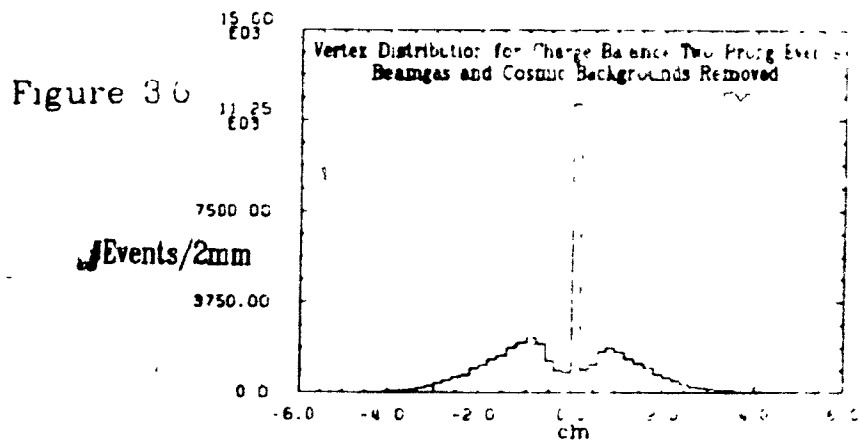
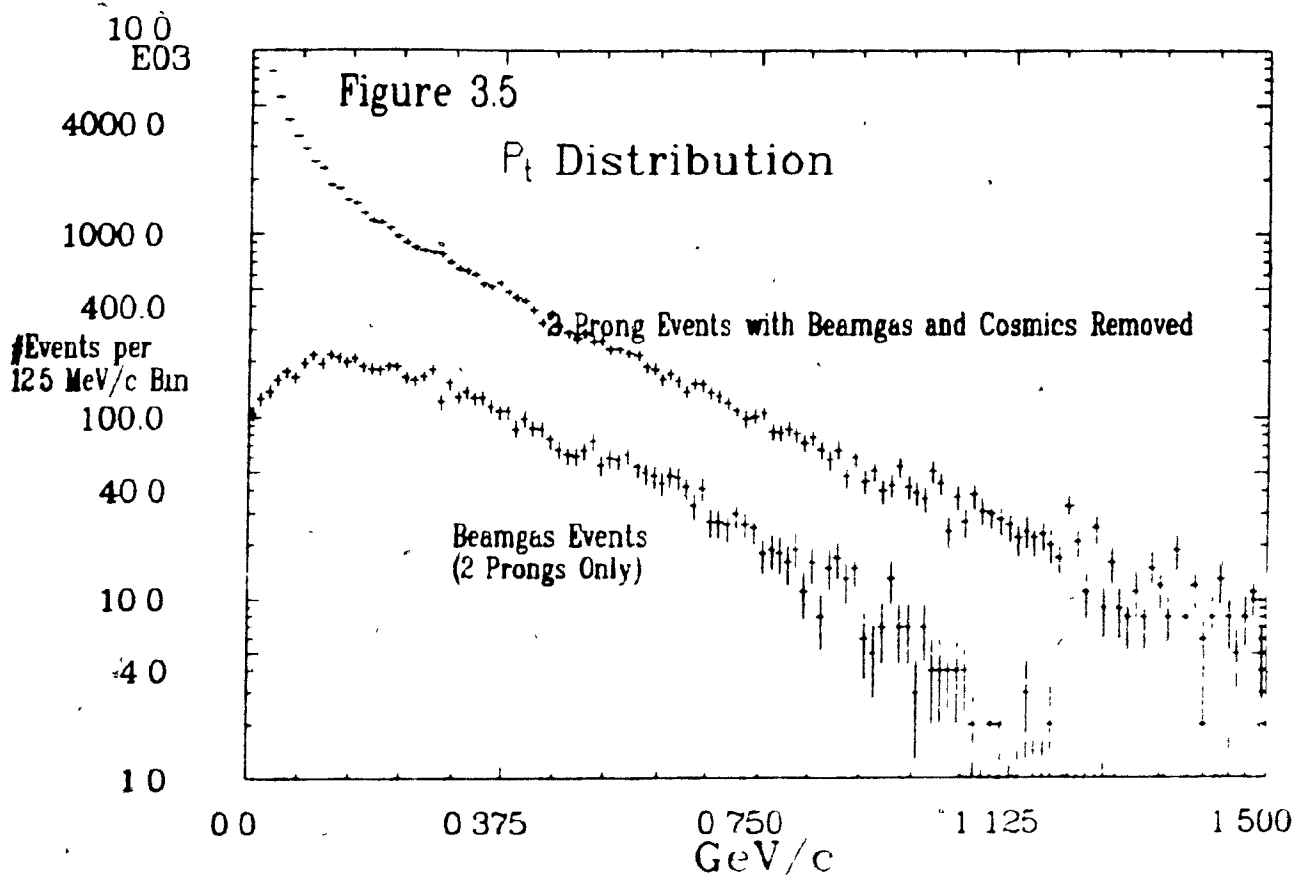


Figure 3.8b

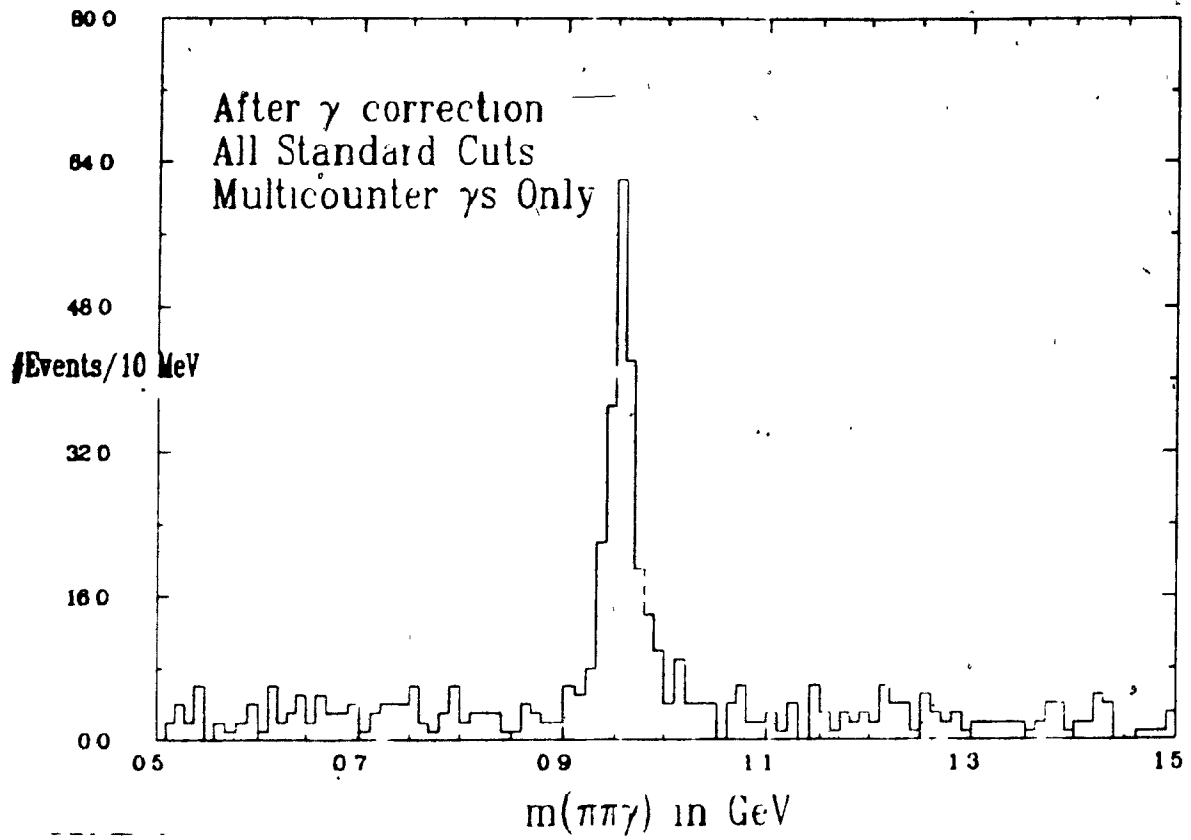


Figure 3.8a

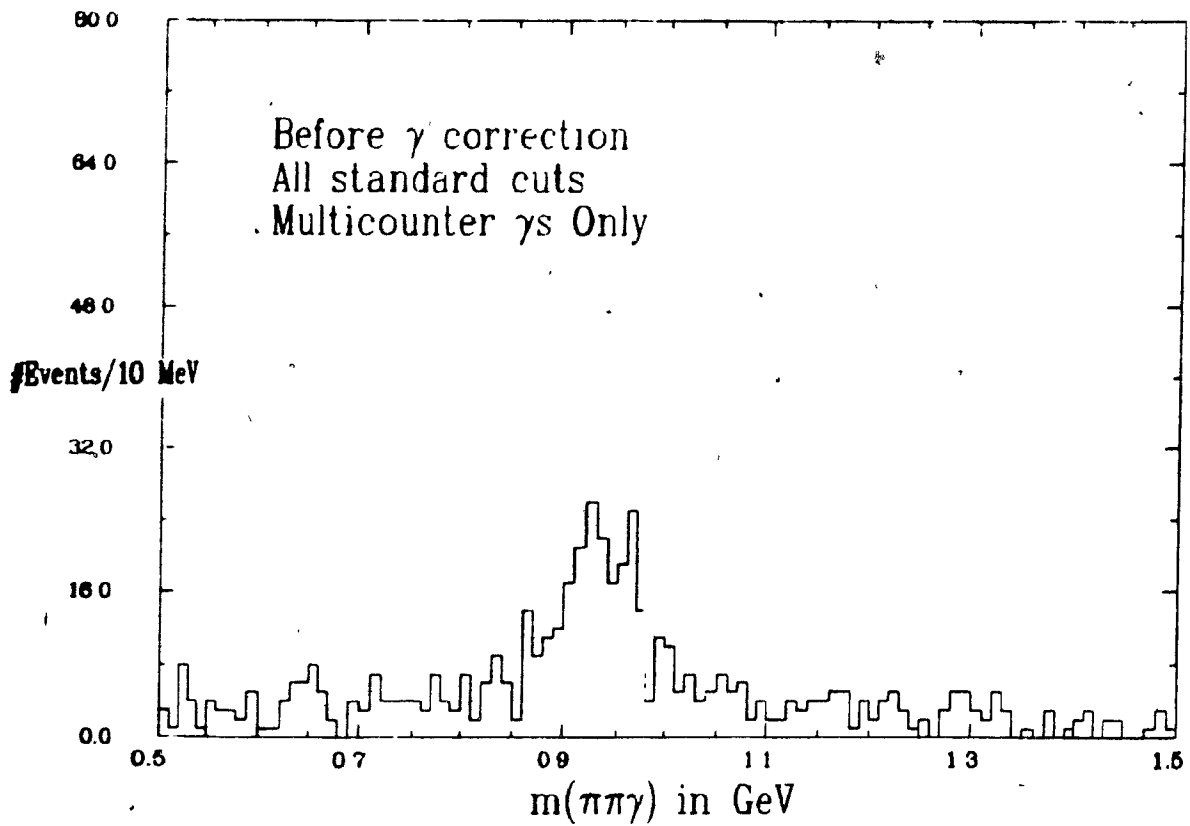


Figure 39a

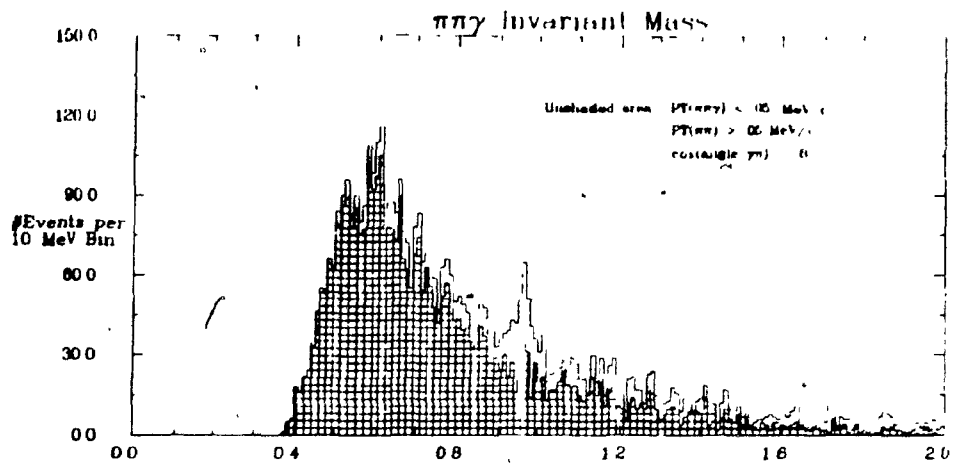


Figure 39b

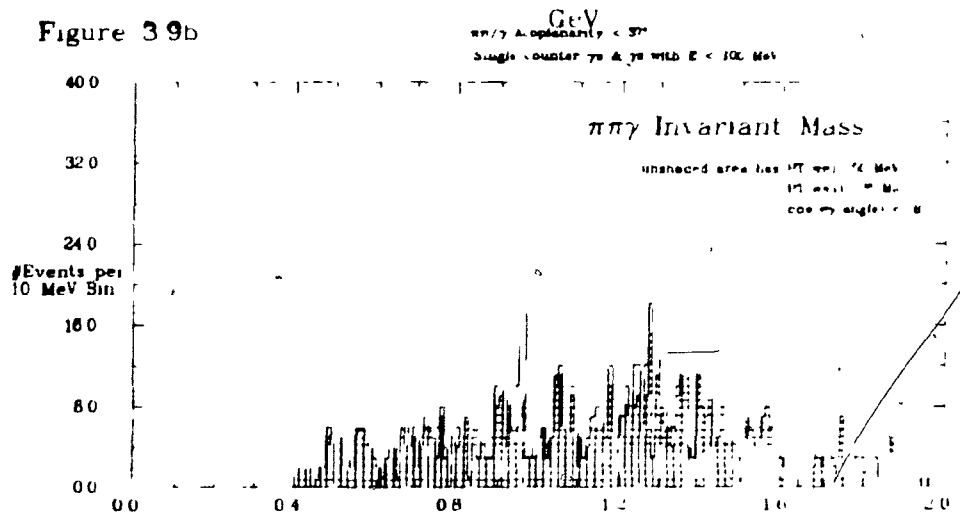


Figure 39c

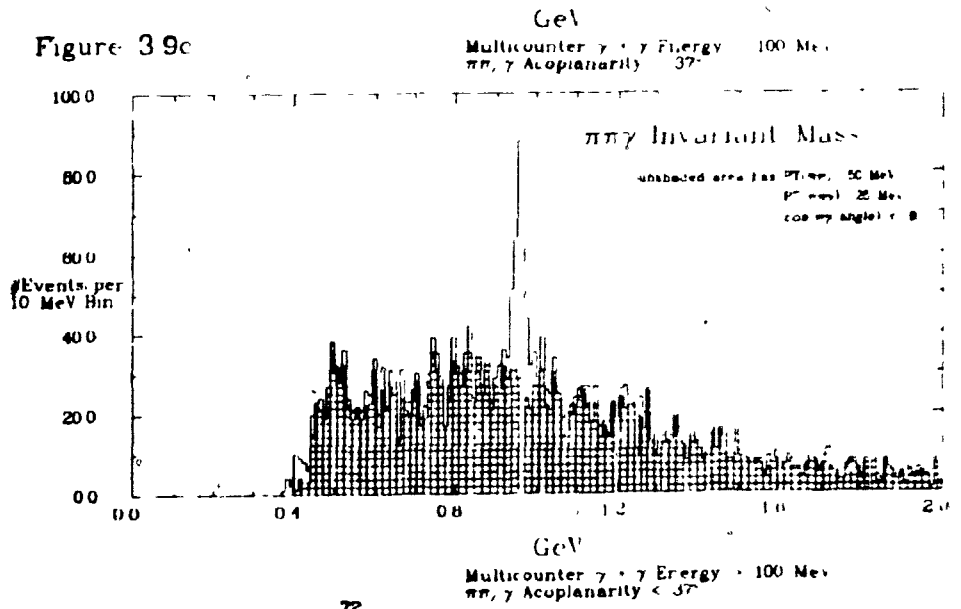


Figure 3.11a

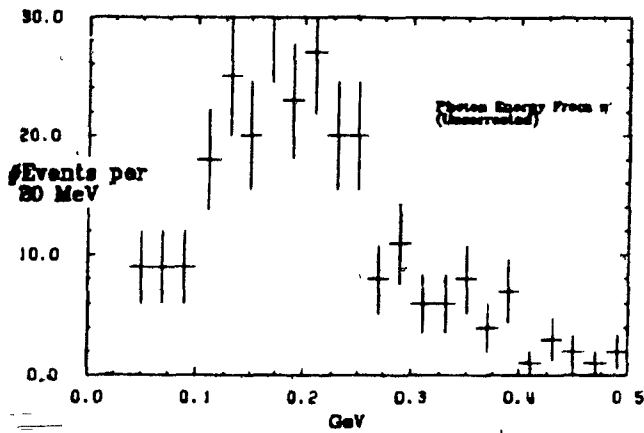


Figure 3.11b

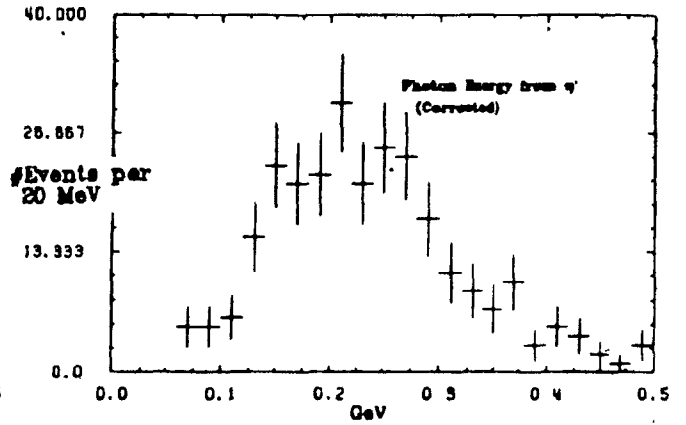


Figure 3.10

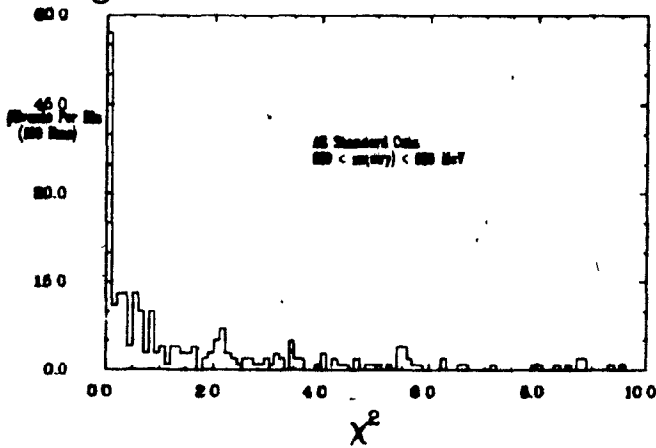


Figure 3.12

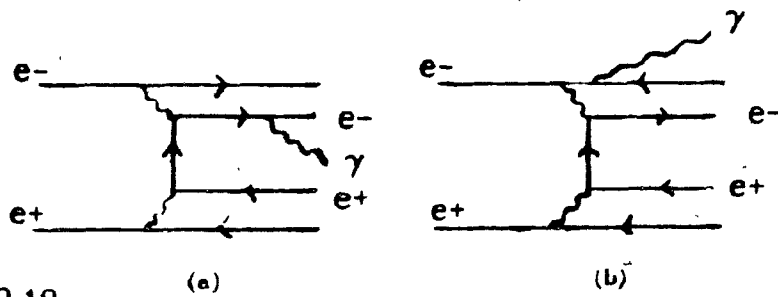
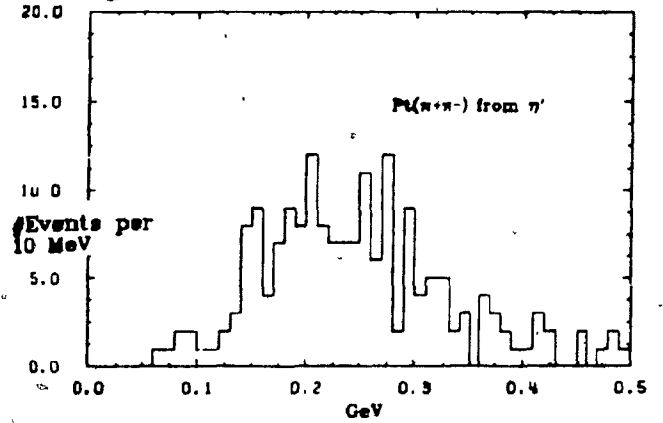


Figure 3.13

Figure 3.14

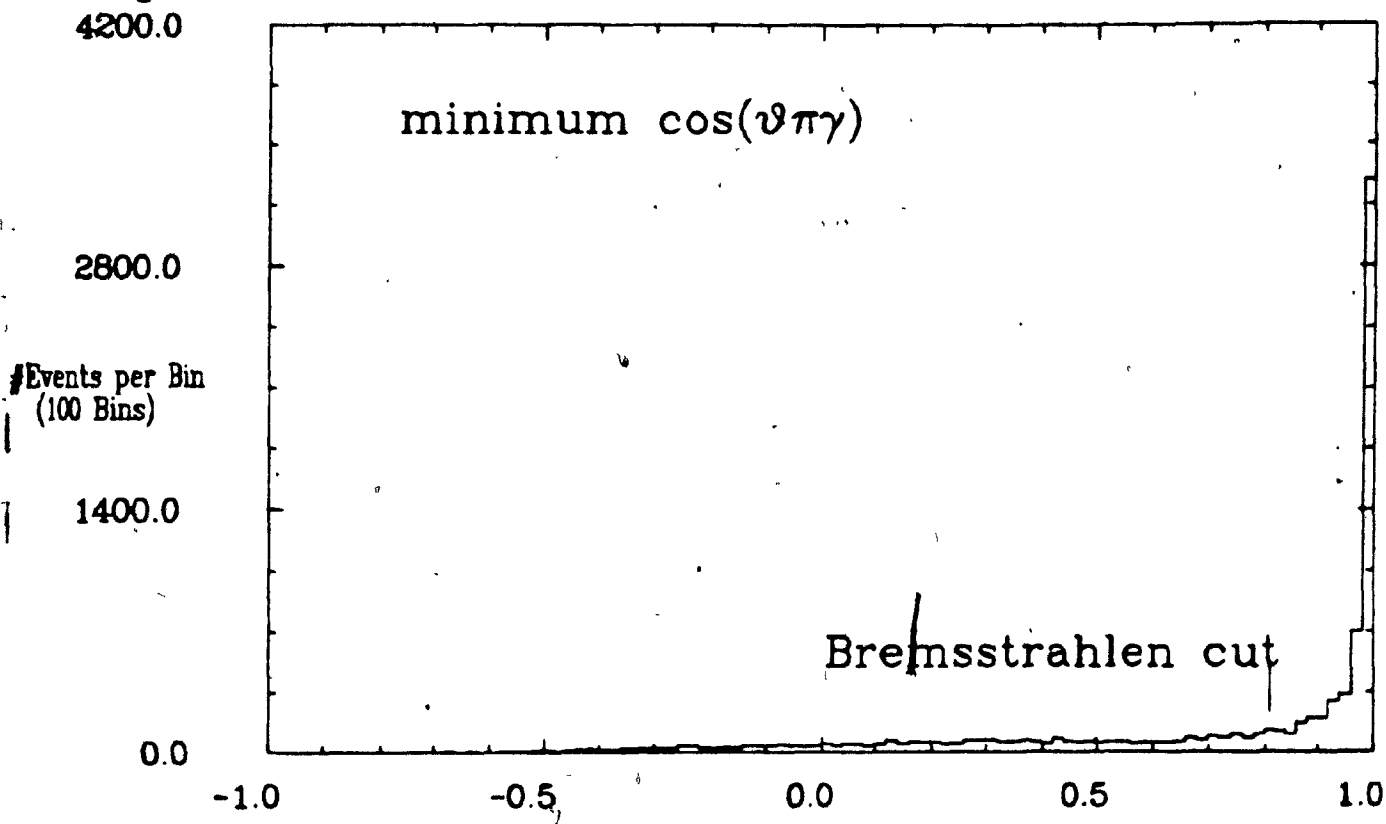
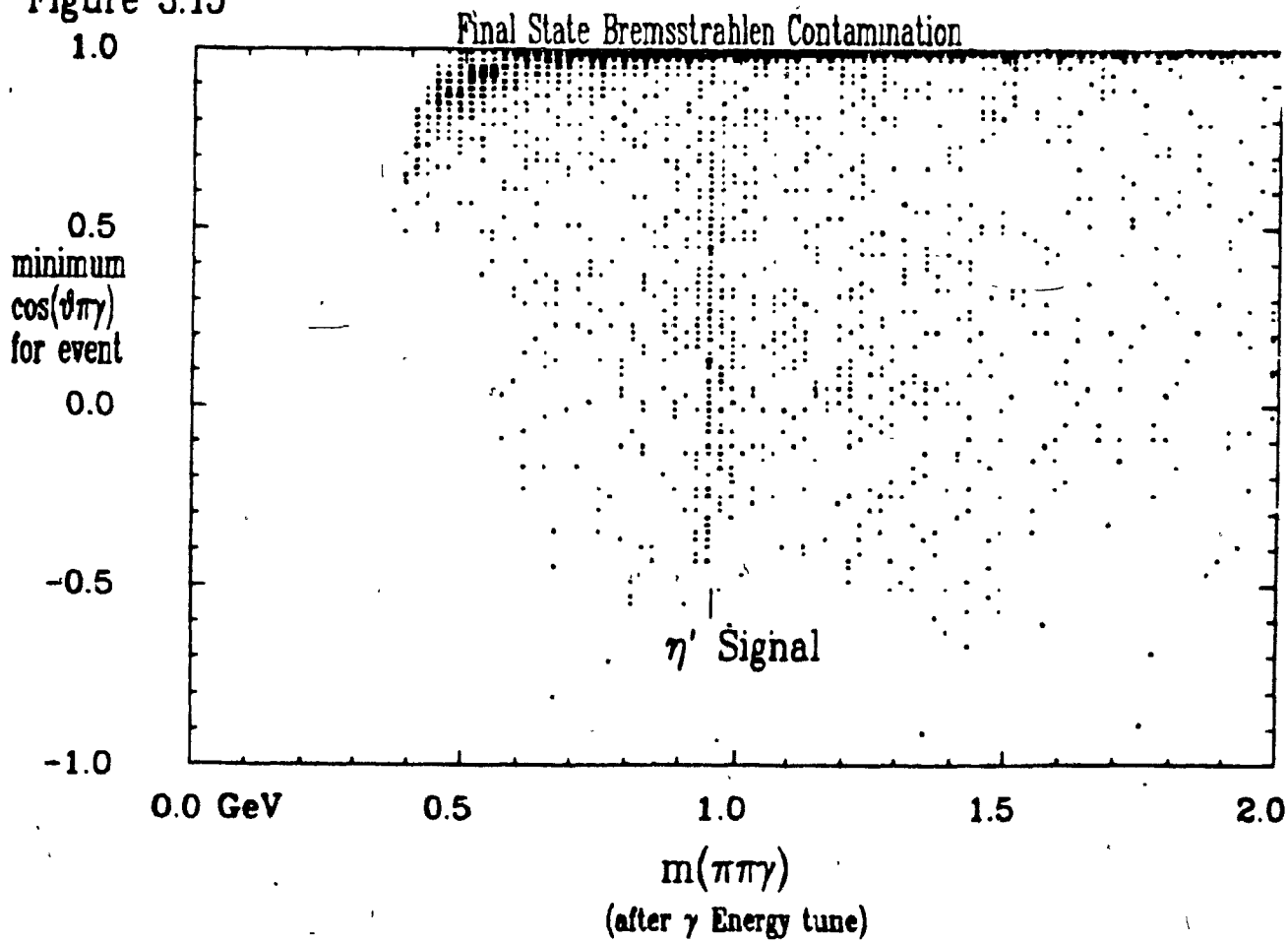
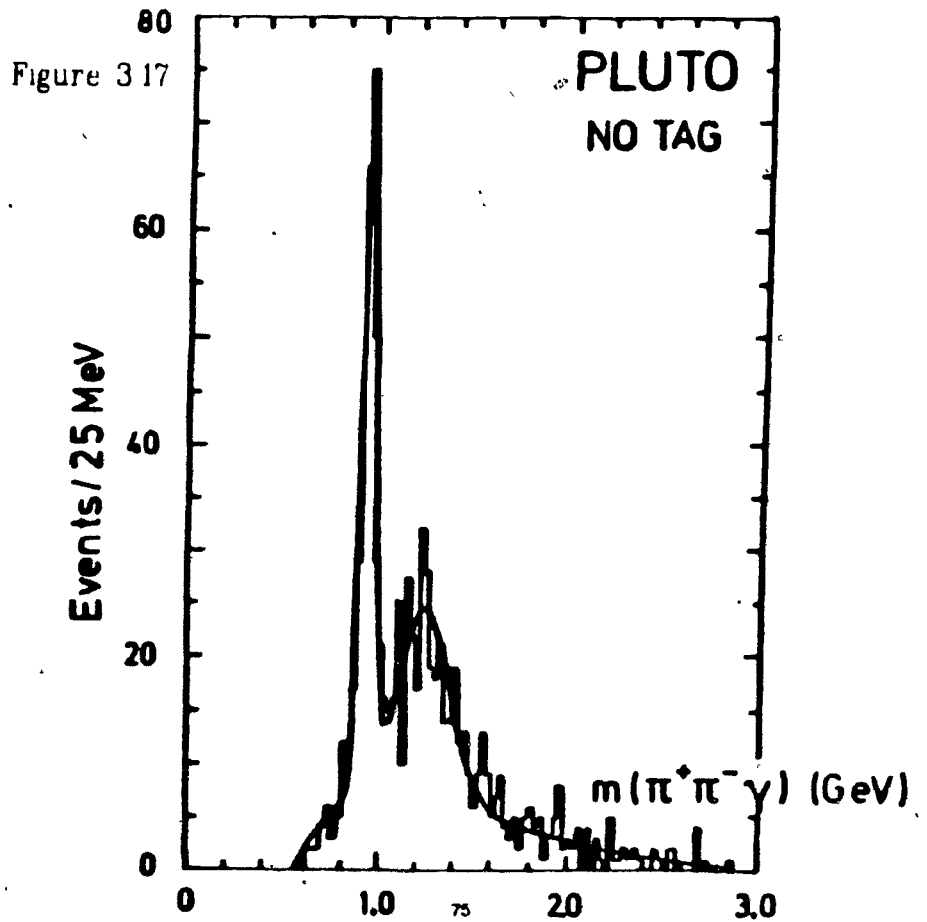
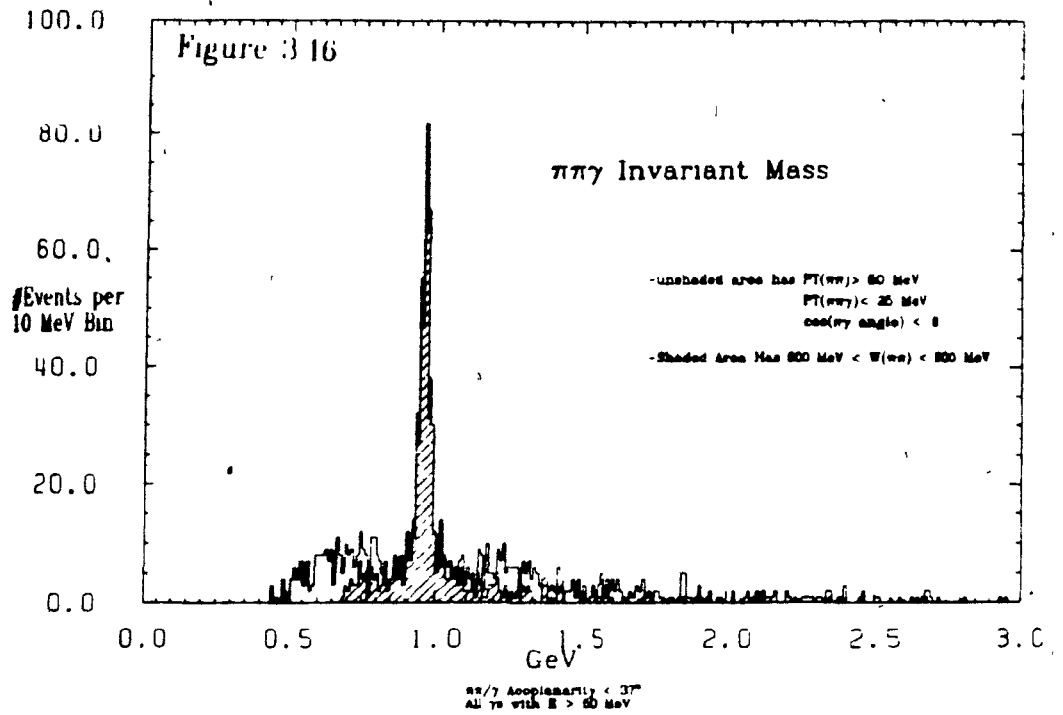
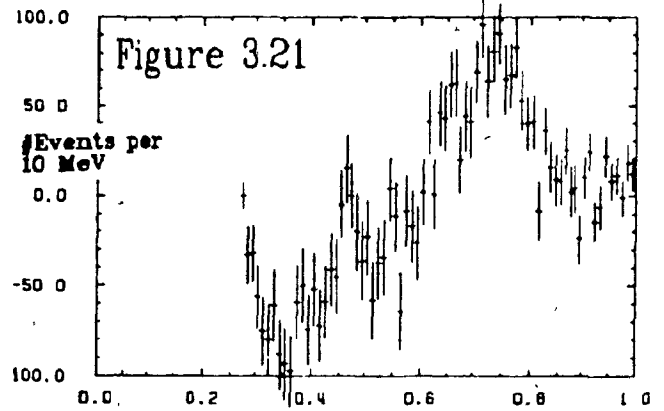
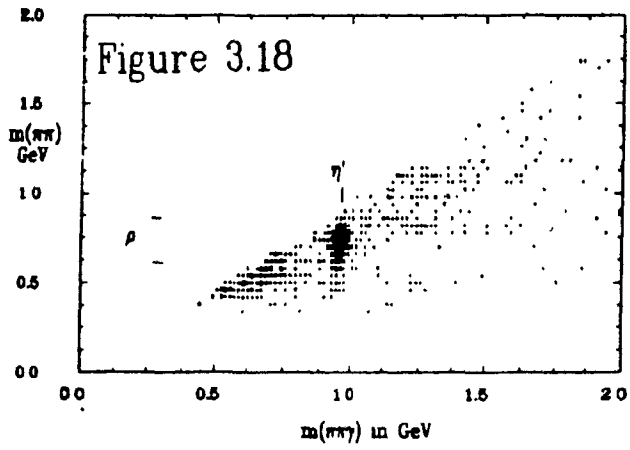


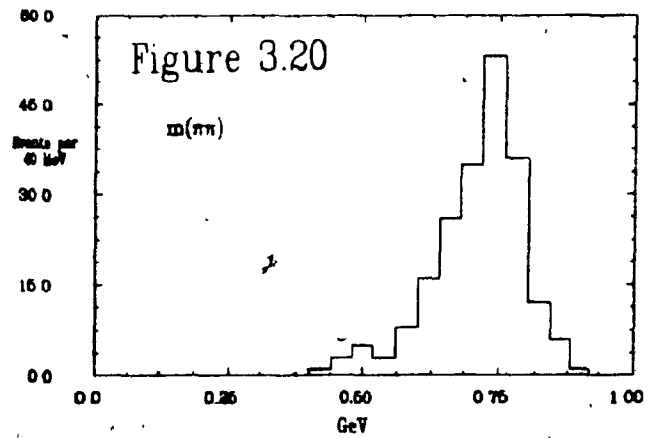
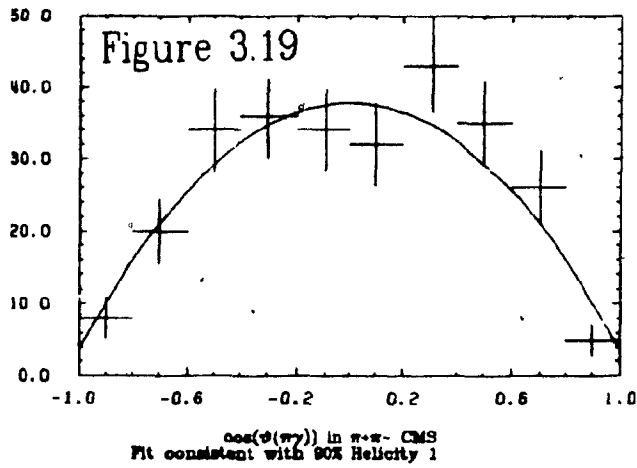
Figure 3.15







○ Invariant mass of $\pi^+\pi^-$ combinations



4.1 The DORIS-II Storage Ring : The original DORIS storage ring (the acronym stands for Double Ring Storage) had two separate beam lines for the electron and positron bunches (Figure 4.1). These intersected with a 25mrad angle at the interaction regions. The ring was constructed in this manner⁴⁰¹ to avoid beam-beam space charge effects, which limit machine luminosities in multibunch operation at low beam energy. When the $T(1S)$ was discovered^{203,209}, DORIS-I operation in the 10 GeV CMS energy region was attempted. As the optimum operating point for DORIS-I was at 7 GeV CMS energy, the increase in beam energy necessary to reach the $T(1S)$ required the use of only the upper circuit so that all magnet and cooling power could be concentrated on it. With some difficulties, a machine luminosity of $10^{30}\text{cm}^{-2}\text{sec}^{-1}$ was achieved but the running conditions were far from optimal.

During 1979-1981 the DORIS-II storage ring was designed⁴⁰¹. The design luminosity was to be an order of magnitude greater than that of DORIS-I. Construction of the improved DORIS ring was completed in 1982. The new machine had a single ring for both e^+ and e^- but retained the vertical bends near each interaction region. The details of the DORIS-II architecture near the ARGUS experiment are shown in Figure 4.2.

4.2 The Proposed ARGUS BGO Taggers : The vertical bends in the DORIS-II beam optics raise the beams by 17 cm about 18 meters on either side of the interaction points. This property may be used to separate particles emitted from the interaction at very small angles ($0-50\text{mrad}$) if their energies differ sufficiently from that of the beams (a particle with $\theta = 0^\circ$ and $E = .94E_{beam}$ will be deflected 1 cm more than the beam at $Z = 17.7\text{m}$). This is a negligible solid angle for most phenomena but in $\gamma\gamma$ collisions this region has the highest concentration of scattered e^+/e^- (the average e^+/e^- scattering angle, for 5 GeV incident beams, is $\sim 57\text{mrad}$). This eccentricity of the DORIS-II architecture can be used to make a high acceptance double tag study of $\gamma\gamma$ processes⁶⁰⁶. The next two chapters concentrate on acceptance studies recommended by the DESY Physics Review Committee on their receipt of the first version of the ARGUS $\gamma\gamma$ proposal⁶⁰⁶. In Figures 4.3,4.4 the acceptance of the beam optics is shown as a function of energy and scattering angles.

For 0° tagging of $\gamma\gamma$ interactions the most important parameters are the energies of the tagged particles. The scattering angle of the particle is largely irrelevant for physics applications so long as it is small - with the ARGUS taggers the average Q^2 of the photon emitted by the tagged e^+/e^- will be $\sim .0002\text{GeV}^2$ with a maximum Q^2 value of $\sim .015\text{GeV}^2$. This corresponds to an average tag angle of approximately 2mrad .¹ The variation of the cross-sections for $\gamma\gamma \rightarrow \text{hadrons}$ on this scale is expected to be negligible. However, the restriction of the Q^2 to be small is important as there is practically no extrapolation required to extend the measurements to the case of real photon collisions. It is also a much better antitag (i.e. $Q^2 \simeq 0$) requirement than that available using the central detector only (the average Q^2 for central detector "antitags" is $\sim .08\text{GeV}^2$).

Unfortunately, the beam optics cannot be used as a magnetic spectrometer. There exist several focusing elements in the beam optics - the mini- β quadrupoles - designed to produce high experimental luminosity. The net effect of these combined with the range of θ allowed for the scattered e^+/e^- is to transport particles with different energies and angles at the interaction to the same point on the tagger plane. These "tagger planes" (this refers to a geometric object not a piece of hardware) are symmetrically located 17.7 meters away from the interaction point - as far away from the bending magnets as possible to insure the maximum lever arm for separation of the e^+/e^- trajectories from the beams. This distance is

¹ These figures are for $E_{beam} = 5\text{GeV}$ and $W_{\gamma\gamma} > 1\text{GeV}$, effects of final state acceptance in the central detector are ignored and a $W_{\gamma\gamma}$ and Q^2 independent final state cross-section is used - in other words, only the initial state luminosity from QED is considered in the calculations. The $\gamma\gamma$ acceptance of the taggers is shown in Figures 6.11-14. with the same restrictions.

limited by permanent features of the DORIS-II architecture - vacuum pump connections and the location of the second vertical bending magnet.

As the energy of the scattered e^+/e^- cannot be determined unambiguously from the location of the tagger hits it is necessary to measure this energy with a calorimeter. The tagger situation imposes various constraints on the material used. Most of the particles hit the tagger plane in a $14 \times 14 \text{ cm}^2$ area due to the limited angular acceptance of the beampipes and magnet apertures. In order to separate tags from background tagger hits, a high spatial segmentation is necessary because of the small area involved. To achieve reasonable $\Delta_{\gamma\gamma}$ resolution (as discussed in Chapter 6) the tagger energy resolution must be $\sim 2\%$. The position of a tagger hit must be known with high accuracy (so that the effect of shower leakage is well-defined) and the material used should have a short radiation length (so that the showers are well contained). The only material that has these properties is Bismuth Germanium Oxide ($\text{Bi}_4\text{Ge}_3\text{O}_{12}$), usually referred to as BGO. This has the required short radiation length (1.13 cm) and results discussed in the next section indicate that its resolution will be sufficient. Low susceptibility to radiation damage is also desirable. The estimated radiation dose averaged over the whole tagger array is ~ 10 rads/hr for a calorimeter made of BGO (1 rad = 6.24×10^{10} MeV/kg deposited energy - it is assumed that most of the energy is deposited in the first 10 radiation lengths of a crystal) but in the lowest center crystal which has the highest rate from $e^+e^- \rightarrow e^+e^-\gamma$ background tags the dose is on the order of ~ 250 rads/hr. The present design calls for a $14 \times 14 \times 20 \text{ cm}^3$ array of BGO crystals for the calorimeter. The size of the individual crystals will be $20 \times 20 \times 200 \text{ mm}^3$. The final design arrangement, whether the crystals are read out by phototubes or photodiodes, whether or not lightguides are used etc. will be determined by test-beam trials expected to be completed in the summer of 1985.

The position of a tag in the BGO matrix will initially be determined by three layers of scintillator hodoscopes shown in Figure 4.5. Since the energy resolution is critical and many of the tags hit the lowest layer of the BGO (see Figure 6.16a) the lowest horizontal element of the hodoscope will be replaced by two layers of 2mm diameter scintillating fibres. These are similar in principle to fiber optics except the light source is provided by scintillations. These will allow the location of the impact point (and, therefore, the shower leakage) to be determined to an accuracy limited only by shower fluctuations. The resolution limitations imposed by shower fluctuations are currently being studied using the EGS (Electron-Gamma Shower) Monte Carlo developed at SLAC. The resolution will also be measured in test beam experiments.

A new conical vacuum chamber must be designed for the area between the first vertical bending magnet and the tagger. At present electrons must traverse a great deal of material at a small angle before the tagger area is reached as the vacuum pipe runs parallel to the beam. This produces a great deal of background from synchrotron light and bremsstrahlen together with an unacceptable loss in resolution due to energy loss and scattering. The new vacuum chamber will be designed so that the electrons that hit the tagger must only pass through a thin (1 - 2mm) copper window at a nearly vertical incident angle. The design of this vacuum chamber has been undertaken by the DESY machine group. RF power dissipation and cooling must be considered to prevent overheating of the chamber which may produce vacuum leaks. Additionally, various effects from an incorrectly designed chamber may lead to difficulties in maintaining beams in DORIS-II.

In order to determine the acceptance for $\gamma\gamma$ double tag events, the tagger location with respect to the beams must be known accurately. This requires electrostatic measurement of the beam position to be done close to the taggers. It is hoped that the taggers will be able to operate approximately 1cm away from the beam to increase acceptance (this separation corresponds to a maximum tag energy of $.94E_{beam}$). The connections between the vacuum chamber and the beampipes in the two bending magnets are made via steel bellows. These allow the taggers to be moved away from the beam during filling to prevent interference with the filling procedure and to reduce the radiation dose to the BGO. The actual distance from the beams at which the taggers will operate will be determined by the storage ring operation conditions and the extent to which the change in the vacuum chamber position perturbs the beams. Synchrotron light will be generated by the second bending magnet (i.e. for the electron taggers the positrons will emit synchrotron light that hits the taggers from behind as the e^+ approach the interaction point and vice versa). This radiation will be absorbed by lead shielding behind the taggers.

In addition to the BGO taggers the final experimental arrangement may include luminosity monitors. These will be situated under the planned vacuum chamber and taggers in front of a second copper window in the vacuum chamber (Figure 4.6) and will detect photons emitted at small angles ($< 2 - 4mrad$) from the reaction $e^+e^- \rightarrow e^+e^-\gamma$. Since this reaction has an immense cross-section (with a minimum photon energy of 200 MeV the cross-section is .17 barns - corresponding to a rate of nearly 1MHz) the variation in instantaneous luminosity can be found quite easily. This implies that the material used for the luminosity monitor calorimeter must be easily regenerable as the radiation dose is much higher than that

in the taggers (there is no physical low energy cutoff in the γ spectrum like that introduced by the tagger geometry). This instantaneous luminosity measurement will aid in optimizing the DORIS beams and will complement the experimental luminosity calculation which is based on Bhabha scattering ($e^+e^- \rightarrow e^+e^-$). The absolute luminosity may be difficult to ascertain due to contributions from beamgas bremsstrahlung and the problem of defining a low energy cutoff for the photons. At low photon energies, several photons from different $e^+e^- \rightarrow e^+e^- \gamma$ events may hit the monitor in the same beam crossing leading to a faked high energy hit. The continued stress on the γ -detector due to the high radiation flux will undoubtedly cause long term stability and calibration problems. It should be remembered that both the tagger and the luminosity monitor are easily accessible and may be moved to a test beam and recalibrated quite quickly. This detector may also be used as an antitagger to help reduce a high level tagger background from the leptons from the reaction $e^+e^- \rightarrow e^+e^- \gamma$.

Parameter	BGO	CsI(Tl)	NaI(Tl)
Density g/cm^3	7.13	4.5	3.7
Radiation Length X_0 (cm)	1.13	1.83	2.6
Hadronic Absorption Length λ_0 (cm)	23	36.4	41.3
X_0/λ_0	.049	.051	.063
Critical Energy (MeV)	8.8	10.2	12.5
Moliere radius (cm)	2.7	3.8	4.3
dE/dX for Minimum Ionizing Particle MeV/cm	9.2	5.6	4.85
Scintillation wavelength (nm)	480	570	410
Decay Time (nsec)	300 6	~1000	230
Temperature gradient of light yield(%/°K)	-1	+6	-.4
Afterglow (% after 3msec)	.05	<5	<5
Melting Point	1050°C	.	.
Effective Atomic Number	74	-	50
Refractive Index	2.15	.	1.85
Resolution Cs137	10%	.	7%
Light Output (relative to NaI)	8-13%	.	100%
Price \$/cm ³	10-13	2.5-3.5	1-2
Price \$/X ₀ ³	14.5-19	15.3-21.5	17.5-35

Table 4.1 Properties of Calorimeter Materials^{402,403}

4.3 e^+/e^- Calorimetry and The Properties of BGO : Calorimeters measure the energy lost by particles in interaction with matter. For electrons this energy loss is mainly due to two types of interaction, ionization of the material of the calorimeter and bremsstrahlung⁴⁰⁴ emission. The process

of bremsstrahlung emission dominates e^+ energy loss at high energies while high energy photons lose energy by e^+e^- pair creation. A high energy e^+e^- or γ passing through a sufficiently dense material will then produce a shower of photons and e^+e^- pairs which will cascade until the remaining particles have an energy below the critical energy for the medium - when the bremsstrahlung energy loss drops below the ionization energy loss. The characteristic length of the shower is the radiation length X_0 , the mean distance travelled between interactions. Monte Carlo simulations of electromagnetic showers suggest that the maximum number of particles in a shower is proportional to incident particle energy. The distance (in the incident particle direction) after which the shower reaches its maximum population and the energy loss as a function of distance are⁴⁰⁴:

$$t_{max} = \frac{X_{max}}{X_0} = \ln \frac{E_0}{E_c} - K, \quad K_{e^+} = 1.1, K_\gamma = .3 \quad (4.1)$$

$$\frac{dE}{dt} = E_0 A t^\alpha e^{-\beta t} \quad t = \frac{X}{X_0}, \alpha = \beta t_{max}, \beta \sim .5, A = \beta^{\alpha+1} / \Gamma(\alpha + 1)$$

The lateral shower size is described by the Moliere radius, $R_M = 21 MeV X_0/E_c$. 99% of an electron's energy will be concentrated within $3R_M$ of its impact point. A calorimeter may be designed to take advantage of these qualities by measuring light emitted by atoms excited by the energy released in the last stages of the shower with a photomultiplier or photodiode. The former have low noise levels but are subject to electronic drift over extended running and cannot operate in strong magnetic fields. Photodiodes have higher noise levels but are nearly impervious to magnetic fields and are more stable⁴⁰⁵. The intrinsic error of an electromagnetic calorimeter of this type is due to the statistical process involved and therefore decreases as $1/\sqrt{E}$ due to photon statistics - the number of particles in the shower is proportional to the incident energy. Additional statistical errors are introduced by energy lost out the sides and rear of a detector. This can be measured in a test beam or simulated using a detailed Monte Carlo such as EGS (the Electron Gamma Shower Monte Carlo). As these represent the shower fringes the statistical fluctuation is much greater - a "rule of thumb"⁴⁰⁶ being that the error introduced by rear leakage is approximately 1/3 of the energy lost. Monte Carlo calculations⁴⁰⁸ of the influence of leakage on resolution are shown in Figure 4.9.

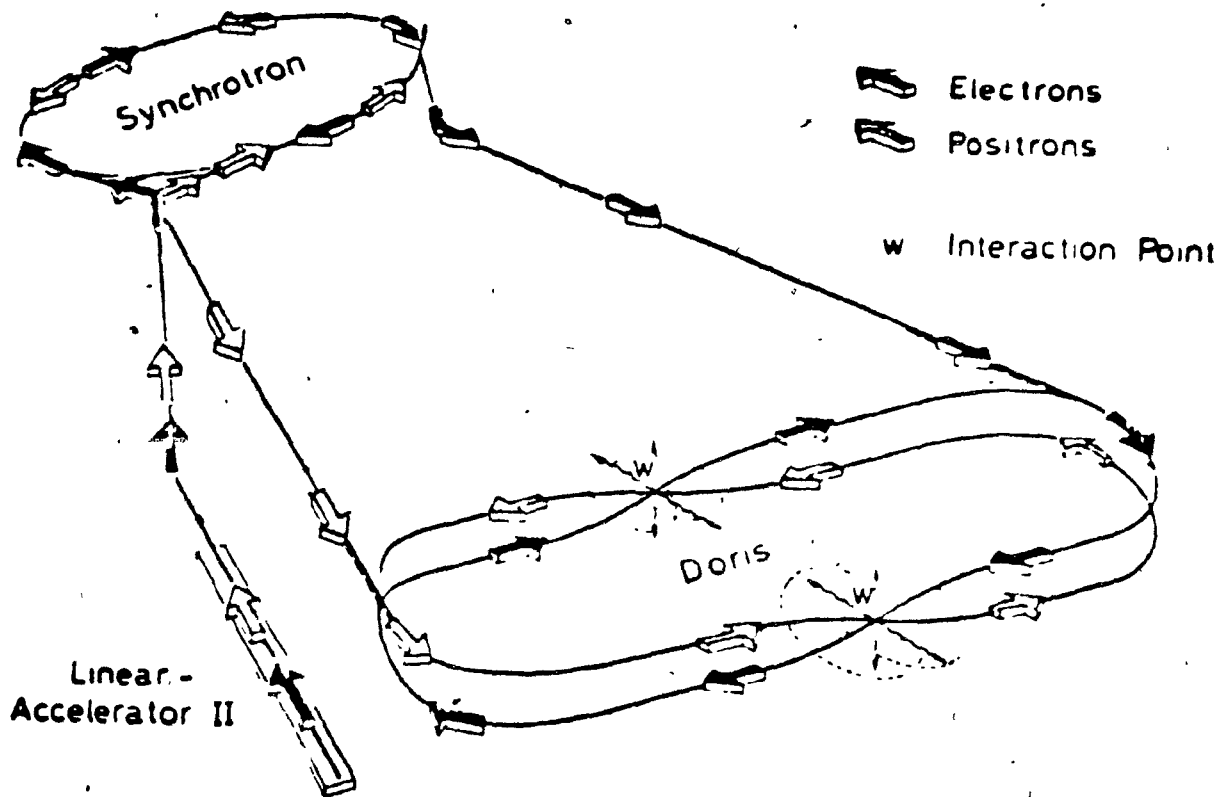
BGO is ideal for the ARGUS 0° taggers. The 20cm length of the crystals is equivalent to 17.7 radiation lengths while a group of nine crystals corresponds to 3.3 Moliere radii. BGO is also much easier to handle than NaI which is hygroscopic. The radiation recovery is good. Bieler et al.⁴⁰⁵ report an initial loss of light output of 26-38% upon irradiation with 40 and 85 rads of Cs137 γ -rays. After 110 days this decreases to 1-13% depending on the individual crystal. Bobbink et al.⁴⁰⁸ observe that the radiation

damage saturates (Figure 4.7) - after an initial loss of ~ 15% of light output after 800 rads of Co60 irradiation the crystals do not deteriorate further after doses of ~ 5000 rads. In comparison, Bobbink et al. find that a large part of the radiation damage in NaI is not recoverable and that CsI shows no recovery. It is also possible to "heal" BGO radiation damage by heat treatment^{402,405}. The radiation recovery is a strong function of temperature and for BGO crystals in a high radiation environment it might be advisable to maintain an elevated temperature⁴⁰⁶. Whatever the temperature is, it should be stable due to the strong change of BGO light output with temperature. The radiation response of BGO is a strong function of crystal quality. This is evident in Figure 4.8 where the light output for BGO crystals of different purities are shown as a function of time after the initial radiation exposures. Bakken et al.⁴⁰⁷ measure BGO energy resolution to as low as 1 GeV with 30x30x200mm³ crystals (Figure 4.9). In this experiment the light output of the BGO was measured with photodiodes. The intrinsic BGO resolution for 4 GeV incident electrons (i.e. leakage and Photon counting fluctuations) was $1.6 \pm .4\%$ while the electronic resolution was $.8 \pm .1\%$. This is consistent with other measurements and with Monte Carlo estimates^{408,407}. It seems feasible that energy resolutions on the order of two percent may be achieved over a large part of the BGO tagger.

4.4 CAPTIONS FOR FIGURES

- 4.1** The original DORIS-I storage ring. From Reference 401.
- 4.2** A section of the DORIS-II storage ring. This shows the machine architecture relevant to the ARGUS Tagger proposal. A preliminary design of the vacuum chamber and the location of the tagger system and bending magnet are shown. The final vacuum chamber will have a second window below the beam to allow antitagging of photons emitted at 0° . This is shown in Figure 4.6.
- 4.3a-j** These diagrams show the trajectory of a particle through the beam optics, the horizontal coordinate (Z) is the distance from the interaction point while the vertical coordinate (Y) is the displacement above the interaction point. The discretization used in the beam transport calculation is actually much finer than that shown. Each trajectory shown in a particular picture had the same particle energy. The trajectory marked with an arrow in each picture represents a particle emitted at 0° , i.e. horizontally. Each line above or below this represents an increase or decrease in the scattering angle, in the vertical plane, of 1mrad respectively. Figures 4.3 and 4.4 were calculated with a program simulating the DORIS beam optics supplied to me by Leif Jönsson of Lund University.
- 4.4a-g** These represent the angular acceptance of the DORIS-II beam optics as a function of energy. Each picture shows the impact points at the tagger plane ($Z = 17.7\text{meters}$) of electrons emitted at fixed energies but varying angles. The difference between successive θ contours is 1mrad while the interval in ϕ is 10° . The $\theta = 0$ point on each picture is easily identified except for Figure 4.4a where the 1mrad contour is labelled.
- 4.5** A BGO small angle tagger.
- 4.6** A crude vacuum chamber design with provision for the luminosity monitors.
- 4.7** Radiation damage and recovery of two BGO crystals produced by Harshaw Chemical Co. From reference 408.
- 4.8** Radiation damage and recovery of BGO crystals after recrystallization (i.e. increased purity). From Reference 403.
- 4.9** BGO resolution and rear leakage for 10 GeV incident photons as a function of crystal length. From Reference 403.
- 4.10** BGO energy + Electronics energy resolution as a function of energy. From Reference 407.

Figure 4 1



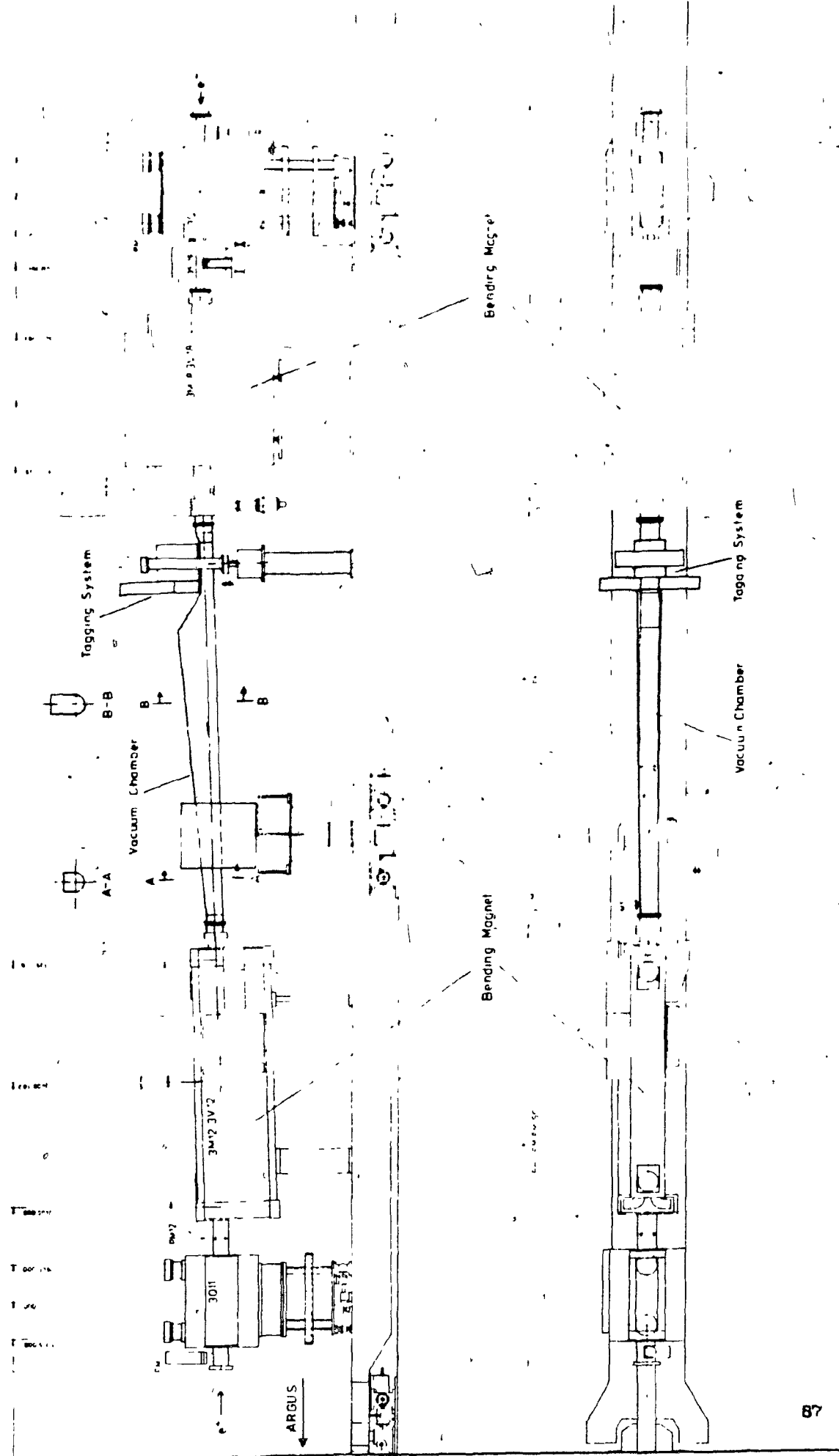
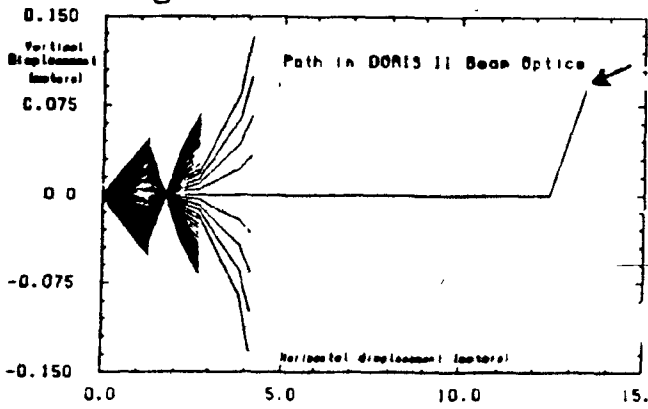


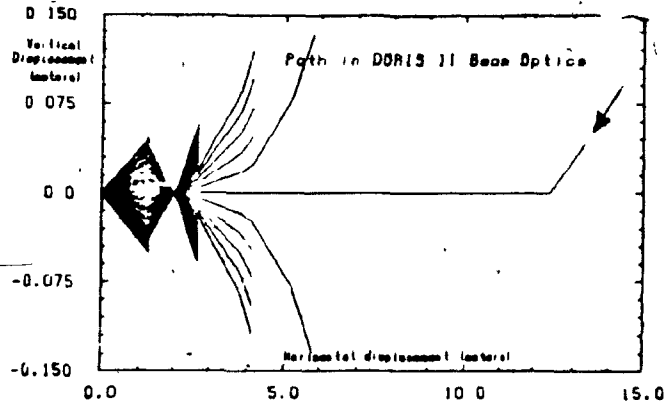
Figure 4.2

Figure 4.3a



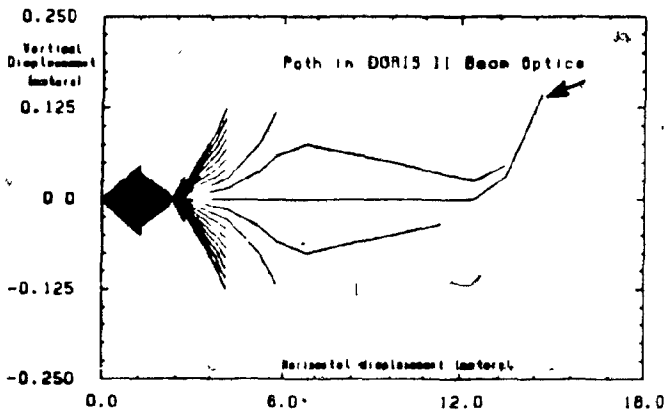
ELECTRONS
500 MEV

Figure 4.3b



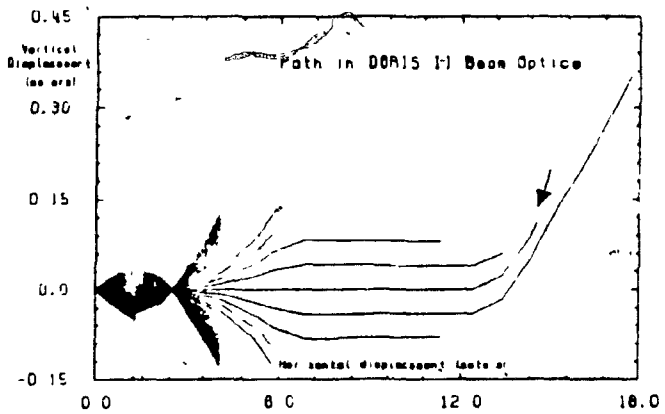
ELECTRONS
1000 MEV

Figure 4.3c



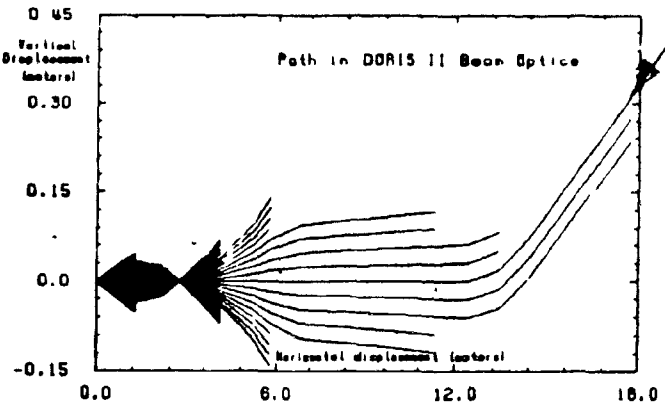
ELECTRONS
1500 MEV

Figure 4.3d



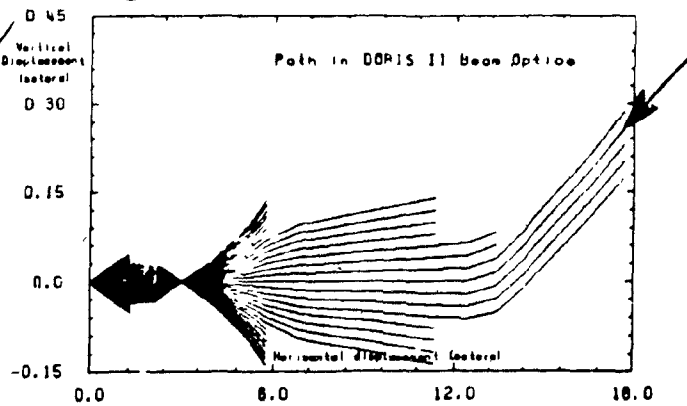
ELECTRONS
2000 MEV

Figure 4.3e



ELECTRONS
2500 MEV

Figure 4.3f



ELECTRONS
3000 MEV

Figure 4.3g

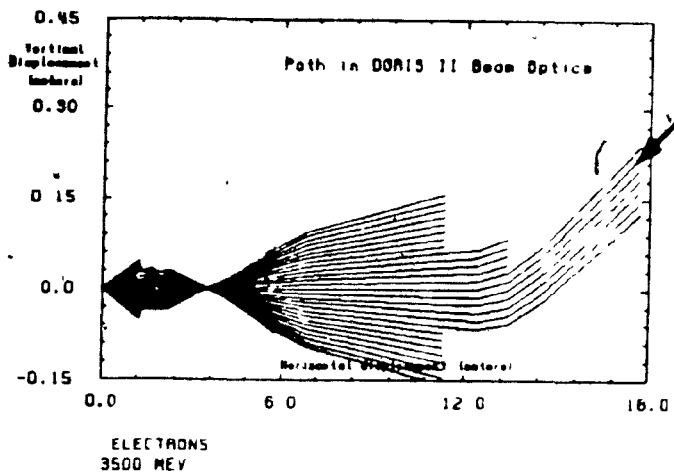


Figure 4.3h

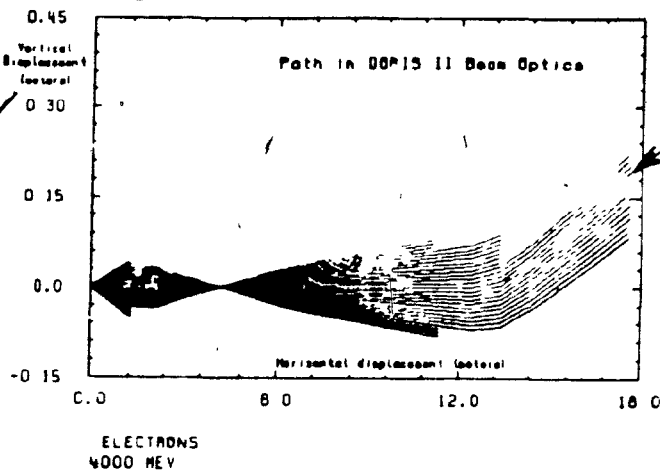


Figure 4.3j

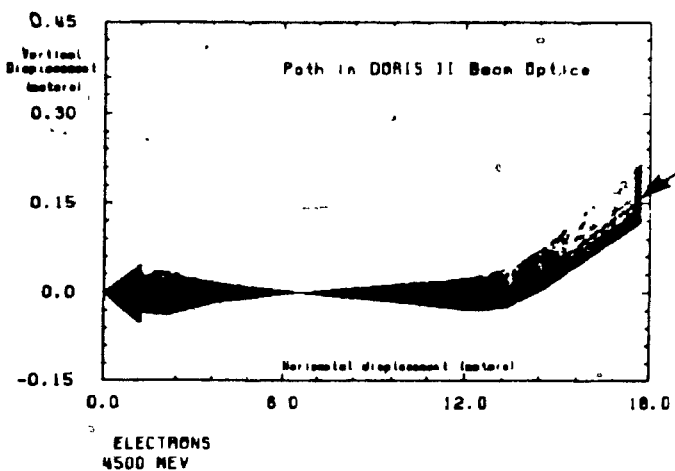


Figure 4.3i

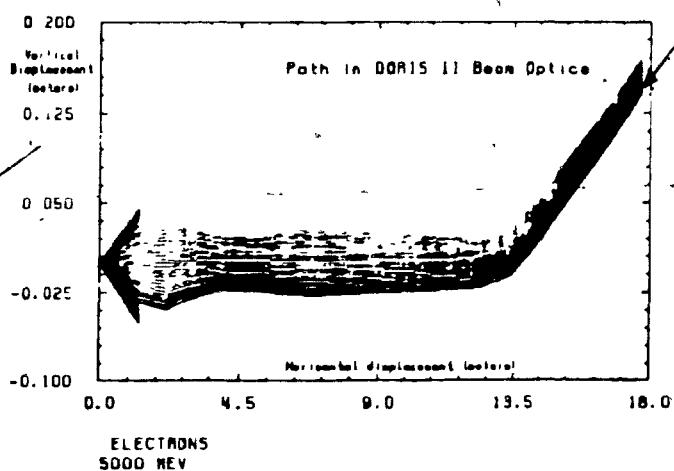


Figure 4.4a

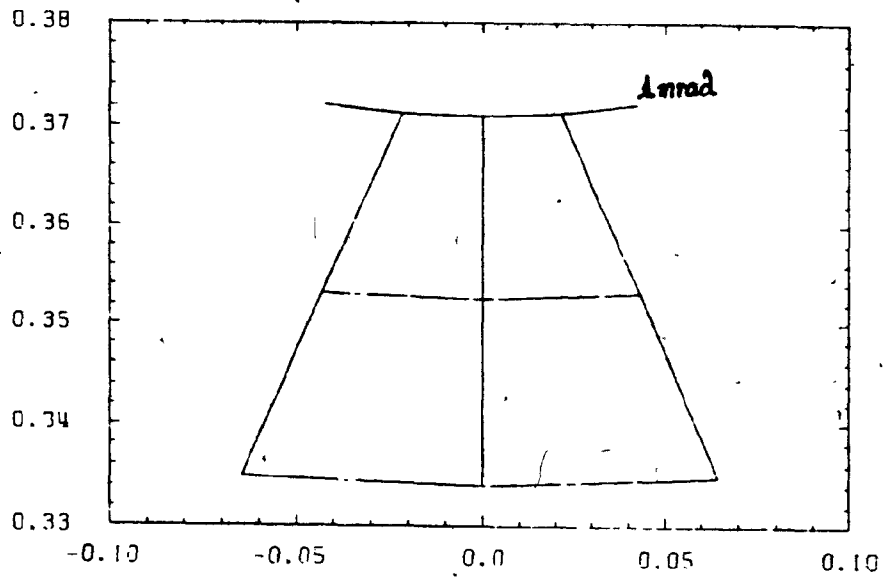
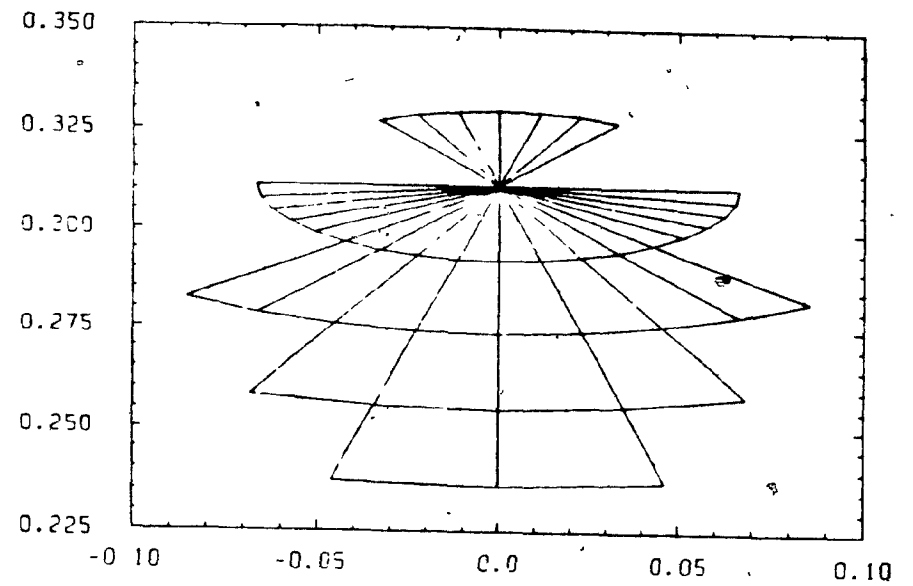


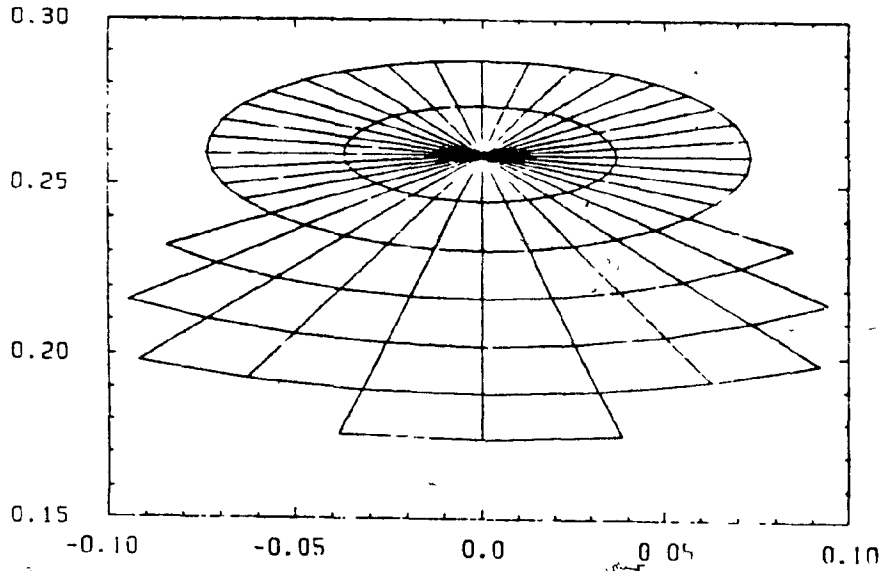
Figure 4.4b



88

2000 MEV

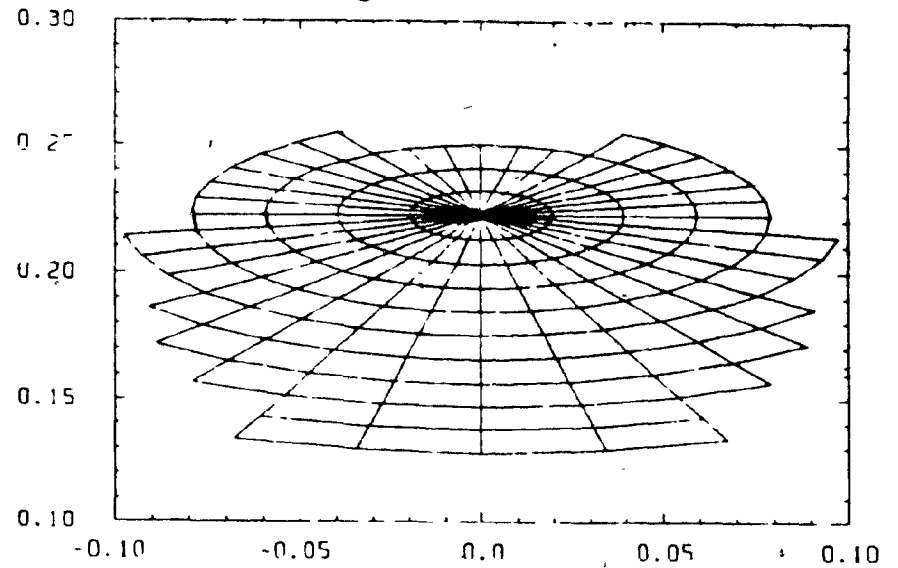
Figure 4.4c



3000 MEV

3500 MEV

Figure 4.4d



3500 MEV

Figure 4 4e

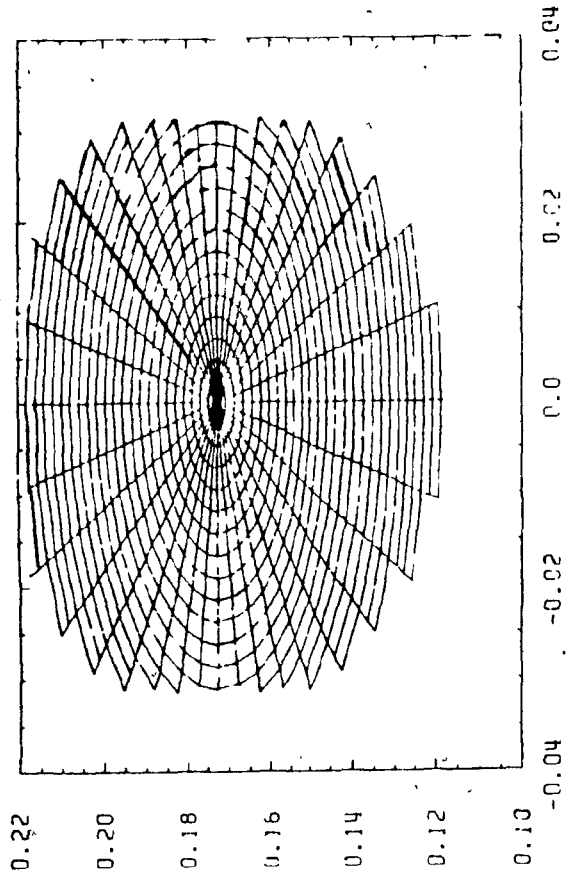
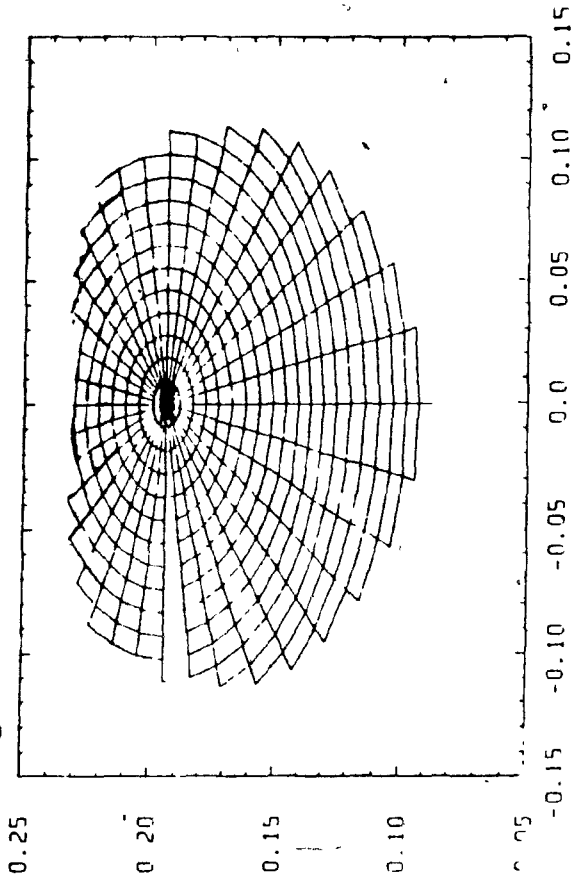


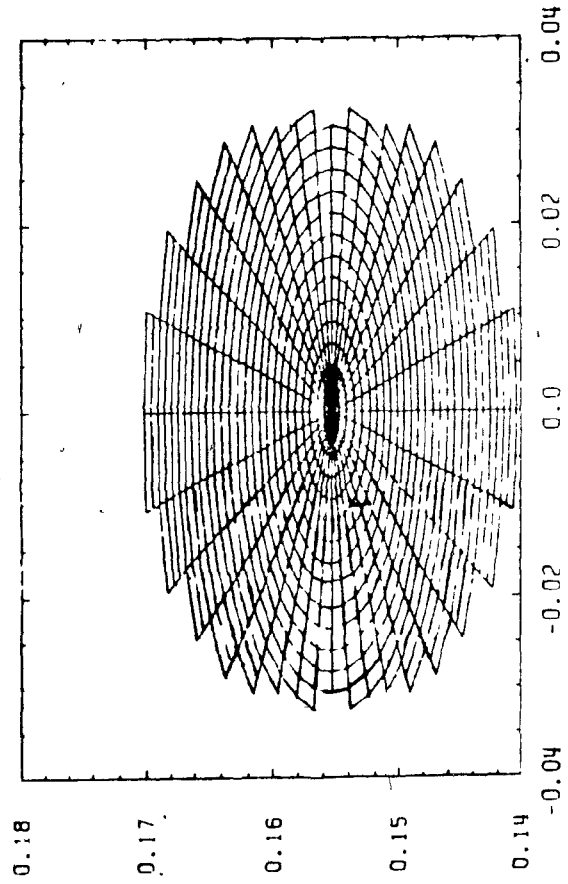
Figure 4 4f



4500 MEV

1000 MEV

Figure 4.4g



5000 MEV

Figure 4.5

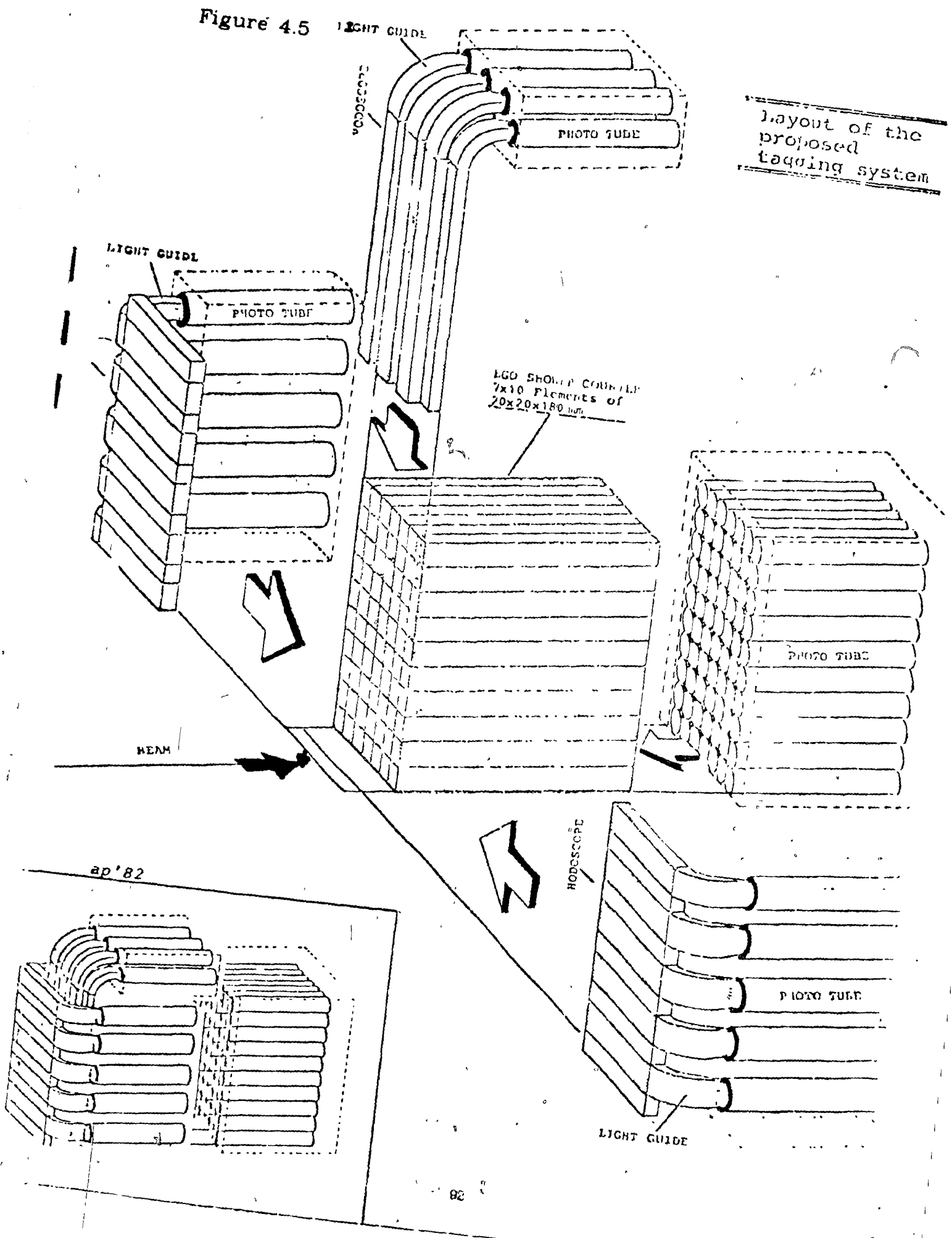


Figure 4.7

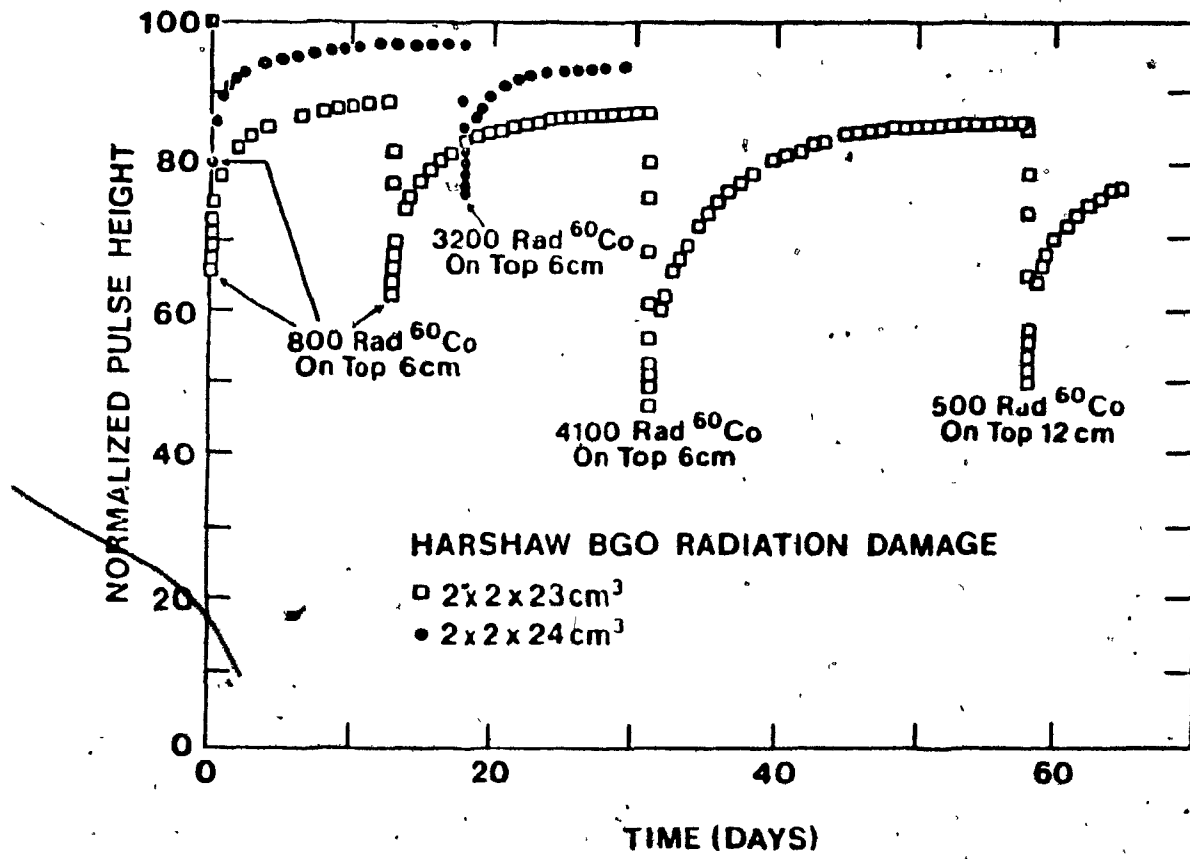
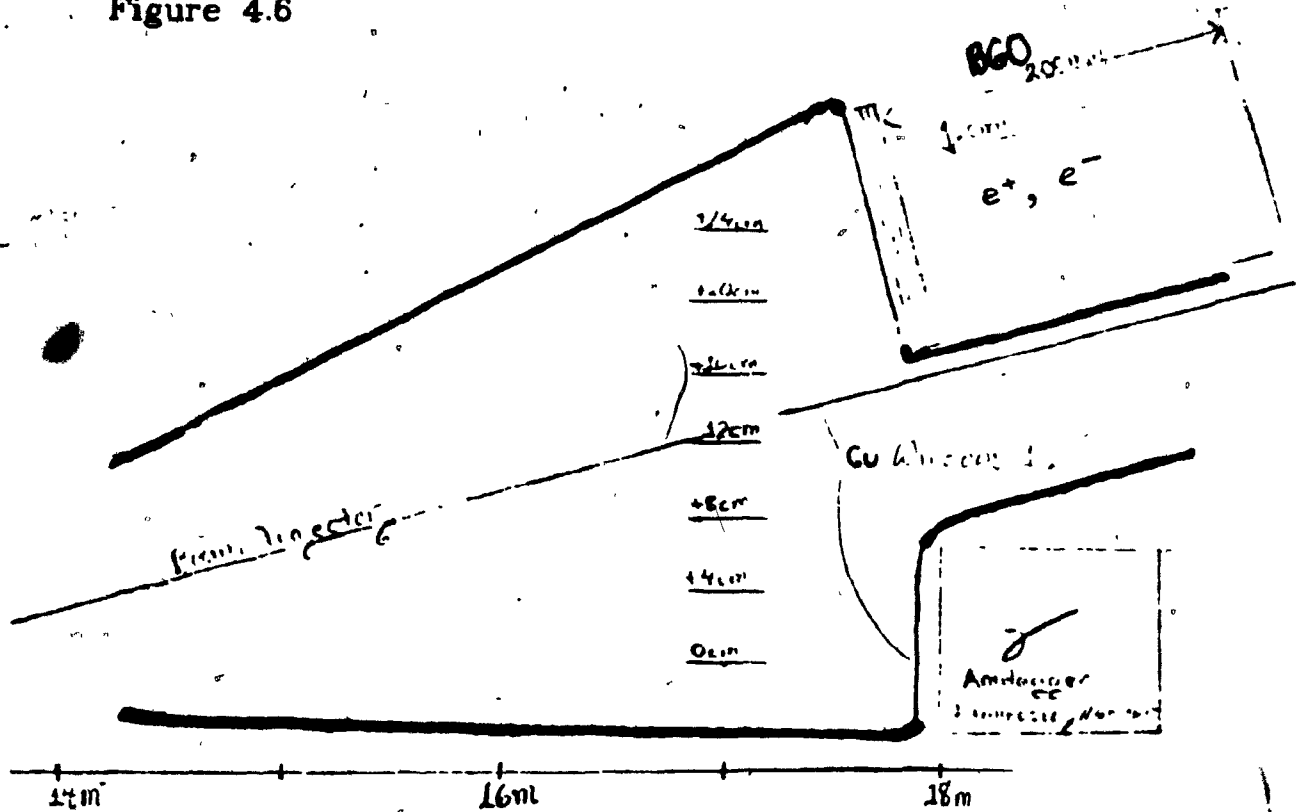
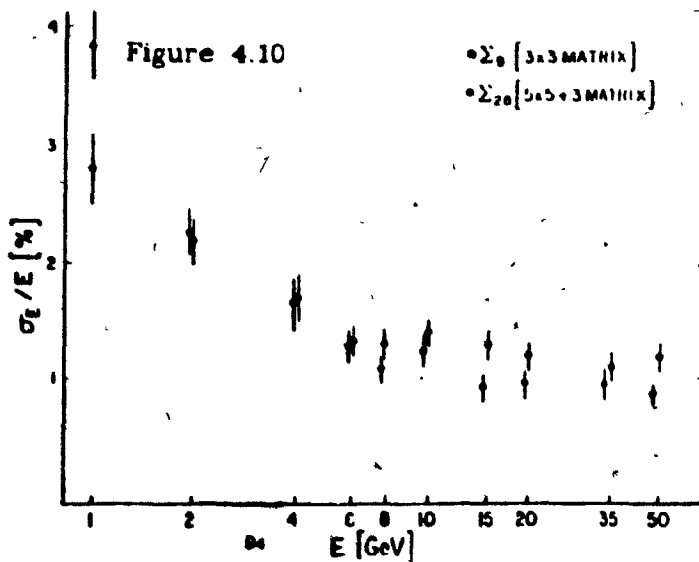
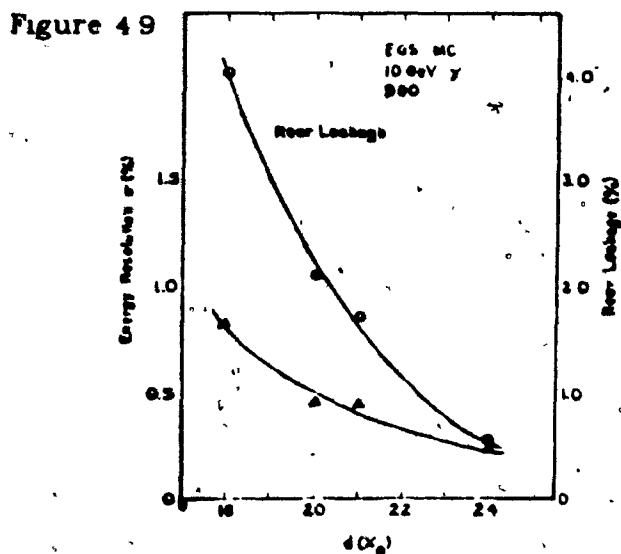
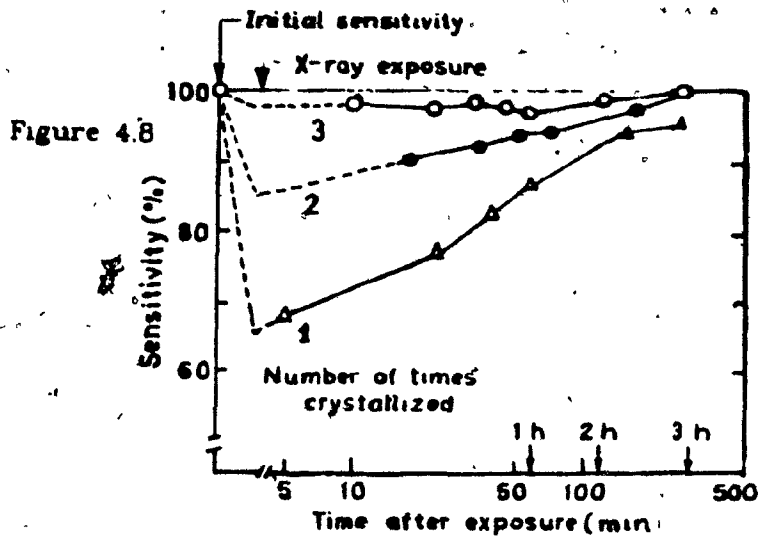


Figure 4.6





CHAPTER 5: QED AND EXCLUSIVE 2 PRONG CHANNELS IN $\gamma\gamma$ COLLISIONS

5.1 Introduction : The effect of QED on light-light scattering via the "box" diagram, shown in Figure 5.1, was considered as early as 1935⁵⁰⁴. The cross-section for visible light scattering was calculated to be on the order of 10^{-29} nb while an experiment with the dark adapted eye provided only an upper limit of $3 \cdot 10^{-30}$ nb. Recently, elastic $\gamma\gamma$ scattering has been seen with the Crystal Ball^{505,506} with an η or π^0 as a resonant intermediate state.

Most QED studies are concerned with $\gamma\gamma$ annihilation into lepton pairs. At CMS energies available from machines currently in operation (5-43 GeV) the cross-sections of the two principal $\gamma\gamma$ QED channels ($e^+e^- \rightarrow e^+e^-e^+e^-$, $e^+e^- \mu^+\mu^-$) are several orders of magnitude above that of $e^+e^- \rightarrow \mu^+\mu^-$. After detector limitations (trigger efficiency and geometric acceptance) are considered, the observable $\gamma\gamma$ rates are approximately the same magnitude as annihilation dimuon production. At ARGUS, the visible $\gamma\gamma$ QED cross section is $\sim 3 - 4$ nanobarns compared to ~ 1 nanobarn for $e^+e^- \rightarrow \mu^+\mu^-$. This disparity increases at PETRA energies, and at LEP (~ 100 GeV), $\gamma\gamma$ processes are being considered for use as luminosity monitoring channels in addition to the Bhabha process ($e^+e^- \rightarrow e^+e^-$) used at existing e^+e^- colliders. The acceptance is limited by the "holes" in the detector geometrically and, in most cases, rather more drastically by the trigger. For instance ARGUS' drift chamber can be used with $\sim 99\%$ efficiency down to $|\cos\theta| \leq .9$ with a minimum particle P_{\perp} of 50 MeV/c, however the present trigger requires two tracks in the barrel ToF (Time of Flight counters), restricting $|\cos\theta| \leq .75$ with a P_{\perp} cut varying between 125 and 250 MeV/c, depending on the exact event geometry.¹ The acceptance "holes", whether they arise from the beampipe or trigger, are magnified by the Lorentz boost of the $\gamma\gamma$ CMS along the beam axis.

The interest in studying QED channels rests mainly on their importance as measures of detector behaviour. Aside from this practical aspect, the channels available in $\gamma\gamma$ collisions are rare instances of α^4 QED processes relevant at high energies and high momentum transfers. These complement the standard measurements of higher order effects, which usually only involve small momentum transfer processes. Strictly speaking, no surprises are expected - the pointlike electron propagator has been

¹Total visible cross-sections for various $|\cos\theta|$ and minimum particle P_{\perp} cuts as a function of beam energy are shown in Figure 5.3 for the reaction $e^+e^- \rightarrow e^+e^- \mu^+\mu^-$.

tested to distances of 10^{-18} cm in e^+e^- annihilation and current ($g_{\mu-2}$) calculations⁵²⁰ test the low momentum transfer QED matrix element to order of α^4 . These reactions are therefore well understood theoretically - the $\gamma\gamma$ diagrams contributing to order α^4 in the cross-section are shown in Figure 5.3. The two diagrams of type 5.3a were first studied in the context of modern particle physics during the early seventies^{502,110,112,119}. These studies used the Double Equivalent Photon Approximation¹¹⁹ to simplify the seven dimensional integration involved in calculating visible cross-sections. The cross-section⁵⁰⁴ for real photon annihilation into lepton pairs is given by:

$$\begin{aligned}\sigma(\gamma\gamma \rightarrow l^+l^-) &= 2\pi\alpha^2 \cdot W_{\gamma\gamma}^{-2} [2\beta^2 - 4\beta + (3 - \beta^4) \cdot \ln(\frac{1+\beta}{1-\beta})] \\ \frac{d\sigma}{d\cos\theta} &= 2\pi \cdot \alpha^2 W_{\gamma\gamma}^{-2} \beta [2\beta^2 \sin^2\theta - \beta^4 \sin^4\theta + 1 - \beta^4] / (1 - \beta^2 \cos^2\theta)^2\end{aligned}\quad (5-1)$$

Here β refers to the velocity, p/E , of the leptons in the CMS ($\beta = 1 - \frac{4m_l^2}{s}$, $s = W_{\gamma\gamma}^2$) and θ refers to the lepton production angle in the $\gamma\gamma$ CMS with the Z axis defined by the colliding photons. The leptons are strongly focused along the collision axis (Figure 5.4) - this restricts acceptance beyond that expected from simple geometric or kinematic effects. Folding equation 5-1 with the DEPA produces¹⁰⁹:

$$\sigma(e^+e^- \rightarrow e^+e^-l^+l^-) = \alpha^4 / (\pi m_l^2) \{ \ln(E^2/m_e^2) \}^2 \ln(4E^2/W_{min}^2) \quad (5-2)$$

This result is very far from perfect. The main sources of error are within the treatment of the calculation and the DEPA itself. The nonDEPA results shown in Figure 5.2 were derived using an event generator written by Kleiss, Daverfelt, and Berends⁵⁰³. Even these results are inaccurate (on the order of 1%) in extreme regions of phase space where the other subprocesses depicted in Figure 5.3 contribute. The 6 extra diagrams derived due to the indistinguishability of the final state particles in the case of $e^+e^- \rightarrow e^+e^-e^+e^-$ (variations of 5.3b) can only interfere with the multiperipheral diagrams significantly at high Q^2 while the virtual bremsstrahlen diagrams (the 16 variations of 5.3c, 4 if a muon pair is produced instead of an electron pair) only become important at low invariant masses. These diagrams trade one factor of $\ln(E/m_e)$ for a $1/W_{l+l-}^2$ factor while the permutations of Figures 5.3d lose both logarithmic factors. The contribution of diagram 5.3c has been observed at PLUTO⁵⁰¹ as an excessive number of events in the lowest mass bin of the sample tagged by the ECT (end-cap tagger) - which is sensitive to the highest range of Q^2 . The negative C-Parity of the final state causes this subprocess to interfere with the even C-Parity processes (Figure 5.3a,b) producing a charge asymmetry in the events i.e. the positively charged electrons or muons tend to be correlated with the incident positron beam. This effect has not yet been detected. Finally, because of the same kinematic advantages as the standard diagram (Figure

5.3a), order α^6 corrections (Figure 5.5) may mimic 4-prong multihadron events. These α^6 QED channels have a total cross-section on the order of several nanobarns¹¹⁰. Asymptotically the total cross-section is:

$$\sigma_{e^+e^- \rightarrow e^+e^-e^+e^-} = .006\text{nbarn} \cdot \left(\ln \frac{4E^2}{m_e}\right)^4 \quad (5-3)$$

Radiative corrections to $\gamma\gamma$ QED collisions have only recently been considered seriously as the precision of the experimental measurements is just beginning to test the limits of the α^4 results. For notag analysis most of the radiative corrections apply to the beam particles because of their higher Lorentz boost. An event generator including these corrections has been prepared by Kleiss et al.⁵⁰⁹.

The QED channels are a major part of $\gamma\gamma$ physics from an experimentalist's point of view. They have simple event signatures in the central detector - the lepton pair is usually produced with a small $|\sum \vec{P}_\perp|$ due to the tendency of the colliding bremsstrahlen to be collinear with the parent lepton beams. This results in a high degree of coplanarity, while the collinearity of the event is destroyed by the Lorentz boost due to the asymmetric energies of the two γ s. QED events can be used to determine luminosities for the $\gamma^*\gamma^*$ final state. This is especially useful if double tagging is attempted - the QED events are then fully constrained allowing studies of intrinsic $W_{\gamma\gamma}$ resolution and acceptance to be made with tagger imperfections included. This information is useful in calculating acceptance corrected luminosities. If one cannot demonstrate a practical understanding of the observed QED cross-section, it suggests a limited understanding of the detector and trigger, which must be improved before progress is to be made on more theoretically interesting channels such as resonance production. For ARGUS, the QED channels will also allow experimental checks of techniques for the removal of false double tag events, as described in the next chapter.

The early experimental observations of $\gamma\gamma$ QED channels were summarized in a talk by G.Barbiellini at the 1980 Aachen Conference⁵⁰⁷. The first observation (acollinear but coplanar e^+e^- pairs) was made at VEPP-2 in Novosibirsk⁵⁰⁸⁻⁵¹⁰ ($E_{cm} = 1.4\text{GeV}$) followed by results from ADONE⁵¹¹⁻⁵¹⁴, ($E_{cm} = 2.4\text{GeV}$, Channels $e^+e^- \rightarrow e^+e^-e^+e^-, e^+e^-\mu^+\mu^-, e^+e^-\pi^+\pi^-$). The ADONE experiment was the first experiment to double tag events using the synchrotron's magnetic lattice for momentum analysis. These experiments produced no surprises except for a suppressed $\pi^+\pi^-$ contribution. The early contributions from SPEAR(SLAC) ($E_{cm} = 4.4\text{GeV}$) are reviewed in John Zipse's thesis⁵¹⁵ which concluded that QED agrees with experiment and the hadronic cross-section observed differs little from the $\gamma\gamma \rightarrow \pi^+\pi^-$ Born

term approximation (i.e. structureless pions). Perhaps the last experiment that can be assigned to this "first generation" of $\gamma\gamma$ analysis is that of DCI⁵²⁴ (Figure 5.6) which took data in double and single-tag modes and found - despite limited statistics - an enhancement of the reaction $\gamma\gamma \rightarrow \pi^+\pi^-$ above that expected from a simple Born term.

5.2 Monte Carlo Studies of $\gamma\gamma \rightarrow e^+e^-, \mu^+\mu^-$ Acceptances. : The original reason for studying the acceptance of $\gamma\gamma$ QED final states via Monte Carlo was to demonstrate that ARGUS had the capability to "understand" these processes for final state masses above 1 GeV. This is important for the measurement of the two-photon total hadronic cross-section. It was thought that ARGUS could separate hadronic events with only two charged particles visible in the final state where the analyses of other experiments had to ignore this topology, as the QED contribution was not well understood. A lower event topology threshold would give ARGUS a greater acceptance and reduce the uncertainty induced by the calculation of trigger efficiency for multihadron events. Special importance is attached to this due to the low multiplicity of hadronic events in the low mass range which the ARGUS $\gamma\gamma$ experiment is designed to investigate (1 - 3 GeV). It was hoped that the particle identification capabilities of the detector could be used to select a significant fraction of the QED events. This would allow the rest to be removed by a Monte Carlo subtraction normalized to the identified samples. The fraction of the events in each QED channel identified would be determined using SIMARG.

The Monte Carlo simulation for the $\gamma\gamma$ QED processes had four major development versions. The Advanced Mini-Monte Carlo refers to the version with CPPT & CMATRIX trigger simulation and detector resolution included while the primitive ARGUS Monte Carlo only used geometric cuts to simulate the detector acceptance.

- (1) Improved DEPA Generator + primitive ARGUS Mini-Monte Carlo.
- (2) Improved DEPA Generator + Advanced Mini-Monte Carlo.
- (3) Exact α^4 Event Generation + Advanced Mini-Monte Carlo.
- (4) Exact α^4 Generation + Full ARGUS Monte Carlo(SIMARG) and trigger simulation (TRIGGR).

The third stage used an event generator written by Kleiss et al.⁵⁰⁸ which represented an exact calculation of the contribution from the two multiperipheral diagrams (Figure 6.3a). This program was a major improvement over the $\gamma\gamma$ QED generator of W. Wagner's Monte Carlo as modified for 0 degree tagging analysis. Originally used by PLUTO in their early analyses, Wagner's program assumed complete factorisability of the luminosity functions for the colliding photons and neglected the electron mass at certain points. This destroyed cancellations in the luminosity functions producing an overestimate of the 0 degree tagging rate. In addition, the final state generator assumed that the colliding photons were real,

i.e. that equation 5.1 applied. This last imperfection was retained in the revised version of the program. The differential cross-section being expressed as:

$$\sigma_{e^+e^- \rightarrow \mu^+\mu^-} \approx \sigma_{\gamma\gamma \rightarrow \mu^+\mu^-}(Q_1^2 = 0, Q_2^2 = 0, W_{\gamma\gamma}) \cdot L_{TT}(E_{\gamma_1}, E_{\gamma_2}, Q_1^2, Q_2^2, \theta) \quad (5-4)$$

Only collisions of transverse photons were considered but the exact¹¹⁰ luminosity function (L_{TT}) was used (Appendix 1). Compared to Kleiss' program, this led to a slightly wider lepton P_{\perp} distribution and a 15% overestimate of the total cross-section. The cross-section overestimate was due to the neglect of the decrease of $\sigma(\gamma\gamma \rightarrow l^+l^-)$ with increasing Q^2 . All the analyses were initially done with the primitive Mini-Monte Carlo, but were repeated with the "Advanced Mini-Monte Carlo" providing the acceptance/trigger cuts when this program was perfected. Kleiss' program was used only for the total leptonic cross-section calculations and the full SIMARG generation, because more DEPA generator events were available for the efficiency calculations. The normalized MiniMC results for the two programs, for acceptance and tagging rates, agree within statistical error.

The main numerical results for various acceptance and tagging arrangements are given in Tables 5.1-3. The visible (i.e. triggered) cross-sections for the two leptonic channels are approximately the same despite the much larger total cross-section for electron pair production. As the electrons have a much smaller mass than muons, their angular distribution is more concentrated along the direction of the incident photons - so a much larger portion of the e^+e^- cross-section is lost in the beam pipe. The results presented in Table 5.1 were calculated with a full detector Monte Carlo (SIMARG). It is interesting to note that for events with a mass of at least 1 GeV, the acceptance is approximately the same for the SIMARG and MiniMC analyses with both the Kleiss and Improved DEPA generators. The situation for events with invariant masses less than 1 GeV is different. The SIMARG analysis predicts rates 1/2 to 1/3 that of the MiniMC - the inefficiency is an effect of trigger discriminator thresholds and efficiencies of the ToF, Shower Counters, and, perhaps, the Little Track Finder. This inefficiency affects particles with low P_{\perp} as these may only graze the shower counters and ToF. For these tracks the fluctuations in shower counter energy deposition must be calculated with a full detector Monte Carlo like SIMARG.

The main emphasis of the results given to the DESY PRC (Physics Review Committee) in October 1983 was the muon identification capability. It was reasoned that ARGUS' e/π separation was better than its μ/π separation since electrons could be identified by ToF at very low momenta, by dE/dX

at intermediate momenta, and by shower counter energy at momenta comparable with the μ chamber acceptance (and with a larger solid angle). Therefore the μ identification capability would be the limiting factor in the analysis. Some results of these calculations are depicted graphically in Figures 5.7-5.9. Here the "visible" cross-section refers to the expected number of events from the process taken as data and the "identified" cross-section refers to the portion of these events passing the geometric and momentum cuts designed to simulate the muon chamber acceptance. The muon chamber identification was simulated by assuming that 1) any muon with energy greater than 1.2 GeV that was found in the drift chamber is identified as a muon by the outer chambers, 2) any muon with $.72 \leq E \leq 1.2$ and $P_x/P_z \leq .571, P_y/P_z \leq .857$ is identified by the inner layer of muon chambers, and 3) any two prong event with at least one identified muon and total energy less than 3.5 GeV is a $\gamma\gamma \rightarrow \mu\mu$ event (it was assumed $e\mu$ events arising from leptonic decays of τ pairs could be eliminated by requirements of $|\sum \vec{P}_\perp|$ balance).

The double tag efficiency and cross-sections for $e^+e^- \rightarrow e^+e^-\mu^+\mu^-$ are shown in Figures 5.10-11 respectively. The double tag efficiency is essentially the same as that discussed in the next chapter as any possible cross-section variation with $Q_i^2, i = 1, 2$ (the virtual photon masses) is ignored in the expressions used for both the hadronic and QED cross-sections. This assumption is particularly good in the double tag case as this restricts the masses of the photons to be negligible compared to any other mass scale in the process. Therefore, even though the total cross-sections (integrated over all kinematically allowed Q^2) may be inaccurate, the double tag cross-sections will be correct, so far as the expressions used for the cross-sections of real photon collisions are correct. Table 5.3 lists the results of calculations of tagging acceptances for $e^+e^- \rightarrow e^+e^-\mu^-\mu^+$. The first section gives the tag probabilities with no requirement on the event in the central detector. The next two sections give the tag probabilities for events setting the barrel trigger and full detector trigger respectively. The double tag probability is enhanced for triggered events because this places a restriction on the rapidity of the $\gamma\gamma$ CMS. The significance of the different tagger situations given is discussed in the next chapter.

Final State:	$\mu^+\mu^-$	$\mu^+\mu^-$	e^+e^-	e^+e^-
Final State Mass Cut:	$W \geq 1 \text{ GeV}$	$W \leq 1 \text{ GeV}$	$W \geq 1 \text{ GeV}$	$W \leq 1 \text{ GeV}, W \geq .25 \text{ GeV}$
Total σ	$3.868 \pm .003 \text{ nb}$	$60.50 \pm .05 \text{ nb}$	$11.828 \pm .007 \text{ nb}$	$333.4 \pm .2 \text{ nb}$
Triggered σ (Barrel)	$.289 \pm .005 \text{ nb}$	$1.63 \pm .06 \text{ nb}$	$.291 \pm .008 \text{ nb}$	$2.41 \pm .2 \text{ nb}$
% in Detector	20.9	21.3	7.03	5.09
% in Barrel Triggers	8.4	3.0	2.78	.800
% in Barrel Triggers,LTF	7.5	2.69	2.46	.72
% in Full Trigger	16.7	6.6	5.5	2.0

Table 5.1 SIMARG+Daverveldt MC QED Acceptances

Final State:	$\mu^+\mu^-, W_{\mu^+\mu^-} \geq 1 \text{ GeV}$	$\mu^+\mu^-, W_{\mu^+\mu^-} \leq 1 \text{ GeV}$
% in Barrel Trigger	7.9	4.6
% in Endcap + Barrel Trigger	17.3	15.3

Table 5.2 MiniMC+Daverveldt MC QED Acceptances

5.3 Preliminary Experimental Studies of $\gamma\gamma \rightarrow e^+e^-, \mu^+\mu^-$ and observation of the $f(1270)$ Meson in $\gamma\gamma$ Collisions. : As described in chapter three, evidence for $\gamma\gamma$ processes was first observed in the analysis of the 1983 ARGUS data. The fraction of this data taken with the full barrel trigger and an LTF threshold of two represents a luminosity of $27.6 \pm .5 \text{ pb}^{-1}$. The pretriggers contributing to this channel being mainly the CMATRIX and CPPT. This initial data sample was analysed with the ARG04 program.¹

¹Analysis of the larger data sample containing $40.8 \pm .5 \text{ pb}^{-1}$ luminosity used for the η' study (which includes data taken in 1984) is not yet complete. This is due to a delay introduced by reprocessing the SIMARG Monte Carlo events with the more advanced analysis program (ARG06) with which the data were reprocessed. The total data available from ARGUS at present amounts to a luminosity of $84 \pm 1 \text{ pb}^{-1}$ and has recently been reprocessed with the most recent version of the analysis program, ARG08.

Final State: $\mu^+\mu^-, W_{\mu^+\mu^-} \geq 1 \text{ GeV}$			
	% No Tag	% Single Tag	% Double Tag
Tagger 1	45.8	37.0	17.2
Tagger 2	58.3	35.8	5.9
Tagger 3	84.6	14.4	.98
% in Barrel Trigger	7.9% Trigger Acceptance		
% in Barrel Trigger + T1	22.2	44.2	33.5
% in Barrel Trigger + T2	36.8	49.6	13.5
% in Barrel Trigger + T3	74.4	24.6	2.0
% in Full Trigger	17.3% Trigger Acceptance		
% in Full Trigger + T1	25.9	45.0	29.1
% in Full Trigger + T2	41.6	47.6	10.8
% in Full Trigger + T3	76.7	21.4	1.9
Tagger 1 (=T1)	14x14 cm 1 cm from beam		
Tagger 2 (=T2)	14x14 cm 2 cm from beam		
Tagger 3 (=T3)	14x14 cm 1 cm from beam with slit		

Table 5.3 MiniMC+Improved DEPA QED Tagging Acceptances

The ARG06 data sample contained 5.2 million events representing 40.8 pb^{-1} luminosity. 228076 were selected as 77 candidates by requiring $\sum_{\pm} |\vec{p}| + \sum_{\gamma} E_{\gamma} \leq 3.5 \text{ GeV}$, ≥ 2 tracks with a distance of closest approach to the interaction point within: $r \leq 1 \text{ cm}$, $|s| \leq 5 \text{ cm}$ or a reconstructed vertex within the same fiducial region. This data was filtered using the techniques for beamgas and cosmic separation discussed in chapter 2. These results are summarized in Table 5.4.

The ARG04 data did not have muon chamber analysis so this category of events was not separated from the charge balance two prongs in the original analysis. The ARG06 dimuon events referred to in Table 5.4 were identified by requiring that the event have at least one hit in the muon chambers. More

Event Type	Fraction of Selected Data
$\gamma\gamma \rightarrow \mu\mu$	1.2%
Cosmic	5.5%
Beamgas	16.3%
Charge Balance Two Prongs	63.8%
Charge Balance MultiProngs	9.1%

Table 5.4 $\gamma\gamma$ Event Candidates

sophisticated analysis of the muon chamber data is planned.

Only the charge balance two prong events without beamgas or cosmic flags were considered further. The $|\sum \vec{P}_\perp|$ distribution for these is shown in Figure 3.5. This suggests that the sample is quite clean as the distribution decreases steeply with increasing $|\sum \vec{P}_\perp|$. A remnant of the proton band is visible in the $(p, dE/dX)$ distribution for the ARG04 data suggesting that there is a small number of beamgas events left in the sample. This contamination disappears in the ARG06 analysis. The invariant mass spectrum for exclusive charge balance pairs is shown in Figure 5.12, with the mass of all particles set to m_π . No cuts are applied except the beamgas and cosmic rejection algorithms. Figure 5.12 displays two sets of data - the experimental data and QED Monte Carlo events generated using the SIMARG Monte Carlo with Kleiss' generator for $ee \rightarrow ee\mu\mu$ and $ee \rightarrow eeee$ as input (only the basic $\gamma\gamma$ diagram, 5.3a, is evaluated in the event generation - the electron exchange diagram, Figure 5.3b, is not included). The QED Monte Carlo data were processed through a complete trigger simulation and normalized to the experimental luminosity for Bhabha events. Above invariant masses of 1 GeV the Monte Carlo "computer" luminosity - the number of SIMARG events produced divided by the calculated cross-section - is comparable to the 1983 experimental luminosity. The "computer" luminosity for the low mass region was limited by available computer time and amounts to 4% of the real signal. The f meson shows up as a clear excess in the appropriate mass region and the signal at higher invariant masses is consistent with 100% QED - an effect observed previously⁵²⁵. A clear signal for the f meson is seen with a mass at approximately 1210 MeV - this is 60 MeV lower than the Particle Data Book value³⁰³. It has been

observed⁵¹⁷⁻⁵¹⁹ that the mass for this resonance appears ~ 50 MeV lower in the $\gamma\gamma$ channel. This can be qualitatively explained by interference with the coherent d-wave background from $\gamma\gamma \rightarrow \pi^+\pi^-$. The T-matrix phase changes by π radians on traversing a resonance, leading to constructive interference below the resonance and destructive interference above - producing a mass shift. Unfortunately, this cannot explain a smaller mass shift seen by the Crystal Ball in the $\gamma\gamma \rightarrow f \rightarrow \pi^0\pi^0$ channel⁵²⁴. The most recent analysis of this problem is given by Menessier⁵¹⁶ whose calculation appears to describe the data⁵²¹. The $\pi\pi$ continuum cannot be calculated by the simple Born approximation due to the effect of strong interactions in the final state. Menessier⁵¹⁶ has used information from $\pi\pi, KK$ phase shift analyses to calculate final state interactions in $\gamma\gamma \rightarrow \pi\pi$ and has also included the effects of vector meson exchange and s-channel resonances (e.g. the $\sigma(600)$). This produces the required mass shifts in both the $\pi^+\pi^-$ and $\pi^0\pi^0$ decay channels.

In Figure 5.13 the observed mass distribution is extended to low values. Unfortunately, it is clear that the Monte Carlo simulation overestimates the experimental signal by at least 25% below 1 GeV. As discussed in the previous section the trigger acceptance for this kinematic region involves thresholds for both the LTF and the CPPT elements and the acceptance is strongly dependent on the SIMARG simulation. The P_{\perp} distributions for the experimental data and Monte Carlo events are shown in Figure 5.14. There is an experimental excess at 600 MeV/c corresponding to $f(1270)$ production but there is also a clear overestimate of the QED background at low P_{\perp} as expected. Changes on the order of 20% have been observed in the visible $\gamma\gamma$ cross-section after trigger adjustments were made. Detailed trigger analysis is planned. The mean energy deposited by minimum ionizing particles in each CPPT unit will be determined both in the data for clearly identified $e^+e^- \rightarrow \mu^+\mu^-$ events and in SIMARG to determine appropriate raw pulse height ratios. The effective CPPT element thresholds can be determined by checking the ToF and Shower Counter pulse height spectrums for each CPPT element set. These thresholds will then be scaled by the pulse height ratios to determine the appropriate thresholds for Monte Carlo events to simulate each trigger period. Similar analysis must be done for events with ETOT triggers as this trigger contributes to the acceptance for channels involving π^0 s or γ s in the final state. Finally, LTF efficiency must be studied in detail for low P_{\perp} tracks. This can be accomplished by selecting events from the annihilation channel that have clear ETOT triggers and studying the LTF information for low P_{\perp} tracks. This analysis is essential for any result on the $\gamma\gamma$ widths of resonances.

The f meson is a member of the 2^{++} nonet and is expected to be produced in $\gamma\gamma$ collisions with helicity ± 2 - as the γ s are nearly real the helicity 1 contribution is suppressed. The helicity 0 suppression can be derived by assuming that only the lowest multipole contributes to the reaction⁶⁰⁴ but more general analyses exist^{622,623}. Previous analyses of the $f \rightarrow \pi^+\pi^-$ have had to use a helicity 2 hypothesis to calculate acceptances because of the problems of QED background subtraction. Crystal Ball⁶²⁴ have studied the channel $f \rightarrow \pi^0\pi^0$ and analysed the observed angular distribution. Their upper limits for helicity 0 and helicity 1 matrix elements are 51% and 13% of the helicity 2 matrix element respectively.

The angular distribution observed by ARGUS for events with invariant masses between 1.1 and 1.3 GeV (as calculated with a pion mass hypothesis) is shown in Figure 5.16 - the lower curve was calculated from Monte Carlo data for QED channels. Figure 5.15 shows the subtracted angular distribution and a second distribution from the "Advanced MiniMC" described above with an event generator that simulates $\gamma\gamma \rightarrow f(1270) \rightarrow \pi^+\pi^-$ assuming complete helicity two dominance. The MiniMC spectrum is normalized to the QED-subtracted data. The $f(1270)$ event generator does not contain any of the final state interaction or continuum interference effects described by the Men essier model. It is clear that the data agrees well with the helicity two hypothesis. The extent to which the contribution of other helicities can be derived from this information is, as yet, unknown as the shape of the observed distribution is determined by acceptance to a significant extent. This is readily apparent if one compares the physical QED angular distribution for $\gamma\gamma \rightarrow \mu\mu$ in Figure 5.4 with the acceptance corrected QED Monte Carlo angular distribution of $\gamma\gamma \rightarrow \mu\mu, cc$ in Figure 5.16.

Very preliminary studies of $\gamma\gamma \rightarrow K^+K^-$ have been made. The resulting spectrum is shown in Figure 5.17 - the progressively lower histograms correspond to increasingly restrictive particle identification cuts. The large peak in the spectrum with the laxest cuts corresponds to misidentified QED events (with the mass translated upwards by the Kaon mass assumption used in the calculation of the X^+X^- mass). The result is limited by the absence of proper ToF calibration in the ARGUS data sample used. The ARGUS data have been calibrated and are in the midst of reanalysis. There does seem to be some evidence of $\gamma\gamma \rightarrow f'(1515)$ production at a 2σ level.

The $\gamma\gamma \rightarrow X^+X^-$ analysis is still very preliminary. Hopefully, with more data and an improved trigger analysis, these results will soon be put on a quantitative level. Additionally, there are many

channels for which ARGUS could improve previous observations or upper limits. For instance, ARGUS' particle identification capabilities and photon resolution make it ideal for studying the production of vector meson (ρ, ω, ϕ) pairs in $\gamma\gamma$ collisions.

5.4 CAPTIONS FOR FIGURES

5.1 QED "Box" Diagram

5.2 Total Observable Cross-sections as a function of beam energy for $e^+e^- \rightarrow e^+e^-\mu^+\mu^-$ (via Diagram 5.3a) for various minimum P_{\perp} and maximum $|\cos\theta|$ cuts.

5.3 $e^+e^- \rightarrow e^+e^-l^+l^-$ Feynmann Diagrams

5.4 $\gamma\gamma \rightarrow \mu^+\mu^-$ CMS $\cos\theta$ distribution.

5.5 An α^6 QED Process.

5.6 DCI Results⁶²⁴ on Single Tagged and Double Tagged Two Prong production.

5.7 Monte Carlo $\gamma\gamma \rightarrow \mu^+\mu^-$ Event identification probability expressed as a function of $\mu^+\mu^-$ invariant mass.

5.8 $e^+e^- \rightarrow e^+e^-\mu^+\mu^-$ visible cross-sections (i.e. the number of Monte Carlo events given 10 inverse picobarns "computer" luminosity).

5.9 Monte Carlo $e^+e^- \rightarrow e^+e^-\mu^+\mu^-$ Identified cross-sections.

5.10 Monte Carlo $e^+e^- \rightarrow e^+e^-\mu^+\mu^-$ Double Tag Efficiency.

5.11 Monte Carlo $e^+e^- \rightarrow e^+e^-\mu^+\mu^-$ Tagged cross-sections.

5.12 Experimental X^+X^- mass spectrum with a pion mass hypothesis. Range .8 - 1.3 GeV. Cosmics and beamgas events have been removed.

5.13 Experimental X^+X^- mass spectrum with a pion mass hypothesis. Range 0-3.5 GeV. Cosmics and beamgas events have been removed.

5.14 P_{\perp} spectrum for Data and MC events (the latter have been selected by a trigger simulation program).

5.15 $f \rightarrow \pi^+\pi^-$ CMS $\cos\theta$ distribution with QED background subtracted using Monte Carlo data simulating $\gamma\gamma \rightarrow e^+e^-, \mu^+\mu^-$.

5.16 X^+X^- CMS $\cos\theta$ distribution and QED background distribution estimated from Monte Carlo data.

5.17 Preliminary X^+X^- mass distribution with K mass hypothesis and dE/dX particle identification cuts. The more densely shaded regions correspond to more restrictive Kaon selection.

Figure 5.1 QED Box Diagram $\gamma\gamma \rightarrow \gamma\gamma$

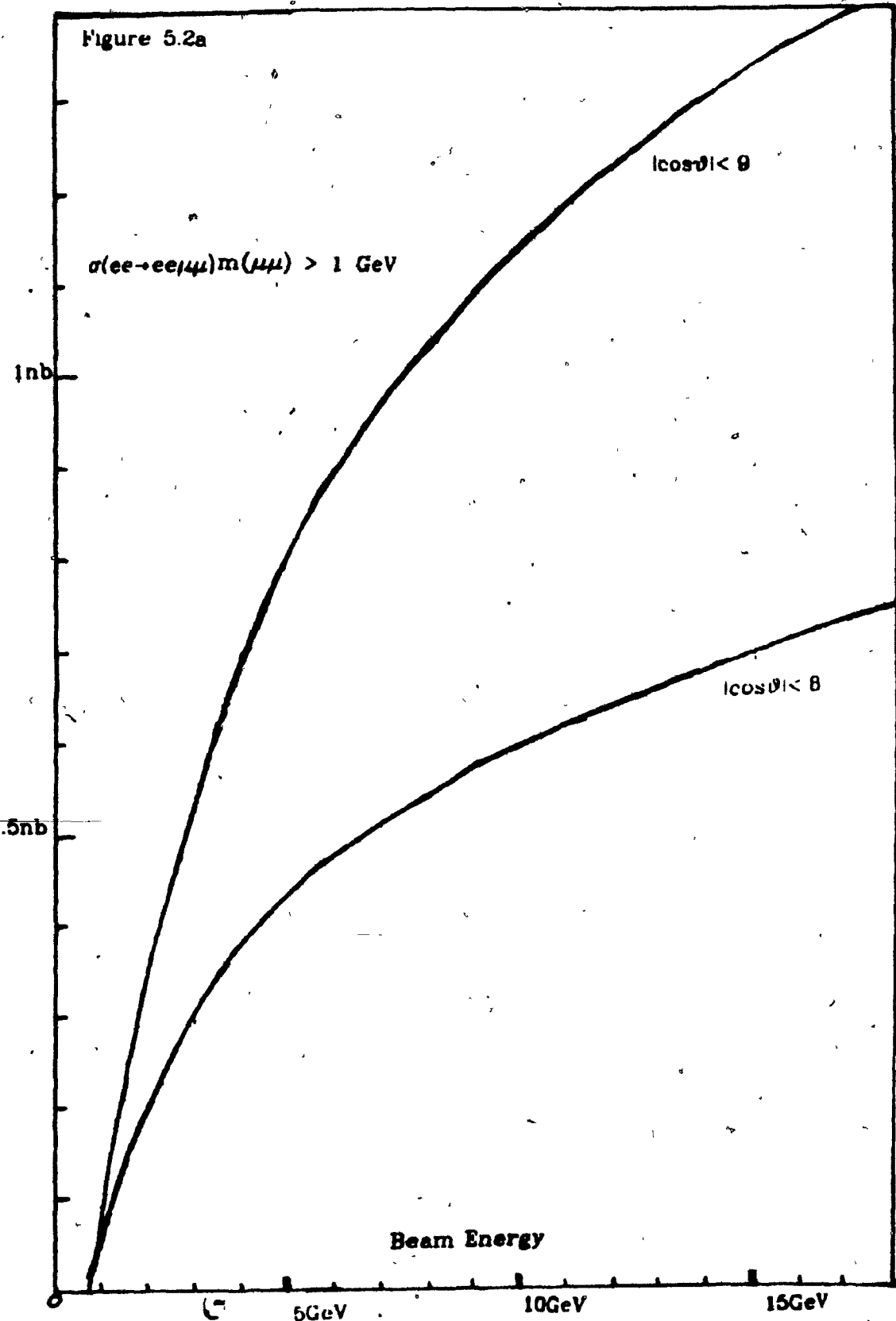
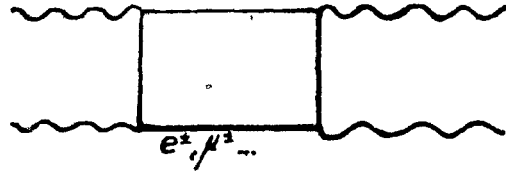


Figure 5.2b

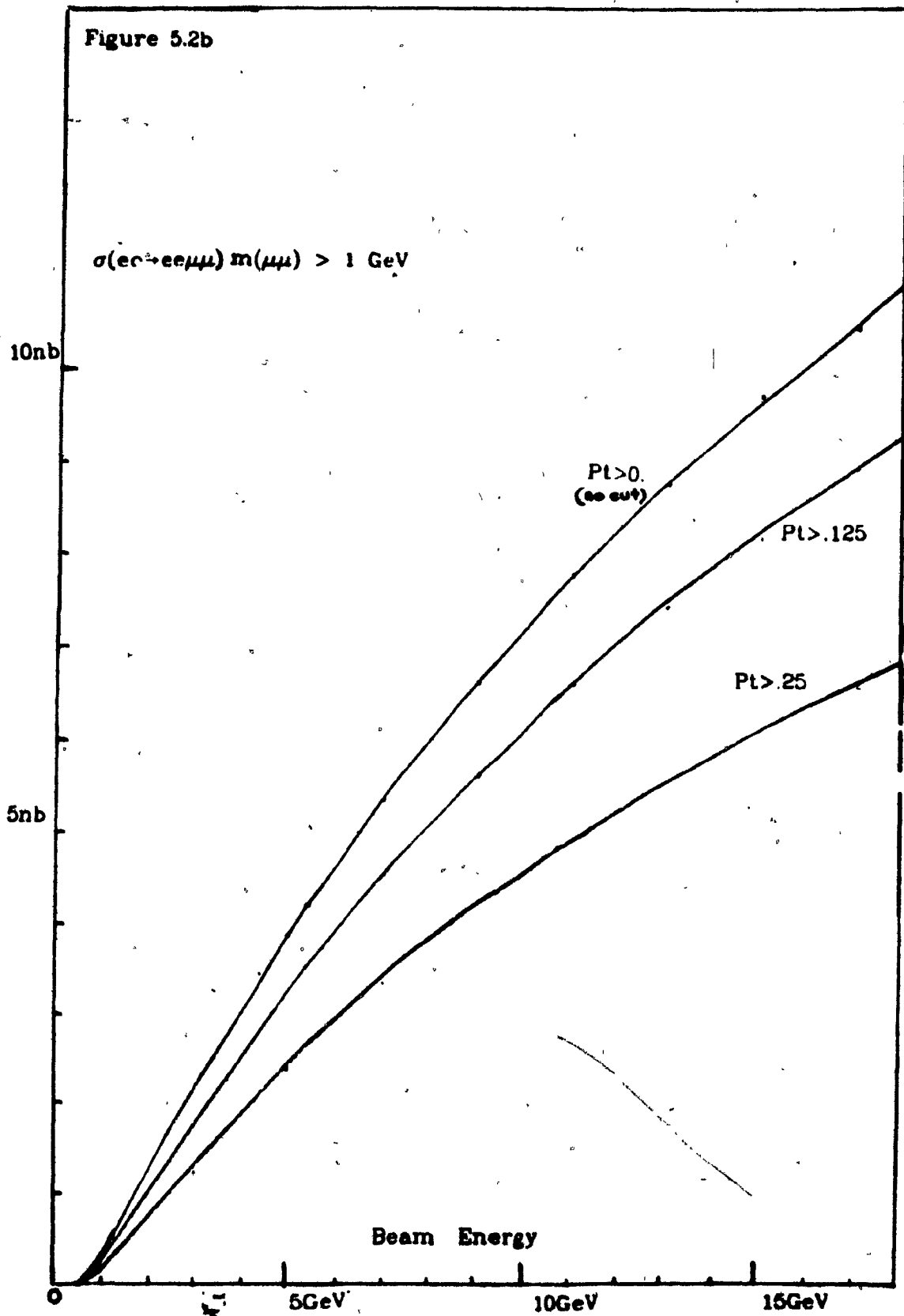


Figure 5.3 $e^+e^- \rightarrow e^+e^-l+l^-$

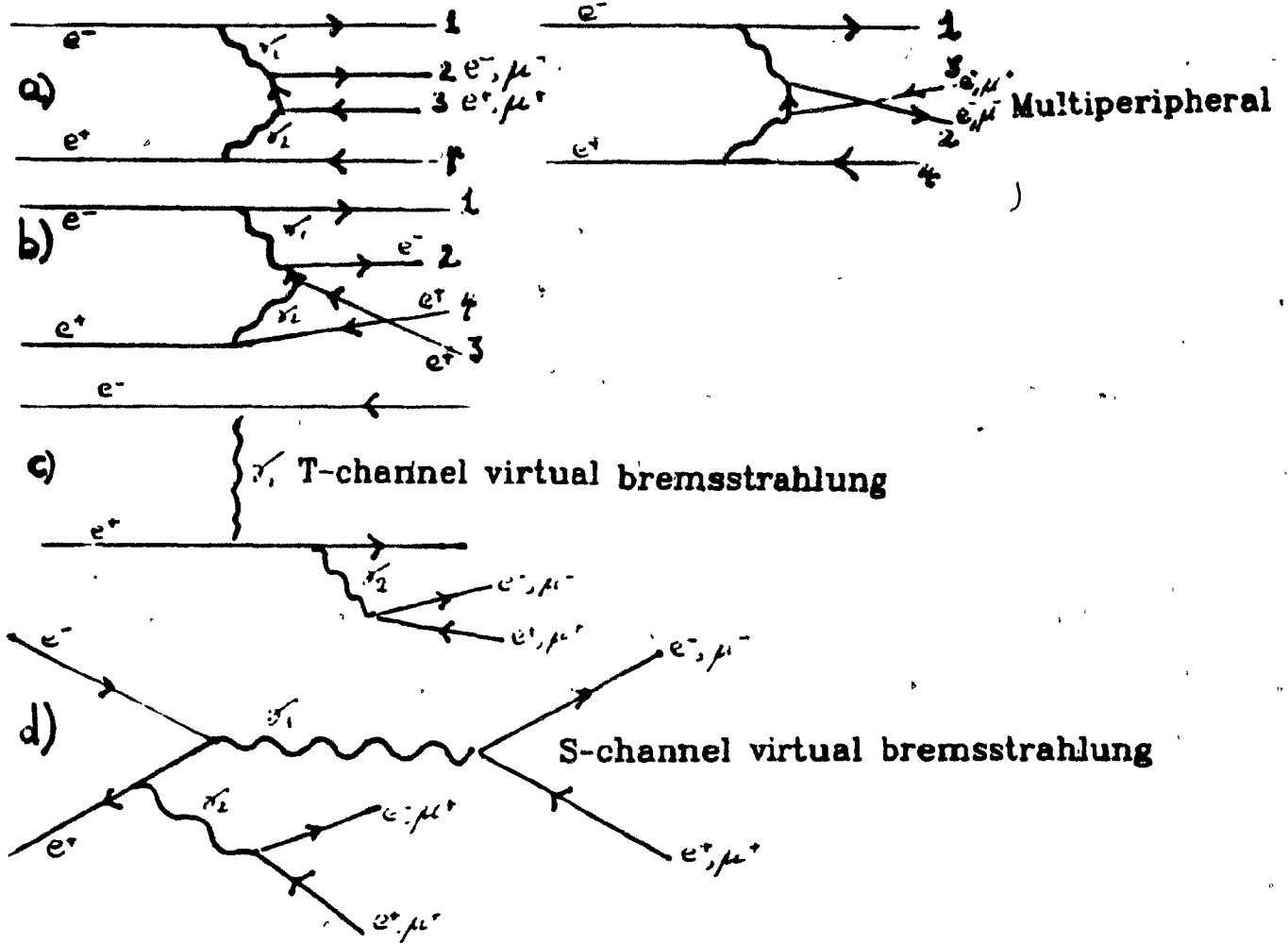


Figure 5.4

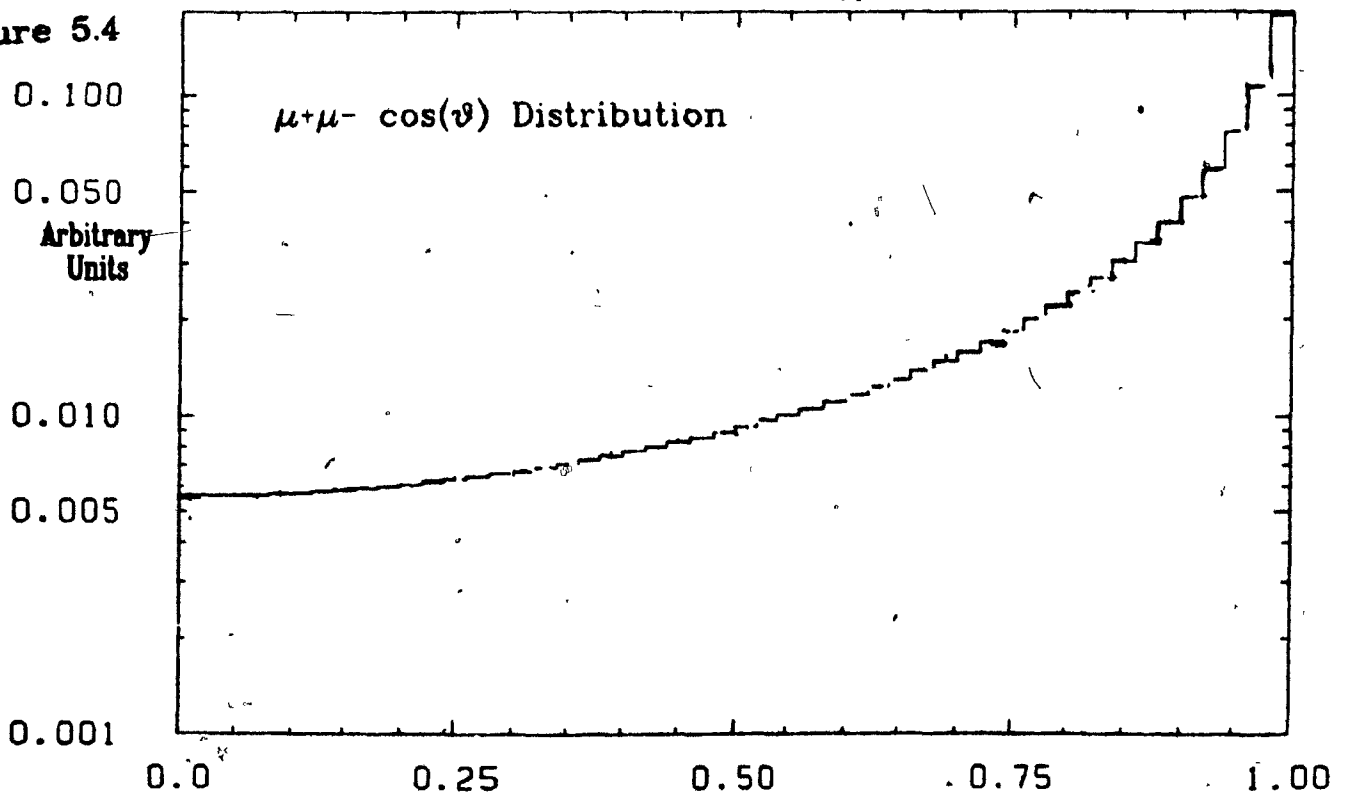


Figure 5.5

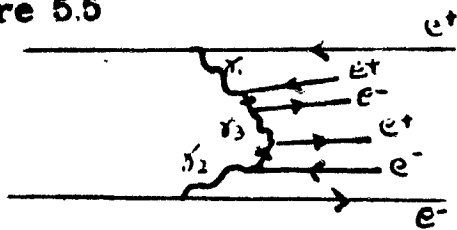


Figure 5.6 DCI Results

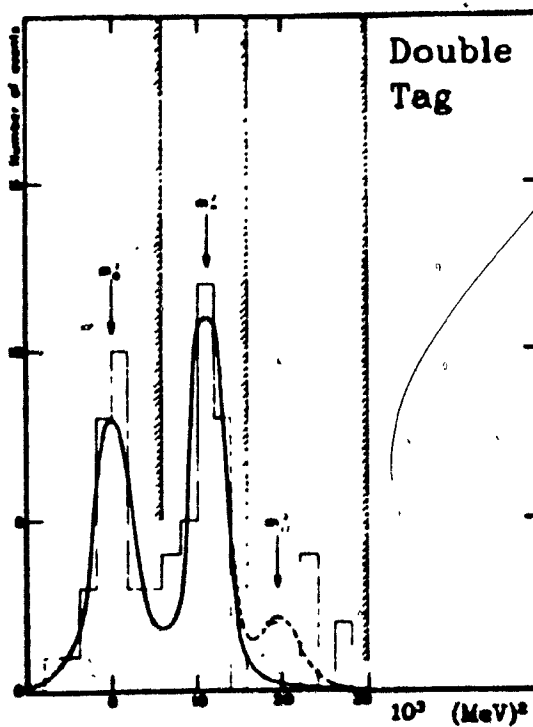
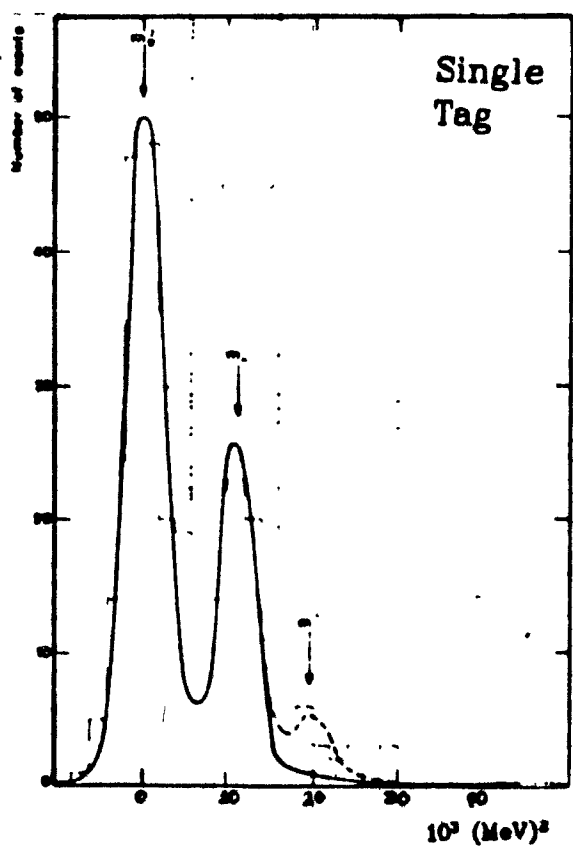


Figure 5.7

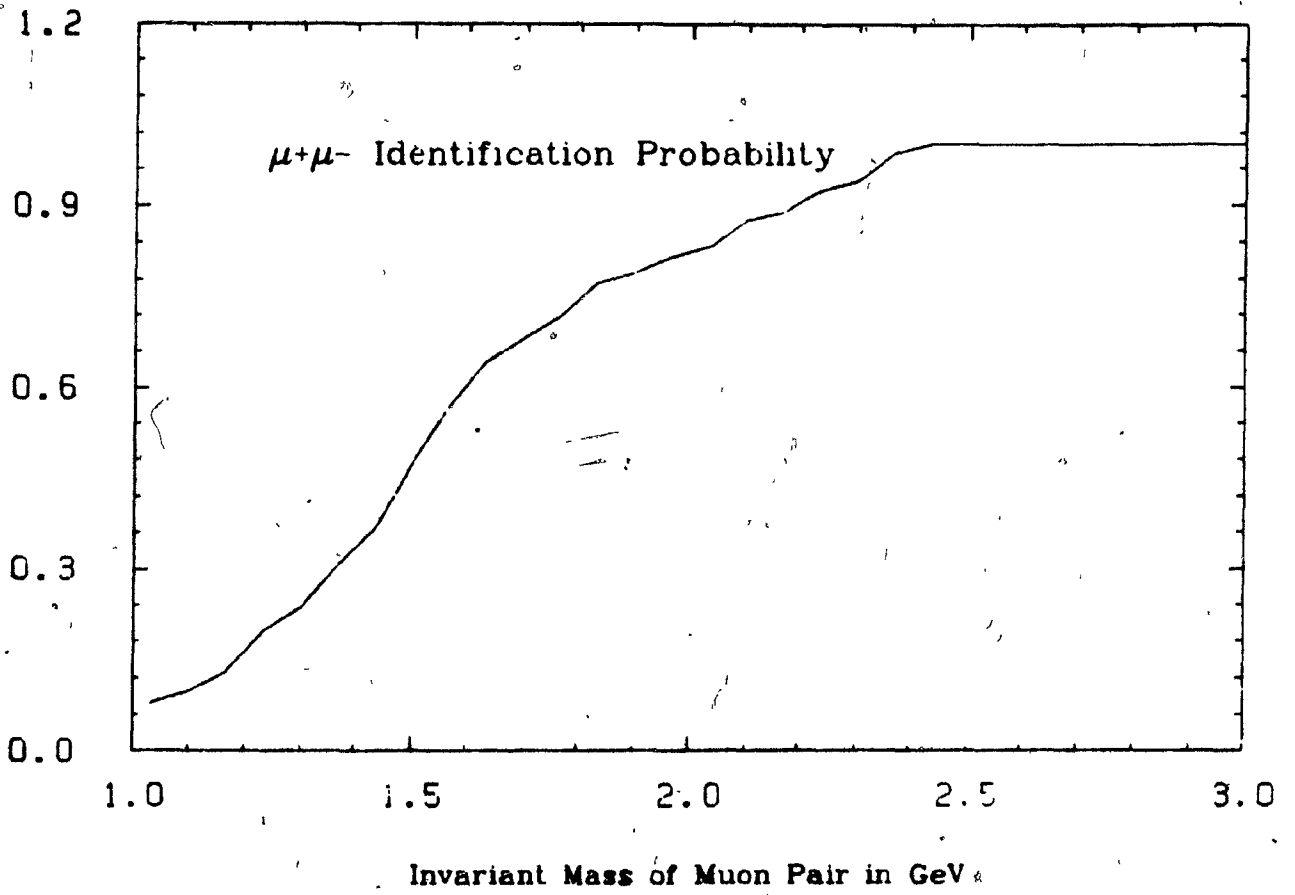


Figure 5.8

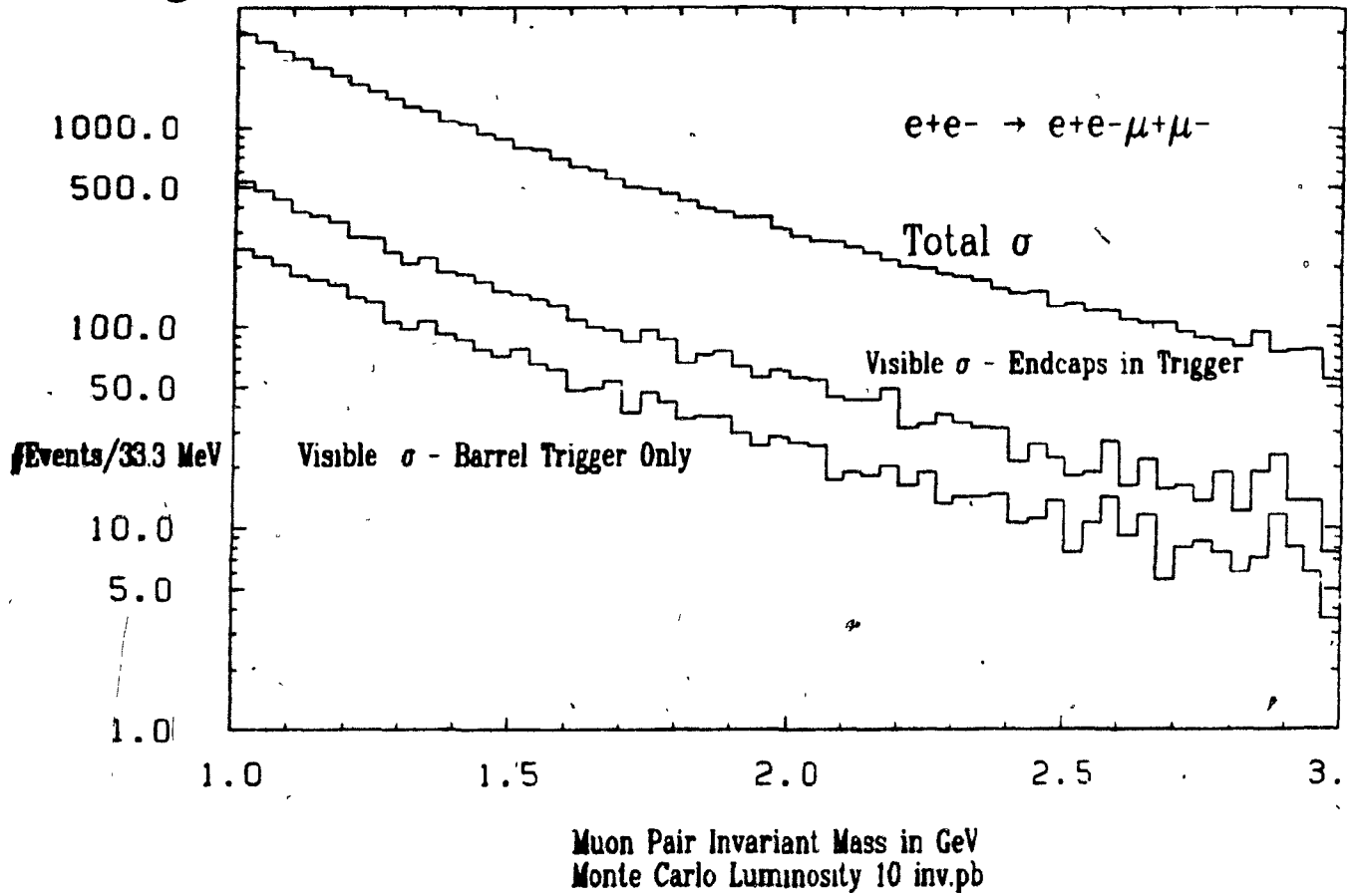
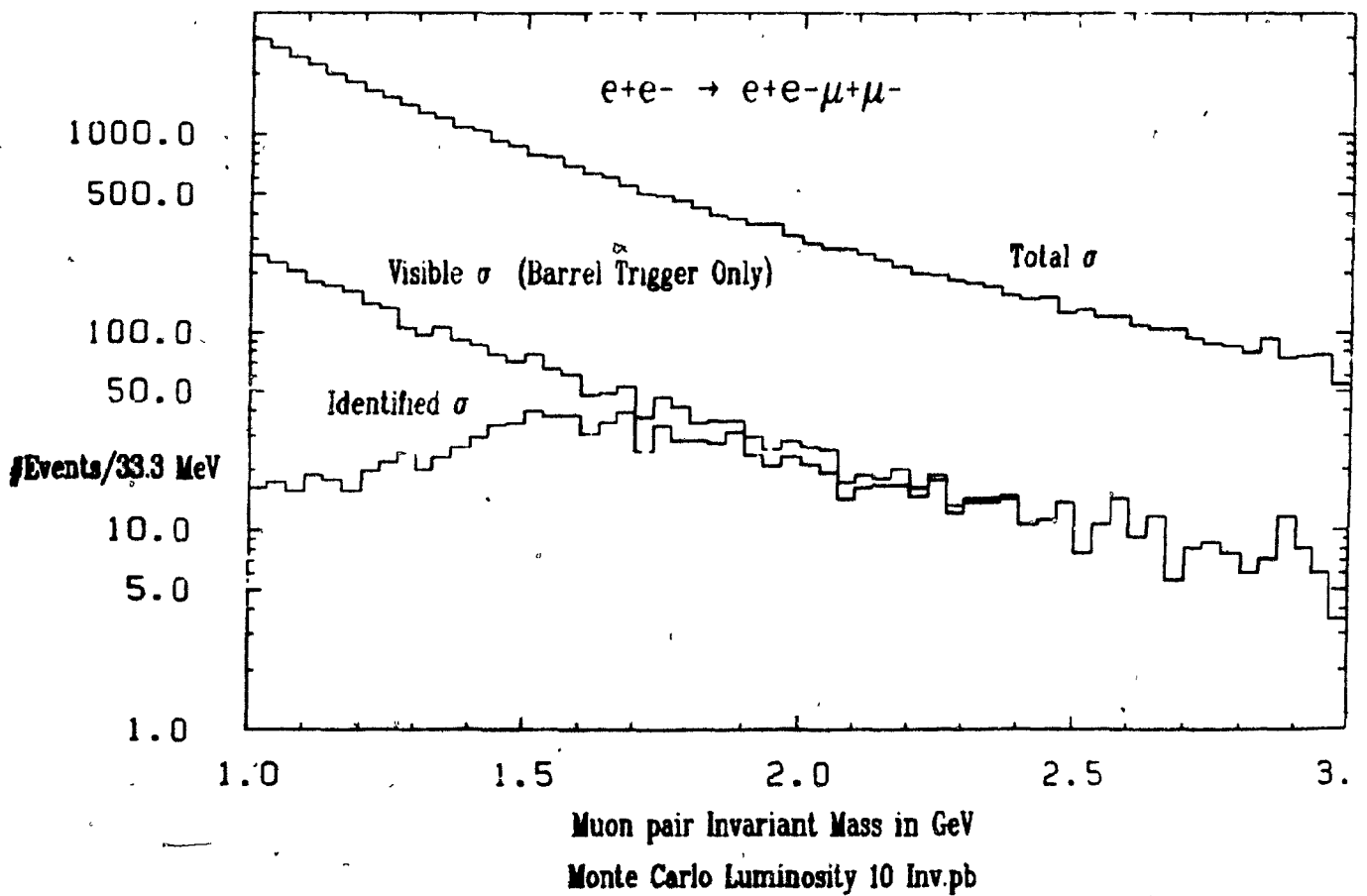


Figure 5.9



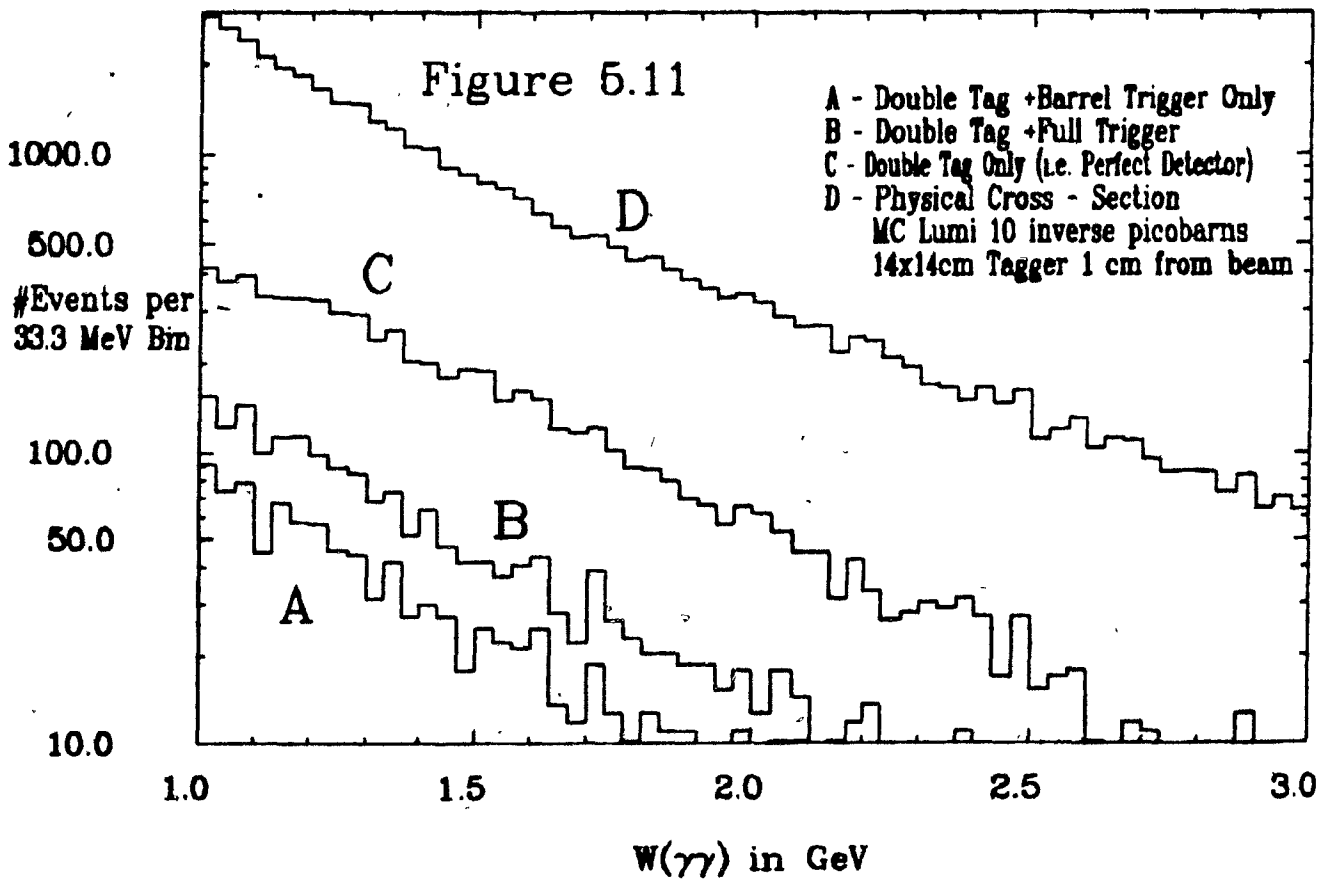
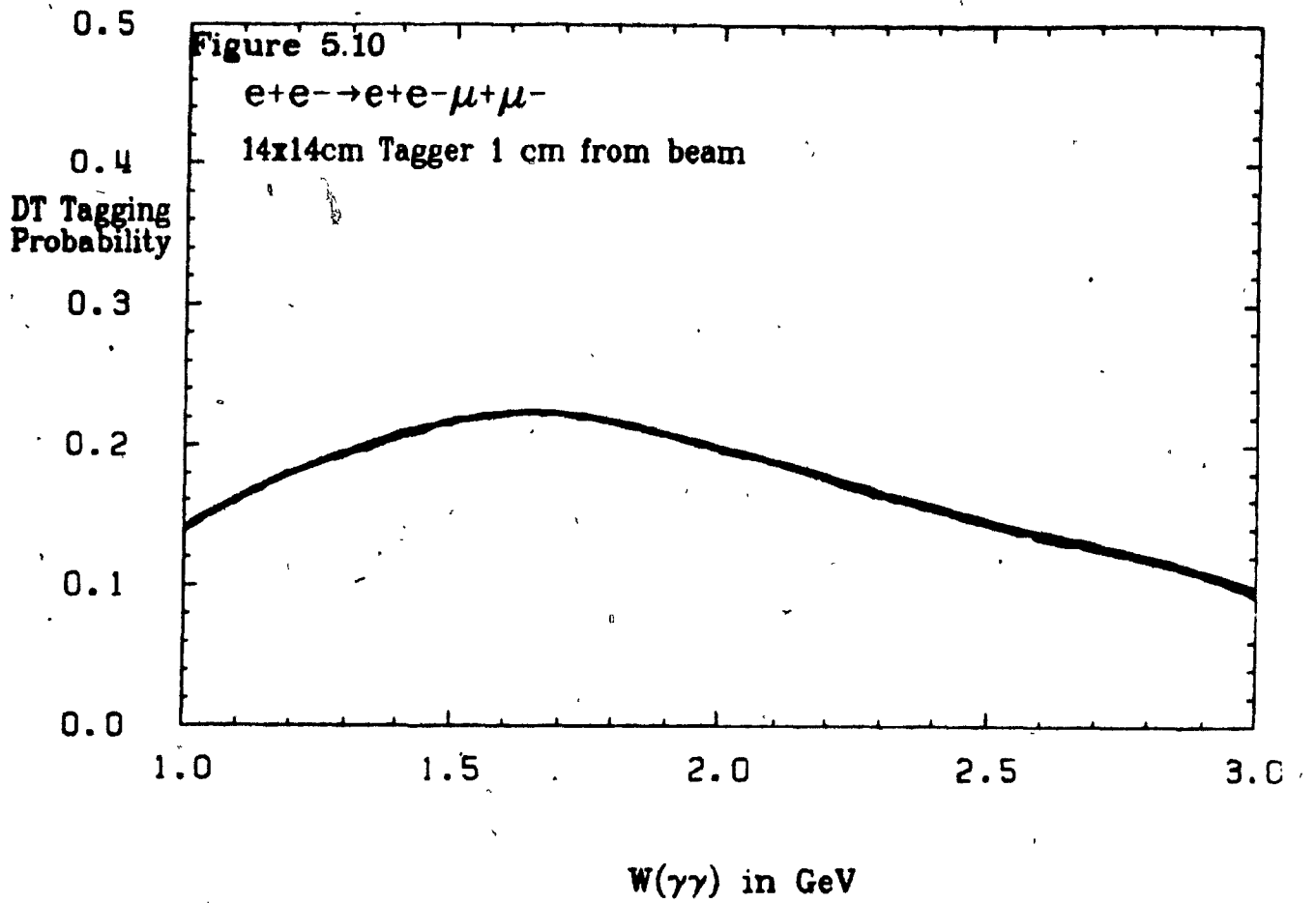


Figure 5.12

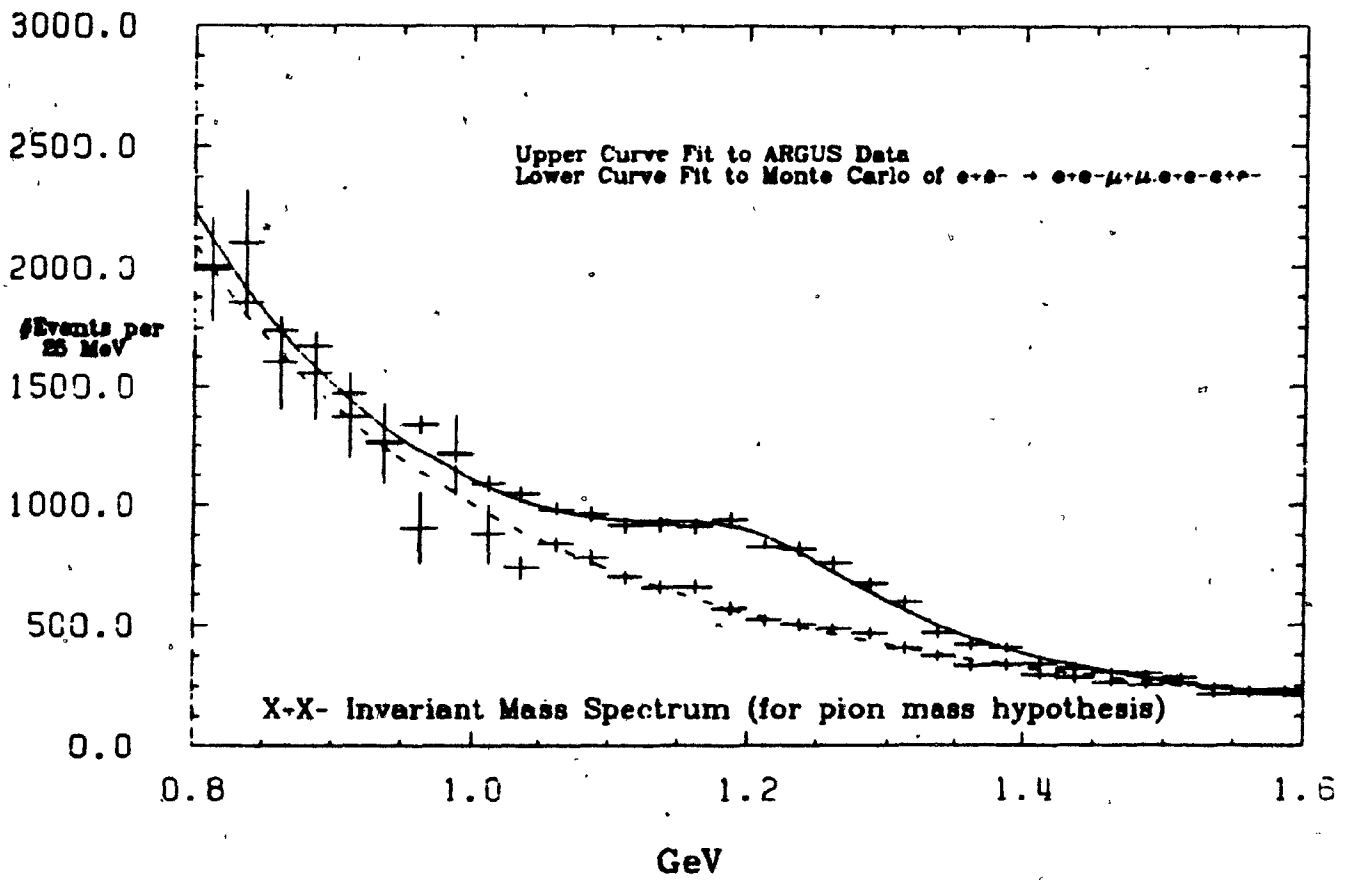


Figure 5.14

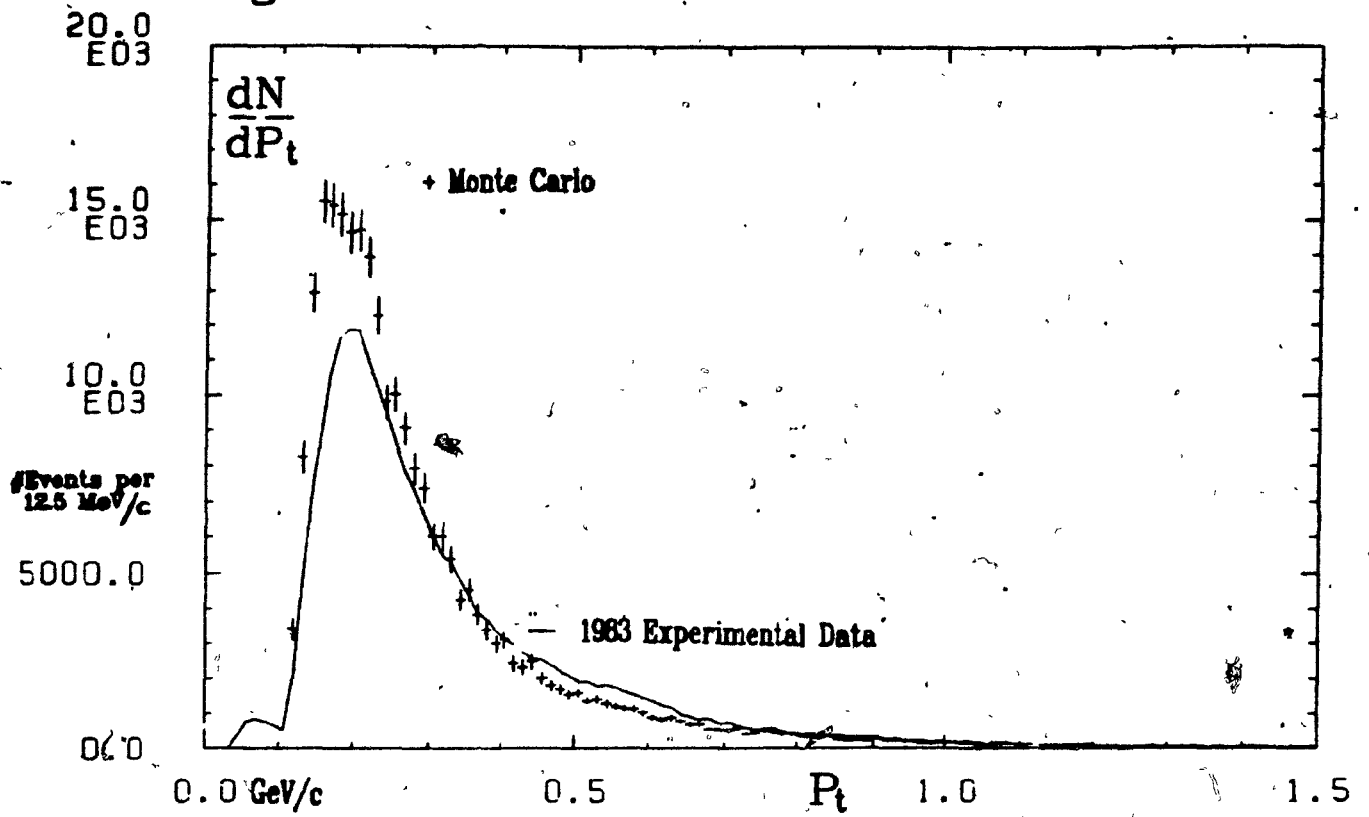
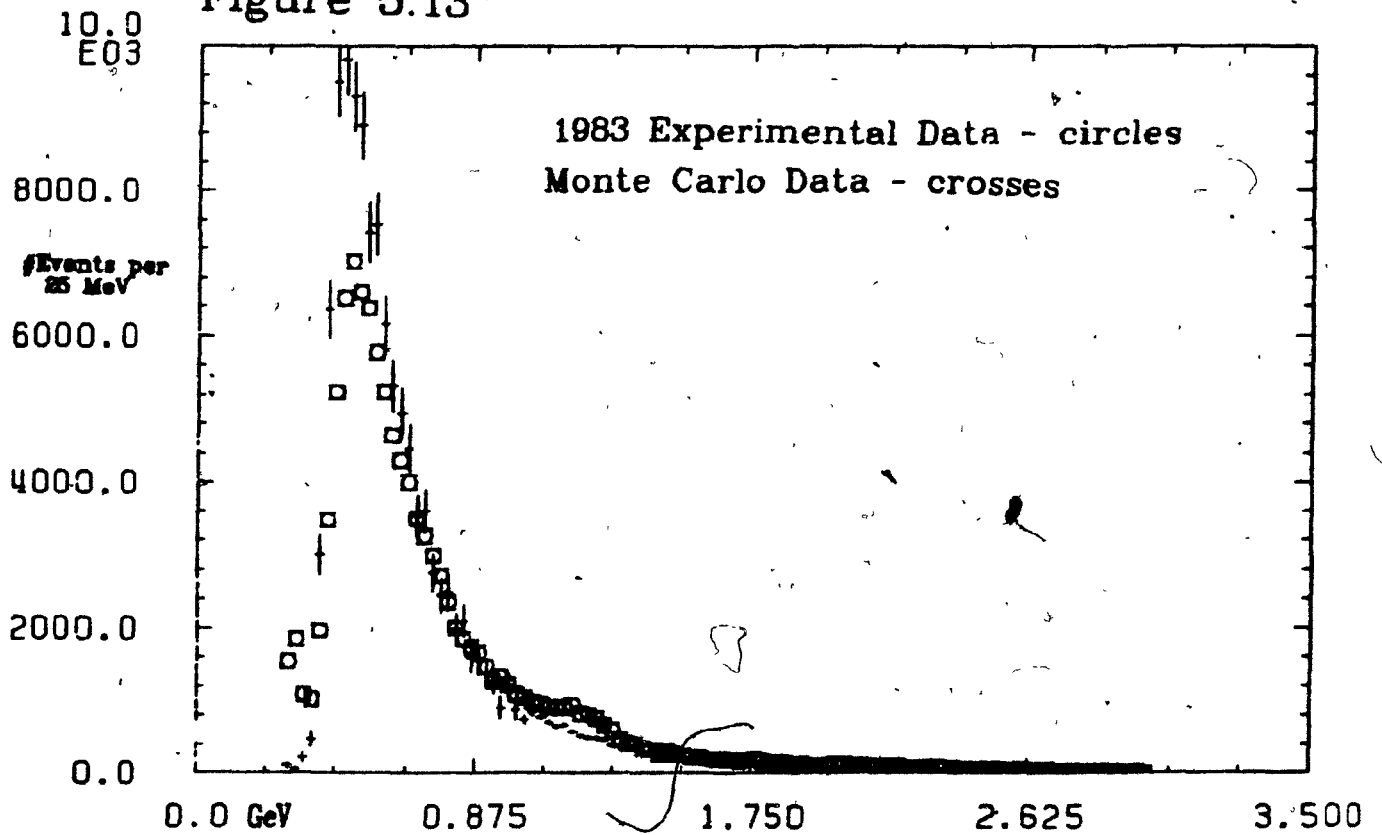


Figure 5.13



$X+X^-$ Invariant Mass Spectrum (for pion mass hypothesis)

Figure 5.15

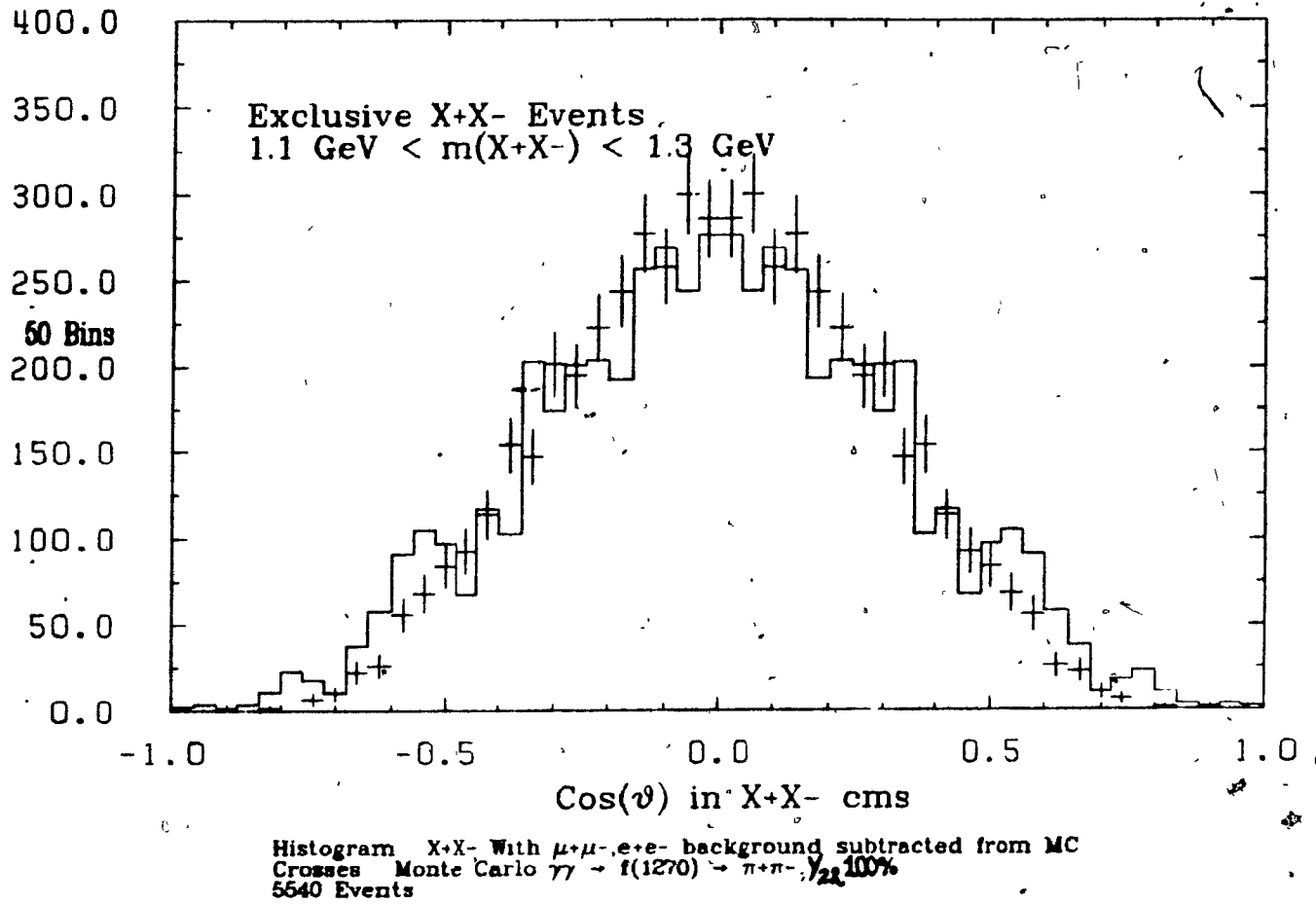


Figure 5.16

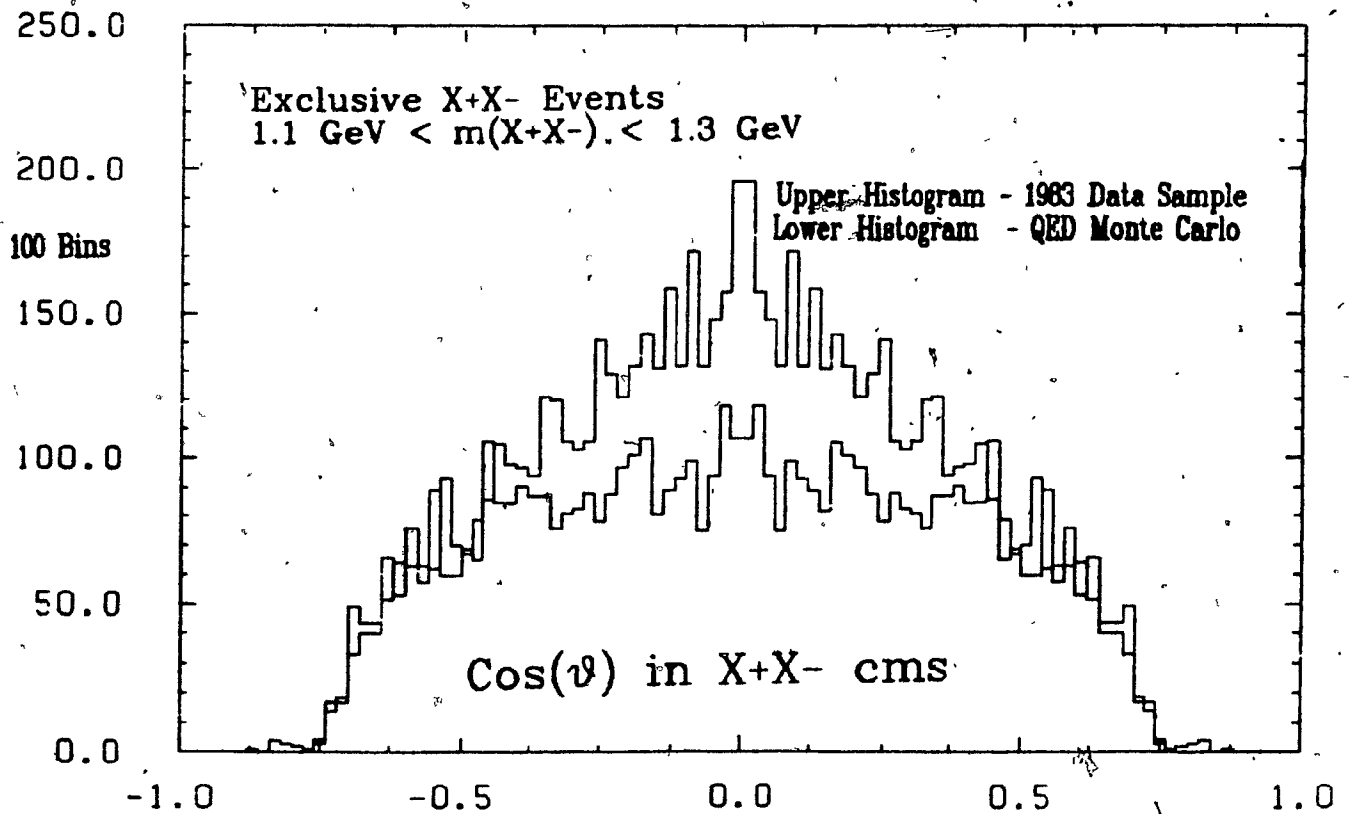
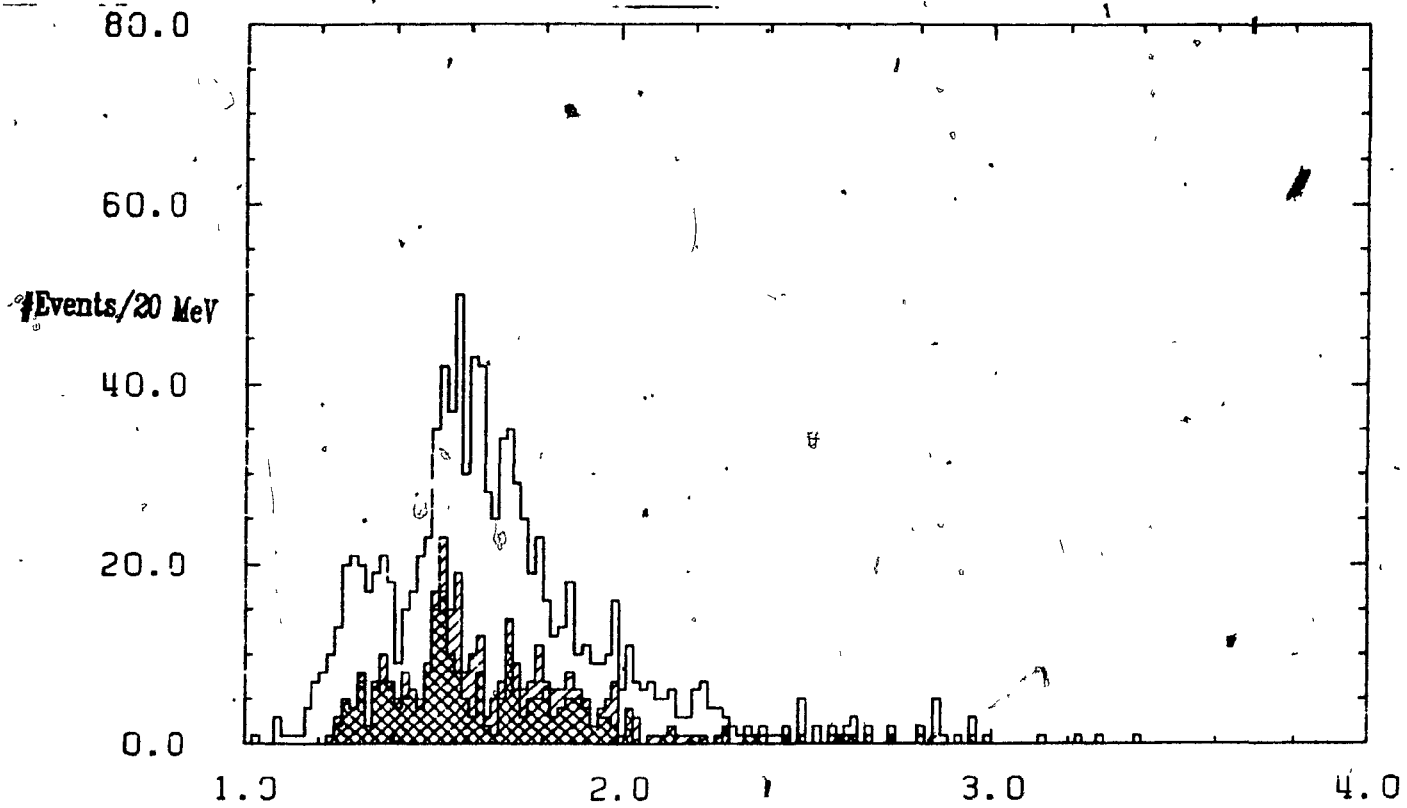


Figure 5.17



X+X- Mass Spectra (With Kaon Mass Hypothesis)
dE/dX: P(K+K-) > 1,5,10% for Histograms (in order of decreasing # of entries)

Chapter 6: Monte Carlo Studies of the Proposed Modifications to the ARGUS Detector and Prospects for the Measurement of The Total $\gamma\gamma$ Hadronic Cross Section

6.1 The ARGUS $\gamma\gamma$ Proposal : In 1982 the ARGUS Collaboration submitted a proposal⁶⁰⁶ to study $\gamma\gamma$ collisions at DORIS II. This was inspired by the unique opportunity provided by the synchrotron's architecture to measure the energies of particles emitted at small angles relative to the incident e^+ , e^- beams. This experiment will use two arrays of BGO shower counters - the "taggers" described in chapter four. The significance of this measurement lies in the opportunity to double tag two photon collisions (i.e. measure both of the scattered e^+/e^-) with a significant counting rate (on the order of 10% of the total $\gamma\gamma$ event rate). Previous experiments were limited by machine geometry to tagging at finite angles (Figure 6.1). The minimum tagging angle was determined by the beampipe size and the structure of the machine's magnetic lattice near the experiment. This drastically limited rates as the angular distribution for the scattered lepton in two gamma interactions falls as $\sim 1/(\theta^2 + \theta_0^2)$ where θ_0 is on the order of 10^{-4} radians. ARGUS has the only opportunity to tag the scattered e^+/e^- down to 0 degrees (provided the γ emitted by the tagged lepton is energetic enough - the threshold is 300 MeV if the tagger is 1 cm away from the beam). Given sufficiently accurate determinations of the e^+/e^- energies the invariant mass of the $\gamma\gamma$ system can be determined:

$$W_{\gamma\gamma} \approx 2\sqrt{(E_{Beam} - E_{e^+})(E_{Beam} - E_{e^-})} \text{ for } Q_1^2, Q_2^2 \sim 0 \quad (6-1)$$

The accuracy of the scattered lepton energy measurement is critical as the calculation of $W_{\gamma\gamma}$ magnifies the error in the e^+/e^- energies (Figure 6.2 shows error distributions of $W_{\gamma\gamma}$ as a function of the tagger energy resolution). A 1-2% tagger resolution is the maximum acceptable if one wants better than 10% $W_{\gamma\gamma}$ resolution. In addition, the resolution is worst for smaller invariant masses. The $W_{\gamma\gamma}$ resolution expected is plotted as a function of invariant mass for selected constant tagger resolutions in Figure 6.3.

The experimental advantage of double tagging lies in the ability to determine the $\gamma\gamma$ invariant mass without resorting to final state fragmentation models to unfold the effect of detector losses. Systematic uncertainties involved with this unfolding problem plagued the early single-tag analyses of the TASSO^{146,147} and PLUTO^{144,145} groups. This produced severe disagreement between the two detector acceptance corrected results at low $W_{\gamma\gamma}$. Uncertainties in detector/trigger acceptance and hadronic fragmentation contribute to large systematic errors for low invariant masses as there is more chance of feed down from

degraded high mass events. It was shown^{604,140} that the calculated shape of the cross-section at low invariant masses was almost completely dependent on the fragmentation model behind the $W_{had} \rightarrow W_{\gamma\gamma}$ unfolding. Even though the double tag technique avoids these problems, some fragmentation model for the hadronic final state is still necessary to determine the trigger acceptance. However, this calculation contains much less theoretical uncertainty, provided the experimental trigger is reasonably efficient. As discussed in the previous chapter, it is also expected that the offline data analysis at ARGUS can require a threshold of two charged tracks for a hadronic event without introducing too much error from QED subtraction. This increases the acceptance while decreasing the trigger uncertainty. This allegation is supported by the success in separating the $f(1270)$ signal. Previous experiments required a minimum of three particles (i.e. $\pi^+\pi^-\pi^\pm$ or $\pi^+\pi^-\gamma$) in the detector for a total cross-section measurement to avoid contamination from QED channels. For the modified ARGUS the problem of cross-section measurement will reduce to one of calculating trigger acceptances, trigger efficiencies, and unfolding the luminosity for the $\gamma\gamma$ collisions - calculating the rates for $e^+e^- \rightarrow e^+e^-\gamma^*\gamma^*$. Most of this information can be derived from the study of double tagged QED events, $e^+e^- \rightarrow e^+e^-l^+l^-$, $l = e, \mu$.

ARGUS is efficient at reconstructing low energy two photon events as it was designed to operate at lower energies than the detectors at high energy e^+e^- storage rings like PEP and PETRA which currently dominate experimental $\gamma\gamma$ physics. Two photon physics is the one area where the dynamics of the physics at DORIS and PETRA are similar - the higher beam energy of PETRA (~ 18 GeV) increases the $\gamma\gamma$ luminosity by a factor between 2 and 4 depending on the final state but a major portion⁶⁰⁷ of this increase usually goes into high CMS-rapidity regions of phase space for which there is poor acceptance (an impressive exception to this rule is the recent PLUTO⁶⁰⁶ analysis of exclusive two prongs events at low $W_{\gamma\gamma}$). Most of the extra $\gamma\gamma$ luminosity at higher e^\pm beam energies comes from events where one of the colliding photons has an energy greater than the DORIS beam energy. Using the following relations:

$$s \approx 4E_{\gamma_1}E_{\gamma_2} \quad (6-2)$$

$$\eta \approx \frac{1}{2} \ln \frac{E_{\gamma_1}}{E_{\gamma_2}}$$

and defining the extreme observable rapidity to be η_{Max} , i.e. $-\eta_{Max} \leq \eta \leq \eta_{Max}$, the following limits on the energies of the virtual photons contributing to observed events can be derived:

$$\frac{W_{\gamma\gamma} \exp(-\eta_{Max})}{2} \leq E_\gamma \leq \frac{W_{\gamma\gamma} \exp(\eta_{Max})}{2} \quad (6-3)$$

For a 1 GeV $\gamma\gamma$ CMS Mass and an $\eta_{max} = 1$, the γ energies of physically observable events¹ are limited

¹Monte Carlo rapidity distributions for hadronic events are shown in Figure 6.4.

to be between .13 and 1.36 GeV. Most of the extra γ luminosity available at high beam energies falls outside this range. For reference, Table 6.1² lists the total and visible cross-sections of two exclusive channels for the ARGUS detector if the e^\pm beam energies are 5 and 18 GeV. On examining this table it is worth remembering that for exclusive channel analysis PETRA detectors have used P_\perp thresholds of up to 400 MeV/c where ARGUS' present trigger P_\perp thresholds range between 125-250 MeV/c depending on the geometry of the event.³ The results given for the ARGUS $\gamma\gamma$ barrel trigger acceptances for 18 GeV beams are greater than one expects from a typical detector designed for this energy range. Figure 6.5 generalizes Table 6.1, displaying the total and visible cross-sections for a hypothetical 2^{++} $\gamma\gamma \rightarrow \pi\pi$ resonance, produced with helicity 2, as a function of mass ($\Gamma = 100\text{MeV}, \Gamma_{\gamma\gamma} = 2.7\text{keV}$). Clearly, PETRA can produce more luminosity for high $W_{\gamma\gamma}$ than DORIS. However, for low invariant masses phenomena (resonance physics and the Total Cross-Section measurement discussed here) DORIS is definitely competitive with other facilities.

Channel	CMS Energy	σ_{Total}	$\sigma_{FullTrigger}$	$\sigma_{BarrelTrigger}$
$\gamma\gamma \rightarrow f, A_2, f' \rightarrow K^+K^-$	36	.106nb	.018nb	.029nb
$\gamma\gamma \rightarrow f, A_2, f' \rightarrow K^+K^-$	10	.040nb	.010nb	.016nb
$\gamma\gamma \rightarrow f \rightarrow \pi^+\pi^-$	36	.99nb	.25nb	.39nb
$\gamma\gamma \rightarrow f \rightarrow \pi^+\pi^-$	10	.38nb	.13nb	.20nb

Table 6.1 MiniMC Acceptances for ARGUS at 10 and 36 GeV in the CMS

Unfortunately, the initial optimistic view of the total cross-section measurement did not survive detailed study. Serious challenges for both the technical and analytic sides of the experiment exist. Practical problems appear in maintaining a 1-2% tagger energy resolution for energies between 2-4.7 GeV over an extended running period. Several experimental background signals have to be understood. The first of these is small angle bremsstrahlung (SAB, Fig. 6.6) - these events produce a false tag rate on

² These results were computed with the $\gamma\gamma$ Monte Carlo used for the total hadronic cross-section calculations as described in the next section. For the channel $\gamma\gamma \rightarrow f, A_2, f' \rightarrow K^+K^-$ the final state is generated as suggested by the TASSO experiment¹⁰. The $\gamma\gamma \rightarrow f(1270)$ simulation follows that of MARK II¹¹.

³ Table 3.1 compares these parameters for the η' analysis of PLUTO, TASSO and ARGUS.

the order of 1 megahertz - which results in each tagger being hit by at least one SAB electron or positron every second beam crossing (the beam crossing frequency is close to 1 megahertz and Poisson statistics for the event distribution are assumed). This is sufficiently intense that given the 350 nanosecond fluorescence decay time for BGO there will still be a significant quantity (i.e. $O(1\%)$) of light emission from the array if an electron associated with a SAB event has hit it during the previous beam crossing - which is more likely to be the norm than the exception! In addition to technical problems like this one (and others such as the problem of radiation damage from the intense SAB counting rate) these SAB false tags occur so frequently that they form random coincidences with normal notag or single tag $\gamma\gamma$ events or annihilation channel events to produce false double tag events. The small angle taggers can therefore no longer be used to flag $\gamma\gamma$ events for triggers or analysis as at PETRA. These false double tag events produce a large combinatoric background to the measurement of the total cross-section. Various attempts at mitigating the effects of this phenomenon will be discussed in section 6.3.

The other major background processes are the α^4 QED processes discussed in chapter five. These channels have mixed benefits, on the one hand they are well understood theoretically and can be used as a check on our understanding of detector and tagger behaviour, while on the other they contribute a huge background that is not easily removed without introducing some uncertainty. It is questionable how important the advantage of a low topology threshold is as the analysis in chapter 5 showed that the $\pi^+\pi^-$ final state can almost entirely be attributed to $f(1270)$ production for $W_{\pi^+\pi^-} \geq 1$ GeV. It has also been suggested⁶⁰⁴ that the statistical final state simulations used for trigger acceptance calculations for high $W_{\gamma\gamma}$ (and in the next section) should not be applied to low invariant mass final states as these are dominated by coherent processes like resonance production. This point of view implies that the simulation of low mass final states can only be done in a full partial wave acceptance analysis for individual exclusive topologies. An unambiguous application of this technique would require an immense experimental luminosity as it requires each topology to be fully reconstructed with enough statistics to determine the partial waves involved.

6.2 Hadronic Acceptance Calculations : The purpose of hadronic event simulation is to determine if a reasonable signal level can be expected from the experiment. The major factor limiting counting rates is the double tag efficiency which varies between 5% and 15% depending on the exact tagger geometry chosen and the synchrotron running conditions. With fixed detector geometry, this rate is determined by initial state kinematics and should not depend on the final state produced except via $W_{\gamma\gamma}, Q_1^2, Q_2^2$ (the mass of the $\gamma\gamma$ system and the individual photons respectively, $Q_i^2 < 0$), and the photon helicities - as discussed in Appendix 1. The average Q^2 of $\gamma\gamma$ events at ARGUS would be .33 GeV², assuming no Q^2 dependence of the final state cross-section, if the taggers each had a perfect 4π acceptance. The Q^2 measured by the proposed taggers is expected to average $2 \cdot 10^{-4}$ GeV². This limited range is in one of the most luminous regions of Q^2 but it is expected to include little variation in the hadronic cross-section. Previous measurements of the Q^2 dependence of the final state cross-section support the GVDM model where the cross-section changes significantly only for $\sqrt{-Q^2}$ on the order of a vector meson mass (i.e. .769 GeV for the ρ meson). Indeed, the tagging acceptance of PLUTO¹⁴⁶ limited the Q^2 to be large enough ($\langle Q^2 \rangle \sim .44$ GeV², $.1 \leq Q^2 \leq 1.$ GeV²) so that the extrapolation back to $Q^2 = 0$ to obtain the hadronic cross-section for real photon collisions was nontrivial. The only critical question in the acceptance estimate is the range of $\sigma(W_{\gamma\gamma}, Q_1^2 = 0, Q_2^2 = 0)$ chosen - which is, after all, what we plan to measure. The different forms of Q^2 dependence expected, at most, introduce a variation of 20% of the estimated total visible cross-section while the tagged cross-section changes little. Using different published measurements or theoretical estimates of the $W_{\gamma\gamma}$ dependence can produce variations of 400% in the visible cross-section estimate! For these reasons we have chosen to use two extreme input cross-sections for the analysis and to largely ignore the possible Q^2 variation.

$$\begin{aligned} \sigma(\gamma\gamma \rightarrow \text{hadrons}) &= 300 \text{ nb} \\ \sigma(\gamma\gamma \rightarrow \text{hadrons}) &= .97(240 \text{ nb} + \frac{270 \text{ GeV nb}}{W_{\gamma\gamma}}) + \frac{2250 \text{ GeV}^2 \text{ nb}}{W_{\gamma\gamma}^2} \end{aligned} \quad (6-4)$$

The first of these represents the asymptotic limit expected from factorization i.e. it was derived from the relative magnitudes of $\gamma p, pp$ hadronic cross-sections. The various theoretical estimates of this vary about 40% around the value given here. The second of these is the PLUTO result and represents an upper limit of available estimates. Of course, it is the lower limit available that should be considered in deciding the viability of the experiment.

Since the major rate limitation arises from the tagger acceptance the results of the simulation should depend weakly on the fragmentation model chosen - i.e. the specific fragmentation model used is not

of paramount importance so long as it is physically reasonable. Indeed, it is not possible to progress much beyond this level as there is still little known about $\gamma\gamma$ phenomena. When one is actually doing the calculations required to extract the cross-section from data, more care must be taken - the technique generally used is to tune the various control parameters of whatever model is chosen to distributions in the observed data via Monte Carlo analysis. The distributions chosen for the tuning shouldn't depend on $W_{\gamma\gamma}$. For example, one might tune the fragmentation to give the correct inclusive particle P_{\perp} and multiplicity distributions for each tagged $W_{\gamma\gamma}$ bin. The main problem with the PLUTO and TASSO analyses was that when unfolding $W_{vis} \rightarrow W_{\gamma\gamma}$ it was necessary to implicitly sum over a range of $W_{\gamma\gamma}$ for any "calibration" distribution as this is an unknown in their analysis. This leads to a "self-fulfilling prophecy" - the derived cross-section is strongly dependent on the fragmentation model no matter how carefully the parameters are adjusted. If $W_{\gamma\gamma}$ is known from double tagging the systematic error can be estimated by varying the fragmentation parametrization so that the results still agree with the observed data within errors and observing the change in the calculated $\gamma\gamma$ cross-section. The dependence of the $W_{\gamma\gamma}$ variation found on the final state fragmentation model is decoupled in a double tag measurement. It was decided that our investigations should use a combination of fragmentation models employed by the PLUTO group in their original analysis (C. Berger⁶⁰¹) and adjusted to the distributions they had observed. The resulting model is based on "limited P_{\perp} phase space" fragmentation:

$$\begin{aligned} \frac{dN}{dP_{\perp}^2} &\sim e^{-6P_{\perp}^2}, 75\% \text{ of events} \\ \frac{dN}{dP_{\perp}^2} &\sim e^{-P_{\perp}^2}, 25\% \text{ of events} \end{aligned} \quad (6-5)$$

This implies that the emission of particles with high momentum transverse to the $\gamma\gamma$ collision axis is suppressed - the hadronic "fireball" tends to decay into two jets following the direction of the incident particles. This view is based on the VMD (Vector Meson Dominance) model of the hadronic interactions of photons. This view naturally leads to a limited P_{\perp} phase space fragmentation as in "soft" hadronic interactions the colliding hadrons tend to pass through each other - disrupting in the process. As vector mesons are bound states their constituents must have P_{\perp} less than half the vector meson mass. If the collision occurs between unbound quarks in the photon structure the available P_{\perp} can be higher. The limited P_{\perp} phase space description agrees reasonably well with data (Figure 1.15) until fairly high P_{\perp} regions where evidence for the quark content of a photon exists in the form of a slower decrease in the inclusive $\frac{d\sigma}{dP_{\perp}^2}$ distribution, characteristic of processes involving pointlike particles. The refined analysis recently published by the PLUTO collaboration⁶⁰² uses an isotropic phase space below $W_{\gamma\gamma} = 3$ GeV

with a limited P_{\perp} phase space gradually mixed in until 90% of the Monte Carlo events above 5 GeV are generated with a limited P_{\perp} phase space algorithm. This represents the decreasing influence of the initial state as incident momenta decrease - annihilation at rest should have a completely isotropic final state. As the photons in $\gamma\gamma$ collisions are emitted almost collinearly to the beams the $\gamma\gamma$ axis is almost parallel to the experiment's axis. Due to this a limited P_{\perp} phase space tends to concentrate the generated hadrons towards the beampipe decreasing the calculated acceptance. Our fragmentation model is therefore conservative and we expect a slightly higher acceptance if the new results of the PLUTO collaboration are applicable at DORIS. It is important to realize that the calculations here are not supposed to duplicate the phenomena, an impossible task, as they are not well known. Rather the emphasis has been on producing a safe lower limit on the visible cross-section.

The next element of the fragmentation algorithm is the exact particle composition of the final state in each event. A great deal of effort by the theoretical community has been concentrated on fragmentation models for e^+e^- annihilation events based on various QCD analyses (LUND, Field-Feynmann etc.). These do not really apply to $\gamma\gamma$ phenomena as they are based on the fragmentation of specified parton states where $\alpha_s \ll 1$ which eventually fragment into states where the perturbative treatment becomes invalid. Various phenomenological models⁶⁰³ have been developed to provide the final fragmentation into mesons. This type of fragmentation model would clearly be the most desirable for a full simulation as they are matched to data in low energy e^+e^- or hadron collisions. To save time a much simpler model was chosen - again in a conservative spirit. In this simulation the final state consists only of pions as there is little data available on inclusive spectra of heavier particles in $\gamma\gamma$ collisions. The multiplicity distribution is parametrized as:

$$\frac{dn}{dW_{\gamma\gamma}} = 2.2\sqrt{W_{\gamma\gamma}} \quad (6-6)$$

based on measurements of e^+e^- annihilation. The actual multiplicity is generated with an algorithm based on KNO⁶⁰⁴ scaling. This phenomenon was first observed in high energy hadronic collisions and is based on the observation that the multiplicity distribution expressed as a function of the fraction of the mean multiplicity is almost independent of energy and initial state. Unfortunately, at the low CMS energies in which we are interested, the application of KNO scaling becomes rather suspect. The resulting multiplicity distributions (Figure 6.8) appear to underestimate the production of high multiplicity states. This is acceptable as it leads to a lower acceptance estimate.

It is assumed that the multiplicity distribution of neutrals is the same shape as that of charged particles and that the mean neutral multiplicity is half the mean charged multiplicity. Also, there can be no completely neutral events. This is reasonable as photons are expected to couple to charged states strongly (however one can point out that this is not the case for the vector mesons of VMD which couple to any strongly interacting particle). In the new PLUTO analysis the ratio of charged to neutrals is taken to be 2:1.3.

The final state fragmentation algorithm described above has been implemented in the same Monte Carlo program used to generate QED events for the miniMC/DEPA acceptance calculations of chapter 5. The $\gamma\gamma$ CMS parameters are generated according to equation 5-4. The exact α^4 calculation of L_{TT} , the luminosity for transverse photon collisions (see Appendix 1 or reference 119), is used but the other luminosity terms due to contributions of scalar photon collisions are ignored. Once the parameters of the $\gamma\gamma$ CMS are available the event is weighted according to the $\gamma\gamma$ cross-section selected (equation 6-4) and the final state is generated by the limited P_{\perp} phase space algorithm supplied by W. Wagner. The events are then passed to the beam-optics program to simulate tagger acceptance. In the last stage of simulation the events are either subjected to a full SIMARG detector and trigger simulation or are tested with the miniMC detector/trigger algorithms.

As a first result of these algorithms, the acceptances, with the fragmentation limited to various fixed event topologies, are displayed in Figure 6.9, while the averaged acceptances weighted with the $\gamma\gamma$ luminosity for events with $W_{\gamma\gamma} \geq 1\text{GeV}$ (this restriction is always in effect unless stated otherwise) are displayed in Table 6.2. The effect of several competing acceptance factors can be seen here. At low invariant masses high multiplicity channels may not have enough P_{\perp} to set a trigger while, geometrically, these events have more of a chance of having two charged tracks in the drift chamber. As one adds neutrals to the topology the acceptance at higher masses actually increases. Once there is sufficient P_{\perp} for the charged particles to reach the trigger, the presence of neutrals divides the P_{\perp} (Lorentz boost) of the $\gamma\gamma$ CMS amongst more particles - decreasing the focusing of the charged particles along the beams. At higher energies, the Lorentz boost of the $\gamma\gamma$ CMS and the limited P_{\perp} fragmentation algorithm tends to concentrate more of the events into the endcap region - decreasing acceptance. These two effects produce a peak in acceptance which moves to higher masses as more neutrals are produced. This effect is balanced by the increase in average multiplicity with $W_{\gamma\gamma}$ which produces a saturation effect - the

Topology		%Barrel Trigger	%Full Trigger
$\#\pi^\pm$	$\#\pi^0$		
2	0	5.7	16.0
2	1	11.9	24.2
2	2	12.9	25.6
4	1	42.9	72.4
4	2	34.2	63.3
4	3	39.7	68.7
4	4	30.6	56.4

Table 6.3 Acceptances for Fixed Event Topology

acceptance tends towards a constant value at high energies. This is evident in Figure 6.10 which shows the acceptance for hadronic events (with the full fragmentation algorithm) as a function of W_{77} for various charged particle thresholds and trigger arrangements.

Table 6.3 displays the results using the improved Mini-Monte Carlo with trigger simulation. The "Barrel Trigger" is the current ARGUS trigger arrangement while the "Full Trigger" includes the endcaps and VDC in the trigger allowing a much increased P_\perp and $\cos(\theta)$ acceptance. In addition to the Q^2 independent cross-section parametrizations there are some results for two parametrizations of the cross-section Q^2 dependence based on the GVDM or VDM propagators discussed in chapter 1. The visible cross-section then can be expected to range between .5 and 4 nanobarns. Current experimental results favor the lower end of this range.

The crucial component in the entire analysis is the trigger acceptance. To a great extent this is limited by experimental factors that are not calculable to any reliable extent. For instance, the closest distance of the BGO matrices to the beam is limited by transient factors relating to the quality of the beams which is a rather arcane function of the DORIS operators' experience and running history. There will also be some perturbation of the DORIS operation by the trigger and the associated vacuum chamber.

Monte Carlo	$\sigma_{\gamma\gamma}$	Total	Barrel Trigger	Full Trigger
Minimum	Flat	2.95nb	.75nb	1.25nb
"	Flat+GVDM	2.33nb	.55nb	.94nb
"	Flat+VDM	2.20nb	.51nb	.88nb
"	PLUTO	12.4nb	2.2nb	4.1nb
SIMARG	Flat	2.95nb	.82nb	1.4nb

Table 6.3 Hadronic Trigger Acceptances

It is expected that the taggers will be operated between 1 and 2 centimeters away from the beam orbit and tagging acceptances will be presented for these two extreme cases. Additionally, there were various plans for removing sections of the taggers to reduce the signal rate from the small angle bremsstrahlung channel. This geometry (Figure 6.19, referred to in Table 6.4 a,b as the "SAB Slit" tagging condition) was optimized to produce the highest SAB tag rejection while maintaining a reasonable $\gamma\gamma$ signal. All tagger acceptance calculations were done with a beam optics simulation program supplied by L. Jönsson of Lund University. The tagging probabilities for various situations are shown in Tables 6.4a,b for the constant $\sigma_{\gamma\gamma}$ and PLUTO $\sigma_{\gamma\gamma}$ parametrizations, respectively.¹ The two results differ only in the weight given to lower invariant mass states since the tagging rates are independent of final state for fixed $W_{\gamma\gamma}$ and no Q^2 dependence is included in the cross-section parametrization. Note that the acceptance for double tagged events is greater than that for untagged events as this restriction creates a strong $\pm Z$ symmetry limiting the rapidity of the $\gamma\gamma$ CMS.

The effect of using a Q^2 dependent cross-section was investigated and, as expected, no significant change in the double tag cross-section was found though the total visible cross-section did change (Table 6.5). This emphasizes another advantage of the proposed experiment - there is very little extrapolation to $Q^2=0$ required with our taggers. The tagger acceptance as a function of $W_{\gamma\gamma}$, Q^2 , E_γ , and the rapidity of the $\gamma\gamma$ CMS is shown in Figures 6.11-14.

¹In Tables 6.4a,b the notation ST,DT,NT refers to the tagging probability with no restriction on the observability of the $\gamma\gamma$ final state while ST*ARGUS(Full Trigger) refers to the tagging probability if the event is triggered upon.

Tagging Condition	1 cm from Beam	2 cm From Beam	SAB Slit
ST(single tag)	.405	.368	.142
DT(double tag)	.148	.070	.008
NT(no tag)	.447	.562	.850
ST*ARGUS(Full Trigger)	.454	.421	.171
DT*ARGUS(Full Trigger)	.173	.094	.010
NT*ARGUS(Full Trigger)	.373	.485	.819

Table 6.4a Hadronic Tagger Acceptances - Constant $\sigma_{\gamma\gamma}$, Systematic Error 10%

Tagging Condition	1 cm from Beam	2 cm From Beam	SAB Slit
ST	.381	.372	.140
DT	.167	.058	.007
NT	.452	.570	.853
ST*ARGUS(Full Trigger)	.461	.454	.188
DT*ARGUS(Full Trigger)	.231	.094	.012
NT*ARGUS(Full Trigger)	.309	.452	.800

Table 6.4b Hadronic Tagger Acceptances - PLUTO $\sigma_{\gamma\gamma}$, Systematic Error 10%

$\sigma_{\gamma\gamma}$ Parametrization	σ_{Total}	σ_{DT}			Visible σ_{DT}		
Distance From Beam:		1 cm	2 cm	SAB Slit	1 cm	2 cm	SAB Slit
Pluto $\sigma_{\gamma\gamma}$, no Q^2 dependence	12.35nb	2.06nb	0.71nb	0.091nb	0.94nb	0.39nb	0.048nb
Flat $\sigma_{\gamma\gamma}$, no Q^2 dependence	2.95nb	0.44nb	0.21nb	0.022nb	0.21nb	0.12nb	0.012nb
Flat $\sigma_{\gamma\gamma}$,GVDM Parametrization	2.33nb	0.44nb	0.21nb	0.022nb	0.21nb	0.12nb	0.012nb
Flat $\sigma_{\gamma\gamma}$,VDM Parametrization	2.19nb	0.44nb	0.21nb	0.022nb	0.21nb	0.12nb	0.012nb

Table 6.5 Comparison of Expected Double Tag $\sigma_{\gamma\gamma}$ Values

6.8 Monte Carlo Studies of Techniques for Small Angle Bremsstrahlung Background Rejection : The small angle bremsstrahlung process (SAB, Figure 6.6) has been known to be a serious background to 0 degree tagging for as long as the measurement was contemplated - virtually every mention of the need for 0 degree tagging in the literature is accompanied by a pessimistic comment as to its impossibility due to this background. The SAB process is described by the formula (calculated by A. Phillip, DESY):

$$\frac{d^2\sigma}{dx dy} = (2\alpha r_0^2) \cdot \frac{1}{x^2} \left\{ [(1+y^2) - y \cdot \frac{x^2}{x^2}] \ln(4y\gamma^2) + \frac{y}{1-y} [(1+y^2) - y^2 \frac{(y-3)}{(1-y)^2} \cdot \frac{x^2}{x^2}] \ln y - \frac{1}{2} \frac{(1+y^2)^2}{(1-y)^2} + 2y \frac{(1+y^2-y)}{(1-y)^2} \cdot \frac{x^2}{x^2} - \frac{x}{(1-y)^2} \frac{[(1+y^2) + 2y^2/(x(1-y))]}{[\frac{x}{y}(\frac{x}{y} + \frac{x}{1-y})]^{1/2}} \ln \left[\frac{1-x+y[\frac{x}{y}(\frac{x}{y} + \frac{x}{1-y})]^{1/2}}{1 + \frac{x}{y} + [\frac{x}{y}(\frac{x}{y} + \frac{x}{1-y})]^{1/2}} \right] \right\} \quad (6-7)$$

Where:

$$2\alpha r_0^2 = 1.16 \cdot 10^{-27} \text{ cm}^2 = 1.16 \cdot 10^6 \text{ nb}$$

$$x = \frac{1}{2(1-y)} (x^2 + (1-y)^2)$$

$$x^2 = \gamma^2 y^2 \tan^2 \theta$$

$$\gamma = \frac{E_{\text{Beam}}}{m_e}$$

$$y = \frac{E_{e^\pm}}{E_{\text{Beam}}}$$

$$\theta = \text{scattering angle of } e^\pm$$

$$dx = \frac{1}{2} \frac{1}{(1-y)} \gamma^2 y^2 \frac{2 \tan \theta}{\cos^2 \theta} d\theta$$

This can be integrated approximately to yield:

$$\frac{d\sigma}{dy} = \frac{2\alpha r_0^2}{1-y} \left[\frac{4}{3} y + (1-y)^2 \right] \left[\ln \left[4\gamma^2 \frac{y}{1-y} \right] - \frac{1}{2} \right] \quad (6-8)$$

This shows the $1/E_\gamma$ spectrum characteristic of bremsstrahlung processes. The angular distribution of the scattered e^+ or e^- behaves approximately as $d\sigma/d \cos \theta \sim 1/\theta^3$ (to be compared to the $1/\theta^2$ distribution of the scattered e^\pm from $\gamma\gamma$ collisions - the exact angular distribution is shown in Figure 6.15). The total cross-section for this process was calculated to be .167 barns with the restriction that the bremsstrahlung must have at least 200 MeV energy.¹ Of this $.11 \pm .01$ barns is tagged with the full 14cm x 14cm tagger 1 cm away from the DORIS beams. These results were calculated with a Monte Carlo generator based on equation 6-7 and the beam optics program used for the $\gamma\gamma$ tagging studies. Assuming a daily luminosity²

¹ The minimum lepton energy seen by the tagger is 4.7 GeV so a 200 MeV photon threshold leaves a good safety margin for edge effects when using Monte Carlo bremsstrahlung events generated with this restriction to calculate tagger backgrounds.

² This luminosity is rather greater than that taken by the experiment in normal running but experimental downtime and machine problems often lead to a reduced daily luminosity. The actual tagger rates are determined by the instantaneous machine luminosity $\sim 6 \cdot 10^{30} \text{ cm}^{-2} \text{ s}^{-1}$ which, assuming 24 hours of continuous operation, yields a daily luminosity of 600 nb^{-1} .

of 500nb^{-1} , an average of $.64 \pm .04$ Tagged SAB events are expected in each tagger every beam crossing (the beam crossing frequency is $\sim 1\text{MHz}$). This background produces a $\sim 50\%$ tagger occupancy - 50% of the DORIS beam crossings result in a tagger hit!

This is obviously a severe problem! It now becomes completely impossible to use the taggers as elements of the trigger. Even using the tagger information in the offline analysis is difficult as any tagger signal is confused by noise of the same order of magnitude as the $\gamma\gamma$ signal. The proposed technique for the removal of this background will be described in section 6.4. The true $\text{DT}_{\gamma\gamma}$ rate is reduced by $\sim 75\%$ by random coincidences with SAB events - i.e. 75% is lost by conversion into triple tags etc. The first solution proposed was the creation of a slit in the tagger to reject the SAB Events. This slit was to correspond to an angular cut of $\sim 1\text{mrad}$ and would reject most of the SAB tags. The tagger hit distribution from the Monte Carlo is shown in Figure 6.16b for the tagged e^\pm from SAB events, assuming divergenceless beams, it is clear why it was originally thought that most of the SAB tags could be rejected by a geometric cut - a narrow vertical slit in the tagger. It was originally claimed that this reduced the observed SAB rate by a factor of 100 while only reducing the $\text{DT}_{\gamma\gamma}$ rate by a factor of 10. However, as soon as the DORIS beam divergence is introduced into the calculation the SAB hit distribution spreads almost uniformly over the entire tagger (Figure 6.16c). The beam divergence parameters used were calculated by D. Barber of the DESY Machine group using a simulation of the DORIS beam optics that neglected the beam-beam interaction. This is a significant effect at DORIS and limits the machine currents to 35-40mA. It is believed that the results must, nevertheless, be representative of the actual situation as the calculation involved yields the correct machine luminosities. The beam divergence is strongly linked to the machine luminosity as this is determined by the mini β quadrupoles situated between the taggers and the experiment. These magnets focus the beam at the interaction point introducing an angular divergence which is the price of high machine luminosity. The beam divergence is worst in the horizontal plane as the size of the beam is increased by the emission of synchrotron radiation in the horizontal bending magnets.

The recognition of the importance of the beam divergence led to a modification of the slit. While the $\gamma\gamma$ tagging acceptance was changed little by the beam divergence, it soon became obvious that to attain the same SAB rejection factor as originally planned most of the BGO would have to be removed. The hit distributions, including beam divergence, were quite similar for $\gamma\gamma$ (Figure 6.16a) and SAB tags

	$E_{Beam} = 4.3 \text{ GeV}$	$E_{Beam} = 5.16 \text{ GeV}$
σ_X	0.60 mm	0.71 mm
$\sigma_{X'}$	0.75	0.90
σ_Y	0.014 mm	0.016 mm
$\sigma_{Y'}$	0.30	0.36
σ_Z	11.8 mm	15.8 mm

Table 6.6 DORIS Beam Parameters

$$X' = \frac{X}{2}, Y' = \frac{Y}{2}, \text{ evaluated at ARGUS}$$

$X, Y, Z =$ coordinates of beam.

(Figure 6.16b) so most partial tagger geometries lost almost as many $\gamma\gamma$ tags as SAB tags.¹ To design a new SAB rejection slit (while retaining some $\gamma\gamma$ signal), the width of the slit was adjusted so that the signal to noise was maximized for every 2 cm vertical layer of the tagger with the restriction that $\sim 10\%$ of the signal remain. The result is displayed in Figure 6.11 and all calculations of tagger acceptances with the "SAB slit" refer to this geometry.

Tables 6.7 and 6.8 list the results of Monte Carlo studies of random coincidences between SAB tags and $\gamma\gamma$ events. It is assumed that a $\gamma\gamma$ event can be identified from central detector information only - this ability has been demonstrated for the η' and QED experimental analysis described previously but it remains to be seen how clean an inclusive $\gamma\gamma$ event sample could be made. There are definite advantages to the low $\gamma\gamma$ mass regions (1-2.5 GeV) which we are interested in. Annihilation channel contamination is limited by the low mass and, of course, is at a minimum at the lower edge of the range. Unfortunately, $|\Sigma \vec{P}_\perp|$ cuts cannot be made as severe as in the analysis of exclusive channels but they are still of some use in separating incompletely reconstructed $\gamma\gamma$ events from degraded annihilation events. Beamgas contamination decreases at small invariant masses as the baryons from these events are slow and easily identified by dE/dX analysis.

¹Table 6.9 gives the probability of a tagged lepton hitting each block in the tagger for SAB and $\gamma\gamma$ tags.

The simulation of SAB/ $\gamma\gamma$ coincidences was carried out as follows:

- (1) Each $\gamma\gamma$ event was generated normally.
- (2) 1-7 Bremsstrahlung Events were generated for each tagger direction in a Poisson distribution, the only restriction on these events being that E_γ be at least 200 MeV. The calculated SAB cross-section with this cut was $.1673 \pm .0003$ barns. It was assumed that the specific luminosity was either 2.4 or $5.8 \cdot 10^{20} \text{ cm}^{-2} \text{ s}^{-1}$ (corresponding to a maximum daily luminosity of 250, 500 nb^{-1} respectively).
- (3) The $\gamma\gamma$ and SAB events were "tagged" independently and only those events with 1 hit in both taggers were included in the background estimate. It is assumed that any event with more than one hit in the same tagger can be separated by the unphysical (i.e. $\geq E_{B_{\text{tag}}}$) energy deposited or the good spatial resolution of the BGO matrix.

Situation	η_{Tagger}	$\eta_{\text{Trigger+Tagger}}$	S/N	S/N With Cuts	ζ	ζ With Cuts
250 nb^{-1} /day, 1 cm from beam	.173	.087	1.01	3.19	8.3	5.0
250 nb^{-1} /day, 2 cm from beam	.117	.063	.902	2.52	10.4	6.3
250 nb^{-1} /day, With SAB slit	.0115	.0064	1.94	5.20	22.0	16.1
500 nb^{-1} /day, 1 cm from beam	.164	.077	.423	1.34	11.2	5.3
500 nb^{-1} /day, 2 cm from beam	.136	.065	.357	.822	13.9	7.7
500 nb^{-1} /day, With SAB slit	.0162	.0081	.913	2.24	20.3	13.0

Table 6.7 SAB Background Contamination Analysis

The probability of any $\gamma\gamma$ event being double tagged (including true tags and SAB coincidence tags) is shown in column 2 of Table 6.7, while column 3 lists the tagger+trigger acceptance for various tagger arrangements. When the machine luminosity increases the double tag rate decreases as more of the $\gamma\gamma$ double tag events are converted to triple tag events etc. However, more $\gamma\gamma$ single tag and notag events are converted into false double tag events so the effects may cancel. Columns 4 and 5 list the $\gamma\gamma$ Signal

to SAB Noise Ratio, " α ", before and after cuts designed to reject the SAB coincidences. It is apparent from Table 6.7 that " α " will never be high enough to allow the SAB contribution to be ignored. It is necessary to subtract this background by constructing artificial random coincidences between Notag or Single tag $\gamma\gamma$ events and SAB tagger signals. If the artificial background sample is as abundant as the real background the statistical error in the subtraction will be $\sqrt{N_{\gamma\gamma} + 2N_{SAB}}$ (the fluctuations in the background and artificial background samples are independent, N_{SAB} is the number of background events). One can calculate the increase in statistical error introduced by the background subtraction. The "statistical error factor", ζ , referred to in Table 6.7 is defined by:

$$\begin{aligned}
 N' &= N_{\gamma\gamma} + N_{SAB \text{ false tags}} = \eta L \sigma_{\gamma\gamma} \\
 \alpha &= \frac{N_{\gamma\gamma}}{N_{SAB}} \\
 N_{\gamma\gamma}^* &= \frac{\alpha N'}{1 + \alpha} = \frac{\eta \alpha}{1 + \alpha} L \sigma_{\gamma\gamma} \\
 \Delta N_{\gamma\gamma} &= \sqrt{N' + N_{SAB}} = \sqrt{N' \frac{(2 + \alpha)}{(1 + \alpha)}} \quad (6-9) \\
 \zeta &= \frac{\Delta N_{\gamma\gamma}}{N_{\gamma\gamma}} \cdot \sqrt{\sigma_{\gamma\gamma} 250 \text{nb}^{-1}} = \sqrt{\frac{(2 + \alpha)(1 + \alpha)}{\alpha^2 \eta} \cdot \frac{250 \text{nb}^{-1}}{L}} \\
 \frac{\Delta \sigma_{\gamma\gamma}}{\sigma_{\gamma\gamma}} &= \frac{\zeta}{\sqrt{250 \text{nb}^{-1} \cdot \sigma_{\gamma\gamma}}}
 \end{aligned}$$

$\zeta = 1$ only for a perfect detector and tagger with no background and $250 \text{nb}^{-1}/\text{day}$ specific machine luminosity. Where η is the probability of finding a double tag signal (including false double tag background) if a $\gamma\gamma$ event is detected by the central detector multiplied by the probability of detecting a $\gamma\gamma$ event. ζ , is an independent measure of the experimental quality of each tagger arrangement. It represents the increase in the statistical error from that of a "perfect experiment" i.e. 100% trigger and tagger efficiency with no background. The value of ζ for various experimental situations is shown in Table 6.7 column 6, it is clear that there is no situation in which the presence of geometrically incomplete taggers is favorable - the gain in Signal to Noise obtained is not sufficient to balance the loss in statistics. Since a statistical subtraction is inevitable, the experiment should run with a high acceptance tagger. It is interesting to notice that, unless the SAB slit is implemented, the ζ factor increases with higher specific luminosity - the increase in statistics is overcome by the increase in background. This is important because the luminosity of the DORIS synchrotron is continuously improved. These results have been calculated as an average over all $\gamma\gamma$ masses using a flat $\sigma(\gamma\gamma \rightarrow \text{Hadrons})$. Due to limits in computer time consumption, results for individual $W_{\gamma\gamma}$ bins could not be calculated with significant statistics.

It is possible to reject SAB events without using a geometric cut on the tagger hits. As the event observed in the detector and the false tags arise from an entirely different e^+e^- collision occurring in the same bunch crossing, the false tag events frequently appear to be quite unphysical. For example, Figure 6.18a shows the total visible energy in ARGUS and the BGO taggers for true double tags and two classes of false double tags as generated by the SAB background simulation. It is apparent that a significant portion of the random SAB coincidences can be removed by appropriate energy cuts. Since small invariant mass $\gamma\gamma$ events have more energy in the taggers, and have a more limited amount of missing energy, the total energy distribution for these events will be narrower and the cuts can be tuned to yield a higher SAB rejection rate. It is not possible to cut too close above the e^+e^- CMS energy due to the finite resolution of ARGUS and the taggers. Cuts can also be made on the ratio of the invariant masses observed in the tagger ($W_{T_{ij}}$) and the detector ($W_{V_{ij}}$). Clearly this ratio should not exceed 1 by any significant amount.

The antitaggers (design to be used mainly as luminosity monitors) can also be useful. If a SAB event is tagged in the BGO matrices, there is a high probability for the bremsstrahlung in the event to hit the luminosity monitors (an "antitag"). An antitag does not immediately imply a SAB tag in the BGO as is possible for the photon from a bremsstrahlung event to be antitagged while the e^+ or e^- is untagged (especially if the SAB rejection slit is used) - this can associate SAB antitags with true $\gamma\gamma$ events. Since the bremsstrahlung spectrum in the antitagger goes to very low energies while the energy threshold for the taggers is introduced by the magnet optics it is possible for several low energy bremsstrahlung events from a single bunch crossing to create a false antitag signal. This effect has only been included in the simulation partially - the minimum photon energy is 200 MeV but simultaneous antitags of these photons to mimic a higher energy photon are possible. It may be possible to check if the energies of the suspect tags and corresponding antitags sum to the beam energy but the antitagger is not envisaged to have a good energy resolution as it will have to be "disposable" due to the high radiation flux from the bremsstrahlen. For these reasons it will be necessary to require a fairly high antitag energy to reject an event. QED events will be useful in investigating the effects of SAB rejection techniques using the antitaggers. In principle, the $\gamma\gamma$ -QED double tag and the SAB event are both fully constrained. Using this data it will be possible to determine the fraction of good events which are rejected by false antitagger signals together with the portion of SAB tags eliminated.

Depending on the spatial resolution achieved with the taggers, it may be possible to define the \bar{P}_1 of the system from the tagger information and demand a certain amount of correlation with the central detector value. This technique is used in high Q^2 single tag analysis with PETRA detectors but is much more difficult for small Q^2 tags.

Table 6.8 shows the effects of various cuts on the background contributions while column 7 of Table 6.7 shows the value of the statistical error factor after all these cuts have been applied. It is apparent that these cuts contribute most in experimental situations where the tagger is complete. Less improvement is possible in the situation where there is a slit in the BGO matrix. In particular, there is a definite $\gamma\gamma$ signal loss when one introduces the bremsstrahlen antitag cuts for the SAB rejection tagger. Note that the increase in the signal to noise ratio induced by the cuts listed in Table 6.8 is greater than that induced by the introduction of the SAB rejection slit! It is believed that the cuts used are conservative and a better result will be obtained once there are double tag QED data available for fine tuning.

As this simulation is very dependent on the details of the experimental arrangement (exact beam geometry, position of scrapers, beampipes etc.) it is essential that some experimental data be available before good estimates of the background rejection abilities can be made. A proposal for the construction of vacuum chambers and a "pre-experiment" with an incomplete BGO matrix to test the SAB distributions in the tagger and antitaggers was approved by the DESY PRC in October 1983.

$L(\frac{nb^{-1}}{fsy})$	D (cm)	Tag Type	Probability of Tag Type (%)	Offline SAB Rejection Cuts			
				(% of each tag type remaining after each cut)			
SAB Rejection Cuts:				$E_{Tot} \leq 10.4$ GeV	$E_{\gamma} \leq 1$ GeV	$E_{\gamma} \leq .5$ GeV	$\frac{W_{Vis}}{W_{Tag}} \leq 1.2$
250	1	<i>DT</i>	50	100	88	88	88
250	1	<i>ST * SAB</i>	39	61	41	35	33
250	1	<i>NT * SAB²</i>	11	39	15	10	10
250	2	<i>DT</i>	47	100	88	87	87
250	2	<i>ST * SAB</i>	42	78	44	35	35
250	2	<i>NT * SAB²</i>	10	64	29	16	16
250	SAB	<i>DT</i>	66	100	84	79	79
250	SAB	<i>ST * SAB</i>	29	77	47	31	31
250	SAB	<i>NT * SAB²</i>	55	75	36	23	23
500	1	<i>DT</i>	30	100	99	99	98
500	1	<i>ST * SAB</i>	46	64	38	32	29
500	1	<i>NT * SAB²</i>	24	40	20	17	16
500	2	<i>DT</i>	26	100	81	79	79
500	2	<i>ST * SAB</i>	50	80	51	44	44
500	2	<i>NT * SAB²</i>	24	60	23	15	15
500	SAB	<i>DT</i>	48	100	73	63	63
500	SAB	<i>ST * SAB</i>	42	74	42	27	26
500	SAB	<i>NT * SAB²</i>	10	65	26	23	23

Table 6.8
SAB Background Contamination Analysis
L=Luminosity, *D*=Distance of Tagger from Beam
D=SAB implies that the SAB Rejection Slit is used
E_γ = energy in antitagger

6.4 Statistical Subtraction of SAB Background : The statistical subtraction of false double tags is inevitable whatever the experimental situation. It is, therefore, presented here in some detail. The following notation will be used in the discussion:

- (1) 3 Tagging classes are considered. These are abbreviated by DT, ST, or NT representing Double Tag, Single Tag, and untagged events respectively.
- (2) DT , ST , and NT are the probabilities of a $\gamma\gamma$ event being in a given tagging class in the absence of any SAB background.
- (3) DT' , ST' , and NT' are the probabilities of a $\gamma\gamma$ event being in a given tagging class in the presence of the SAB background processes i.e. false tags included.
- (4) DT^* , ST^* , and NT^* represent the probabilities of a $\gamma\gamma$ event occurring in the specified tagging class and remaining there after the SAB background process is "turned on", i.e. a DT , ST or NT event which remains bremsstrahlen-free.

Assuming Poisson Statistics the probability of n single bremsstrahlung events hitting a tagger in one beam crossing is:

$$P_{SAB}(n) = n^n \exp(-n)/n! \quad (6-10)$$

where $n = \sigma \cdot L_{Crossing}$ is the average number of SAB events per bunch crossing. The occupancy rate (probability per beam crossing of ≥ 1 events in a tagger) for the SAB process is:

$$O_{SAB} = 1 - \exp(-n) \quad (6-11)$$

As mentioned above, for 500pb^{-1} a day luminosity, $n = .968$ for all SAB events in one hemisphere and $.64 \pm .04$ for those events with an electron hitting the tagger. These rates are for one direction only - the rates in each tagger direction are assumed to be independent. The average number of SAB events per beam crossing can be determined to good accuracy by looking at the taggers rates for Bhabha or annihilation channel events or by measuring the raw rates from the taggers with no trigger required in the central detector. The probabilities for the various types of double tags are:

$$\begin{aligned} DT^* &= P_{DT} \cdot (1 - O_{SAB})^2 = \frac{P_{DT}}{\exp(2n)} \\ ST \cdot SAB &= 2 \left\{ \frac{P_{ST}}{2} \cdot P_{SAB}(0) \cdot P_{SAB}(1) \right\} = \frac{P_{ST}n}{\exp(2n)} \\ NT \cdot SAB^2 &= P_{NT} \cdot P_{SAB}^2(1) = \frac{P_{NT} \cdot n^2}{\exp(2n)} \\ DT' &= DT^* + ST \cdot SAB + NT \cdot SAB^2 \end{aligned} \quad (6-12)$$

From this the $\gamma\gamma$ signal to SAB noise ratio can be calculated to be $P_{DT}/(n \cdot P_{ST} + n^2 \cdot P_{NT})$. Similarly, the probabilities for the other tagging classes are:

$$ST^* = \frac{P_{ST}}{\exp(2n)}$$

$$NT \cdot SAB = \frac{2 \cdot P_{NT} \cdot n}{\exp(2n)}$$

$$ST' = ST^* + NT \cdot SAB \quad (6-13)$$

$$NT^* = \frac{P_{NT}}{\exp(2n)}$$

$$NT' = NT^*$$

This information can be used to calculate the $\gamma\gamma$ signal to noise ratio in terms of measured tagging rates and n .

$$ST^* = ST' - NT' \cdot 2n$$

$$DT^* = DT' - ST^* n - NT' n^2 = DT' - nST' + n^2 NT' \quad (6-14)$$

$$S/N = DT^* / (n \cdot ST^* + n^2 NT^*)$$

It is clear that the experiment can determine the signal to noise ratio from measurements only. This information can be used to calculate negative weights for "artificial coincidence" samples created by mixing ST' and NT' events with an appropriate number of randomly picked tagger signals. The random tagger signals can be taken from any central detector event class that is reasonably free of $\gamma\gamma$ events, insuring that the tagger signals are due to SAB tags. This can also be achieved by associating a second tagger signal with each event online - each normal tagger signal could be accompanied by a tagger signal from another bunch crossing that had been saved by the software routines - the probability that this would be a good tag from another $\gamma\gamma$ event is minimal. The "clean" ST^* sample can be manufactured by assigning a weight of $-2n$ to every event in an artificial ST sample composed of all NT' events with a randomly picked tagger signal. The ST' and NT' samples can then be mixed with DT' events by creating artificial DT events and assigning them weights of $-n$ and $+n^2$ respectively. It is important to note that these artificial coincidence samples reproduce the SAB background exactly, actually repeating the process that generated it originally. One can then calculate any experimental distribution and the simulated background events, correctly weighted, will cancel the background contribution while introducing extra statistical error. The systematic error in this technique can arise from two sources: variations of n ; and the quality of $\gamma\gamma$ event separation. The former can be determined quite accurately, even for individual runs, because of the high SAB rate. The problem of $\gamma\gamma$ event separation is more difficult to study but will improve at lower $\gamma\gamma$ masses as previously discussed. This is critical as the entire process of subtraction rests on the correct separation of the notag sample. In general, there will be some kinematic regions

where the SAB process will drown out $\gamma\gamma$ and vice versa - the statistical errors presented here are only averages but a cleaner sample can be separated in well-defined way by cutting on the error introduced in each bin by the statistical subtraction. This is the only consistent way to suppress kinematic regions with a high SAB background. It is much better than introducing a physical cut in the tagger as the effect of a slit can easily be reproduced in offline analysis if necessary. The only valid reason for introducing a physical cut would be to reduce an unmanageable hardware rate in a particular BGO crystal.

If the background subtraction is calculated by associating a random SAB tag with each ST' or NT' event the ζ factor is different than that calculated in Table 6.7 as the populations of the background and simulated background samples are no longer identical. The correct "statistical error factor is:

$$\zeta' = \sqrt{\frac{250 \cdot \sigma_{Total}(DT + (n + n^2)ST + (3n^2 + 2n^3 + n^4)NT')}{L \cdot \sigma_{Visible} \cdot DT^2 \exp(-2n)}} \quad (6-15)$$

The results of the modified ζ' factor calculation are listed in Table 6.10. These were calculated from the values of n shown and the acceptance and tagging efficiencies shown in Tables 6.3, and 6.4a,b. The results for the unmodified ζ factor are slightly different from those in Table 6.7 as Table 6.7 used a smaller data sample due to lack of computer time for the full simulation.¹ There is no drastic change in ζ after these modifications are made. Table 6.10 also displays the ζ_0 factor for the utopian experimental situation where there is no background and the ratio ζ'/ζ_0 . Figure 6.17 shows the statistical error in the $\gamma\gamma$ hadronic cross-section measurement expected from tagger and detector efficiency as a function of invariant mass of the double tagged system. These errors have been scaled by the ratio of statistical error factors, ζ'/ζ_0 , from Table 6.10 (which is an weighted average over all masses).

¹It is expected that the results in Table 6.10 are the more accurate of the two. The results in Table 6.7 were calculated from the observed contamination in a computer simulated measurement while those in 6.10 were calculated from equations 6-9...16.

.0012	.0015	.0016	.0015	.0016	.0015	.0012
.0014	.0020	.0027	.0026	.0027	.0020	.0014
.0018	.0029	.0037	.0038	.0037	.0029	.0018
.0015	.0035	.0060	.0074	.0060	.0035	.0015
.001	.0040	.011	.015	.011	.0040	.0010
.00015	.0022	.016	.034	.016	.0022	.00015
< .0001	.0002	.016	.095	.016	.0002	< .0001
< .0001	< .0001	.0025	.3450	.0025	< .0001	< .0001

Table 6.9a

Probability per beam crossing of each $2 \times 2 \text{ cm}^2$
 BGO block being hit by a lepton from an $e^+e^- \rightarrow e^+e^-\gamma$ event.
 The center of the lower edge of the bottom
 row is 1 cm above the beam path.

.0023	.0032	.0047	.0049	.0047	.0032	.0023
.0033	.0053	.0063	.0062	.0063	.0053	.0033
.0045	.0066	.011	.011	.011	.0066	.0045
.0043	.0081	.018	.022	.018	.0081	.0043
.0038	.0082	.028	.047	.028	.0082	.0038
.0025	.0060	.034	.12	.034	.0060	.0025
.0015	.0030	.017	.40	.017	.0030	.0015

Table 6.9b

Probability per beam crossing of each $2 \times 2 \text{ cm}^2$ BGO
 block being hit by a lepton from a $\gamma\gamma$ event.
 The center of the lower edge of the bottom
 row is 1 cm above the beam path.

Tagger	Luminosity	\bar{n}	ζ	ζ'	ζ_0	ratio
1 cm from Beam	250 nb ⁻¹ /day	.30	8.5	8.2	3.7	2.2
2 cm from Beam	250 nb ⁻¹ /day	.21	11.2	10.5	5.0	2.1
SAB Slit	250 nb ⁻¹ /day	.026	22.3	20.1	15.4	1.3
1 cm from Beam	500 nb ⁻¹ /day	.60	11.3	12.5	2.6	4.8
2 cm from Beam	500 nb ⁻¹ /day	.42	13.7	14.4	3.5	4.1
SAB Slit	500 nb ⁻¹ /day	.052	20.5	18.5	10.9	1.7

Table 6.10 SAB Background Contamination Analysis

6.5 Conclusion : It is apparent that the measurement of $\sigma_{\gamma\gamma} \rightarrow \text{hadrons}$ as initially envisaged is severely compromised by the persistence of the small angle bremsstrahlen background. The statistical subtraction of this background, when tagger and detector efficiency are considered, produces an increase in the statistical error compared to that expected from a "perfect experiment" of 8.5-14.4. Without the bremsstrahlen background this factor varies between 2.6-5 depending on the arrangement of the tagger geometry. Additionally, improved machine luminosity makes the situation worse as this increases the SAB tag frequency. From this point of view it is far better to have continuous low luminosity running than sporadic bursts of high specific luminosity. From Figure 6.17 it is apparent that statistical error on the order of 10% for 100 MeV bins can be achieved in the $\sigma_{\gamma\gamma}$ measurement with as little as 32pb⁻¹ integrated luminosity for $W_{\gamma\gamma} \sim 1$ GeV if the taggers can operate 1cm from the beam. To achieve this level of uncertainty for $\gamma\gamma$ masses between 1 and 3 GeV would require ~ 16 times this luminosity. It is possible to reject a significant fraction of the background events by offline cuts. The preliminary studies of this, described above, suggest that a factor of two reduction in the statistical error factor, ζ , is possible. This would reduce the required luminosity by a factor of four. For the worst case situation of 500 nb⁻¹/day specific luminosity with the taggers operating 2cm from the beam orbit, $\sim 170\text{pb}^{-1}$ integrated luminosity would be required for the $\gamma\gamma$ total cross-section measurement.

In order to improve these estimates it is essential that measurements with a "pre-experiment" start

as soon as possible. The vacuum chambers should be installed in DORIS allowing an incomplete tagger, using about 15% of the total BGO, to measure background rates. This arrangement would be used to determine the exact running conditions - distance from beam, radiation exposure, antitagging capability etc. - allowing a much better estimate of the statistical uncertainty introduced by the SAB background to be made. The results of the present simulations suggest that somewhere between 60 and 200 pb^{-1} integrated luminosity would be necessary for the total cross-section measurement. The average experimental luminosity per year will probably not exceed 100 pb^{-1} . It appears that the measurement is still feasible.

The systematic uncertainties involved in this measurement are difficult to estimate. It is expected that the double tag technique is less subject to these problems than methods involving $W_{vis} \rightarrow W_{\gamma\gamma}$ unfolding. However, the suitability of employing a statistical simulation of the final state for the unfolding of trigger and analysis efficiencies is doubtful due to the effect of resonances and coherent particle production at low $W_{\gamma\gamma}$. One can argue that if a flexible enough fragmentation parametrisation is used any data may be fitted. The cost of this is, of course, expressed in larger systematic uncertainty as measured by the allowed variation in the fragmentation parameters. This problem is avoided, to an extent, if the analysis requires at least three charged particles. Then the systematic uncertainties reduce to that of the other measurement attempts - without, of course, the additional systematic uncertainty from the $W_{vis} \rightarrow W_{\gamma\gamma}$ unfolding. The loss of the low multiplicity channels is not crippling as it is these channels that can best be treated in notag analyses.

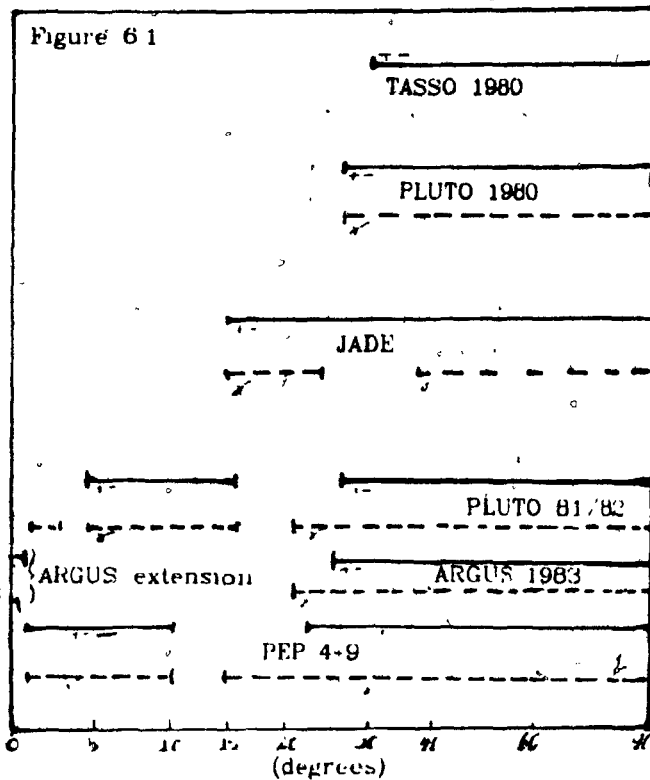
6.6 CAPTIONS FOR FIGURES

- 6.1** Angular acceptances for detectors at e^+e^- storage rings.
- 6.2** Distribution of error in $W_{\gamma\gamma}$ as a function of tagger resolution.
- 6.3** Standard deviation of $W_{\gamma\gamma}$ as a function of tagger resolution.
- 6.4** True CMS rapidity of $\gamma\gamma$ events: (a) All events; (b) Events with full detector trigger (endcaps included); (c) Events with only barrel trigger.
- 6.5** Total and visible cross-sections for a hypothetical 2^{++} resonance in $\gamma\gamma \rightarrow \pi^-\pi^+$ for $E_{Beam} = 5, 18$ GeV as a function of resonance mass. $\Gamma_{Total} = 100$ MeV, and $\Gamma_{\gamma\gamma} \cdot Br(X \rightarrow \pi^+\pi^-) = 1.5$ keV. The final state is produced with helicity two.
- 6.6** Feynmann diagram for $e^+e^- \rightarrow e^+e^-\gamma$.
- 6.7** Total and visible cross-sections for $e^+e^- \rightarrow e^+e^-\gamma\gamma \rightarrow e^+e^- hadrons$ as a function of $W_{\gamma\gamma}$. $\sigma_{\gamma\gamma} = 300$ nb
- 6.8** Probability of production of $n/2 \pi^+\pi^-$ pairs in the $\gamma\gamma$ final state. Comparison of KNO algorithm explained in text with data from low energy e^+e^- and $p\bar{p}$ annihilation.
- 6.9** Acceptance, for various topology thresholds, for final states of fixed topology with limited P_{\perp} phase space decay of the $\gamma\gamma$ CMS. The upper curve in each of these diagrams corresponds to the acceptance with the full trigger while the lower curve corresponds to the barrel trigger acceptance. n_{\pm} refers to the number of charged particles visible in the detector.
- 6.10** Acceptance for $\gamma\gamma \rightarrow hadrons$.
- 6.11** Efficiency of various tagger configurations as a function of γ energy.
- 6.12** Single tag efficiency of various tagger configurations as a function of (a) $W_{\gamma\gamma}$ and (b) the rapidity of the $\gamma\gamma$ CMS.
- 6.13** Double tag efficiency of various tagger configurations as a function of (a) $W_{\gamma\gamma}$ and (b) the rapidity of the $\gamma\gamma$ CMS.
- 6.14** Efficiency of various tagger configurations as a function of Q^2 (photon mass).
- 6.15** Angular distribution of the leptons from $e^+e^- \rightarrow e^+e^-\gamma$ events with (circles with error bars) and without (crosses) beam divergence.
- Hit distributions in the tagger plane for: (a) $\gamma\gamma$ events with beam divergence; (b) $e^+e^- \rightarrow e^+e^-\gamma$ events with no beam divergence; and (c) $e^+e^- \rightarrow e^+e^-\gamma$ with beam divergence.
- 6.17** Statistical error expected in 100 MeV bins for various tagger situations as a function of $W_{\gamma\gamma}$. The

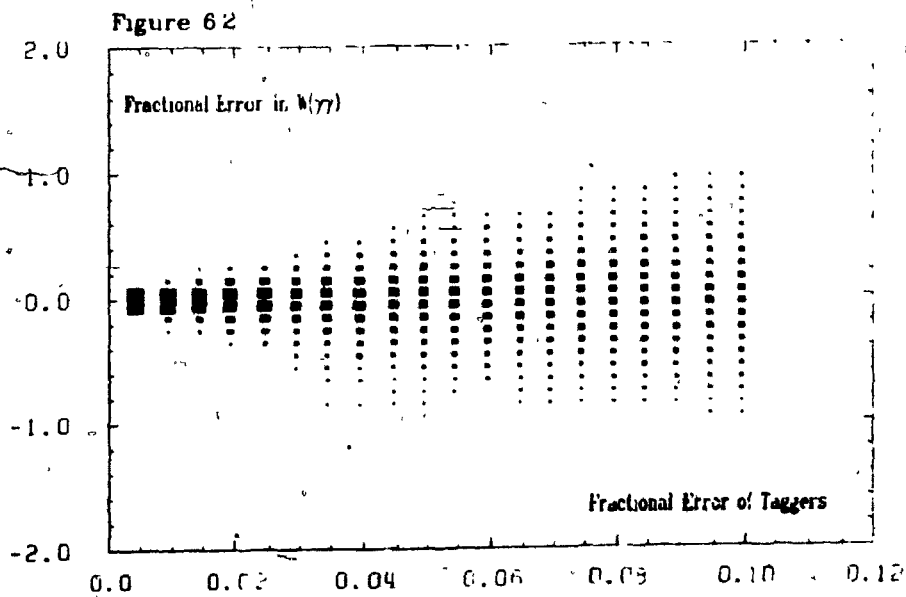
calculation includes the effect of the SAB background subtraction averaged over all $W_{\gamma\gamma} > 1$ GeV.

6.18 Total visible energy for $\gamma\gamma$ double tag events and for false double tag events (a) before and (b) after the SAB event rejection cuts described in Table 6.8.

6.19 Proposed SAB rejection cut in tagger. The lower edge of the matrix is 1 cm from the e^+e^- beams.



Angular Acceptances for Detectors at the Storage Rings



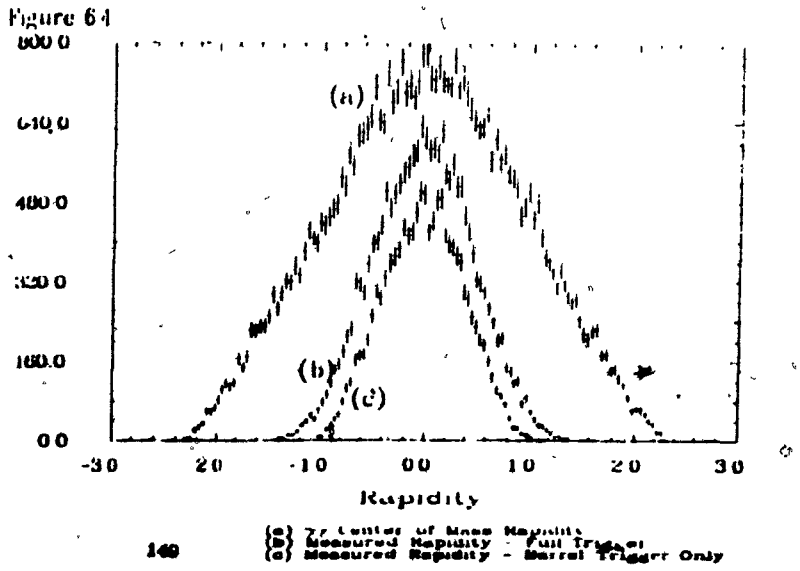
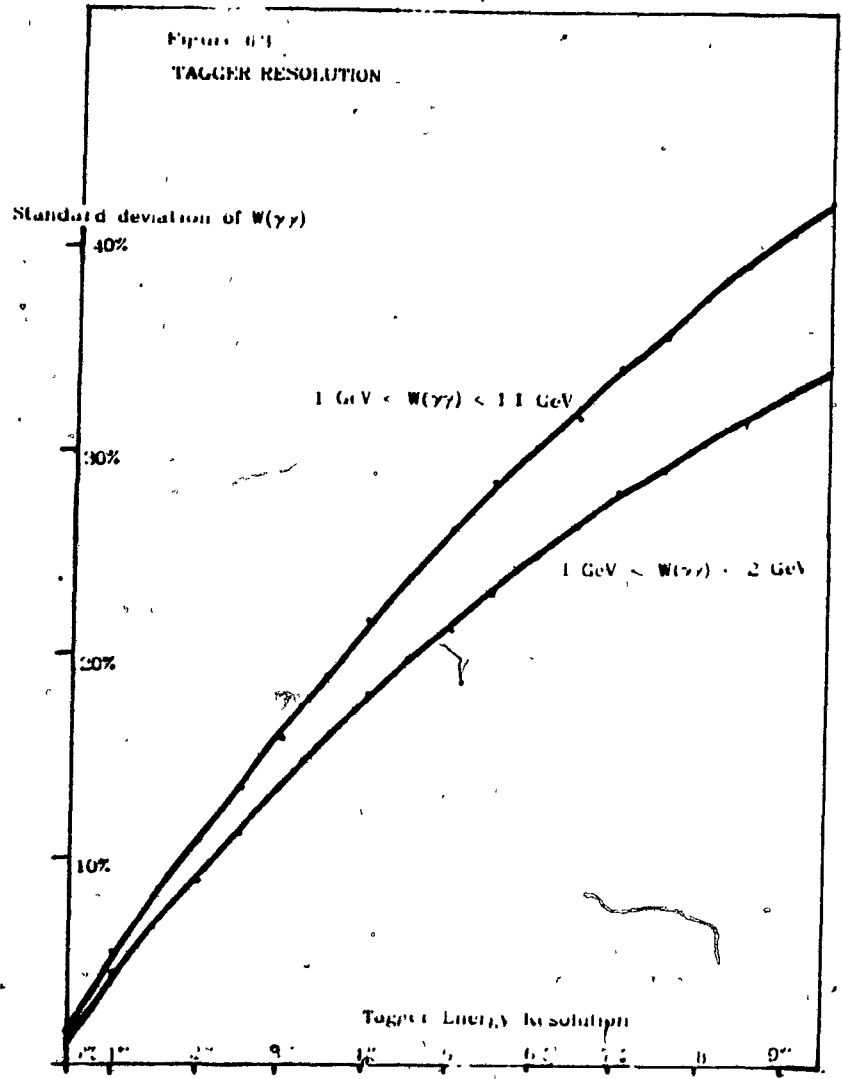
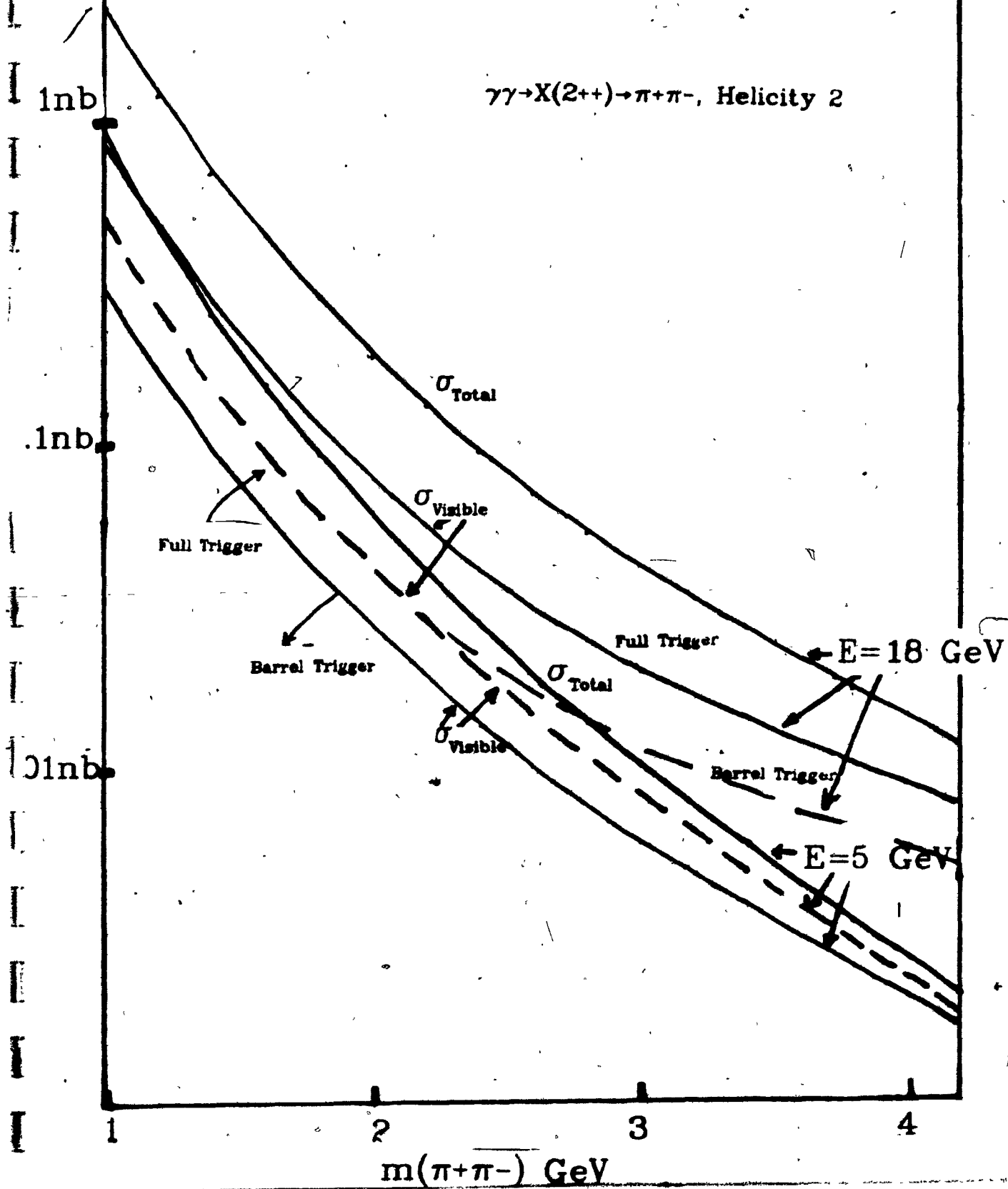


Figure 6.5

$\gamma\gamma \rightarrow X(2^{++}) \rightarrow \pi^+\pi^-$, Helicity 2



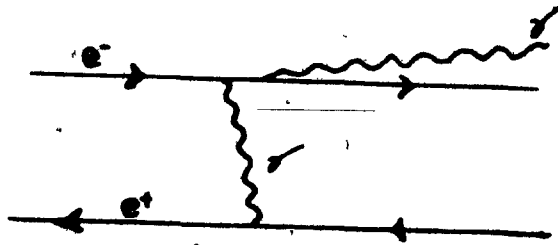


Figure 6.6

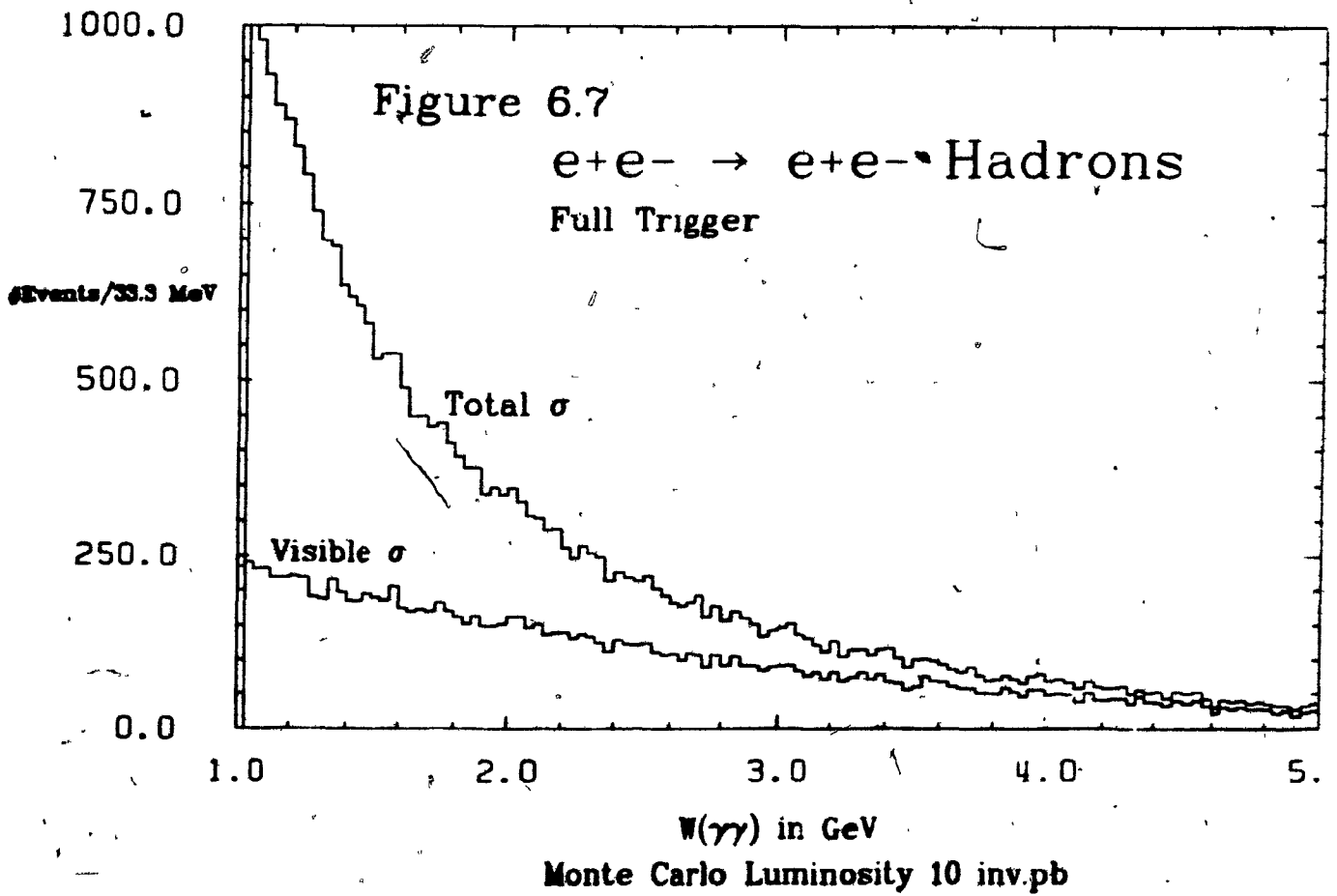
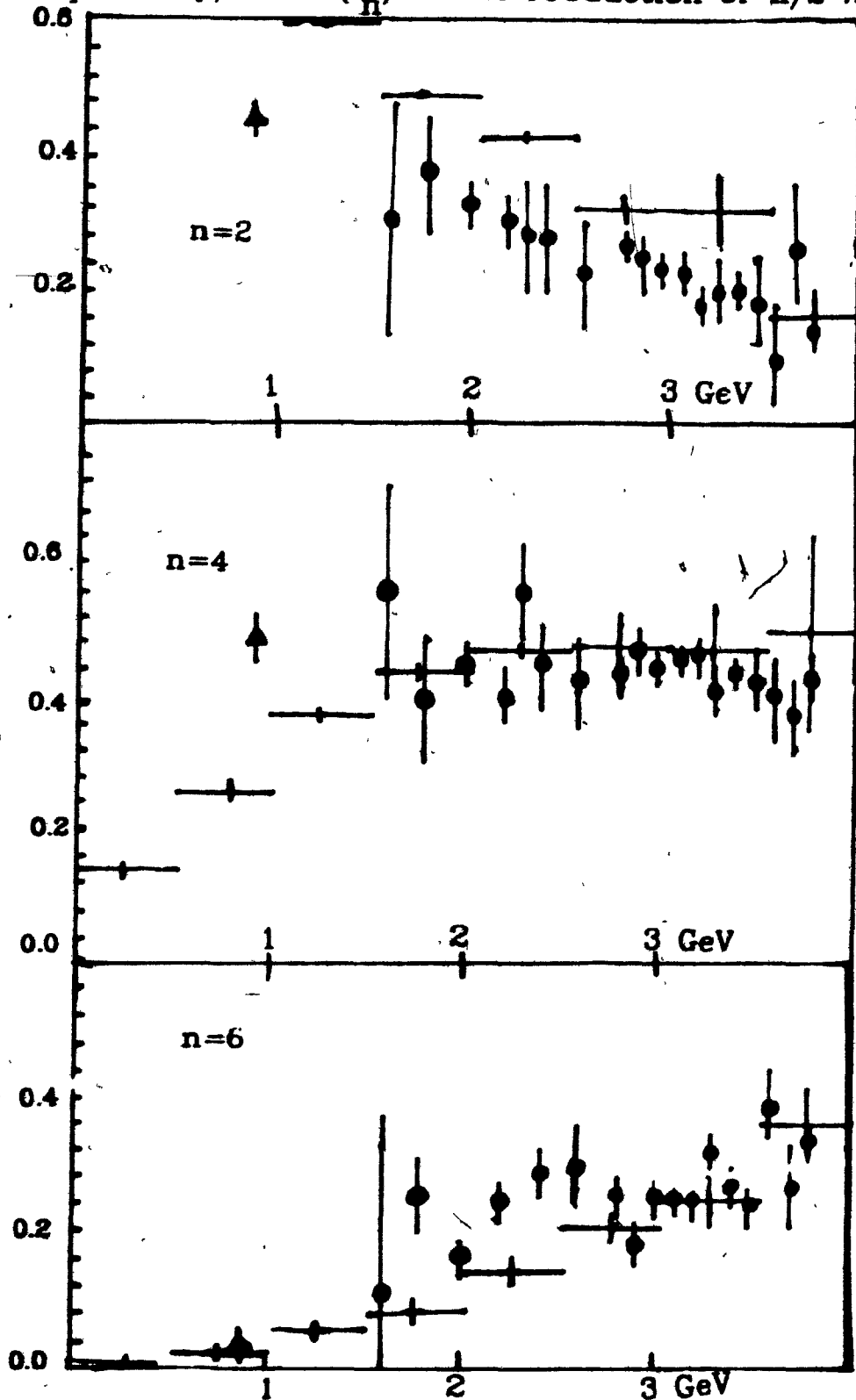
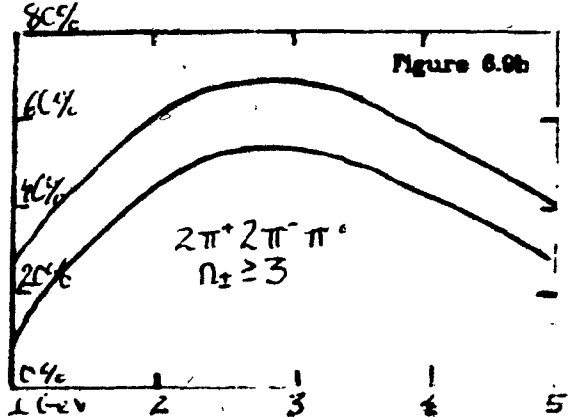
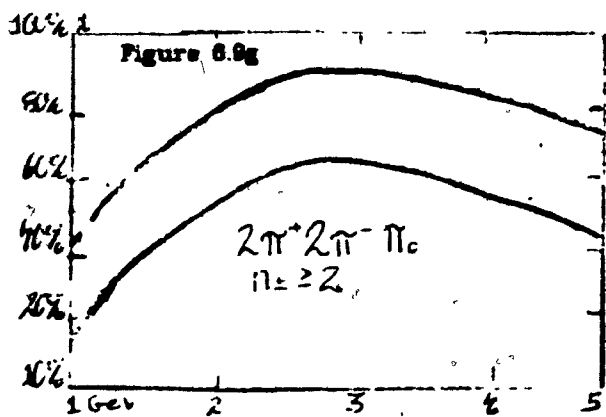
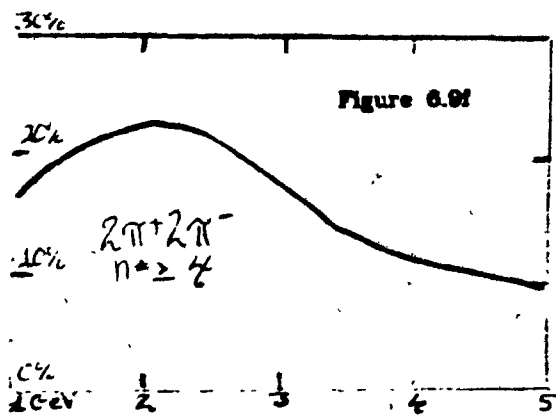
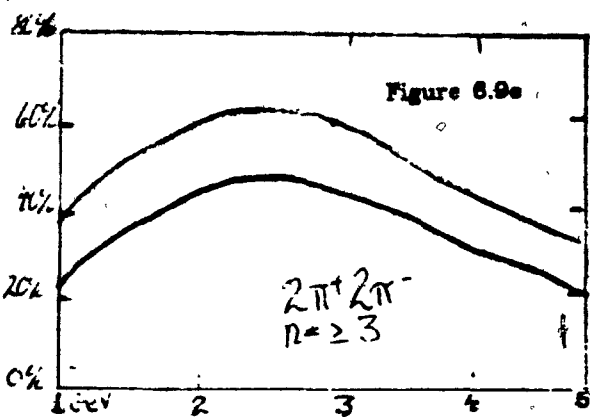
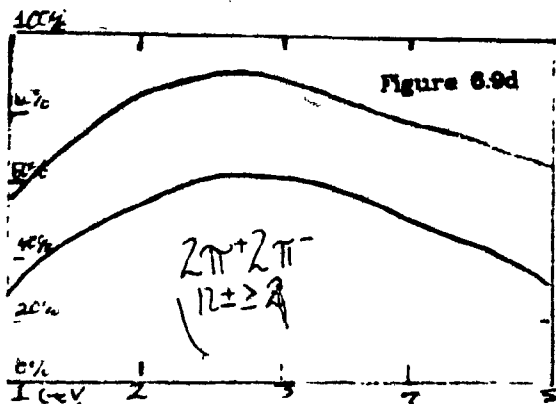
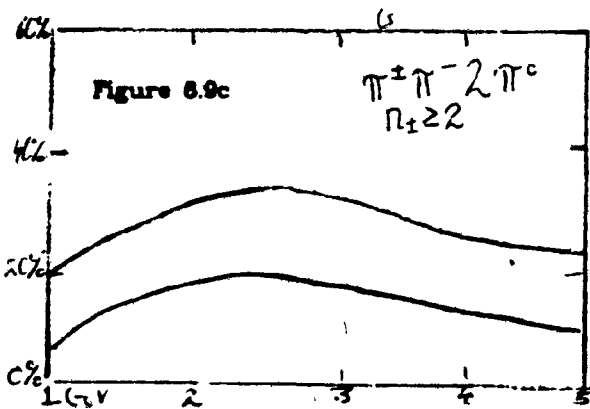
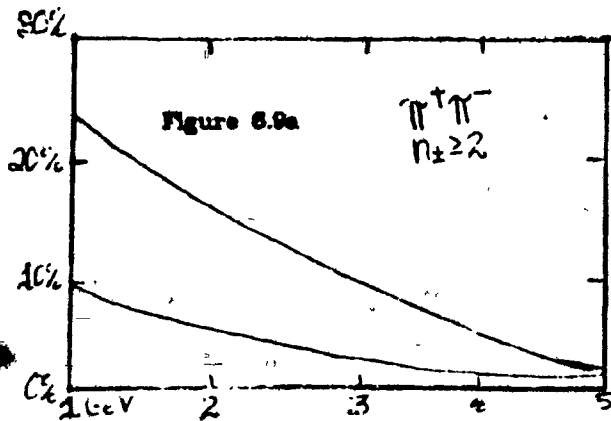


Figure 6.8

Probability/event (f_n) of the Production of $n/2 \pi^+\pi^-$ pairs



Filled Circles - data from e+e- collisions at Mark I
Filled Triangles - data from proton/antiproton annihilation
Crosses - Result of KNO algorithm described in text.



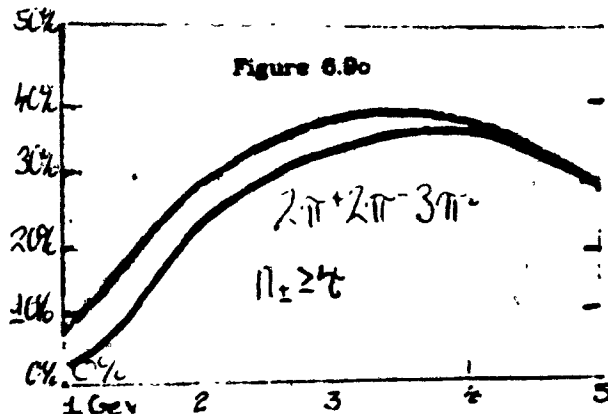
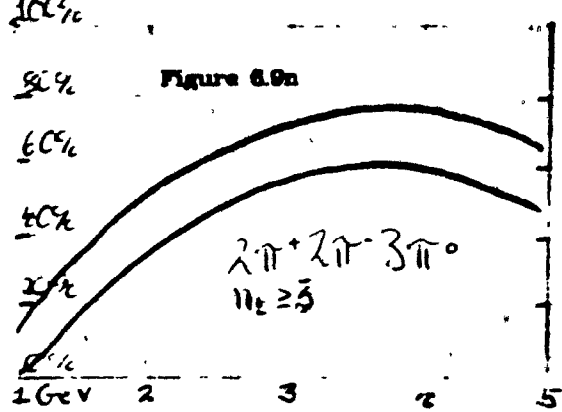
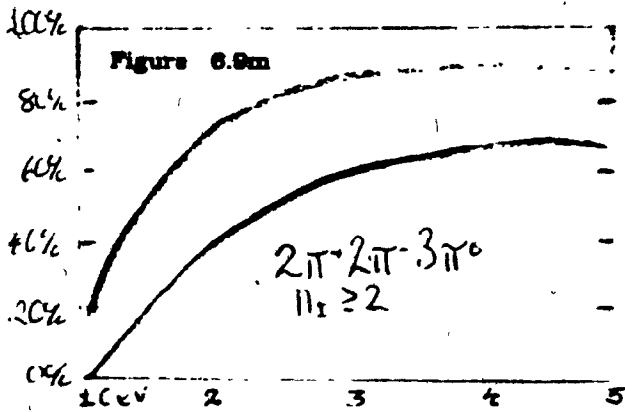
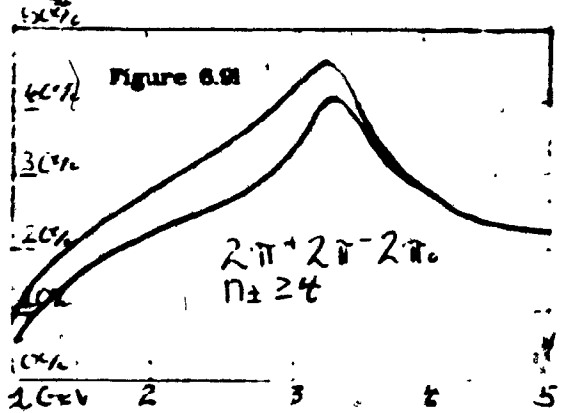
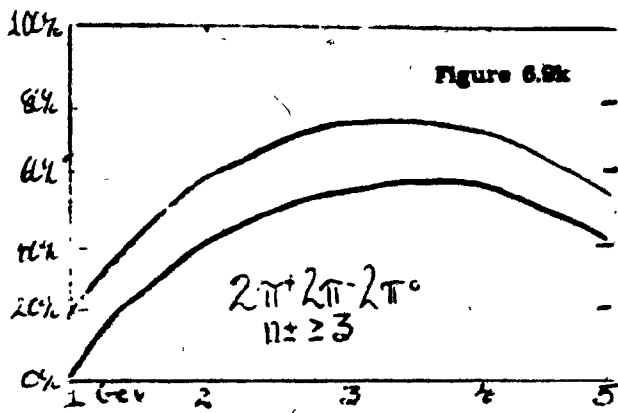
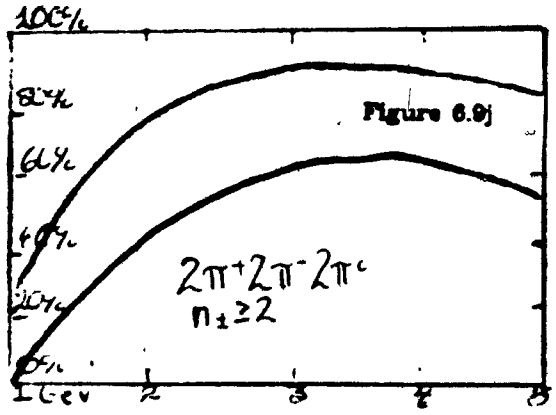
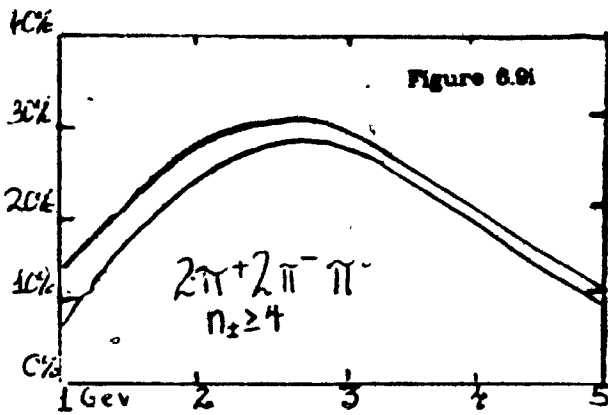


Figure 6.10a

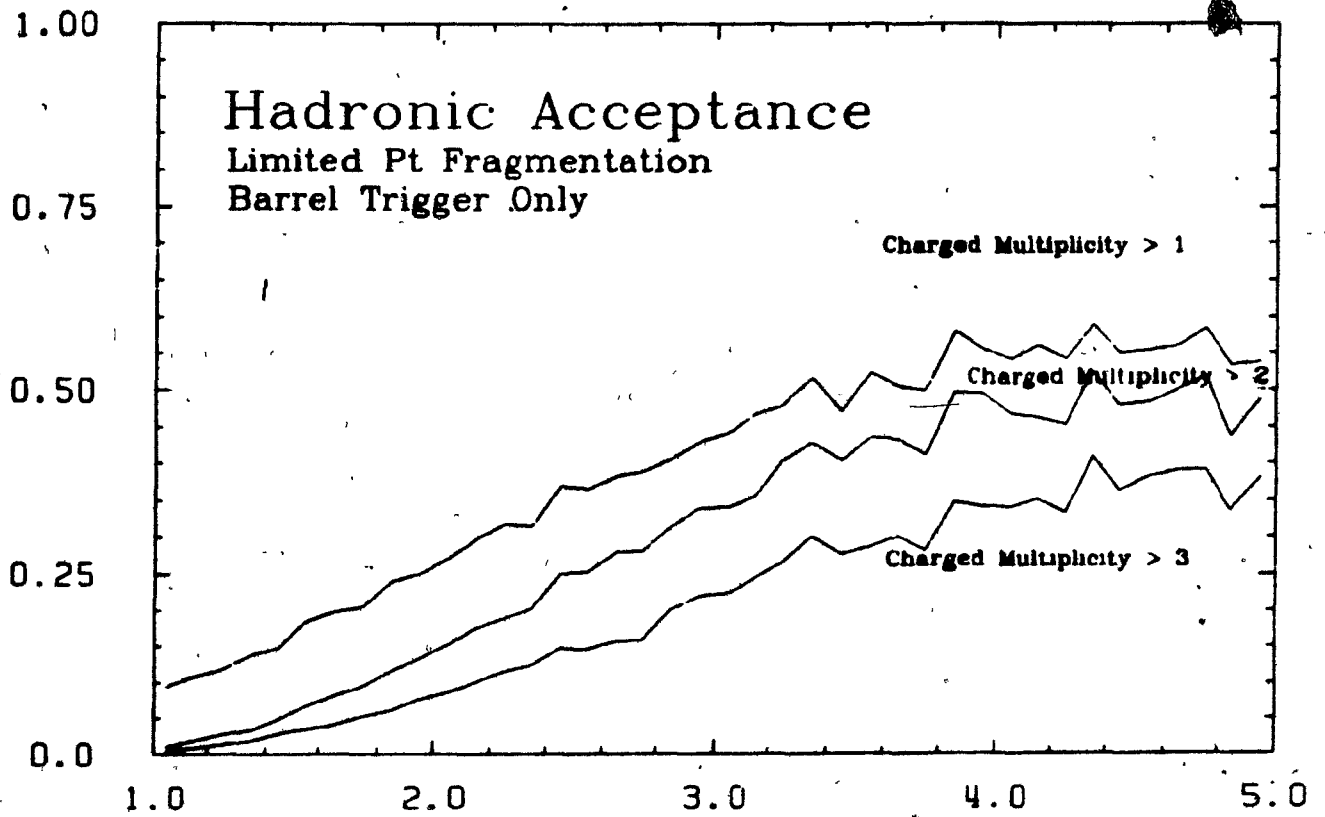
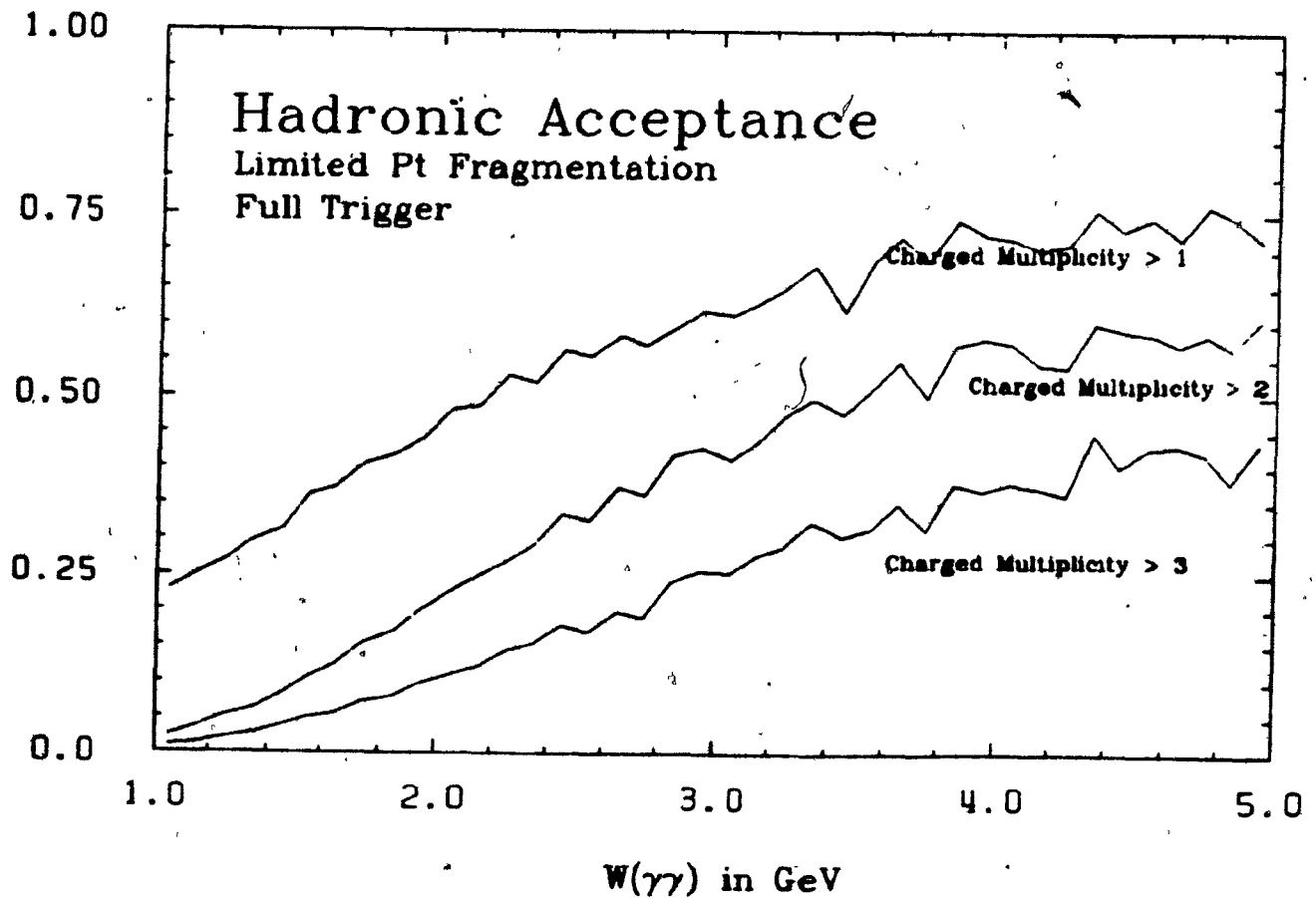


Figure 6.10b $W(\gamma\gamma)$ in GeV



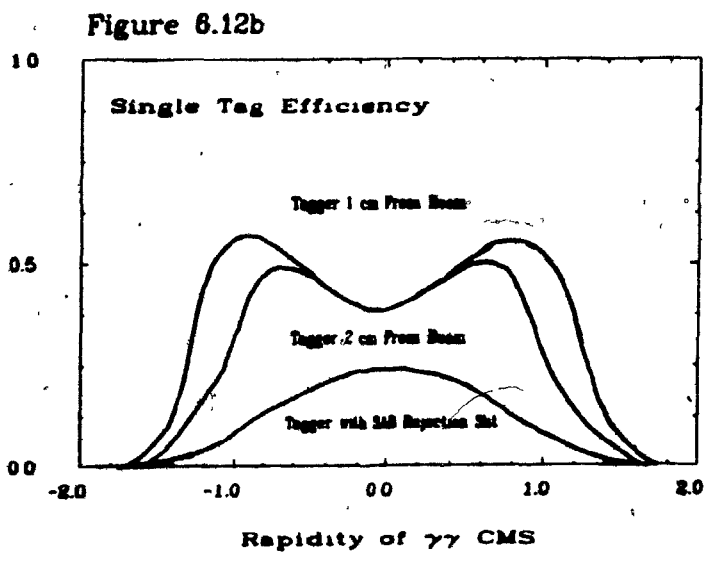
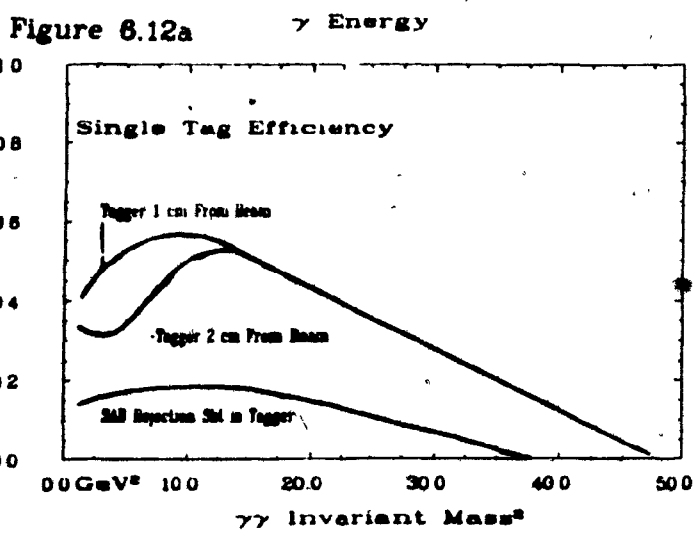
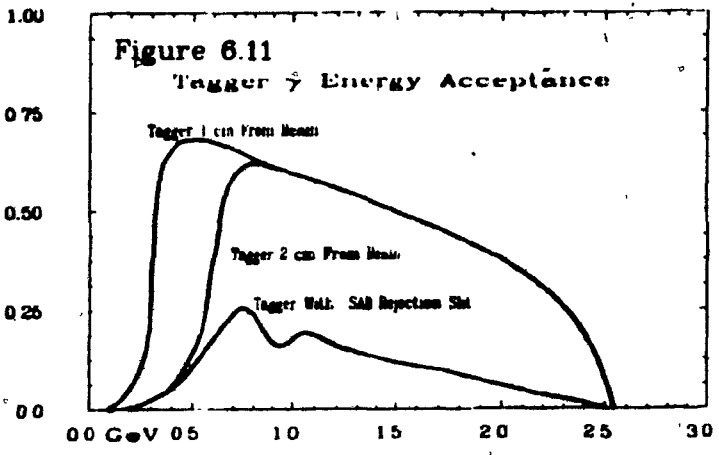


Figure 6 13a

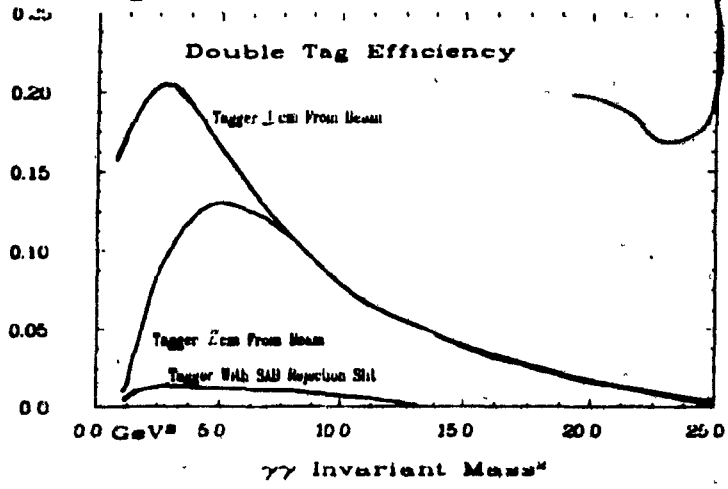


Figure 6.13b

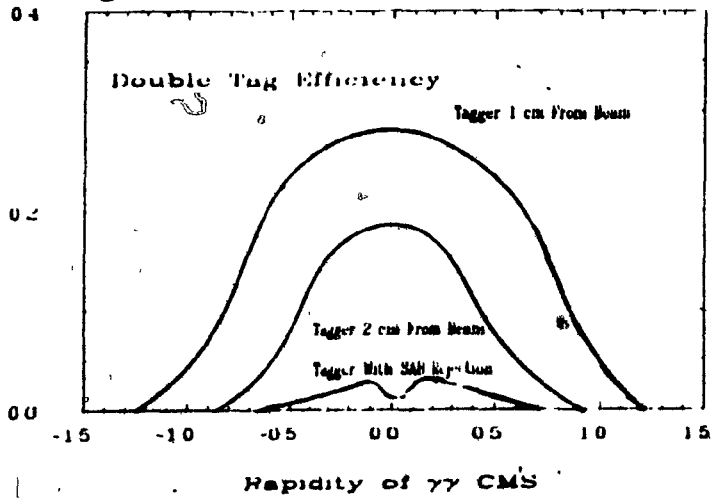


Figure 6 14

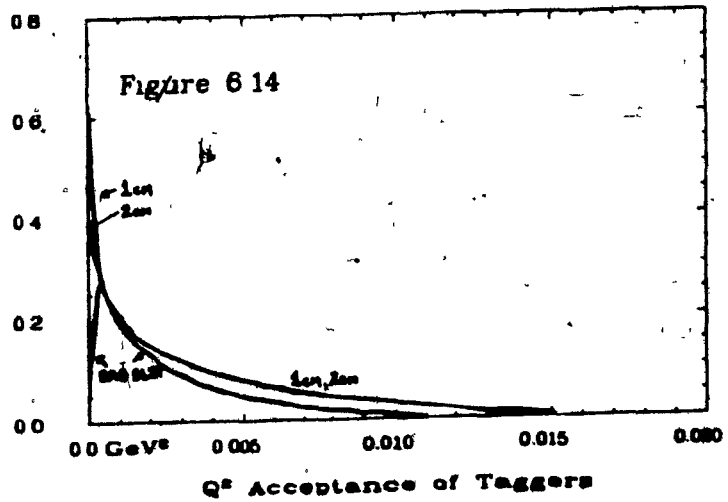
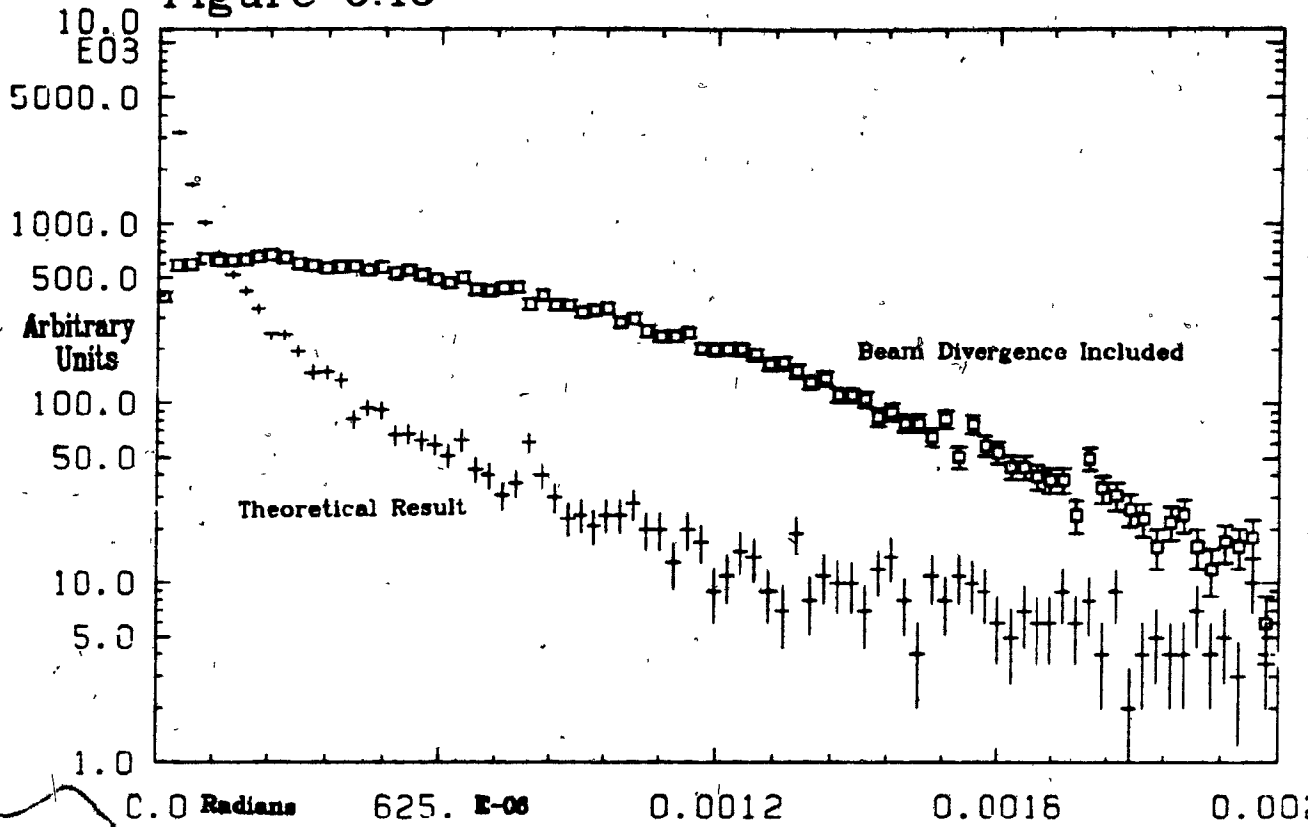
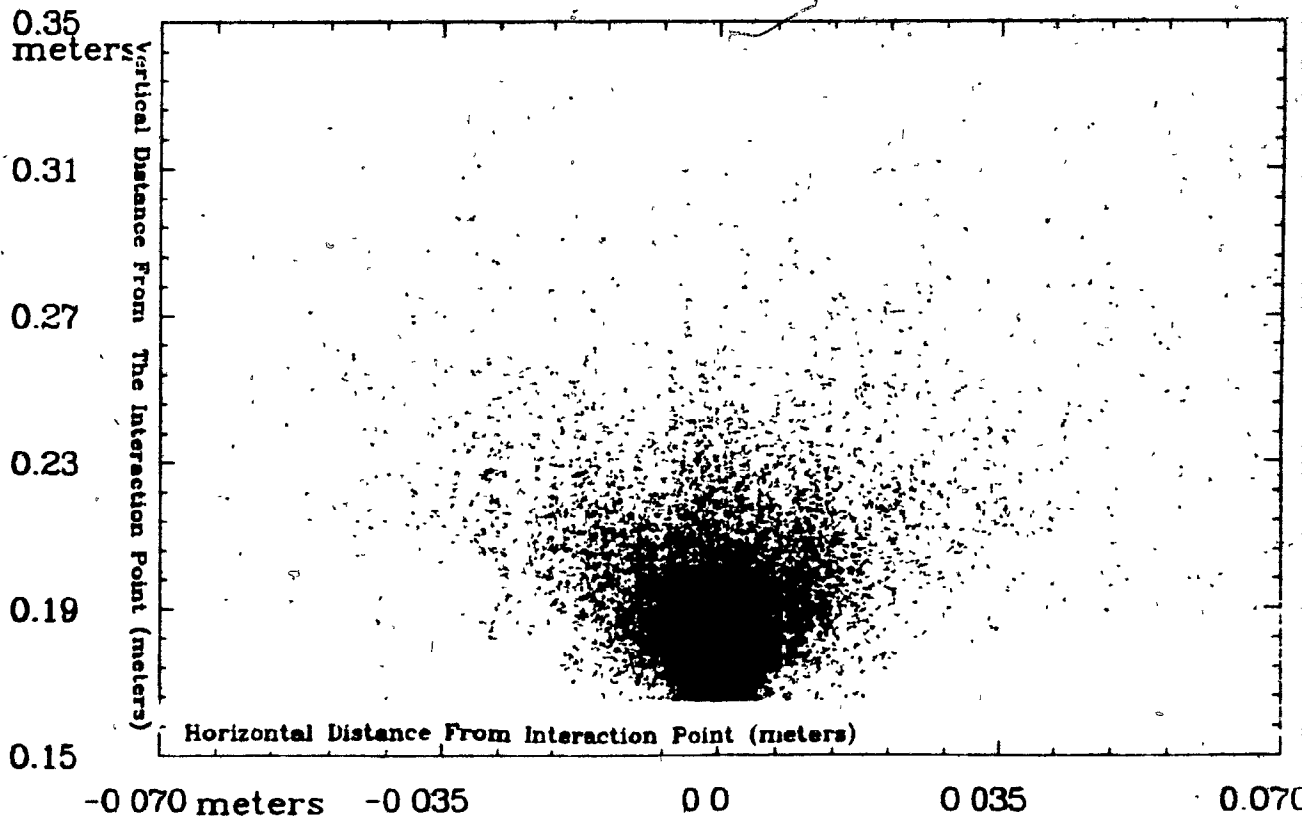


Figure 6.15



Angular Distribution of e_{\pm} from $e^+e^- \rightarrow e^+e^-\gamma$

Figure 6.16a



Tagger Hits from $\gamma\gamma$ Events

Figure 6.16b

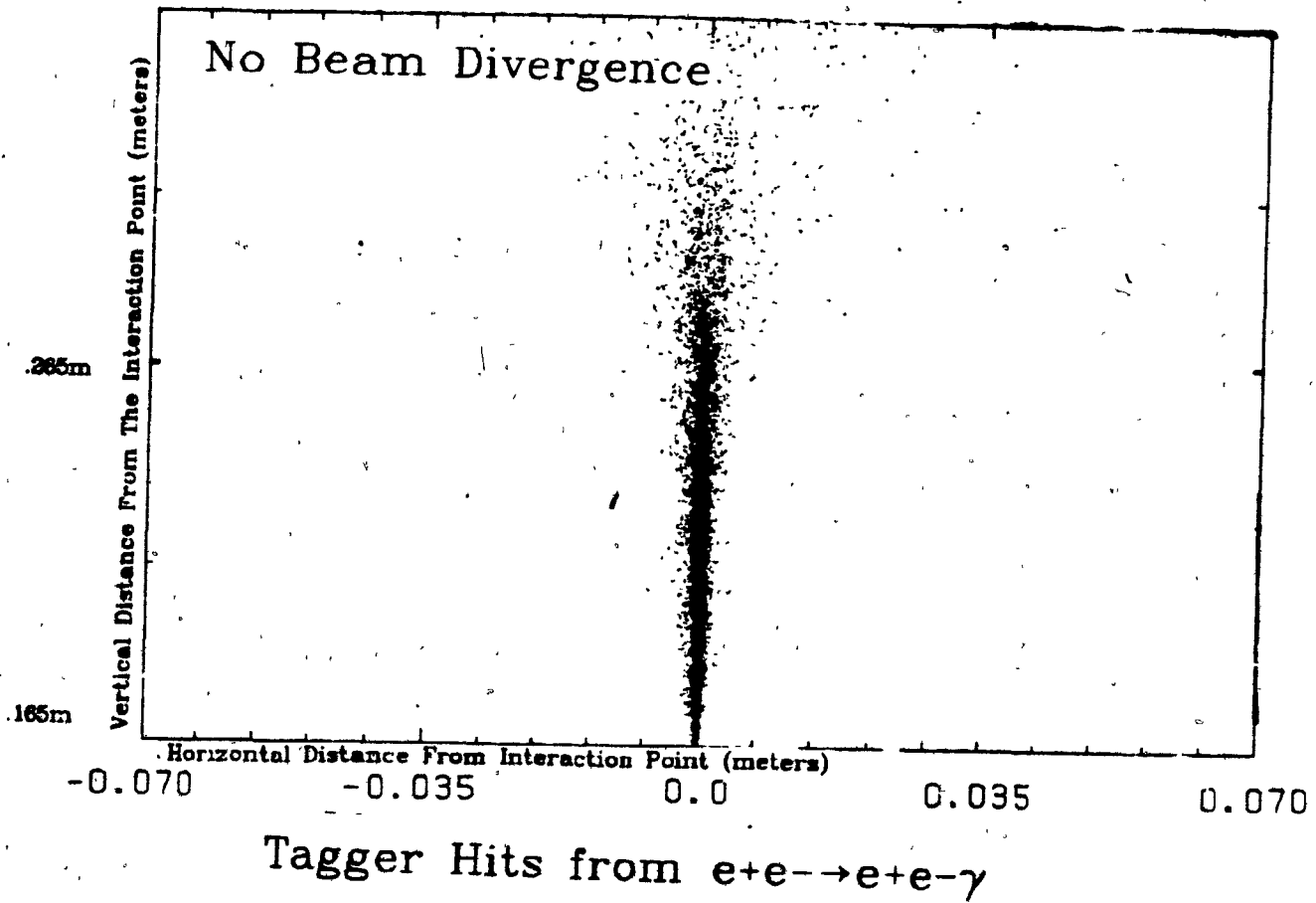


Figure 6.16c

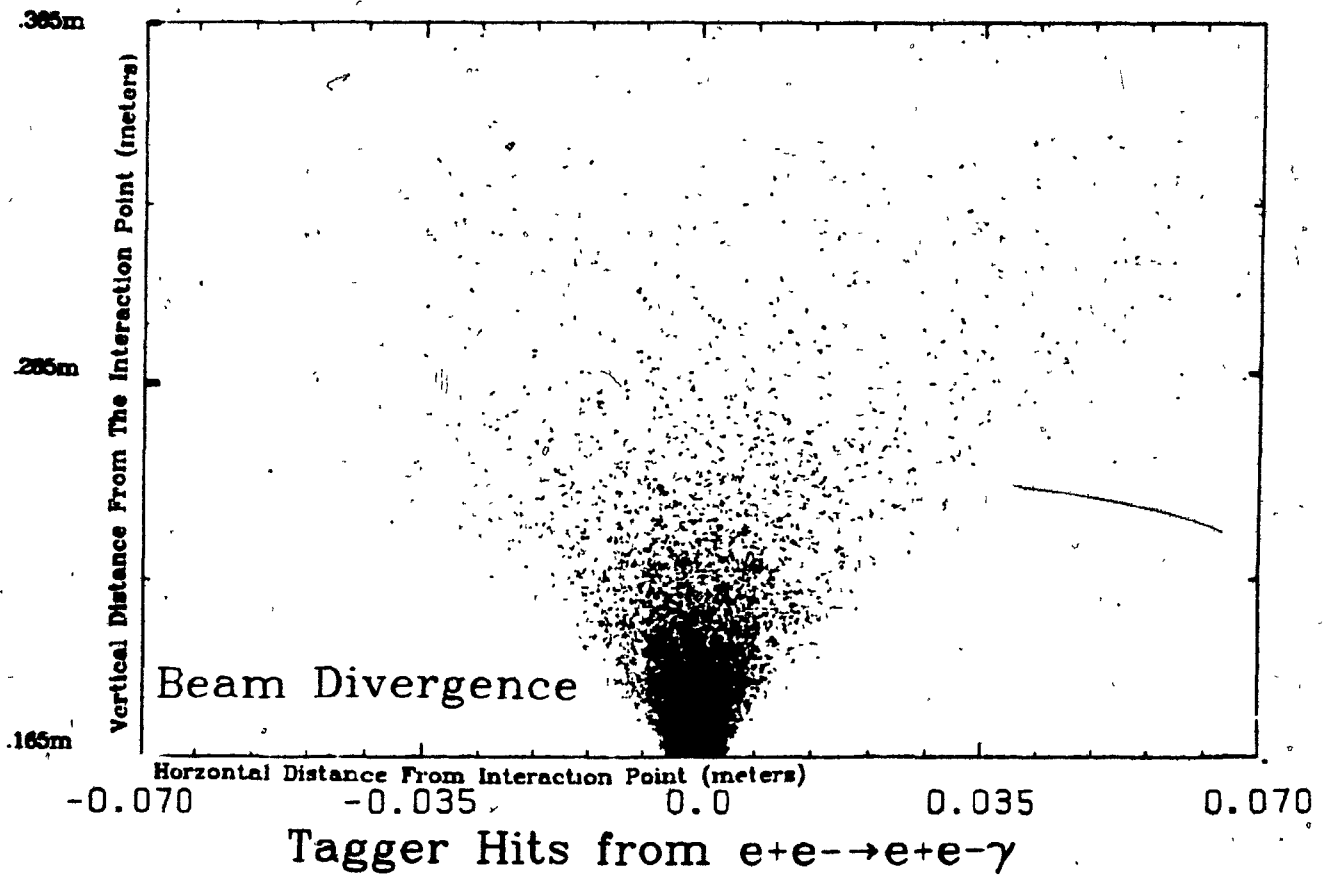


Figure 6.17a

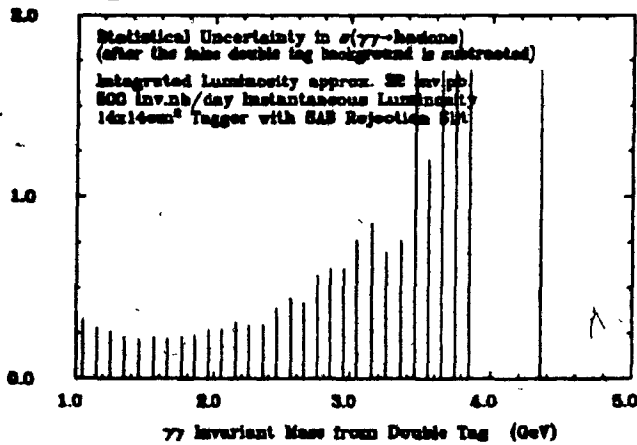


Figure 6.17b

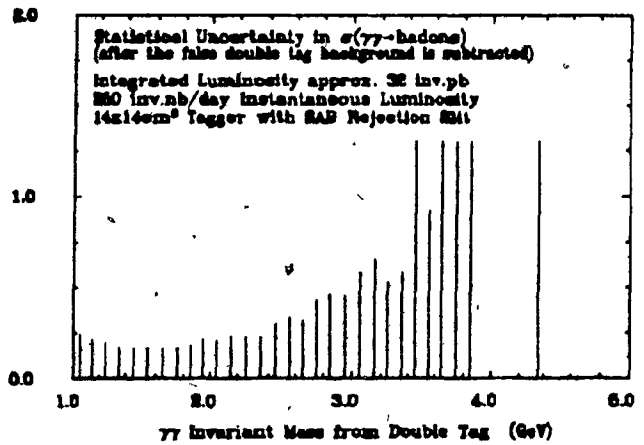


Figure 6.17c

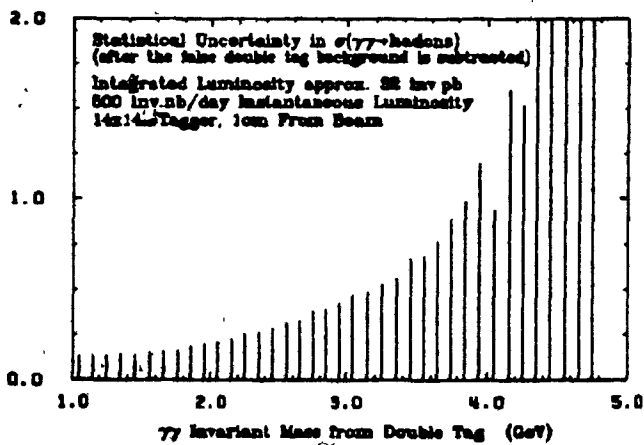


Figure 6.17d

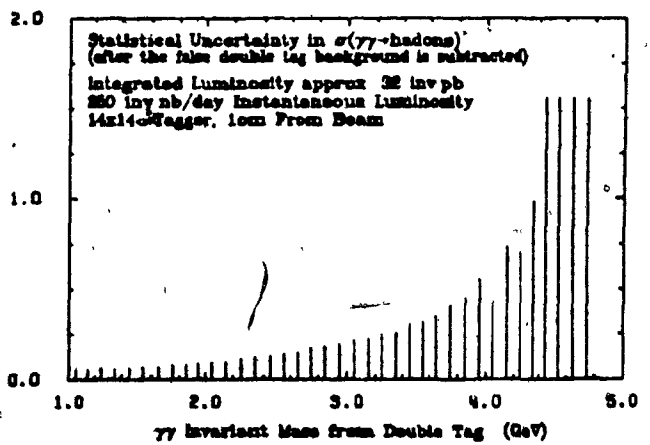


Figure 6.18a

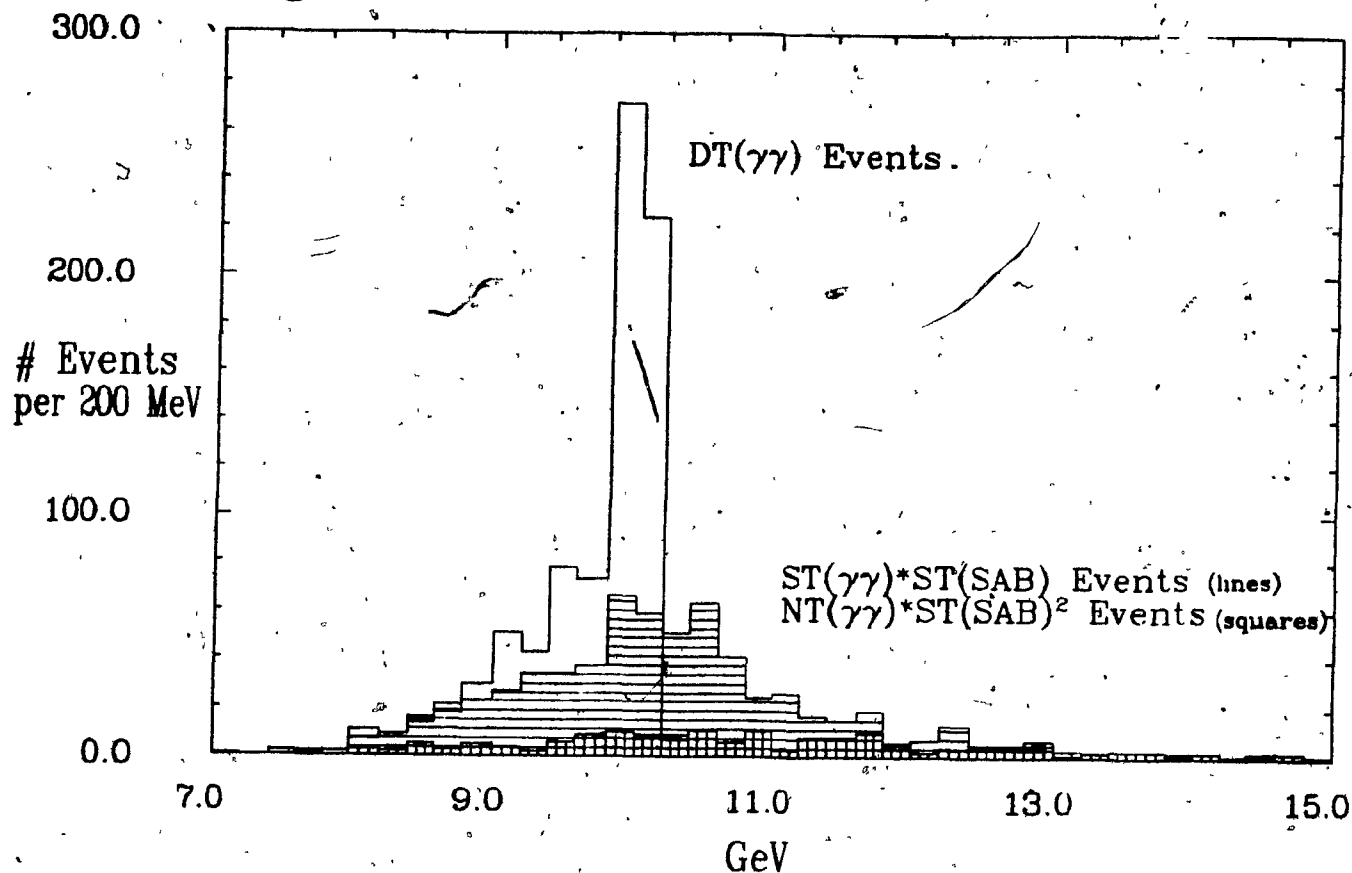
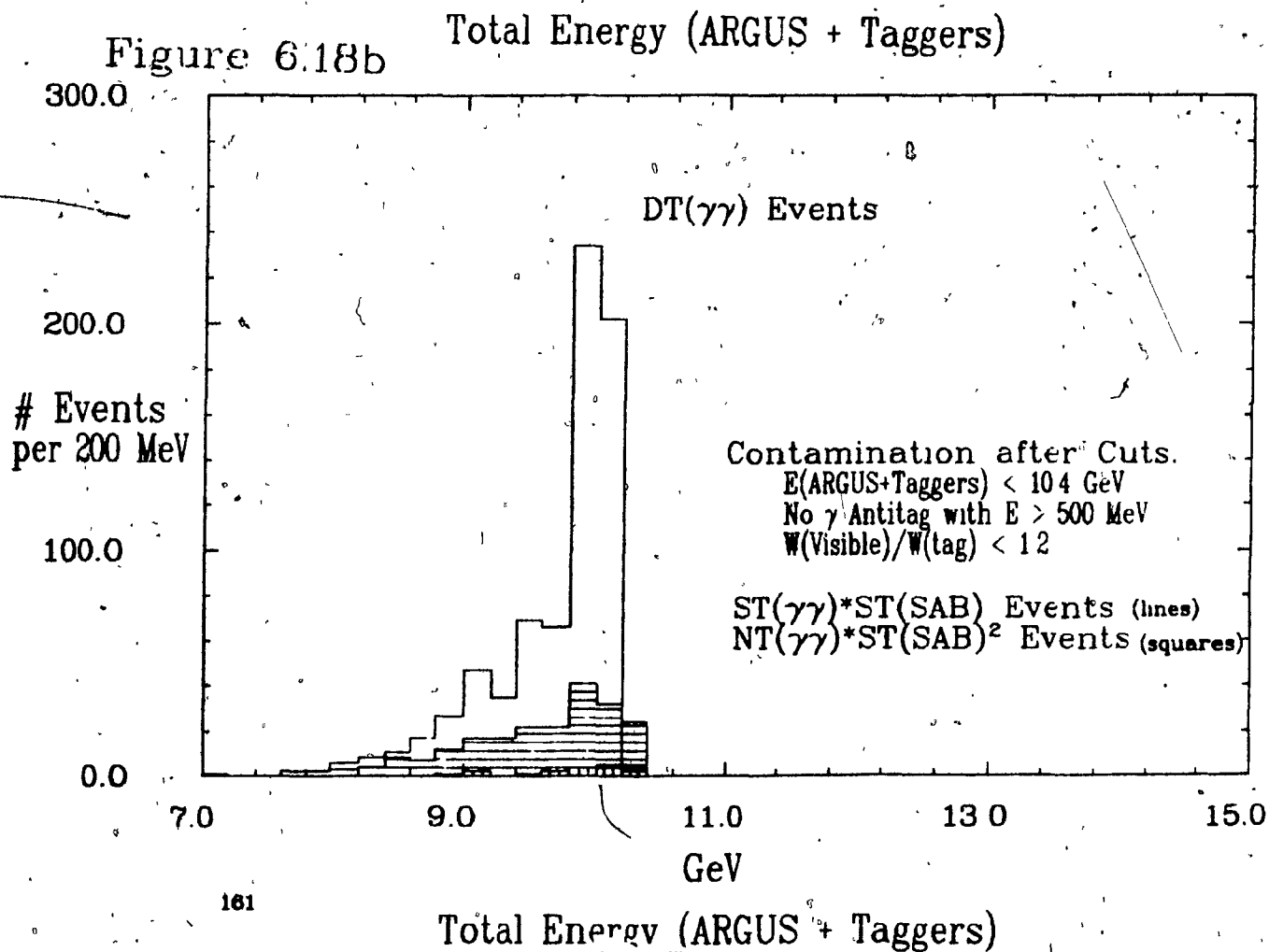


Figure 6.18b



CONCLUSION

The measurement of the total cross-section for $e^+e^- \rightarrow e^+e^- \gamma\gamma \rightarrow e^+e^- \text{hadrons}$ is a considerable experimental challenge - especially at low $W_{\gamma\gamma}$. It has been shown that the proposed double tag measurement of this quantity is feasible with a modified ARGUS detector despite a considerable background from e^\pm tags from small angle bremsstrahlung events. The acceptance for hadronic final states was calculated in a conservative manner to set a lower limit consistent with previous information on these phenomena. It was calculated that an integrated luminosity between 60 and 200 pb^{-1} will be necessary to limit the statistical uncertainty in the measured cross-section to be below 10% in the 20 100-MeV $W_{\gamma\gamma}$ bins between 1 and 3 GeV. The accuracy of this result is limited by the exact running conditions of the experiment which are, as yet, undetermined. As this luminosity is expected to be an upper limit on that needed it seems possible to perform the experiment during less than two years of normal running. The systematic uncertainties in the measurement are not well known but they are expected to be less than those of the single tag measurements of the TASSO and PLUTO experiments. The double-tag measurement eliminates the strong coupling between the parameters of the fragmentation model used for acceptance calculations and the $W_{\gamma\gamma}$ dependence of $\sigma(\gamma\gamma \rightarrow \text{hadrons})$.

Studies of $\gamma\gamma$ resonance production are very promising. The $\eta'(957)$ and $f(1270)$ have been observed as strong signals and the $f'(1515)$ and $A_2(1318)$ have been seen. Quantitative results of these analyses have been delayed because of problems with calculation of trigger acceptances near threshold. This is currently under investigation.

In summary, the study of $\gamma\gamma$ Physics with the ARGUS detector seems promising. The experimental situation presents a unique opportunity to measure $\sigma(\gamma\gamma \rightarrow \text{hadrons})$ at low invariant masses and ARGUS' acceptance for $\gamma\gamma$ resonances seems to be at least as good as that of other detectors investigating these phenomena. This situation may improve in the future if a full detector trigger is introduced.

APPENDIX 1: EXPRESSIONS FOR $e^+e^- \rightarrow e^+e^-\gamma\gamma$ KINEMATICS

This appendix derives the principle formulae describing the kinematics of the $\gamma\gamma$ CMS using procedures outlined by Bonneau⁷⁰³ and Budnev¹¹⁰. Two-photon collisions at e^+e^- storage rings can also be described as inelastic Bhabha scattering events - it is only the weak-coupling of electromagnetic interactions that allows these processes to be interpreted as collisions between photons. The general kinematics of the final state are determined by QED - the process being separable into two distinct steps: the production and decay of the $\gamma\gamma$ CMS. The former is exactly calculable while the latter is largely unknown except in the case of pure QED processes and resonance production. The full matrix element for the process $e^+e^- \rightarrow e^+e^-\gamma\gamma \rightarrow e^+e^-X$ (Figure A.1) is then:

$$T^X = \frac{e^2}{q_1^2 q_2^2} [u(p'_1, \sigma'_1) \gamma^\mu u(p_1, \sigma_1)] [v(p'_2, \sigma'_2) \gamma^\nu v(p_2, \sigma_2)] A_{\mu\nu}^X \quad (A1-1)$$

The conventions used are those of Bjorken and Drell⁷⁰¹ except that $\hat{p} = \gamma^\mu p_\mu$. The notation used is given below

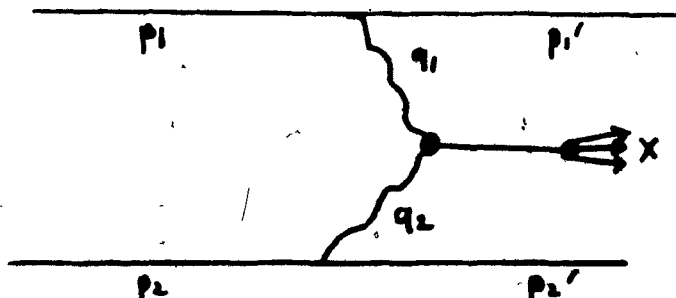


Figure A 1

p_i → momenta of colliding e^+e^- .

p'_i → momenta of scattered e^+e^- .

$q_i = p_i - p'_i$ → momenta of virtual photons.

e_i → polarization vectors for virtual photons.

$s = W_{\gamma\gamma}^2 = (q_1 + q_2)^2$ → Invariant mass squared of the $\gamma\gamma$ CMS.

$E'_i = p'^0_i$ → energy of scattered e^+e^- .

$\omega_i = q^0_i$ → Energy of virtual photons.

θ_i → Scattering angle of beam particle i .

k_j → Momenta of the j th particle in the final state $\gamma\gamma \rightarrow X$.

The matrix element for $\gamma\gamma \rightarrow X$ depends only on s, q_1^2, q_2^2 and the helicity states of the colliding photons.

Since the photons are virtual, scalar helicity states are allowed but the contribution of these to the

cross-section are suppressed e.g. $\sigma_{SS} \sim q_1^2 q_2^2$. Squaring the matrix element, averaging over the spins of colliding particles and summing over the final state spins yields:

$$|M|^2 = \frac{1}{4} \frac{(4\pi\alpha)^2}{(q_1^2 q_2^2)^2} \text{Tr} \left[\frac{(\not{p}'_1 + m_e) \gamma^\mu (\not{p}_1 + m_e) \gamma^{\nu'}}{4m_e^2} \right] \left[\text{Tr} \left[\frac{(\not{p}'_2 - m_e) \gamma^\mu (\not{p}_2 - m_e) \gamma^{\nu'}}{4m_e^2} \right] \cdot A_{\mu\nu}^{X_0} \cdot A_{\mu\nu}^X \right] \quad (\text{A1-2})$$

$$I_i^{\mu\nu} = \text{Tr} [(\not{p}'_i \pm m_e) \gamma^\mu (\not{p}_i \pm m_e) \gamma^{\nu'}]$$

$$= 4m_e^2 g^{\mu\nu} + 4[p_i^{\mu'} p_i^{\nu'} + p_i^{\nu'} p_i^{\mu'} - g^{\mu\nu} (p_i \cdot p_i')]$$

The trace was evaluated using the following formulae:

$$\text{Tr}(\hat{a}\hat{b}\hat{c}\hat{d}) = 4[(a \cdot b)(c \cdot d) + (a \cdot d)(b \cdot c) - (a \cdot c)(b \cdot d)] \quad (\text{A1-3})$$

$$2m_e^2 = q_i^2 + 2p_i \cdot p_i'$$

Including factors for normalization of the incident and scattered e^+e^- wavefunctions, final state phase space, and the relativistic flux factor, the cross-section for $e^+e^- \rightarrow e^+e^- \gamma^0 \gamma^0 \rightarrow e^+e^- X$ is derived to be:

$$d\sigma = \frac{(\pi\alpha)^2}{q_1^2 q_2^2} p_1^{\mu'} p_2^{\nu\nu'} A_{\mu\nu}^{X_0} A_{\mu\nu}^X \frac{\delta(q_1 + q_2 - \sum_{j \in X} k_j) (2\pi)^4}{\sqrt{(p_1 \cdot p_2)^2 - m_e^4}} \frac{d^3 p'_1 d^3 p'_2 d\Gamma}{(2\pi)^6 E_1 E_2}$$

$$= \frac{(\pi\alpha)^2}{q_1^2 q_2^2} p_1^{\mu'} p_2^{\nu\nu'} \frac{W_{\mu\nu}{}^{\mu'\nu'}}{\sqrt{(p_1 \cdot p_2)^2 - m_e^4}} \frac{d^3 p'_1 d^3 p'_2}{(2\pi)^6 E_1 E_2}$$

$$I_i^{\mu\nu} = -2q_i^2 p_i^{\mu\nu} \quad (\text{A1-4})$$

$$d\Gamma = \sum_{S_{\text{final}}} \prod_{j \in X} \Pi_{j \in X} \left[\frac{N_j d^3 k_j}{E_j (2\pi)^3} \right]$$

$$W_{\mu\nu}{}^{\mu'\nu'} = \int A_{\mu\nu} A_{\mu'\nu'} \delta(q_1 + q_2 - \sum_{j \in X} k_j) (2\pi)^4 d\Gamma$$

Note that the definition of $W^{\mu\nu}{}^{\mu'\nu'}$ given above differs from that of Budnev¹¹⁰ by a factor of 1/2. N_j accounts for the difference in wavefunction normalizations for fermions ($N_j = m_j$) and bosons ($N_j = \frac{1}{2}$). The hadronic tensor, $W^{\mu\nu}{}^{\mu'\nu'}$, can be related to the imaginary part of the forward scattering amplitude in $\gamma^0 \gamma^0 \rightarrow \gamma^0 \gamma^0$ via the optical theorem. Naively this tensor has $256 = 4^4$ independent components. However, due to gauge invariance this number can be reduced to 81:

$$q_{1,\mu} W^{\mu\nu}{}^{\mu'\nu'} = q_{1,\nu} W^{\mu\nu}{}^{\mu'\nu'} = q_{2,\mu'} W^{\mu\nu}{}^{\mu'\nu'} = q_{2,\nu'} W^{\mu\nu}{}^{\mu'\nu'} = 0 \quad (\text{A1-5})$$

If the process is invariant under Parity, Rotation, and Time-Reversal transformations the number of independent amplitudes reduces to 8. This is most easily observed when all tensors are represented in the helicity basis as the Parity transformation simply changes the sign of the helicity (in the $\gamma\gamma$ CMS this corresponds to interchanging the colliding photons). Rotation invariance forces (in terms of the helicity basis defined below) $a - a' = b - b'$. Invariance under the exchange of the primed and unprimed

superscripts corresponds to Time-Reversal Invariance. The helicity basis, $e(\pm 1)$, $e(0)$ is defined as:

$$\begin{aligned}
 q_i^\mu e_{i,\mu} &= 0 & e^*(a)e(b) &= (-1)^a \delta_{ab} \\
 e_2(\pm 1) &= e_1(\mp 1) & e_i^*(\pm 1) &= -e_i(\mp 1) \\
 e_1(0) &= iQ_1 & e_2(0) &= -iQ_2 \\
 Q_1 &= \sqrt{\frac{-q_1^2}{(q_1 \cdot q_2)^2 - q_1^2 q_2^2}} \left[q_2 - q_1 \frac{(q_1 \cdot q_2)}{q_1^2} \right] \\
 W_{a'b',ab} &= e_1^{*a'}(a') e_2^{b'}(b') W^{a'b',a'b} e_1^a(a) e_2^b(b) \\
 W_{a'b',ab} &= W_{-a'-b',-a-b} = W_{ab,a'b'}
 \end{aligned} \tag{A1-6}$$

The Q_i four vector is orthogonal to the "ith" photon momentum vector and its transverse helicity vectors - it is therefore parallel to the scalar helicity vector. Similarly, one can define a tensor, $R_{\mu\nu}$, that projects any vector into the two-dimensional subspace orthogonal to both the photon and the helicity-0 vectors, i.e. that subspace generated by the helicity ± 1 vectors:

$$\begin{aligned}
 R^{\mu\nu} &= R^{\nu\mu} = -g^{\mu\nu} + X^{-1} [(q_1 q_2)(q_1^\mu q_2^\nu + q_1^\nu q_2^\mu) - q_1^2 q_2^\mu q_2^\nu - q_2^2 q_1^\mu q_1^\nu] \\
 X &= (q_1 q_2)^2 - q_1^2 q_2^2
 \end{aligned} \tag{A1-7}$$

Using $R^{\mu\nu}$ and the Q_i^μ one can construct projection operators to select each symmetry class of the hadronic tensor. These operators project the appropriate helicity state from the density matrices: $\rho_i^{\mu\nu}$. The $\gamma\gamma$ cross-sections for various combinations of photon polarizations are given below. σ_{SS} and σ_{TT} represent the cross-sections for scattering of scalar, and transversely polarized virtual photons, respectively. As they represent the collisions of off-shell photons these are not, strictly speaking, "physical" cross-sections. On the other hand, they represent the hadronic matrix element in the process without the QED contribution muddying the waters. It is also easier conceptually to view the process as two-photon collisions with the QED factors absorbed in the "Luminosity" for the initial state.

$$\begin{aligned}
 W_{SS} &= 4\sqrt{X}\sigma_{SS} = W_{00,00} \\
 W_{TS} &= 4\sqrt{X}\sigma_{TS} = W_{+0,+0} = W_{-0,-0} \\
 W_{TS}^+ &= 4\sqrt{X}\tau_{TS}^+ = \frac{1}{2}(W_{++00} + W_{0+,-0}) \\
 W_{TS}^- &= 4\sqrt{X}\tau_{TS}^- = \frac{1}{2}(W_{++00} - W_{0+,-0}) \\
 W_{TT} &= 4\sqrt{X}\sigma_{TT} = \frac{1}{2}(W_{++++} + W_{+-,-+}) = \frac{1}{2}(W_{--,-} + W_{-+,-+}) \\
 W_{TT}^+ &= 4\sqrt{X}\tau_{TT}^+ = W_{++,-} = W_{--,+} \\
 W_{TT}^- &= 4\sqrt{X}\tau_{TT}^- = \frac{1}{2}(W_{++++} - W_{+-,-+})
 \end{aligned} \tag{A1-8}$$

Some of the corresponding projection operators are:

$$R_{SS}^{\mu\nu\rho\sigma} = Q_1^\mu Q_1^\nu Q_2^\rho Q_2^\sigma = e_1^\mu(0)e_1^\nu(0)e_2^\rho(0)e_2^\sigma(0)$$

$$R_{TS}^{\mu\nu\rho\sigma} = R_1^{\mu\nu} Q_2^\rho Q_2^\sigma = (e_1^\mu(1)e_1^\nu(1) + e_1^\mu(-1)e_1^\nu(-1))e_2^\rho(0)e_2^\sigma(0) \quad (A1-9)$$

$$R_{TT}^{\mu\nu\rho\sigma} = R_1^{\mu\nu} R_2^{\rho\sigma} = (e_1^\mu(1)e_1^\nu(1) + e_1^\mu(-1)e_1^\nu(-1))(e_2^\rho(1)e_2^\sigma(1) + e_2^\rho(-1)e_2^\sigma(-1))$$

\sqrt{X} is the flux factor for the $\gamma\gamma$ collision given in A1-7 and the factor of 4, in A1-8, arises from the normalization of boson wavefunctions (i.e. $1/2E$ for "external" Boson lines or m/E for external fermion lines, the $E_{\gamma_1}E_{\gamma_2}$ factor from the wavefunction normalization is absorbed into the invariant flux factor - Bjorken and Drell⁷⁰¹, p.113). The r amplitudes correspond to spinflips for both photons and do not contribute if the scattering planes of the beam particles are unmeasured. The r^0 amplitudes only contribute if the beam particles are polarized⁷⁰³ i.e. if the $R_{TS}^{\mu\nu\rho\sigma}$ were calculated explicitly using equations A1-3 and A1-9 the result would cancel to zero - one must include the correct spin projection operators in the trace calculation. Only the TT terms survive for real photons as the scalar degree of freedom disappears in this limit. The final expression for the cross-section - the form that most commonly appears in the literature - is then:

$$d\sigma = \frac{\alpha^2}{16\pi^4 q_1^2 q_2^2} \sqrt{\frac{(q_1 \cdot q_2)^2 - q_1^2 q_2^2}{(p_1 \cdot p_2)^2 - m_e^4}} [4\rho_1^{++}\rho_2^{++}\sigma_{TT} + 2|\rho_1^{+-}\rho_2^{+-}|r_{TT} \cos 2\phi + 2\rho_1^{++}\rho_2^{00}\sigma_{TS} + 2\rho_1^{00}\rho_2^{++}\sigma_{ST} + 2\rho_1^{00}\rho_2^{00}\sigma_{SS} - 8|\rho_1^{+0}\rho_2^{+0}|r_{TS} \cos \phi] \frac{d^3 p_1' d^3 p_2'}{E_1' E_2'} \quad (A1-10)$$

Where:

$$q_i^2 = -4E_i E_i' \sin^2(\theta_i/2) - q_{min}^2 < 0, \quad q_{min}^2 = m_e^2 \omega_i^2 / (E \cdot E_i')$$

$$2\rho_1^{++} = \rho_1^{\mu\nu} R^{\mu\nu} = X^{-1} (4E\omega_2 - q_2^2 - q_1 \cdot q_2)^2 + 1 + 4m_e^2/q_1^2$$

$$\rho_1^{00} = \rho_1^{\mu\nu} Q_1^\mu Q_1^\nu = X^{-1} (4E\omega_2 - q_2^2 - q_1 \cdot q_2)^2 - 1 \quad (A1-11)$$

$$|\rho_1^{+0}| = \sqrt{(\rho_1^{00} + 1)} |\rho_1^{+-}|$$

$$|\rho_1^{+-}| = \rho_1^{++} - 1$$

APPENDIX 2: MONTE CARLO METHODS

A "Monte Carlo" is basically an extravagant numerical integration program - the term is derived from the random money-losing techniques developed in a Mediterranean city-state of the same name. The basic purpose of this type of computer program, as it is commonly applied in particle physics, is the generation of a set of n -dimensional vectors distributed according to a given mathematical function e.g. a set of four-vectors representing particles whose production is described by a known differential cross-section. One advantage of this representation, even for a simple distribution that is analytically integrable, is that cuts can be applied that are difficult to express in terms of the integration variables. The Monte Carlo programs described here attempt to calculate the visible cross-sections for various processes with the acceptance losses introduced by detector geometry and trigger arrangements included. It is difficult to integrate the $\gamma\gamma$ differential cross-sections analytically even for simple final state topologies as the $\gamma\gamma$ center of mass is always Lorentz boosted relative to the detector.

All Monte Carlo programs must use some sort of random number generator. The most commonly used program of this type is called a "pseudorandom" number generator, and is supplied as a standard part of most computer system libraries. A pseudorandom number generator⁷⁰⁴ produces a well defined and reproducible sequence of numbers evenly distributed on the interval $(0, 1)$. The most common algorithm used produces an integer sequence - each number being produced by multiplying the previous number (starting with a seed number provided by the user) by a very large number. The operation of multiplication then produces an integer overflow (i.e. it results in a number greater than the largest integer allowed by the CPU word size, 2^{n-1} where $n = 16, 32, \text{ or } 60$) which is automatically truncated leaving the least significant digits behind. The truncated number is then divided by the largest integer allowed to produce a number in the range $(0, 1)$. This procedure results in a nearly uncorrelated sequence, but since only a finite number of integers are available from the computer the sequence must repeat itself eventually. For an optimized algorithm the maximum period of the generator approaches 2^{n-1} numbers - the maximum number of different integers given a computer word length n .

The simplest Monte Carlo algorithm is known as the "Hit or Miss" method. For a one dimensional function this can be visualized quite easily. Given a function, $x \rightarrow f(x)$, representing an unnormalized differential probability distribution, the extremes of x and $f(x)$ define a rectangular area in the $(x, f(x))$ plane. Many (x, y) are then generated evenly throughout the rectangle using a pseudorandom number

generator. For each x value generated the $f(x)$ is calculated and if the second random number, $y \leq f(x)$, the "event" is accepted, i.e. the accepted numbers, (x, y) , will have the required distribution. In other words, the program generates points evenly distributed in the rectangle defined by the extreme values of dependent and independent variables and the fraction of these points that falls in the area under the function is used to calculate the area of the function. The normalized value of the function, $w(x) = f(x)/f(x)_{max}$, is often called a "weight". It is apparent that:

$$I = \int_{x_{min}}^{x_{max}} f(x') dx' = \frac{V \cdot N_{accepted}}{N} = \frac{V}{N} \sum_N w = V \cdot \bar{w} \quad (A3-1)$$

Where N is the total number of points in the rectangle, $N_{accepted}$ is the number of these that fall inside the function's area, and V is the area of the rectangle. There are two ways of calculating the result of the integration: one uses the number of accepted events, $N_{accepted}$, and the other uses the sum of weights. The latter method reduces to a simple numerical integration method with the independent variable points chosen randomly. It is more CPU-time efficient as the extra random numbers used to decide if an event is accepted or not are not needed. It is also more accurate as the error of a Monte Carlo integration behaves as $V \cdot \sigma(w(x))/\sqrt{N}$, where $\sigma(w(x))$ is the variance of the function weights:

$$\begin{aligned} M(w(x)) &= \frac{\int \dots \int w(x) d^n x}{\int \dots \int d^n x} = \frac{1}{V \cdot f_{max}} \int \dots \int f(x) d^n x \\ \sigma(w(x)) &= \sqrt{\frac{\int \dots \int (w(x) - M(w(x)))^2 d^n x}{\int \dots \int d^n x}} \\ \sigma(w(x)) &= \sqrt{(\sum w^2 - (\sum w)^2/N)/N} \end{aligned} \quad (A3-2)$$

If one only uses the number of accepted "events" the error is $1/\sqrt{N_{accepted}}$ - only a small portion of the available information is used so the error is increased. For an N-dimensional integration the "Hit or Miss Method" generalizes very easily:

- (1) Given N-independent variables $\{(x'_{min}, x'_{max}), 1 \leq i \leq N\}$ and the dependent variable $0 \leq f(\vec{x}) \leq y_{max}$ generate a random number within the specified limits for each of the $N + 1$ variables $\{x; y\}$. Count these trial events by incrementing n_T .
- (2) If $y \leq f(\vec{x})$ count the "event" as accepted, i.e. increment n_A . These accepted events have weight one.
- (3) Calculate cuts on the function (i.e. $m \leq n$ dimensional hypersurfaces) if the events survives then count this as a "detected" event, i.e. increment n_D .
- (4) Repeat steps 1-3 as many times as possible given computer time cost and availability etc.

(5) The value of the integral with just the cartesian limits is:

$$I = \int \dots \int f(x) d^n x = \frac{n_x}{n_y} y_{max} \prod_{i=1, N} (x_{max}^i - x_{min}^i) \quad (A3-3)$$

while the value with cuts is obtained by substituting $n_d \rightarrow n_c$. If $f(x)$ represents a cross-section for a physical process the events passing the cut in section (2) can be treated as real events for detector design, background, or acceptance calculations.

One can calculate partially integrated distributions by filling histograms with the appropriate coordinate x^i or with a function of several coordinates. This procedure can easily be extended to noncartesian functions. For one-dimensional integration many better integration methods exist. The trapezoidal rule divides the integration region into sections and takes the value of the function at the center of each section, approximating the function by a set of trapezoids. The error of this method⁷⁰⁶ is $\sim 1/n^2$. The trapezoidal rule integrates exactly polynomials of degree 1 (straight lines). Higher order quadrature techniques exist - these integrate exactly polynomials of increasingly high degree, but convergence for these methods slows as dimension of integration increases while Monte Carlo convergence is independent of dimension. Monte Carlo techniques have the conceptual advantage that they can be used to produce "events of weight one". The relative errors of various integration algorithms⁷⁰⁶ is shown in Table 1.

Integration Method	Uncertainty for d-dimensions, N events
Monte Carlo	$\sim 1/\sqrt{N}$
Trapezoidal Rule	$\sim N^{-2/d}$
Simpson's Rule	$\sim N^{-4/d}$
Gauss' Rule (of order m)	$\sim N^{-(2m-1)/d}$

Table A3.1 Uncertainty of Various Integration Algorithms

More efficient methods of Monte Carlo event generation exist. If a one-dimensional distribution is analytically integrable and the integrand invertible, the distribution can be generated exactly using a flat

random number distribution as input to the algorithm. Consider:

$$\begin{aligned}
 F(x) &= \int_{x_{\min}}^x f(x') dx' \\
 u &= \frac{F(x)}{f(x)_{\max}} \\
 \frac{dn}{dx} &= \frac{f(x)}{f(x)_{\max}} \\
 \frac{dn}{du} &= \frac{dn}{dx} \cdot \frac{dx}{du} = 1
 \end{aligned}
 \tag{A3-4}$$

The variable, u , therefore has a constant distribution. From this one calculates $x = F^{-1}(F(x_{\max}) \cdot u)$. If the u 's are generated by a pseudorandom number generator the numbers, x , will have the desired frequency distribution, $f(x)$. For a multidimensional distribution, e.g. $f(x, y) = g(x)h(x, y)$, this becomes slightly more complicated. One must first generate x using $F_y(x) = \int_{y_{\min}}^{y_{\max}} f(x, y) dy$ as the input distribution (i.e. generate x for any y) and having generated x generate y from the full distribution with x fixed - $f(x, y)$ is proportional to the conditional probability of x given y . If the function can be written as $f(x, y) = g(x)h(y)$ both distributions can be generated independently. When a complicated distribution can be separated into several additive positive definite expressions and exact algorithms can be built for each of these separately, the Monte Carlo can be split into "sub-generators". In this case the final distribution is generated by giving each additive term a probability defined by its contribution to the total integral and branching to one of the "sub-generators" accordingly (each decision being decided by a "dice-roll" i.e. a new pseudorandom number).

One can combine the "Hit or Miss" and the "Exact" methods to produce an algorithm known as "Importance Sampling". In this technique the complicated cross-section that is being integrated, $f(\vec{x})$, is first approximated by a simpler function, $g(\vec{x})$, which is amenable to the "Exact" method and the N dependent variables are generated according to this distribution. The generation of these random vectors replaces the generation of vectors over the larger volume used in the "Hit or Miss" method - if the approximation is good only a small fraction of the "wasted volume" of the simple algorithm remains. For a given \vec{x} the probability of an event lying inside the $(N+1)$ -volume defined by $f(\vec{x})$ is $w(\vec{x}) = f(\vec{x})/g(\vec{x})$ i.e. $g(\vec{x})$ replaces $f(\vec{x})_{\max}$ in the weight calculation resulting in a higher average weight. It is assumed that $g(\vec{x})$ is normalized so that the weight has a maximum value ≤ 1 . The main advantages of this method are dependent on the quality of the approximation. If this is good the efficiency for producing events of weight one, $\frac{\# \text{accepted}}{\# \text{generated}}$ is improved, and the variance is much smaller leading to faster convergence. It occasionally becomes necessary to use several different approximations to the function in different regions

of phase space. This is more complicated but can improve the convergence of the program. Each region is then given a weight, proportional to the maximum weight of the approximation used (ideally they should all be equal to 1) and the integral of the approximate function.

In summary, the general problem treated by Monte Carlo techniques is the evaluation of:

$$R = \int \dots \int_V r(\vec{\beta}) d^n \rho \quad (\text{A3-5})$$

Which can be discretized as (via the "Hit or Miss" Method):

$$R = \frac{V}{N} \sum r(\vec{\beta}_i) = V \langle r \rangle_V \quad (\text{A3-6})$$

Where $\vec{\beta}_i$ are N points randomly distributed in the n -dimensional volume of integration. One can change the variables of integration ("Importance Sampling") $\vec{\beta} \rightarrow \vec{\alpha}$:

$$R = \int \dots \int_W r(\vec{\beta}) J(\vec{\beta}) d^n \alpha = W \langle rJ \rangle_W = \frac{W}{N} \sum r(\vec{\beta}_i) \cdot J(\vec{\beta}_i) \quad (\text{A3-7})$$

If the Jacobian of the transformation, $J(\vec{\beta}_i)$, is chosen so as to smooth the dynamic range of the integration the efficiency of the Monte Carlo improves. Clearly the optimum is $J(\vec{\beta}) = r(\vec{\beta})^{-1}$ which in effect requires an analytic solution to the integral - it also, reasonably enough, causes the variance of the result to go to zero:

$$\Delta R = \frac{W}{\sqrt{N}} \sigma(rJ)_W = \frac{1}{N} \sqrt{\sum (w - \bar{w})^2} = \frac{1}{N} \sqrt{\sum w^2 - (\sum w)^2 / N} \quad (\text{A3-8})$$

The integrands in A3-4,6 are generally referred to as statistical weights. These determine the relative importance of the event. The last step in the "Importance Sampling" algorithm turns these into "events of weight one", i.e. events of equal importance or probability. If one calculates an observable using every weighted event the statistical fluctuation is less. Using $w = 1$ events only the standard "experimental" $1/\sqrt{N}$ fluctuation remains.

APPENDIX 3: THE ARGUS COLLABORATION

H. Albrecht, U. Binder, G. Drews, G. Harder, H. Hasemann,
A. Philipp, W. Schmidt-Parzefall, H. Schröder,
H. D. Schulz, F. Selonke, R. Wurth.
DESY, Hamburg, Germany.

A. Drescher, B. Gräwe, W. Hofmann¹, A. Markees²,
U. Matthiesen, H. Scheck, J. Spengler, D. Wegener.
Institut für Physik, Universität Dortmund³, Germany.

R. Heller⁴, K. R. Schubert, J. Stiewe, R. Waldi, S. Weseler.
Institut für Hochenergiephysik;
Universität Heidelberg⁵, Germany.

N. N. Brown⁶, K. W. Edwards⁶, W. R. Frisken⁷, Ch. Fukunaga⁷,
D. J. Gilkinson⁸, D. M. Gingrich⁸, M. Goddard⁷,
P. C. H. Kim⁸, R. Kutschke⁸, D. B. MacFarlane⁸,
J. A. McKenna⁸, K. W. McLean⁸, A. W. Nilsson⁸, R. S. Orr⁸,
P. Padley⁸, P. M. Patel⁸, J. D. Prentice⁸,
H. C. J. Seywerd⁸, B. J. Stacey⁸, T.-S. Yoon⁸, J. C. Yun⁸,
Institute of Particle Physics⁹, Canada.

R. Ammar, D. Coppage, R. Davis, S. Kanekal, N. Kwak.
University of Kansas¹⁰, Lawrence, Kansas, USA.

P. Bockmann¹¹, L. Jönsson, Y. Oku.
Institute of Physics, University of Lund¹², Sweden.

M. Danilov, V. Lubimov, V. Matveev, N. Nagovitsin,
V. Ryltsov, A. Semenov, Yu. Semenov, V. Shevchenko,
V. Soloshenko, V. Sopov, I. Tichomirov, Yu. Zaitsev.
Institute of Theoretical and Experimental Physics,
Moscow, USSR.

R. Childers, C. W. Darden, and H. Gennow¹³.
University of South Carolina¹⁴, Columbia, S.C., USA.

¹Now at UC, Berkeley, USA

²Now at Swiss Administration, Berne, Switzerland

³Supported by the Bundesministerium für Forschung und Technologie, Federal Republic of Germany.

⁴Now at DESY.

⁵McGill University, Montreal.

⁶Carlton University, Ottawa.

⁷York University, Downsview.

⁸University of Toronto, Toronto.

⁹Supported by the Natural Sciences and Engineering Research Council, Canada.

¹⁰Supported by the U.S. National Science Foundation and a University of Kansas Faculty Improvement award.

¹¹Now at CERN.

¹²Supported by the Swedish Research Council.

¹³On leave of absence from the University of Stockholm, Sweden.

¹⁴Supported by the U.S. Department of Energy, under contract DE-AS09-90ER10000.

REFERENCES

101. M. Jacob, *History of ISR Physics*, CERN preprint TH/84-2207 (1984).
102. S. L. Wu, *e^+e^- Physics at PETRA - The First Five Years*, DESY Preprint 028 (1984).
103. E. Radermacher, CERN Preprint EP/84-041.
104. K. H. Mess, B. H. Wiik, *Recent Results in Electron-Positron Interactions*, DESY Preprint 011 (1983).
105. H. Euler and B. Kockel, *Nass. Wiss.* **23** (1935), p. 246.
106. A. I. Akheiser, *Phys. Zeits. Sow.* **11** (1937), p. 263.
107. E. Iacopini, CERN Preprint EP/84-060 (1984).
108. L. D. Landau E. M. Lifshitz, *Sov. Phys.* **6** (1934), p. 244.
109. W. Wagner, *Photon-Photon Reactions*, Physikalisches Inst. Aachen Preprint 83-08.
110. S. J. Brodsky, T. Kinoshita, H. Terasawa, *Phys. Rev. D* **4** (1971), p. 1532.
111. F. E. Low, *Phys. Rev.* **120** (1960), p. 582.
112. F. Calogero, C. Zemach, *Phys. Rev.* **120** (1960), p. 1860.
113. H. Terasawa, *Rev. Mod. Phys.* **45** (1973), p. 618.
114. N. Arteaga-Romero et al., *Phys. Rev. D* **3** (1971), p. 1869.
115. V. N. Baier, V. S. Fadin, *Sov. Phys. JETP* **34** (1971), p. 263.
116. A. M. Akukhov, *Sov. Jour. Nucl. Phys.* **14** (1972), p. 220.
117. H. Cheng, T. T. Wu, *Nucl. Phys.* **B22** (1971), p. 461.
118. P. L. Csonka, *Phys. Lett.* **B24** (1967), p. 625.
119. V. M. Budnev, I. F. Ginzburg, G. V. Maelidin, and V. G. Serbo, *Physics Reports* **15** (1975), p. 181.
120. E. Witten, *Nucl. Phys.* **B120** (1977), p. 189.
121. J. B. Dainton, Rutherford Lab Preprint RL-83-103 (1983).
122. D. M. Binie et al., *Phys. Lett.* **85B** (1979), p. 141.
123. P. Jenni et al., *Phys. Rev.* **D27** (1983), p. 1031.
124. D. L. Burke, "Proc. 21st Conf. on HEP, Paris", (*J. de Phys. Suppl.* **12**, Coll. C-3, ed. P. Petiau and M. Porneuf), 1982, p. 7.
125. K. Wacker, "Proc. 18th Rencontre de Moriond, La Plagne", 1983.
126. M. Oreglia, "Proc. 18th Rencontre de Moriond, Les Arcs", 1980.
127. D. Luke, "Proc. 21st Conf. on HEP, Paris", (*J. de Phys. Suppl.* **12**, Coll. C-3, ed. P. Petiau and M. Porneuf), 1982, p. 7.
128. E. D. Bloom and C. W. Peck, *Ann. Rev. Nucl. Part. Sci.* **33** (1983), p. 143.
129. C. N. Yang, *Phys. Rev.* **77** (1950), p. 242.
130. F. M. Renard, SLAC Preprint 8126 (1983).
131. MARKII, J. R. Smith et al., SLAC Preprint 8205 (1983).
132. F. M. Renard, "Proc. 5th Int. Coll. on $\gamma\gamma$ Inter., Aachen", (ed. Ch. Berger, *Lecture Notes in Physics*), Springer-Verlag, 1983, p. 74.
133. M. Gell-Mann, *Phys. Lett.* **8** (1964), p. 214.
134. M. Han, Y. Nambu, *Phys. Rev.* **139** (1965), p. 1006.
135. F. M. Zerwas, Institut. fur Theor. Physik, Aachen Preprint 24 (84).
136. G. Kopp, T. F. Walsh, and P. Zerwas, *Nucl. Phys.* **B70** (1974), p. 461.
137. J. H. Field, Lab. de Phys. Nucl. et des Hautes Energies preprint 83-08 (1983).
138. S. L. Adler, *Phys. Rev.* **177** (1969), p. 2426.
139. J. S. Bell and R. Jackiw, *Nuovo. Cim.* **60A** (1969), p. 47.

140. N. Wermes, "Proc. 5th Int. Coll. on $\gamma\gamma$ Inter., Aachen", (ed. Ch. Berger, Lecture Notes in Physics), Springer-Verlag, 1983, p. 119.
141. Ch. Berger, Physik. Institut. Aachen preprint 83/22 (1983).
142. G. W. S. Leith, "Proc. 11th Scottish Universities Summer School in Physics", (ed. J. Cummings, H. Osborn), Academic Press, 1970.
143. I. F. Ginsburg and V. G. Serbo, Phys. Lett. 109B (1982), p. 331.
144. Ch. Berger, PLUTO Collaboration, Phys. Lett. 89B (1979), p. 120.
145. Ch. Berger, PLUTO Collaboration, Phys. Lett. 99B (1981), p. 387.
146. W. Hillen, (Thesis), Bonn University.
147. E. Hilger, DESY Preprint.
148. C. J. Biddick et al., Phys. Lett..
149. N. Wermes, (Thesis), Bonn University.
150. G. Knies, (Talk given at the Lake Tahoe $\gamma\gamma$ Conference, 1984).
151. W. Wagner, "Proc. 5th Int. Coll. on $\gamma\gamma$ Inter., Aachen", (ed. Ch. Berger, Lecture Notes in Physics), Springer-Verlag, 1983, p. 206.
152. G. P. Lepage and S. J. Brodsky, Phys. Rev. D22 (1980), p. 2157.
153. G. P. Lepage and S. J. Brodsky, Phys. Rev. D24 (1981), p. 1808.
154. P. H. Damgaard, Nucl. Phys. B211 (1983), p. 495.
155. G. Alexander, U. Maor, and C. Milstene, Phys. Lett. 131B (1983), p. 224.
156. G. F. von Darandel et al., CERN Preprint CERN-EP84-67 (1984).
157. M. Aihara et al. PEP 4/9 Collaboration, Proc. XXII Conf. on HEP, Leipzig (1984).
158. M. Althoff et al. TASSO Collaboration, (submitted to Physics Letters), DESY Preprint 084 (1984).
159. M. Aihara et al. PEP 4/9 Collaboration, University of California Preprint UCSD-HEP-84-01 (1984).
201. H. Albrecht et al., Phys. Lett 146B (1984), p. 111.
202. ARGUS Collaboration, H. Albrecht et al., ARGUS, A New Detector For DORIS, DESY Internal Report F15/Pro 148 (1979).
203. Innes et al., Phys. Rev. Lett. 39 (1977), p. 1240.
204. J. C. Yun, A Vertex Chamber for ARGUS, (M.Sc. Thesis, Carleton University, Ottawa, Canada).
205. M. Danilov et al., Nucl. Instr. Meth. 217 (1983), 153-159.
206. R. Heller et al., (submitted to Nuclear Instruments & Methods), Heidelberg Preprint IHEP-HD/84-08 (1984).
207. A. Drescher et al., DESY Preprint 028 (1983).
208. ARGUS Collaboration, H. Albrecht et al., (contributed paper), XXIInd International Conf. HEP, Leipzig (1984).
209. S. W. Herb et al., Phys. Rev. Lett. 39 (1977), p. 252.
201. JADE collaboration, W. Bartel et al., Phys. Lett. 118B (1982), p. 190.
202. CELLO collaboration, H. J. Behrend et al., Phys. Lett. 114B (1982), p. 378; Erratum, Phys. Lett. 125B (1984), p. 518.
203. Particle Data Group, Review of Particle Properties, Phys. Lett. 111C (1982).
204. PLUTO Collaboration, (to be published in Physics Letters), DESY Preprint 086 (1984).
205. TASSO Collaboration, M. Althoff et al., Z.Phys. C16 (1982), p. 13.
206. TASSO Collaboration, R. Brandelik et al., Phys. Lett. 97B (1980), p. 448.
208. MARK II Collaboration, D. L. Burke et al., Phys. Lett. 108B (1981), p. 153.
209. CELLO Collaboration, H. J. Behrend et al., Z.Phys. C21 (1984), p. 205.
210. TASSO Collaboration, M. Althoff et al., Phys. Lett 121B (1983), p. 216.
211. MARKII Collaboration, G. S. Abrams et al., Phys. Rev. Lett. 43 (1979), p. 477.
212. TASSO Collaboration, M. Althoff et al., (to be published in Physics Letters), DESY Preprint 069 (1984).

313. Michael Feindt, PLUTO, *Diplomarbeit*, DESY Internal Report 008 (1984).
401. K. Wille, (to be published in *Physics Letters*), DESY Preprint 047 (1981).
402. E. Lorenz, Max Planck Institute für Physik und Astrophysik Preprint MPI-PAE/Exp.B1.139 (1984).
403. G. Blamar et al., (Extended version of a Contributed Paper to the EPS International Conference on High Energy Physics, Lisbon, July 1981), Max Planck Institute für Physik und Astrophysik Preprint.
404. K. Kleinknecht, *Physics Reports* 84 (1982), p. 85.
405. Ch. Bieler et al., (submitted to *Nuclear Instruments & Methods*), DESY Preprint 84-041 (1984).
407. H. Dietl et al., Max Planck Institute für Physik und Astrophysik Preprint MPI-PAE/Exp.B1.134 (1983).
407. J.A. Bakken et al., (submitted to *Nuclear Instruments & Methods*), CERN Preprint CERN/EP 84-89 (1984)
408. G.J. Bobbink et al., (submitted to *Nuclear Instruments & Methods*), Carnegie-Mellon Univ. Preprint HEP-15/Rev (1984).
501. PLUTO Collaboration, Ch. Berger et al., (to be published in *Physics Letters*), DESY Preprint 098 (1984).
502. S.J. Brodsky, T. Kinoshita, and H. Terazawa, *Phys. Rev. Lett.* 35 (1970), p. 972.
503. F.A. Berends, P.H. Daverveldt, and R. Kleiss, U. of Leiden Preprint (1984).
504. H. Kolanoski, "Two-Photon Physics at e^+e^- Storage Rings", (*Springer Tracts in Modern Physics*), Springer-Verlag, 1984.
505. A. Weinstein et al., *Phys. Rev. D* 28 (1983), p. 3896.
506. A. Cordier, Lab. de l'Accel. Linéaire Preprint 84/41 (1984)
507. G. Barbiellini, "77 Collisions, Amiens", Proc. of 4th International Workshop ed. G. Cochard and P. Kessler, *Lecture Notes in Physics*, Springer-Verlag, 1980, p. 9.
508. V.A. Sidorov, *Journal de Physique, Colloq.* C3 (1974), p. 15.
509. V.E. Balakin et al., *Phys. Lett. B* 34 (1971), p. 663.
510. V.E. Balakin et al., *Sov. Phys. JETP. Lett.* 11 (1970), p. 38.
511. G. Salvini, *Journal de Physique, Colloq.* C3 (1974), p. 1.
512. C. Bacci et al., *Lett. Nuovo Cimento* 8 (1972), p. 709.
513. L. Paolusi et al., *Lett. Nuovo Cimento* 10 (1976), p. 435.
514. G. Barbiellini et al., *Phys. Rev. Lett.* 33 (1974), p. 365.
515. J. Zipse, "Quantum Electrodynamics with the Spear Magnetic Detector", (Berkeley publication, LBL 4281), 1975.
516. G. Menessier, *Z. Phys.* C16 (1983), p. 241.
517. PLUTO Collaboration, Ch. Berger et al., *Phys. Lett.* 94B (1980), p. 354.
518. TASSO Collaboration, R. Brandelik et al., *Z. Phys.* C10 (1981), p. 117.
519. SPEAR Collaboration, A. Roussarie et al. *Phys. Lett.* 105B (1981), p. 304.
520. T. Kinoshita, B. Nisic, and Y. Okamoto, *Phys. Rev. Lett.* 53 (1984), p. 717.
521. J.E. Olsson, "Proc. 5th Int. Coll. on 77 Inter., Aachen", (ed. Ch. Berger, *Lecture Notes in Physics*), Springer-Verlag, 1983, p. 45.
522. B. Schremp-Otto, F. Schremp and T. Walsh, *Phys. Lett.* 86B (1971), p. 463.
523. P. Grassberger and R. Kögerler, *Nucl. Phys.* B106 (1976), p. 451.
524. C. Edwards et al., *Phys. Lett.* 110B (1982), p. 82.
524. A. Coureau et al., *Phys. Lett.* 96B (1980), p. 402.
601. Ch. Berger, "77 Collisions, Amiens", Proc. of 4th International Workshop ed. G. Cochard and P. Kessler, *Lecture Notes in Physics*, Springer-Verlag, 1980, p. 82.
602. Ch. Berger et al., PLUTO Collaboration, DESY Preprint 080 (1984).
603. T.D. Gottschalk, CalTech Preprint CALT/68-1080 (1963).
604. Z. Koba, H.B. Nielson, and P. Oleson, *Nucl. Phys.* B40 (1972), p. 317.
605. Ch. Berger et al., DESY Preprint 074 (1984).

606. ARGUS Collaboration, DESY PRC Report 06 (1983).

607. P.Jenni, "77 Collisions, Amiens", Proc. of 4th International Workshop ed. G.Cochard and P.Kessler, Lecture Notes in Physics, Springer-Verlag, 1980, p. 83.

701. J.D.Ejorsten, S.D.Drell, "Relativistic Quantum Mechanics", McGraw-Hill, 1964.

702. G.Bonneau, M.Gourdin, and F.Martin, Nucl.Phys. B84 (1973), p. 573.

703. D.A.Dicus, Phys.Rev. D14 (1977), p. 2684.

704. K.Binder and D.Stauffer, "Applications of the MC Method", (Topics in Current Physics), Springer-Verlag, 1983, p. 1.

705. F.James, "Formulas and Methods in Experimental Data Evaluation", (Numerical Integration - Section N), 1984, p. 1.